

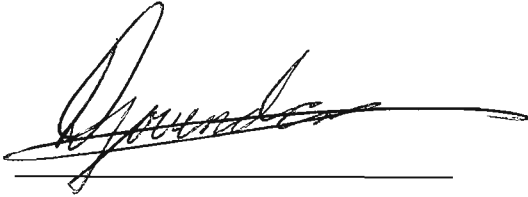
VIRTUAL PROTOTYPING OF AN ARTICULATED DUMP TRUCK

In fulfillment of the degree MScEng (MECH)

Date of submission : 01st September 2003
Candidate : Mr. Deena Govender
Supervisor : Dr. S. Kaczmarczyk

DECLARATION

I state unequivocally that the work presented herein is my own unaided effort and that all external sources have been explicitly stated and referenced. This work has not been submitted in whole or part, for any degree to any institution previously. I hereby submit this dissertation in whole fulfilment of the requirements for the degree of MSc Eng (MECH) to the University of Natal, Durban on this the 1st Day of September 2003.

A handwritten signature in black ink, appearing to read 'Deena Govender', is written over a horizontal line.

Mr. Deena Govender

ID No. 7612275054083

ACKNOWLEDGEMENTS

The author would like to place on record his thanks to the following individuals and organisations:-

- **Dr. S. Kaczmarczyk** for his sincere support and understanding throughout this project.
- **BELL Equipment (PTY) Ltd.** for their financial support and providing the impetus for this research effort.
- **Danie du Plessis** and **Rick Chianese** (BELL Equipment) for being the link to the BELL ADT and for their time and advice.
- **Shaun Savy** and **Desmond Rooplal** (School of Mechanical Engineering, UND) for their assistance with computing matters at odd hours and without whom this project would have been immeasurably more difficult.
- **Clinton Stone** (MSC Africa) for assisting with ADAMS and for always being a valuable source of advice.
- The various members of the **ADAMS ASK** online mailing list for their often eleventh-hour advice.
- The students of the undergraduate teams who assisted with this project in 2000 and 2001.
- **BMW S.A.** for allowing me time off work to complete important stages of the project.
- **Mr. Ewald Fischer** and **Arne Margold** (EF-31, BMW AG) for their assistance with the use of ADAMS during October to December 2002.
- **Mr. Hans Heltmann** (EG-32, BMW AG) for his advice on analysing test data from automotive compliant suspension components.
- **My parents and family** for their encouragement throughout.
- **My friends** who provided me with support in times of need and for being prepared to discuss the merits of this work with me.
- **Dinesh Balliah** who was my pillar of strength through times when the task ahead of me seemed insurmountable and who always believed I could complete this work.

ABSTRACT

In the modern automotive industry product times to market are being increasingly compressed. In the earthmoving and construction machine industry this is also true with the manufacturer having to respond to new customer requirements quickly and decisively. Virtual prototyping is a vital tool in the vehicle engineer's armoury, allowing a large portion of developmental investigation to be done on the virtual model with the attendant savings in time and cost and allowing often dangerous manoeuvres to be predicted and investigated prior to actual physical prototype testing. The University of Natal/BELL Equipment collaborative effort involves the vehicle dynamics modelling and model validation of a BELL Equipment manufactured B40C Articulated Dump Truck (ADT). The modelling was completed using the multibody system (MBS) simulation software package, ADAMS. Initial modelling and simulation results are presented with specific attention paid to the introduction of valid data for compliant joints in the MBS as well as modelling of the tire. The physical testing of the ADT is also presented as well as a discussion of the data acquisition system. Key results from the physical testing of the ADT are also presented and discussed.

KEYWORDS: Vehicle dynamics, Virtual Prototyping, Articulated Dump Trucks, Vehicle testing, Multibody Systems Simulation

CONTENTS

Declaration	ii
Acknowledgements	iii
Abstract	iv
Contents	v
1. Introduction	1
2. Fundamentals of Vehicle Dynamics	7
2.1. The Pneumatic Tire	7
2.1.1. Tire Fundamentals and Construction	8
2.1.2. Axes, Notation and Principle Forces and Moments	10
2.1.3. Mechanics of Force Generation at the Contact patch	12
2.1.4. Rolling Resistance	15
2.1.5. The Generation of Principle Forces and Moments	21
2.1.5.1. Stationary In-Plane Dynamics	21
2.1.5.2. Stationary Out-of-Plane Dynamics	25
2.1.5.3. Combined Slip and Non-stationary Behaviour	34
2.1.6. Tire Modelling for Vehicle Dynamics Simulation	40
2.2. Approaches to Modelling of Compliant suspension components in MBS codes	46
2.3. General Vehicle Dynamics Fundamentals	49
3. Vehicle Testing and Data Analysis	56
3.1. Vehicle Tests	57
3.1.1. Steady State Track Lapping	58
3.1.2. Single Lane Change Tests	59
3.1.3. Straight-line Acceleration and Brake Tests	60
3.1.4. Bump Test	60
3.2. Measurement Equipment and Sensors	61
3.3. Test Setup	64
3.4. Test Results	68
3.4.1. Steady-State Handling Tests	68

3.4.2. Transient Handling Tests	73
3.4.3. Vertical Response tests	77
4. ADAMS Modelling	82
4.1. ADAMS Modelling Principles	82
4.2. Constructing the rigid body model in the ADAMS environment	86
4.3. Compliant suspension components	94
4.3.1. Determining the Stiffness and Damping Values	95
4.3.2. Spherelastic Bearing	100
4.3.3. A-Frame Bearing	102
4.3.4. Sandwich Box	106
4.3.5. Asymmetric Bearing	109
4.3.6. Suspension Strut	111
4.3.7. Discussion of Test Results for Compliant Suspension Components	119
4.3.8. Implementation of the Compliance Force Effects in ADAMS	121
4.4. Modelling the Tire and Road	125
4.4.1. The Fiala Tire Model in ADAMS	127
4.4.2. The Road Model in ADAMS	146
4.4.3. Discussion of the Various Methods of Constructing ADAMS Road Data Files	150
4.5. Dynamic Controllers	155
4.5.1. Modelling Controllers in ADAMS	156
4.5.2. The Speed Controller	159
4.5.3. The Path-following Controller	162
5. Simulation of the ADAMS ADT Model	170
5.1. Simulating the ADAMS ADT model	172
5.2. Simulation Results	179
6. Conclusion	200
A. Appendix A	203
B. Appendix B	206
C. Appendix C	211
D. Appendix D	214
E. Appendix E	220
References	229

1. INTRODUCTION

This work has as its focus the vehicle dynamics modelling of the BELL Equipment B40C articulated dump truck (ADT) via the construction and validation of a virtual prototype. More specifically the study is a first attempt at virtual prototyping of the construction, mining and agricultural machinery manufactured at BELL Equipment. Virtual prototyping for vehicle dynamics applications has fast become a valuable conceptualisation and design tool of the modern automotive engineer. This chapter begins by introducing the concept of virtual prototyping and examines the reasons for its increasing value in automotive design along with discussing the enabling technologies that have brought it to the fore. The section concludes by outlining the structure of this project and presents an overview of this dissertation.

In a conventional design process many physical prototypes have to be built. This is because the physical system is the ultimate model of reality. It is reality. As analytical techniques are developed engineers are able to predict to a greater extent beforehand how a desired system will behave. But it is still a requirement, given our current technological capabilities that physical prototypes have to be built. For a complex system like a vehicle, whose physical behaviour is impossible to understand in its entirety prior to its complete construction, many physical prototypes have to be built. Thus there is a gradual development of the vehicle using a combination of analytical techniques to predict behaviour and testing of physical prototypes to validate that prediction. Generally many subsystems of the desired system are tested in isolation and typically the process is iterative, requiring a significant number of prototypes, which have to be manufactured at significant cost. Due to the large number of tests that need to be conducted for a manufacturer to be able to manufacture and market a product within the parameters of the stringent safety and environmental requirements in place today, this process of gradual development is costly in terms of time as well. In addition sometimes the system being designed is required to operate in dangerous environments and situations. Without absolute knowledge of how a system under test will behave, the safety of test personnel is compromised when testing prototypes under these dangerous conditions. With the traditional methodology of a product's or system's development, testing of a prototype suggests improvements, which in turn needs to be verified, necessitating the modification, or building, of further prototypes. It is obvious that the more *a priori* knowledge a designer has of the physical behaviour of a desired system, the more efficient the development of the system can proceed in terms of three key parameters, cost, time and safety of test personnel.

This is where virtual prototyping comes to the fore. Virtual prototyping as the name suggests is the construction of a prototype in the virtual environment of a computer. By simulating the boundary conditions and physics of a system's behaviour on a computer, a system prototype can be constructed to be tested virtually. A virtual prototype immediately attacks the three key impediments to a traditional design cycle mentioned above. By having a virtual prototype, the requirement of having to build many prototypes saves a design project money, with the initial capital outlay for virtual prototyping software and computing hardware being rapidly recovered as the project proceeds. Changes to a prototype suggested by virtual tests can be implemented rapidly on the virtual prototype negating the need to modify or manufacture a new prototype, again saving costs but also time. Dangerous system behaviour can be tested safely with the virtual model. Simulations such as this can predict or highlight dangerous situations, and suggest precautions to be taken when the system is finally tested with a physical prototype.

With specific regard to virtual prototyping of automotive vehicle behaviour, the technology is used during many different and sometimes all the stages of a design process. A detailed design of a suspension can proceed directly from the customer or engineering requirements, for e.g. minimum toe angle change with vertical wheel travel. The parameters relating to the requirements can be identified and weighted according to their importance using 'design of experiment' techniques available in automotive virtual prototyping software. These identified parameters can then be optimised to design a virtual suspension assembly that meets the engineering requirements. The various forces generated at key points in the proposed design can be exported as load cases for finite element analysis (FEM) simulations that result in a strength optimised physical design of the system which is then finally tested physically to ensure that it meets the initial engineering and customer requirements. It can be appreciated that using virtual prototypes for design negates the need for a large number of prototypes that is typical of a traditional design process.

In addition to detailed design, virtual prototypes are frequently used at the concept stage of a new engineering project. At the start of a project a design engineer is presented with the requirements that the new design must fulfil, most probably in the form of customer requirements from the marketing arm of an institution. The designer will then process this information, reduce these customer requirements to engineering requirements and then formulate a finite number of conceptual designs, from experience, applicable literature or even lower level analytical mathematical models [76]. The choice of concept on which to expend further engineering effort is critical. A wrong initial concept choice can lead to costly re-engineering at advanced project stages. In many cases despite significant experience of the engineering team, choice of concept can be impossible without manufacture and testing of the

various concepts, especially with a complex system such as a vehicle. Two typical examples of the value of virtual prototypes for evaluating concepts are presented in [23] and [14].

In [23] engineers at the United States army, Tank-automotive and Armaments Command (TACOM) research and development centre utilised a virtual prototype of a six axle army transport truck to investigate the effects of replacing a dual tire configuration, (four tires per axle) with a super single tire with larger diameter and track width, on the yaw stability of the vehicle. By performing many steady state and transient handling tests with the virtual model the engineers were able to conclude that the dual tire configuration provided far more inherent yaw stability to the vehicle than the super single concept. Reference [14] details the work done in validating virtual models of two concepts being considered for the replacement of the United States Military Command, Logistic Vehicle System (USMC LVS). The two replacement concepts for the LVS were 10x10, five axle, 45ton articulated trucks, one concept having independent suspension at all wheels while the other having a combination of trailing arm and walking beam arrangements at the rear three axles. In this instance, physical prototypes of both the concepts were built in addition to the virtual prototypes. The virtual prototypes were validated against the physical prototypes over a predefined proving ground course for military vehicles of this nature. The validated virtual prototypes were then used to conduct further exhaustive tests to evaluate each concept's competitiveness and to eventually choose a suitable replacement. The value of virtual prototyping is clearly visible from these two cases.

The concept of virtual prototyping stems from the need to have *a priori* knowledge of a how a proposed new design will behave. In fact any analytical technique that proposes to predict the behaviour of a physical system before its construction and testing, points one toward a virtual prototype. It can be argued that virtual prototyping was humankind's intent ever since a human was able to analyse the behaviour of the physical world around it. With specific regard to the virtual prototyping of a vehicle's dynamic behaviour, a report conducted in 1976 on the effects of tire properties on the handling of busses and trucks [15] recommended that testing of new handling regimes or new designs be preceded by computerised and laboratory simulation. This was after significant damage was caused to facilities and injury to the human driver, during an extreme handling manoeuvre of a heavy truck. With such early justification for the need of virtual prototypes, the question of why a sudden increase in the usage of virtual prototyping has been precipitated only over the last decade [35] or so must be asked. The answer lies in the enabling technology of the computer. The rapid advancement of computing power and data storage has allowed the efficient implementation of analytical techniques developed over the past few centuries.

The reason for the advance in computing technology enabling a growth in the use of virtual prototyping for dynamic systems lies in the nature of the analytical techniques used to model the dynamic behaviour of systems of interconnected bodies or multibody systems (MBS). An automobile inarguably represents a MBS. In its simplest case a MBS consists of a system of rigid bodies connected by ideal joints that restrict the relative motion of the bodies it links. More complex MBS include joints that are not ideal but have relative motions defined by force relationships as well as bodies that are not strictly rigid i.e. they have some degree of elasticity that cannot be ignored under specific conditions.

In order to determine the behaviour of a MBS, the equations of motion (EOM) of the MBS under the influence of generalised and applied forces must be developed and then solved. There have been many techniques utilised to determine these equations but essentially they can be reduced to two fundamental theories; that of vector mechanics utilising Newton-Euler methods and Lagrangian mechanics derived from the principles of virtual work [67], [76]. In principle these EOM can be developed manually using the theory of Newton-Euler mechanics and Lagrangian methods. However as the number of rigid bodies increases this becomes very difficult and prone to human error. It is possible though due to the algorithmic nature of the methods of developing the EOM for MBS systems, to implement this on a computer in an automated way.

Toward this end various multibody formalisms, or automated methods of assembling the EOM for MBS, have been developed and researched [67], [76]. They can be classified as recursive and non-recursive [67]. The non-recursive methods involve appending a set of Cartesian coordinates to each body that defines its position and orientation in three-dimensional space. The various non-recursive methods differ only in their choice of the Cartesian coordinates. ADAMS utilises a non-recursive formalism for assembling the EOM. ADAMS defines the position and orientation of each rigid body in the MBS via a set of Cartesian co-ordinates fixed to the mass centre [76]. For each body six co-ordinates are used to describe the body's configuration, representing the six degrees of freedom (DOF) of a body in three-dimensional space. The connectivity of the various rigid bodies is introduced to the EOM in the form of constraint equations in the form of differential algebraic equations (DAE) using Lagrange multipliers [67]. The EOM are thus presented in terms of the individual co-ordinates of each rigid body. This approach has an advantage in that the dynamic formulation of the EOM is straightforward and allows in general easy additions of complex forcing functions and constraint equations [67]. Its disadvantage is that is not as computationally efficient as the recursive formalisms. With the recursive formalisms the EOM are based on the minimum set of

differential equations of motion and are written in terms of the systems DOF. This is in general a more difficult way to formulate the EOM [67] but is computationally more efficient [76].

In addition to the formulation of the EOM, to simulate the dynamic behaviour of the MBS, the EOM must be solved. The solution of strongly non-linear MBS EOM and constraint equations cannot be considered in closed form even in simple cases. Thus the only possibility lies with numerical techniques [76]. If the EOM can be represented as a set of ordinary differential equations (ODE) then a number of classical numerical integrators (discrete time) can be used, for e.g. Runge-Kutta. However [76] and [35] present literature, which indicates that classical numerical integration techniques are not particularly suited to the solution of MBS dynamic models. Toward this end special integrators suited to MBS model solution such as the DIFSUB procedure by Gear (1971) [76] have been developed. In addition many if not most MBS systems are not represented by ODE but rather by differential algebraic equations (DAE). The solutions of DAE's are in general computationally difficult due to the solution of non-linear functional equations having to be recomputed at every integration step [35]. One method around this problem is to reduce the DAE's to ODE's whose solution is relatively simpler and much research continues in an attempt to find more efficient methods of solution of DAE's [35], [76].

As can be seen from the above discussion, modelling the dynamic behaviour of a MBS such as a vehicle requires the synthesis and solution of hundreds or even thousands of differential equations, which was not possible before the advent of the digital computer [67]. Even in the early years of the digital computer, the solution of such large-scale MBS models was highly inefficient. But in the last decade due to the accelerated pace of the development of the digital computer and the development of efficient numerical techniques for the synthesis and solution of MBS models, virtual prototyping of complicated MBS such as vehicles have become possible even on desktop personal computers.

This dissertation presents the work done on the first stages of a virtual prototyping project involving the BELL Equipment B40C articulated dump truck (ADT). Chapter 2 is a review of fundamental theory governing the vehicle dynamics behaviour of wheeled vehicles in general. Literature is presented on the pneumatic tire, the understanding and correct modelling of which is critical to the success of any virtual prototyping exercise involving wheeled vehicles. Included in Chapter 2 are issues surrounding the modelling of other compliant components in a vehicle, such as rubber suspension components. Finally Chapter 2 presents some theory of ground wheeled vehicle dynamics.

The testing program conducted on the physical vehicle is detailed in Chapter 3. In order to establish the validity of a virtual prototype, testing of a physical model is vital. The test data needs to be compared to the data generated from the virtual prototype, simulated under the boundary conditions of the physical test program. The data acquisition equipment and sensors used are presented along with the testing regime that encompassed both steady state and transient handling tests, as well as vertical response tests. Some key results from the tests are presented.

Chapter 4 presents the actual modelling of the ADT in the MBS software package ADAMS (Automated Dynamic Analysis of Mechanical Systems). The chapter presents the initial 3-D modelling of the ADT in order to determine the mass and inertia properties of the rigid bodies that comprise the ADT. The assembly and connectivity of the rigid bodies using idealised joints (representing kinematic pairs) in order to check the kinematic validity of the mechanical system is also detailed. Results from an undergraduate student project initiated to characterise the behaviour of the compliant suspension components are presented. The analysis of these test results is presented in some detail. The methodology of introducing these results into the ADAMS model of the ADT in the form of force elements is also present.

Chapter 5 contains the modelling of the tire and terrain in ADAMS. The determination of the parameters for the FIALA tire model is presented along with the construction of the various road data or terrain files used in the ADT ADAMS model simulations including the BELL EQ. Test track in Richards Bay, KwaZulu Natal. Include also in Chapter 5 are the design and modelling of the speed and path following controllers used in the simulations. The results of the simulations conducted are presented.

Chapter 6 concludes the thesis and makes some recommendations on further work on the virtual prototyping project.

2. FUNDAMENTALS OF VEHICLE DYNAMICS

2.1 The pneumatic tire

The pneumatic tire is the prime generator and reactor of the forces and moments developed between a wheeled-vehicle and the surface it travels on. With the exception of aerodynamic and gravitational forces all forces and moments acting on a vehicle are applied through the tire-ground contact area or contact patch [87]. The pneumatic tire serves two purposes, to attenuate the transmission of harsh vibrations to the rest of the vehicle and to maintain or influence the directional stability of the vehicle. It is thus of major importance to understand the mechanics of the force generation at the contact patch if the goal of successfully modelling a vehicles' dynamics is to be achieved.

The mechanics of the tire-ground interaction is a complex process, which is the subject of intensive and continuing research [58]. The object of this discussion on the pneumatic tire in this section is not to provide a comprehensive introduction of tire mechanics but rather to introduce and explain those concepts that pertain directly to the forces and moments generated by the tire-ground interaction so as to offer an insight into tire behaviour as affects vehicle dynamic simulations. As such no attempt will be made to discuss the effects of differing material type and tire construction on the above-mentioned forces and moments in detail, except to note fundamental effects were appropriate. In addition the surface with which a pneumatic tire interacts is also of major importance in determining the forces produced by the interaction. While the object of this vehicle modelling study, the BELL Equipment ADT, spends most of its time on craggy or deformable-soil type terrain and at best on loose gravel surfaces with a hardened sub-layer, the current work proceeds with the requirement that the road surface be perfectly rigid and contributes no deformable stresses to the vehicle at the tire road contact patch. The only available tire model within the ADAMS Full Simulation environment available for this project was an analytic, quasi steady state model that required a rigid road. The development of a suitable soft-soil tire interaction model was beyond the scope of this study. Ref. [87], [87] and [1] provide an introduction to the theory of teramechanics while [69], [86] track current research efforts in this regard.

This section proceeds by first introducing the basic pneumatic tire and the primary forces and moments of interest along with a sign convention. The mechanics of the generation of these forces and moments will then be discussed in the various tire planes as defined by the axes system. Finally tire modelling for vehicle dynamics simulation will be discussed closing off with an overview of the tire model to be used in the ADT model that is the subject of this study.

2.1.1 Tire fundamentals and construction

The pneumatic tire in its most generic form is a bladder filled with compressed air that supports the load of the vehicle and is the interface at which the vehicle directional control forces are applied. In reality this simple description of the tire is the result of various constructional features of the tire working to give particular load carrying characteristics as well as ride and handling properties. The tire has the following basic elements in its construction; carcass, bracing belt, beads, sidewalls and tread [26].

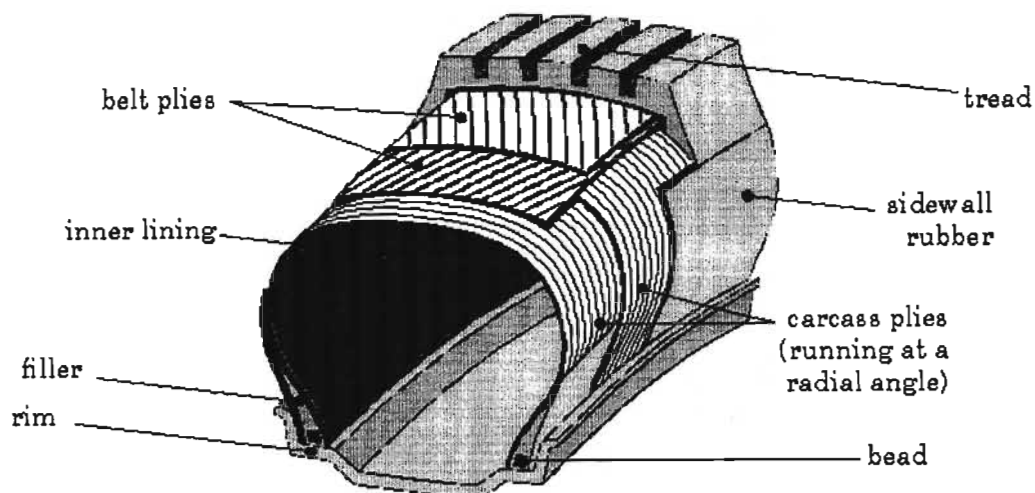


Fig. 2.1 Pneumatic tire construction [89]

With reference to **Fig. 2.1** the following descriptions apply: -

Carcass - The most important structural element of the tire is the carcass [87]. While it is the compressed air that provides most of the structural stiffness of the tire in the vertical direction it is the carcass that must provide the strength to contain the air and be resilient enough to be flexible to accommodate road impacts and lateral stresses induced by cornering. The carcass consists of a number of layers of cords (plies) made of natural or synthetic material or metal encased in a moulded rubber compound with a relatively low modulus of elasticity [87]. **Fig. 2.2** shows the two basic types of tyre construction in use today, the bias ply and the radial ply tire. The difference lies in the direction of the strengthening cords with the radial ply tire having the cords run radially at 90° to the tire circumference while with the bias ply tire, the alternating ply layers run at a different angle (crown angle) to each other. The different ply arrangements affect the tire vertical flexibility and tire handling ability with the radial ply arrangement making for a flexible sidewall and hence a softer ride while the bias ply makes for a higher tire lateral stiffness thereby improving cornering ability [21]. In terms of application, radial ply tires are used almost exclusively for car and light truck tires today. Even though the trend is towards radial ply because of the high wear rate and rolling resistance of bias ply tires [87] bias ply tires still find application in military and heavy duty earthmoving vehicles [87], [21].

Bracing belt – These are found always on radial ply tires and in some instances on bias-ply arrangements as well (bias-belted) although these are not produced today [21]. The function of the belt is to provide a strengthening brace around the tire circumference and aids the cornering ability of the tire. The belt is formed by several layers of cords of high modulus of elasticity, mainly steel, at crown angles of about 20 degrees to each other. Fitted between the tread and the carcass, the belt is essential to the proper functioning of the radial ply tire, helping to stabilize the tread and keep it flat on the road surface despite the low lateral stiffness of the radial ply carcass [21].

Beads – The ply cords are anchored around the beads, which are the interface between the tire and the wheel rim. The beads are high strength endless cords arranged at each rim circumferential end and are have an interference fit with the rim. In addition to anchoring the ply cords, the bead also serve to provide adequate seating and sealing of the tire on the rim [87].

Sidewalls – Sidewalls make up the outside of the tire carcass and need to be very flexible and still be strong enough to protect the tire from damage through abrasion and penetration from sharp objects. The sidewalls are covered with a rubber compound [26].

Tread – This is the outer surface of rubber and is the main wearing element of the tire construction. [11]. This is where the eventual interaction forces between tire and road occur. The tread is patterned with grooves, slots and sipes or incisions. Their primary purpose is to allow easier drainage of water from underneath the tire in wet weather. It also assists in cooling in the dry [11] The tread rubber must be hard enough to give good wear resistance while soft enough to give good traction so there is always a design specific trade-off in determining the hardness of the tread rubber [11].

Despite the differences in construction of pneumatic tyres which influence the characteristics of the tyre in terms of many criteria such as wear, durability, and as concerns this discussion directly, ride and handling, the *basic mechanics* of operation are similar [87]. This is the subject of discussion of the following sections.

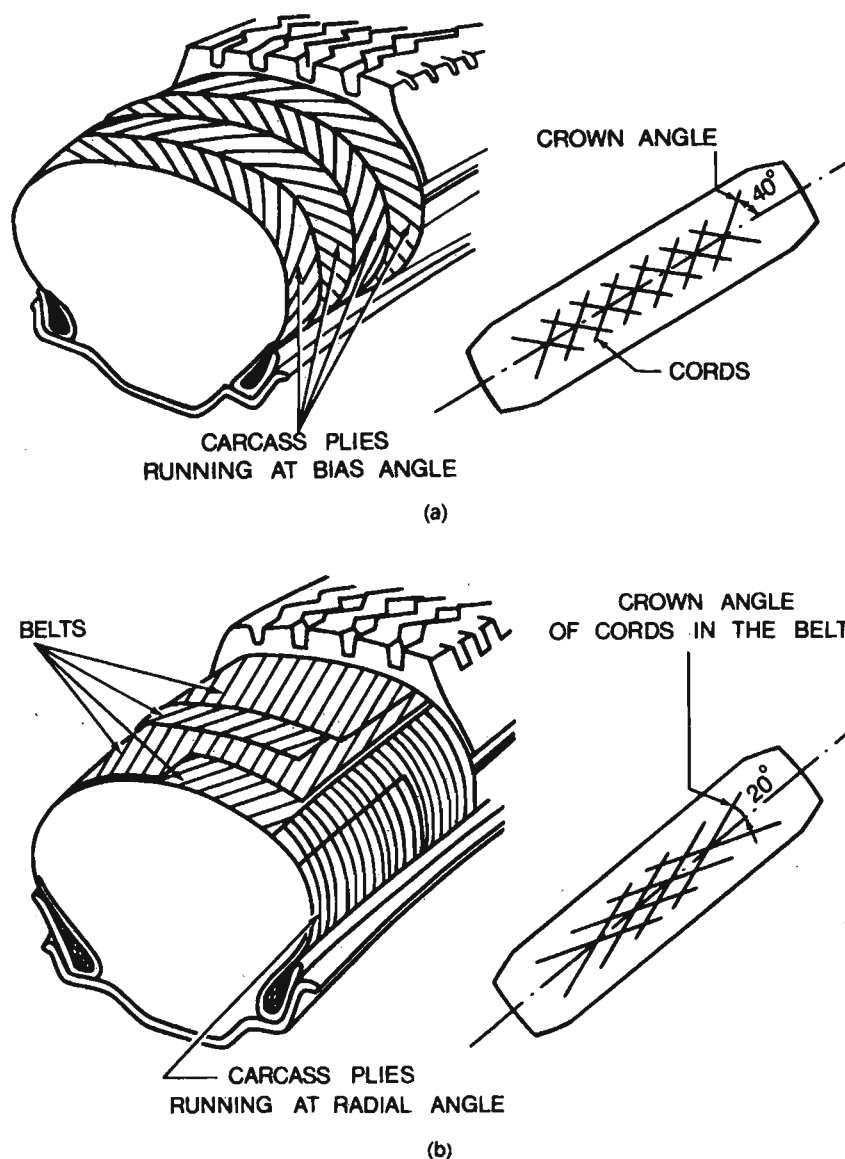


Fig. 2.2 Pneumatic tire construction (a) Bias-ply tire. (b) Radial-ply tire [87]

2.1.2 Axes, notation and principle forces and moments

As much work has been and continues to be done in trying to understand and model the behaviour of tires, a common axis system is necessary to describe the notation of the various forces and tire parameters. The Society of Automotive Engineers (SAE) axes system has been widely adopted although efforts have been made to standardise to the ISO axes system [80]. The SAE axes system is described here and all the principle forces, moments and related parameters are defined with this axis system. **Fig. 2.3** presents a simplified version of the SAE axes system for the purposes of this discussion being not as cluttered as presented in [64]. The SAE axes system is a 3-dimensional Cartesian coordinate system with the origin situated at the centre of the tire-road contact patch. The X-axis points in the direction of the wheel heading (i.e. not the direction the wheel is actually pointing towards), the Y-axis is to the right of the X-

axis and the Z-axis forms a right-handed orthogonal axis system by pointing vertically downward.

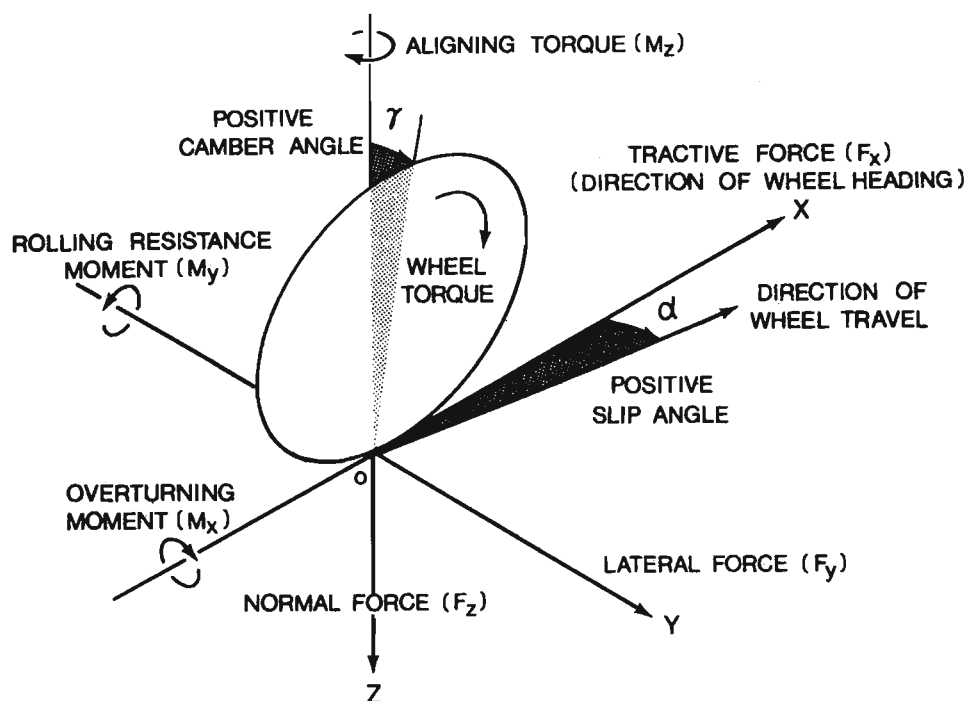
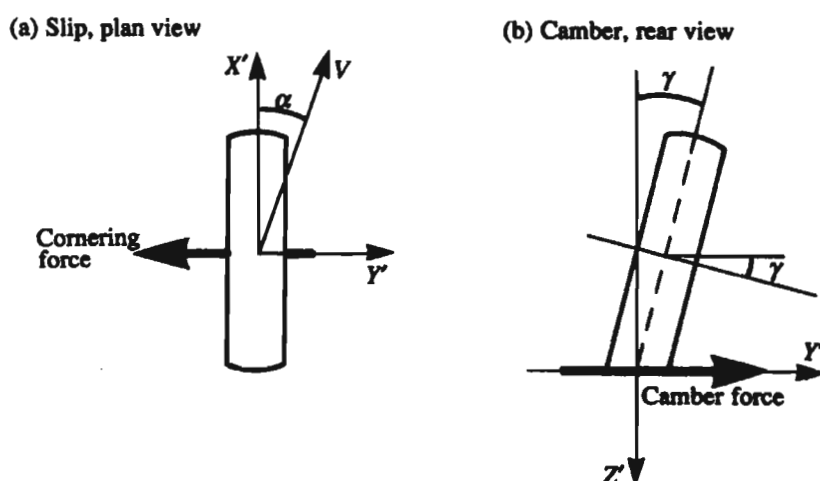


Fig. 2.3 SAE tire axis system [87]

There are three principal forces and three principle moments that arise from the definition of the axis system, which bears a physical similarity to the actual force-moment generation. In beginning to describe the forces generated by the tire road interaction one should consider the various states that a tire undergoes. In its simplest state of rest as attached to a vehicle the only force present that acts on the tire is the normal force (F_z), which is the reaction force of the road on the tire due to the weight of the suspended mass of the vehicle – this varies when the tire is in motion due to road displacement inputs and tire behaviour. By the definition of the SAE axis system this force is negative i.e. acting upward. As a torque is applied to the tire about its spin axis (wheel torque), the reaction force (F_x) generated at the contact patch acts to move the wheel longitudinally in a fore-aft vehicle direction. F_x is positive for a tractive wheel torque and negative for a braking wheel torque. If a steering input is now applied to the tire such that it turns about the Z axis (if there is no tire inclination angle) a lateral force (F_y) acting to move the tire sideward is generated. This F_y is a function of the slip angle (α) which is defined as the angle between the instantaneous direction of wheel heading and the direction of wheel travel. Its sign is dependant on which way the wheel is turned and is intuitively realised from **Fig. 2.3**. F_y is not solely dependant on α . Material, constructional and environmental aspects notwithstanding, F_y is also dependant on an additional kinematic parameter defined within the axis system, the camber angle (γ) or to use the generic description inclination angle. Inclination

angle is defined as the angle between the wheel and vertical planes and acts to produce an additional force component to F_y . The sign of γ is as follows: that for a positive right hand rotation of the wheel about the X-axis γ is positive. However in keeping with SAE convention, camber angle is positive when the top of the wheel tilts outward from the car longitudinal (fore-aft) centre line. Thus for an outwardly leaning wheel on the right hand side of a vehicle from the drivers perspective, camber angle equals inclination angle and on the left hand side camber angle equals the inclination angle with reversed sign [11]. Fig. 2.4 shows the direction of the road reaction forces acting on the tire along the Y-axis due to slip and camber angles.



**Fig. 2.4 Road reaction forces exerted on the tire due to
(a) Slip angle and (b) Camber [11]**

In addition to the forces acting along the three axes of the co-ordinate system, moments exist about the axes as well (ref. Fig. 2.3). The moment about the X-axis (M_x) is known as the overturning moment and acts to increase or decrease the camber angle (γ) while the moment about the Y-axis is known as the rolling resistance moment (M_y) and acts against the wheel torque applied about the spin axis. The moment about the Z-axis is known as the aligning moment or self-aligning torque (M_z) and acts to reduce the slip angle (α) and bring the direction of wheel travel back to the direction of wheel heading.

2.1.3 Mechanics of force generation at the contact patch

The special material properties of rubber as an engineering material have the largest impact on the mechanics of the force generation in a tire at the contact patch. Notwithstanding the contribution of the strengthening cord plies and compressed air in determining to a large extent the rigidity and stiffness of the tire, it is the rubber that dominates the mechanics of a tire, namely rubber's ability to grip the road surface and its flexibility. The two mechanical phenomena related to grip and flexibility are friction and hysteresis and will be discussed below.

The hysteresis effect of an engineering material or system under load is that result from a load verses displacement or stress verse strain relationship, which shows the loading and unloading paths not tracking each other. This relationship is shown as an example graph in **Fig. 2.5**.

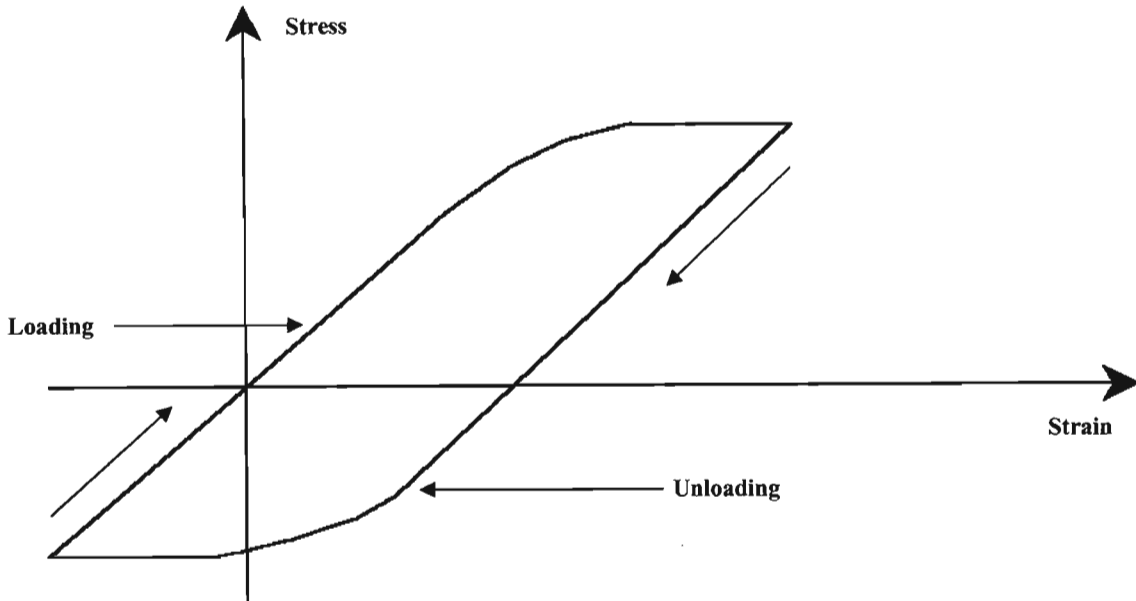


Fig. 2.5 Hysteresis effect [32]

The area in the loop created by the graph of a loading and unloading cycle is the energy that is lost to the system. Damping is the term used to describe the non-conservative forces acting in a mechanical system that act to dissipate energy [32] and can be determined from the hysteresis loop area. In general for rubber the area of these loops and hence the damping, varies with frequency and the amplitude of excitation. It is difficult to determine the type of mathematical model to be used to determine the effect of damping in a system in general [32]. Two damping models are used commonly in the literature; viscous and coulomb damping. The total tire friction at the tread-road interface is primarily a combination of both damping mechanisms in varying degrees depending on the boundary conditions (speed of travel, wetness of surface etc) [21]. While the reader is referred to the literature (e.g. [32]) for mathematical descriptions of the two damping models it suffices this discussion to understand that viscous damping results from the energy lost in the rubber flexing and coulomb damping results from the energy lost due to the tire sliding. **Fig. 2.6** shows these two phenomena as applies to a block of tread rubber with the 'hysteresis' indicating viscous damping due to rubber flexing and adhesion indication coulomb damping due to the rubber sliding. From now onwards the friction force experienced by the tire will be taken to include the total friction force that encompasses both the mechanics of friction discussed above.

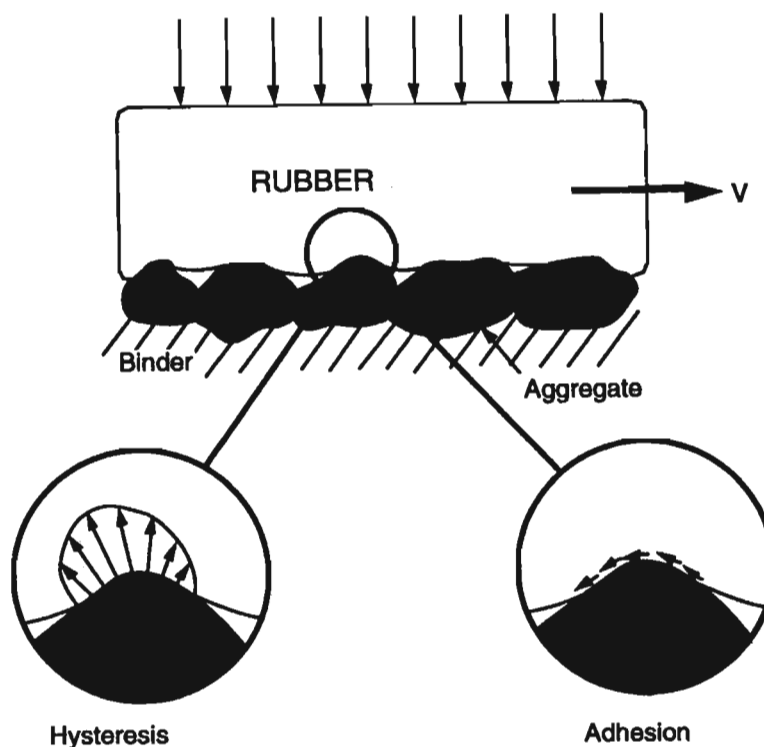


Fig. 2.6 Two mechanisms of rubber energy loss at the tire contact patch [21]

The energy loss in rubber is a function of frequency and there is an intermediate frequency at which the non-conservative force causing the energy loss i.e. the friction force, is at a maximum. As it is a goal to maximise the friction to increase grip of the tire, it is of importance to know where this maximum is. Ref. [11] reports that for a pure rubber block sliding on glass the friction coefficient (μ) is a function of sliding speed and temperature with a definite optimal maximum for a particular temperature. **Fig. 2.7** indicates the Williams-Landel-Ferry (WLF) combined temperature graphs for pure rubber on glass and a rough surface (SiC) as well as rubber with vulcanising agents. It is noted that the friction co-efficient can be greater than 1.0 and that the rubber-road friction co-efficient approaches more realistic values as found on tires with the addition of vulcanising compounds to rubber to increase its wear resistance.

As well as having a higher static value of μ as compared to sliding as is known to be the case with sliding material pairs in general, peak friction force involving rubber as one of the sliding materials displays two interesting differences. Unlike most other material pairs, the co-efficient of friction for rubber as part of a sliding pair shows a dependency on area and load. In particular for a given load, increasing the area of contact increases the friction force and increasing the load increases the friction load but at a slower rate i.e. the friction coefficient decreases with load [11], [15]. Ref. [11] attributes this to the spreading of the rubber over the asperities in the road surface resulting in an increase in the viscous damping hysteresis effect.

Fig. 2.8 is an example of actual test data from a heavy duty road going truck tire and a light pickup tire indicating the friction co-efficient dependency on load and vehicle speed for peak static and full sliding conditions.

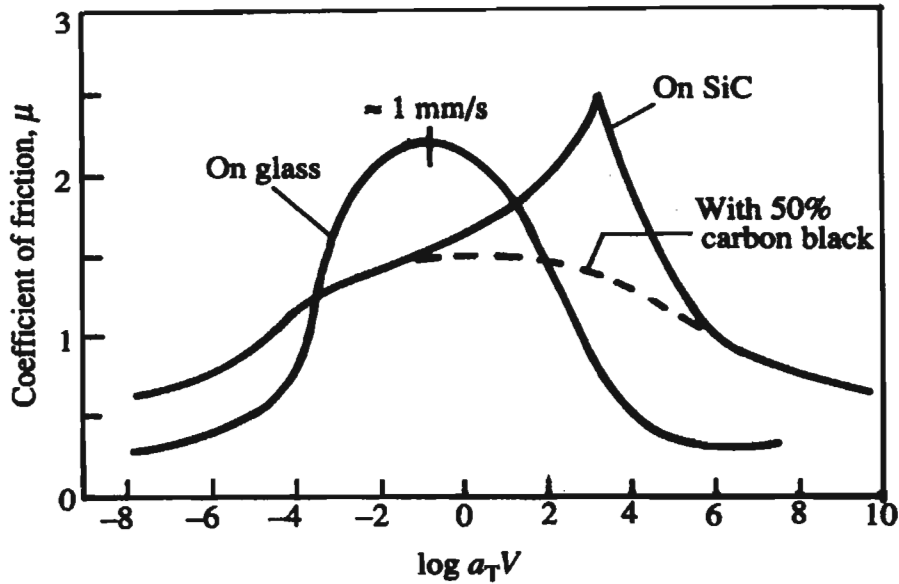


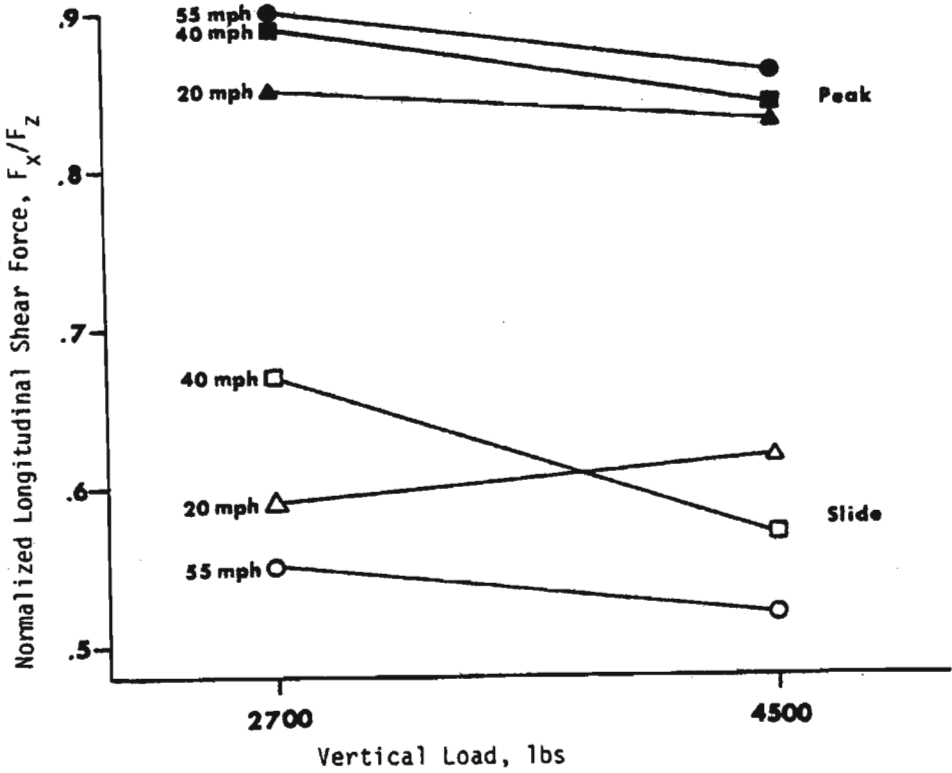
Fig. 2.7 WLF-model of rubber friction on glass and SiC as a function of temperature and velocity [11]

2.1.4 Rolling resistance

While exploiting the hysteresis in rubber to maximise the non-conservative frictional force at the tread-road interface is the goal of getting the tire to grip the road, hysteresis is the main cause of loss of available energy to move the vehicle in the chosen direction. This loss of useful energy is referred to as rolling resistance. A rolling tire will dissipate energy and have a rolling resistance that is made up largely (90-95%) of hysteresis losses in the flexing of the rubber sidewall of the tire [87]. Other energy dissipating mechanisms contributing to the loss in energy are the effects of the frictional loss due to slip at the contact patch and the air resistance due to the fan effect of the rotating tire on the surround air [87]. These latter two are however less significant.

While rolling resistance is a relatively small force that has little effect on the handling of a vehicle except to impact on steering feel to the driver [11], it does impact in the longer term on the running costs of the vehicle especially off-road vehicles operating on sandy terrain.

(a)



(b)

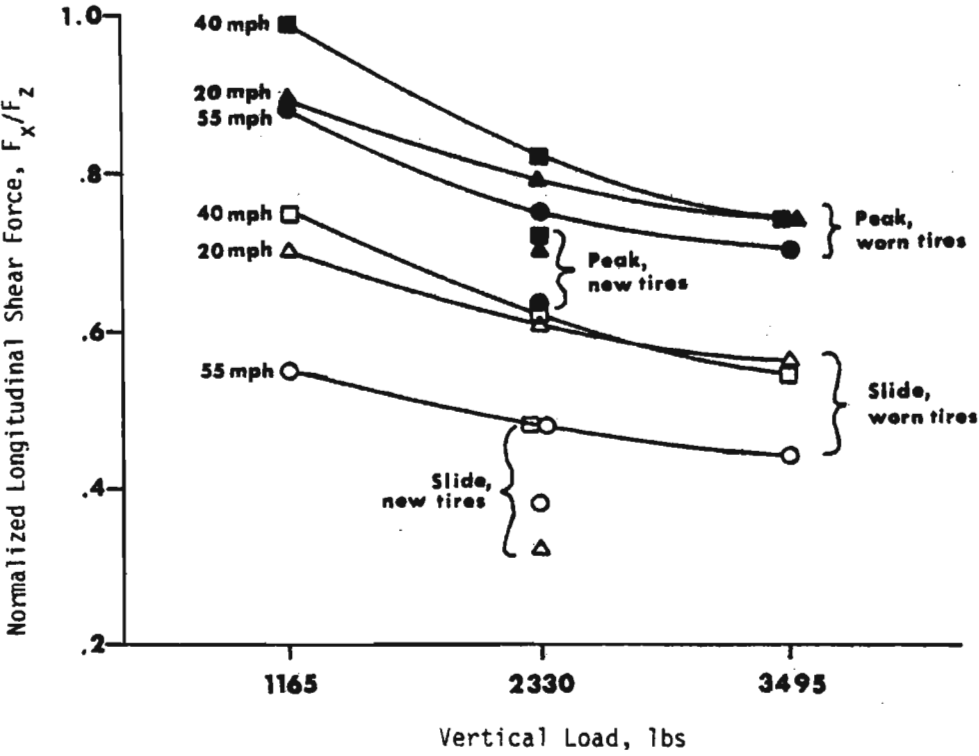


Fig. 2.8 Variation of peak and sliding coefficient of friction for an (a) heavy commercial road going truck and (b) a light pickup [15]

While this discussion on rolling resistance considers the generation of a resistance to rolling purely through the tire deformation, the increase in rolling resistance on sandy terrain is due to energy spent in deforming and removing the tractive surface as well as large slippage effects. All these effects are lumped together to indicate a rolling resistance force [1].

While rubber hysteresis is the principle cause of the loss in energy applied to a tire it translates into different mechanisms that add up to give the total hysteresis rolling resistance. These mechanisms are in turn influenced by other operating parameters that depend on each other in a non-linear manner [17].

In addition to the energy loss that results in generation of heat due to flexing of the side walls, two other mechanism stemming from the flexibility of rubber are mentioned in the literature that contribute to rolling resistance, the compression of the leading edge of the rolling tire and standing waves. These mechanisms are in turn affected by different parameters such as tire construction and material, road surface and condition, tire inflation pressure, speed, operating temperature and tire diameter [87].

In free rolling or traction conditions under applied torque in the forward direction, the leading edge of the tire in the contact patch is compressed as indicated in **Fig. 2.9**. This acts to shift the vertical pressure distribution in the tire forward of the spin axis. The centroid of the area under the pressure distribution curve is thus shifted forward of the spin axis in the tire vertical plane and acts to create a moment resisting the forward rolling motion of the tire.

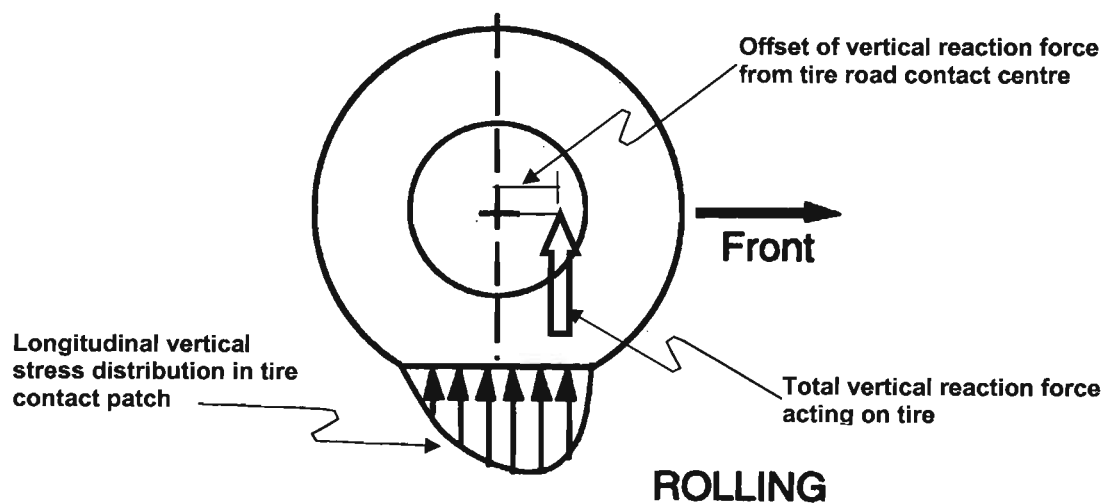


Fig. 2.9 Vertical stress distribution in free rolling driven tire (adapted from [21])

Ref. [11] gives a brief but substantial introduction of the standing wave (also called traction wave) phenomena. Instead of the tread in the crown at the trailing edge of the contact patch, leaving the ground smoothly and following the circumference of the tire, the crown of the tire goes through a wave [11] (see Fig 2.10). This wave causes a dissipation of energy and hence an increase in temperature and rolling resistance. Standing wave energy dissipation is dependent largely on speed and there is a speed at which the standing wave amplitude is substantial and energy loss increases rapidly. This acts to rapidly increase temperature and rolling resistance, and the tire is no longer in a safe operating condition. While this critical speed is fairly high for passenger cars, factors such as load temperature and tire construction also play a role in standing wave energy loss for particular tires and each make of tire has a safety critical speed rating. [17]. In addition even at low speeds the energy loss via the standing wave phenomena under sustained travelling can give rise to substantial increases in temperature [17]. In addition the centrifugal stresses present at high speeds at the outer tread elements in the crown impact on the standing wave phenomena [11]. While for large off road wheels the centrifugal accelerations are lower due to lower speeds of operation the larger mass of the outer tread elements as compared to cars means that significant stresses can be present in the crown of the tire even at low speeds hence still impacting on the standing wave phenomena and hence rolling resistance.

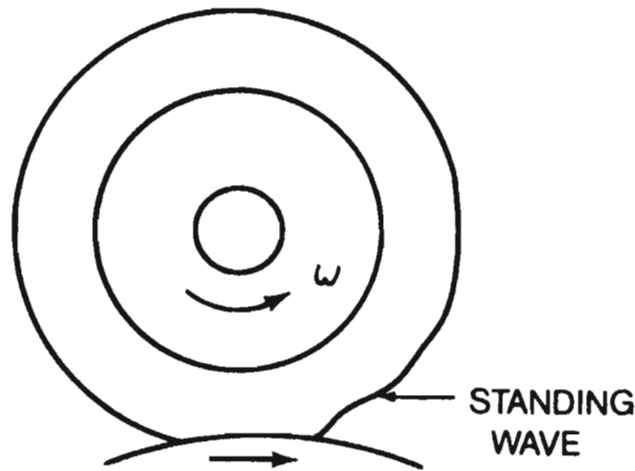


Fig. 2.10 The standing wave phenomena in a rolling tire [87]

Reference [87] presents various graphs to show the influence various parameters have on rolling resistance, mainly for passenger and light truck tires. As a summary from [87] and [26], the influences of the parameters of interest, in the absence of any influence from other parameters, are presented in **Table 2.1**. The reader is referred to [87] for graphs detailing the various interactions of the different parameters as affects rolling resistance.

Parameter	Influence
• Construction	<i>Bias-ply tires tend to have larger rolling resistances than radial-ply</i>
• Materials	<i>Natural rubber tends to have a lower rolling resistance than synthetic compounds</i>
• Road surface condition	<i>Hard smooth surfaces cause lower rolling resistances than rough surfaces</i>
• Inflation pressure	<i>On hard surfaces higher inflation pressure reduces the rolling resistance while on deformable surfaces two opposing mechanisms are at work having differing impacts on inflation pressure to minimise rolling resistance – deformation of the surface (requiring lower pressures) and hysteresis loss due to flexing of the tire sidewalls (requiring higher pressures). There is thus an optimal pressure to minimise rolling resistance.</i>
• Speed	<i>Rolling resistance Increases with speed up to a limiting point where energy losses (due to the standing wave phenomena) cause drastic increases in tire temperature so as to render the tire unsafe</i>
• Operating temperature	<i>Affects the rolling resistance by increasing pressure (hence decreasing rolling resistance on hard surfaces) and changing the stiffness (hence hysteresis losses) of the material. Both effects act to decrease the rolling resistance with increasing temperature however higher temperature increases rubber hysteresis.</i>
• Diameter	<i>Increasing tire diameter decreases the rolling resistance but is negligible on hard ground but substantial on soft surfaces</i>
• Tractive effort	<i>Increasing the moment about the tire spins axis increases the rolling resistance and tends to be more pronounced under traction than braking</i>

Table 2.1 Summary of parameter influences on rolling resistance [87], [26]

Reference [17] indicates in an investigation of the coupled influences of various parameters for passenger car tires, that wheel vertical load, speed and inflation pressure are the dominant factors influencing the rolling resistance on a hard surface. In addition to investigating the overall sensitivity of rolling resistance to each of the above three parameters in the presence of changing and static values of the remaining two, the study concluded that the repeatability and hence applicability of tests of rolling resistance versus speed were not guaranteed at low, (below 5km/h) and extremely high speeds (approaching the safety limit). This bears particular significance to the BELL ADT as the vehicle spends large amounts of its operating life under low speed conditions and modelling of low speed ADT behaviour requires extra scrutiny of the tire behaviour. In addition in testing various sets of replicate tires the study showed that the standard deviation of rolling resistance values is unlikely to decrease beyond 0.22N of retarding force for an increased data set indicating a high reliability of tested rolling resistance coefficients across a sample. The study concludes by indicating that breaking in times before measurements of rolling resistances on tires were conducted, were longer for new as compared

to old tires, and noted a significant decrease in the rolling resistance of old or used bias-ply tires as compared to very little decrease for used radial-ply tires.

Rolling resistance is in essence retardation force acting to decrease and dissipate the useful energy available to move the vehicle. It can be represented as a force acting on the tire in many ways as indicated in **Fig. 2.11**. In general it is expressed as a quotient of retardation force per unit vertical load and is taken to act at the tire vehicle attachment point opposite to the direction of travel as represented by the leftmost diagram in **Fig. 2.11**.

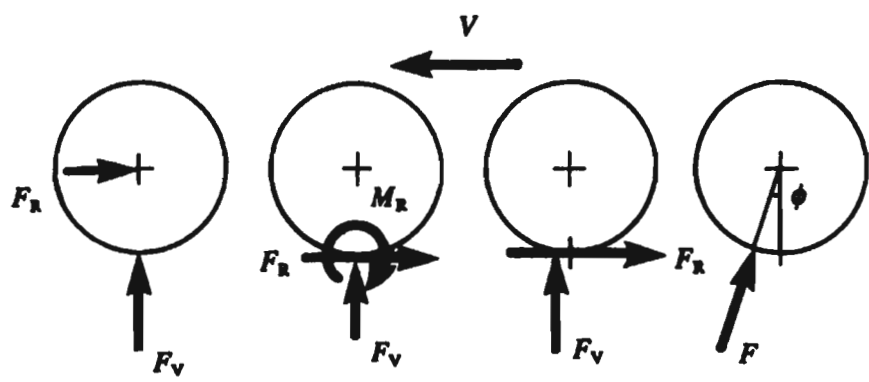


Fig. 2.11 Various forms of representing rolling resistance [11]

While empirical formulas for calculating rolling resistance do exist they tend to be specific for particular types of tyres [87] and are expressed as functions of speed squared but with the contribution from speed being significant only at extremely high velocities. For the relatively low speed operation of the ADT it is sufficient to model rolling resistance as a constant coefficient obtained from rolling resistance tests. **Table 2.2** adapted from [87] indicates average values of rolling resistance coefficients for tires on various vehicles on different terrains.

<i>Tire Type</i>	<i>Surface</i>		
	<i>Concrete</i>	<i>Medium Hard Soil</i>	<i>Sand</i>
<i>Passenger car</i>	0.015	0.08	0.30
<i>Commercial truck</i>	0.010	0.06	0.25
<i>Tractor</i>	0.02	0.04	0.02

Table 2.2 Coefficients of rolling resistance (*adapted from [87]*)

2.1.5 Generation of the Principle Forces and Moments

The physics of tire force and moment generation is a complicated science with, non-linear dependencies on a number of parameters w.r.t. amplitude and frequency of excitation. In trying to develop an understanding of the physics, assumptions are made in simplifying the theory to suit a particular application. In the literature the physics of the tire is frequently discussed in terms of four distinct regimes, viz. stationary and non-stationary behaviour and both of which encompass two further regimes, in-plane longitudinal dynamics and out of plane lateral dynamics. Even though a tyre is always undergoing non-stationary behaviour on some level and lateral and longitudinal behaviour are essentially coupled, there are situations where only the influence of one regime can be considered or where they can be assumed to be acting independently from each other, with a good correlation to reality. Such situations simplify the theory and also aid in understanding overall tire behaviour. It is this approach of considering the regimes separately that will be adopted in this section.

2.1.5.1 Stationary in-plane dynamics

In plane tire dynamics refer to the behaviour of the tire in the plane of rotation. Specifically it is the longitudinal tractive and braking forces that are the most important as well as the ride or vertical excitation forces that constitute the in-plane dynamics of the tire. The SAE refers to the longitudinal forces (F_x) as those acting in the direction of wheel heading [64]. These forces act to accelerate or brake a vehicle.

A positive wheel torque, as indicated in **Fig. 2.3**, acts to move the tire and vehicle forward. Under the action of such a positive wheel torque the vertical load (normal pressure) and the longitudinal stress distribution along the contact length of the contact patch, as viewed from the side, is as shown in **Fig. 2.12**. As the tread elements enter the contact area upon rolling they cannot immediately sustain a friction force because of their compliance and must bend to sustain a force [21]. As the tread elements move backward through the contact patch and with the increasing vertical load they begin to sustain an increasing friction force resulting in an increased longitudinal stress of the tread elements until the point of maximum vertical load. After this point the vertical load declines at the rear of the contact patch, to zero at the trailing edge causing a decline to zero of the longitudinal stress in the tread elements. While the shapes of the vertical load distribution, friction force and relative slip might differ amongst authors [21], [53], [87] according to what force moment models they propose, the basic principles are the same.

The centroid of the vertical pressure distribution of a rolling tire lies ahead of the tire road contact centre point whether under a tractive or braking wheel torque [87]. This offset also acts

to introduce a rolling resistance moment that contributes to the overall rolling resistance as indicated in **Fig. 2.9**.

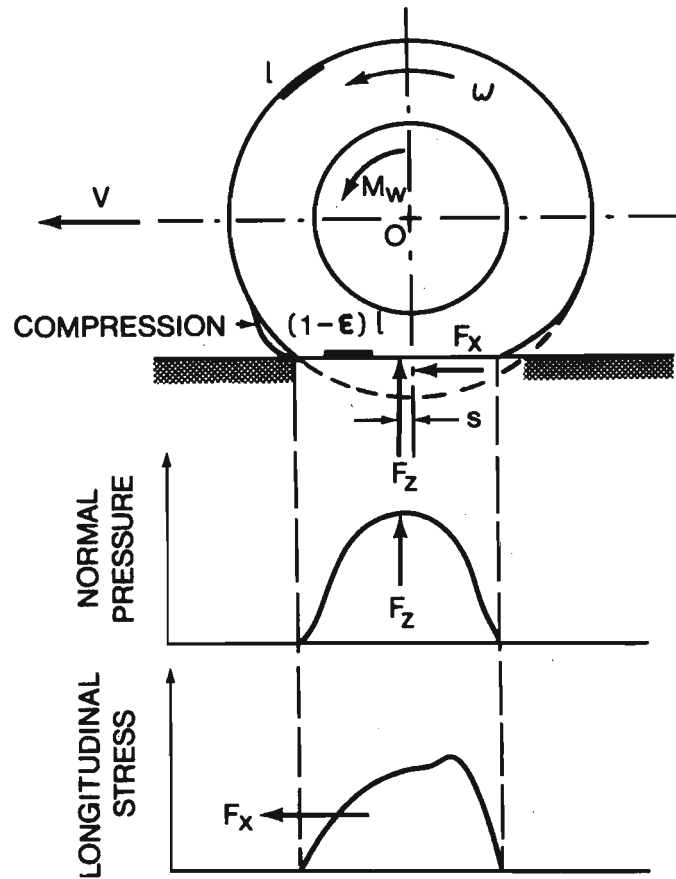


Fig. 2.12 Behaviour of tire contact patch in the longitudinal direction under a tractive force [87]

Perhaps the most important characteristic curve determining longitudinal force development is the longitudinal force versus longitudinal slip curve. In the contact patch the leading part of the rolling tire will have the most “grip” as the vertical force builds up along the contact length and the longitudinal stress concentration (and hence the contribution to the overall longitudinal force) builds up gradually in accordance. At the rear of the contact patch the vertical force decreases and the longitudinal stress concentration and the longitudinal force contribution decreases. In fact at the end of the trailing edge of the contact patch the tread will be slipping completely. As greater wheel torque is applied and the friction limits starts to be approached the slip region moves forward towards the leading edge until the entire contact patch is slipping with respect to the road i.e. 100% slip.

Slip is defined according to the SAE as [87]: -

$$\kappa = \left(\frac{r\omega}{V} - 1 \right) \times 100\%$$

where

- κ = Slip
- r = Tire free rolling radius
- ω = Rotational speed of the tire
- V = linear speed of the tire centre

For traction $r\omega$ is greater than V and hence slip is positive for traction. For braking $r\omega$ is smaller than V and hence slip is negative. Some authors [87], [21], [11] define slip slightly differently such that slip is negative for traction and positive for braking. This is the definition use by ADAMS [41]. Some authors [87] also define the slip equation in different ways for traction and braking, ostensibly to avoid the anomalous situation for a fully slipping wheel under traction giving infinite slip [87]. In this alternative separate definition braking slip and traction slip, braking slip is termed *skid* and both slip and skid are always positive [87].

A typical curve of longitudinal force (F_x) (normalised by dividing by vertical load F_z) versus longitudinal slip is given by **Fig. 2.13**. Maximum tractive effort is obtained at a slip value of approximately 15-20% [26]. The curve for braking effort is very similar with slightly different slopes and peak values [26]. Other parameters also influence the development of F_x . While the longitudinal slip determines the general shape of the F_x vs. κ curve other parameters act as modifiers of the curve. Of course the tire road surface friction coefficient (μ) is a fundamental modifying parameter with higher values of μ resulting in larger positive (traction) and negative (braking) values of F_x . Speed changes have an impact indirectly on the development of F_x by modifying μ . Friction coefficient (μ) decreases with speed. While standard models of friction use constant value friction coefficients for peak, pre-sliding, (μ_p) and sliding (μ_s) friction, some models relate μ_p and μ_s via non-linear functions [11]. The constant values serve well for many applications and highlight the decrease in frictional coefficient with increasing speed. An important parameter is vertical load (F_z). While the increase in load causes a corresponding increase in F_x , the friction coefficient (μ) is reduced with an increase in load hence the peak and slide longitudinal forces do not increase proportionately [21]. Other parameters such as inflation pressure, material and tire construction affect the development of the longitudinal force and the reader is referred to the literature for further elaboration of their effects.

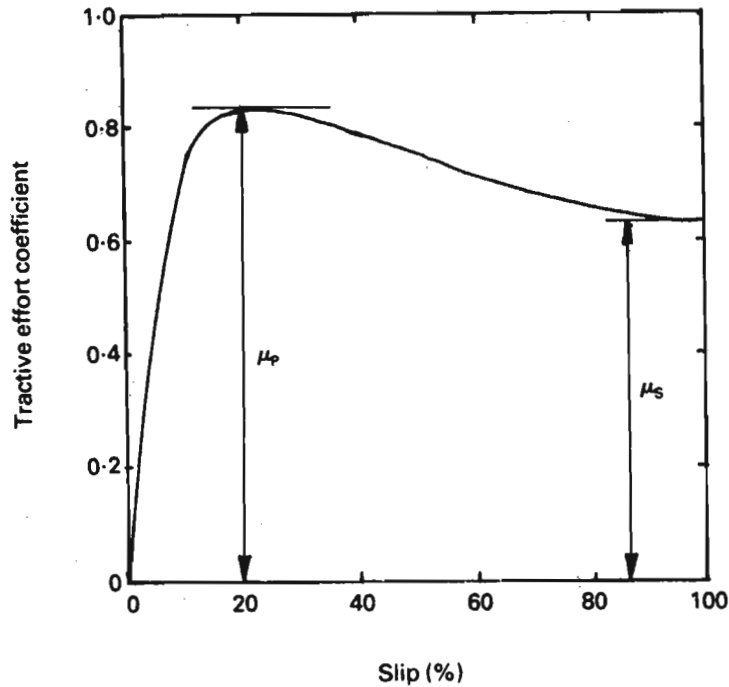


Fig. 2.13 Typical curve of longitudinal force (normalised) vs. longitudinal slip [26]

The other aspect of the in plane tire dynamics is ride. This entails the dynamic variations of the vertical force on the tire (F_z), which is transmitted to the vehicle. While F_z concerns handling only in terms of how it affects F_x and F_y , the vertical force transmitted by the tire to the wheel axle hub is the primary focus of study, in ride aspects of tire behaviour.

Perhaps the first major parameter to consider in understanding the ride behaviour of tires is the vertical stiffness of the tire. The tire, due the compressibility of the trapped air within it and also to a smaller degree the compliance of the tire sidewall and the tread, will deflect under an increasing load. The slope of this static load deflection curve is the static stiffness of the tire. This static stiffness value tends to have a linear increase with pressure in the operating range of interest [87].

In representing the tire for ride and vibration handling the tire is modelled as the classical 1-DOF spring-mass-damper system [87]. The system is then used to determine the stiffness and damping of the tire in the vertical direction via various test methodologies [87]. Three types of stiffness are considered, static, non-rolling dynamic and rolling dynamic stiffness depending on the test methodology used to obtain them. Ref. [87] describes each, as well as methods used to obtain the stiffness and associated damping. Of importance to vehicle simulations of ride is the rolling dynamic stiffness, it representing the conditions under which a tire is normally operating. In a study of the rolling dynamic stiffness and damping of a 13.6R38 radial tractor tire at 1.4bar

inflation pressure and 1825kg load [87] it was observed that rolling dynamic stiffness drops off rapidly from the static value with increasing speed up to a value of approximately 8km/h at which point it converges to an asymptote. The rolling dynamic stiffness decreases approximately linearly with inflation pressure. With regards rolling dynamic damping the tractor tire exhibited a sharp increase of approximately 15% at about 1,5km/h from its quasi static damping coefficient value and then decreased to an asymptote of about 45% of its quasi-static value at a speed of 20km/h. The dynamic coefficient of damping increased approximately linearly with increasing pressure for a constant test speed of 5 km/h. At speeds above and below this the increase tended to be more non linear. Reference [87] suggests that these general relationships hold true for passenger car, truck and tractor tires, although no literature was found that supports a direct extrapolation to large earthmoving type tires as found on the BELL ADT. No general conclusions have been made about the relationship between static and dynamic stiffness of tires although some reports indicate that the rolling dynamic stiffness may be 5% less than static stiffness for heavy commercial truck tires and 26% less for tractor tires [87].

2.1.5.2 Stationary out of plane dynamics

The in-plane behaviour of the tire dealt with ride aspects and longitudinal and braking force. The out of plane dynamics deal with the forces and moments acting on the tire that affect directional control and directional stability, these being the lateral force (F_y) the aligning moment (M_z) and the overturning moment (M_x). There are various mechanisms at work in the development of these forces and similarly various parameters that influence the forces. Here again the discussion of these forces and influencing parameters will be limited to the case of steady state operation in this section.

The parameter that most influences the development of the lateral forces is side-slip or more specifically, slip angle (α). It is an analogous parameter to the slip that determines longitudinal forces in the tire spin plane but is defined in a different manner for consideration of out of plane lateral force and moment generation. The definition of this parameter as slip angle is something of a misnomer as will be explained but it is the generally accepted definition of the parameter.

Ref. [46] uses a physical model of the tire as depicted in **Fig. 2.14** to explain the concept of slip angle and its relationship to lateral force of the tire. The model consists of a flat rubber disc sandwiched concentrically by two metal discs of smaller diameter. The protruding rubber models the tire sidewall and tread compliance, a property of the rubber pneumatic tire that enables the generation of a slip angle.

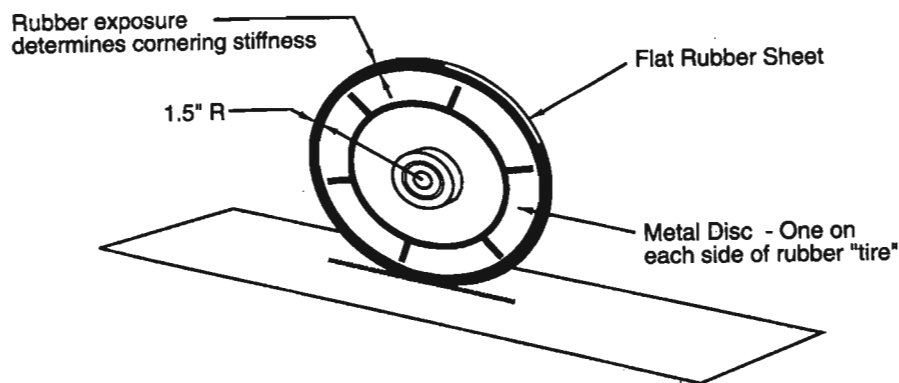


Fig. 2.14 Physical model of tire used to indicate phenomenon of lateral slip angle [46]

If a lateral force is applied to the model with a finite vertical load, the rubber distorts as depicted in the rear view of **Fig. 2.15**. This occurs as a reaction force is generated at the rubber ground interface due to the friction between the rubber and ground. This reaction force is proportional to the lateral deflection of the tire by a factor representing the lateral stiffness of the tire rubber model. The model distortion mimics the combined effects of a real tire's lateral tread and carcass stiffness albeit with exaggerated deflections. Now if the model tire is made to roll in the presence of the applied lateral force without any turning or steering, the model will head off in a direction that is not collinear with the tire plane projected onto the ground. The angle thus formed between the direction of tire heading and the tire plane projection onto the ground is the slip angle (α).

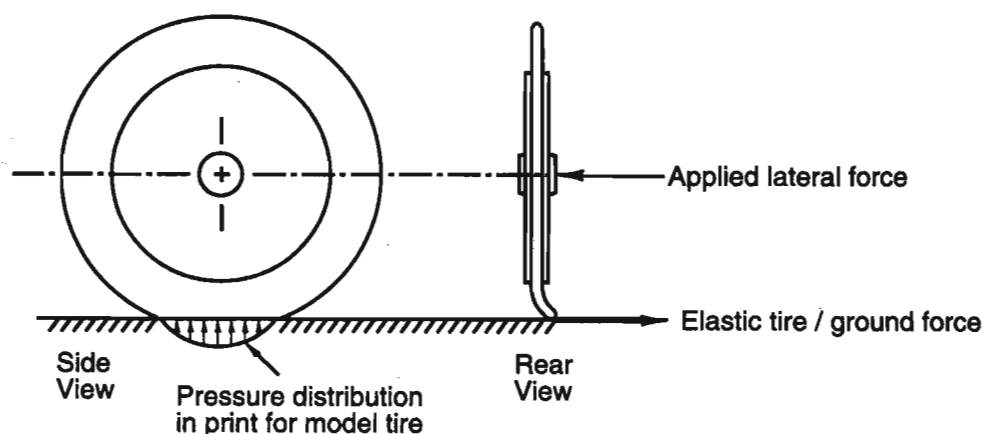


Fig. 2.15 Distortion of the rubber disc in the physical model of Fig. 2.14 due to an applied lateral force [46]

Fig. 2.16 represents the model as viewed from below and will be used to explain what happens at the contact patch.

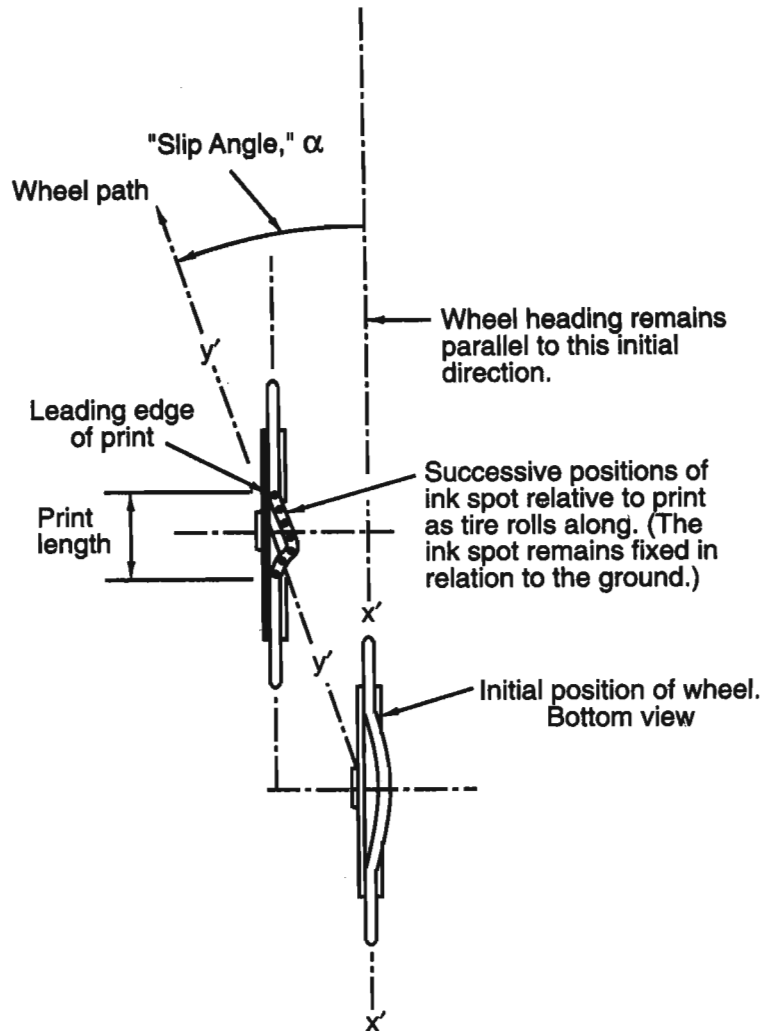


Fig. 2.16 Distortion of the rubber 'tread' of the physical tire model as viewed from below while rolling under the action of an applied lateral force [46]

A series of ink spots were placed on the circumference of the rubber disc in the experiment cited by [46]. An ink spot on the circumference (representing a point on the tread of a tire) which rolls into the contact patch at the forward leading edge, gradually starts to feel the effects of the lateral reaction force which increases along the model-ground contact length (print length) in the fore-aft direction. This is due to the increase in the vertical force along the contact length as the centre of vertical pressure is approached. Thus as the lateral force felt by the point on the circumference of the model increases, the lateral strain in the rubber disc starts to increase and hence the ink spot is displaced further sideward from the tire vertical plane as the point of maximum vertical force in the contact length is approached. Once this point is passed the lateral reaction force decreases towards the trailing edge of the contact length as the ink spot

lifts off the contact area and ceases to be distorted from the tire vertical plane. (Even though the ink pots are 'stuck to the ground' it is convenient to imagine them moving through the contact length). We can thus see that for a tire with slip angle (α) every point on the circumference entering the contact patch is displaced sideward from the points already in the forward part of the contact patch and is hence at an absolute lateral position that has not been covered by the previous point. Thus the tire rolls in a direction that is not coincident with the tire plane. It is the compliant nature of the rubber tire that allows the tire to roll with a slip angle without actually slipping (except at the extreme trailing edge of the contact patch when the decreasing vertical force cannot sustain a high enough frictional force to react the applied lateral force). The tire will however start to slide in the presence of a high enough slip angle or side force which represents the limiting slip angle / side force combination for a particular tire design. Reference [46] also points out that lateral force can cause a slip angle for example a gust of wind acting on the side of a car or a slip angle can cause a lateral force when the wheels of a vehicle are steered to counteract the centrifugal force generated from traversing a curved path.

Fig. 2.17 represents the distribution of vertical force, lateral force and lateral velocity over the contact length of a tire contact patch. The axis Y represents the centre of the tire ground contact. As mentioned earlier the centroid of the vertical force distribution curve causes the normal force (F_z represented by this author in a positive sense as F_N) to act forward of the tire contact centre hence adding to the rolling resistance (see § 2.1.5.1). The centroid of the lateral force distribution curve is aft of the contact centre which means that F_y acts aft of the contact centre as well. Point G on the lateral force distribution graph is the point in the contact patch at which sliding begins in the contact patch. For low slip angles and lateral forces this point is confined to the extreme trailing edge of the tire and the tire rolls effectively without slipping. However for increased slip angles, accompanying the rise in F_y , is a shift of the point G, as well as a forward shift of the centroid of the lateral force distribution curve. Reference [53] indicates in **Fig. 2.18** how the sliding region develops from the trailing edge of the contact patch, with an increase in slip angle and side force, to a point at a critical slip angle where the start of the sliding region and F_y coincide with the tire contact centre and the tire is in a full lateral slide. **Fig. 2.19** indicates a typical F_y vs. α curve. The figure also indicates the linear elastic region, where the lateral force generated by the tyre is due purely to the stress developed by the tire lateral stiffness, the frictional region, where the peak lateral force the tire is able to develop is exceeded (with the lateral force being purely due to tire-ground friction) and the transitional region in between.

Fig 2.17 indicates another important consequence of the slip angle formation. As mentioned for a tire that is not sliding fully in a lateral direction, the lateral force F_y acts aft of the tire ground

contact centre. The distance (t) of the point at which F_y acts to the contact centre is known as the pneumatic trail.

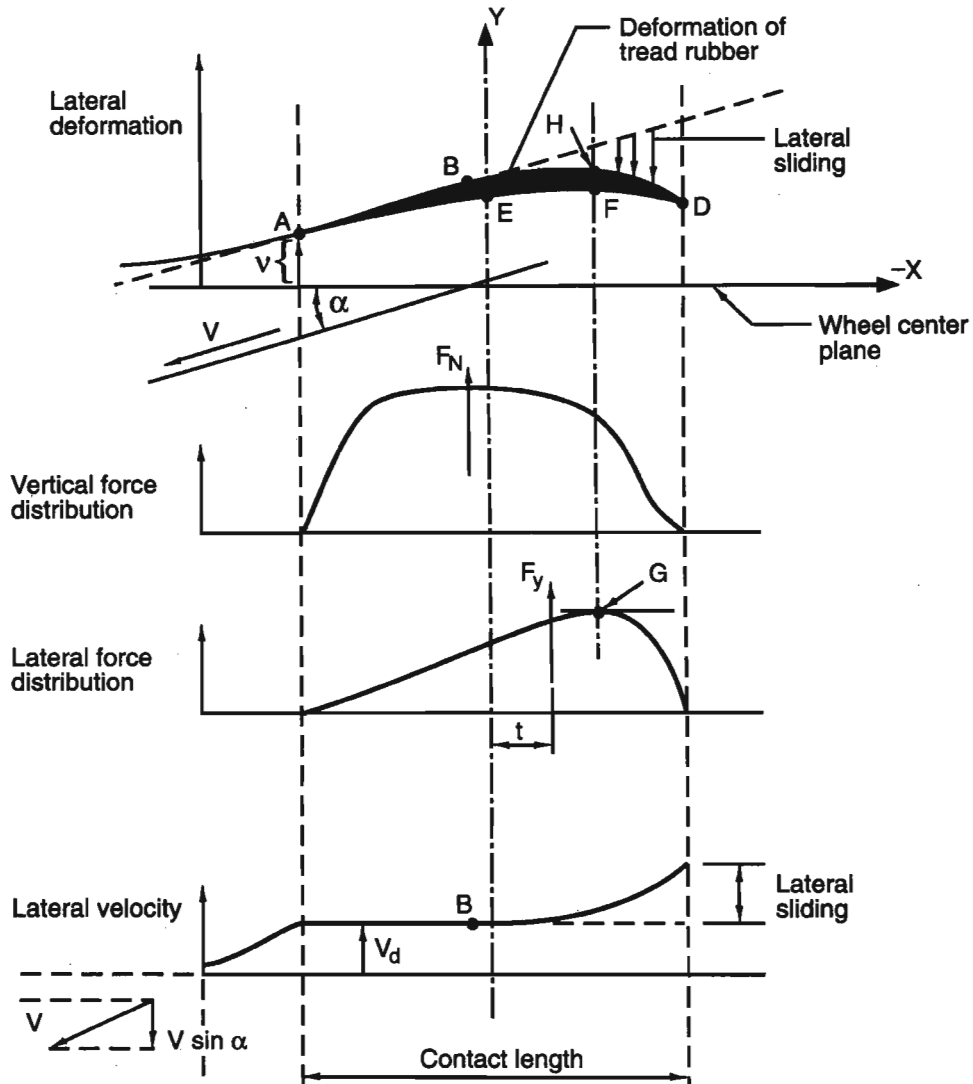


Fig. 2.17 Distribution of forces and local tread velocity along contact patch [46]

The product of the lateral force and the pneumatic trail results in the aligning moment (M_z), which acts to align the wheel vertical plane with the direction of wheel motion. Even though the aligning moment per tire for a given load is typically of an order less than the equivalent yaw moment generated by the lateral and longitudinal forces about the yaw centre of the vehicle (for a four wheeled car), it has an effect on the steering forces required by the driver and has a decisive affect at the limit of road holding behaviour of the tire-vehicle system. Also because of the reduction in M_z with increasing slip angles (due to a reduction in pneumatic trail), it can give warning to a driver of impending breakaway of the tire. Ref. [46] suggests that in the absence of mechanical trail (i.e. a zero degree castor angle) for a high performance car tire, as much as a 30% reduction of steering wheel rim force can occur in the last 1° of slip angle before breakaway.

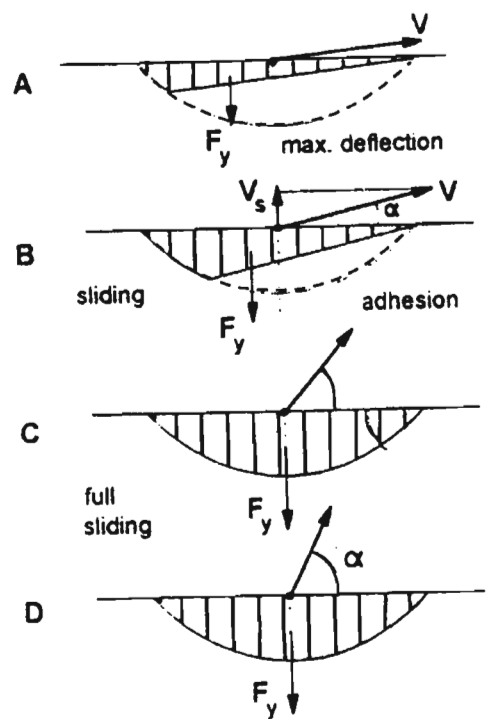


Fig. 2.18 Development of the lateral sliding region from the trailing edge of the contact patch with an increase in slip angle (α) [53]

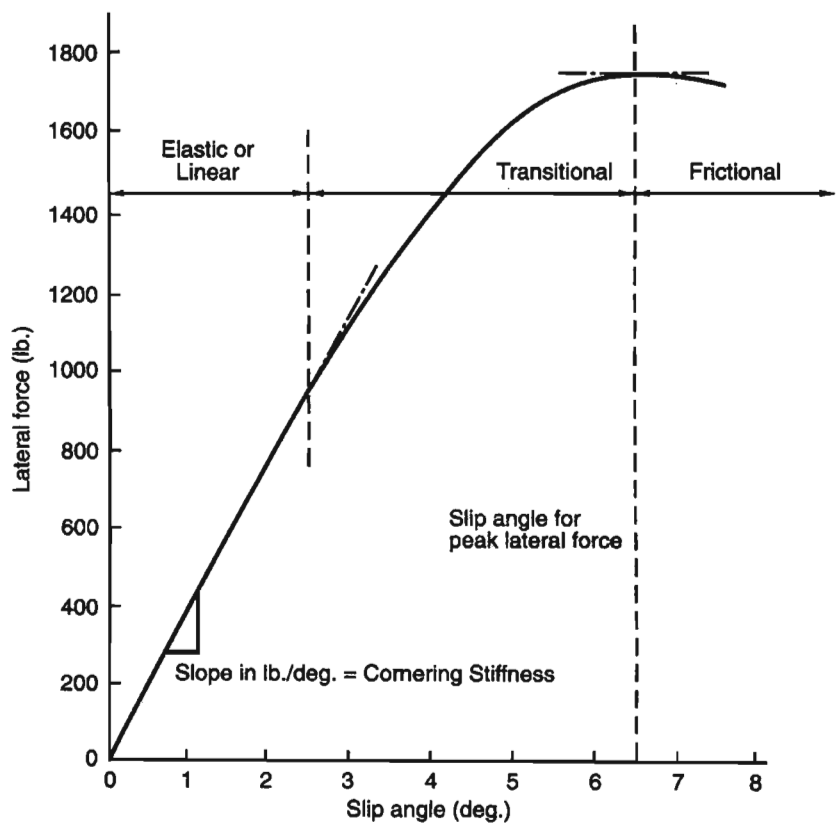


Fig. 2.19 Typical lateral force vs. slip angle curve [46]

Perhaps of all the parameters that act to modify the aligning moment and lateral-force verse slip angle characteristics, vertical load is the most influential. With regards lateral force, increasing the load results in an increased lateral force. However the rise is not proportional and generally the maximum cornering force per unit increase in load is achieved at the lightest loads [21]. Load also decreases the peak frictional coefficient that can be achieved in cornering [21]. An increase in load also causes an increase in aligning moment although unlike the relationship between load and lateral force, the increase gets proportionally greater per increase in unit load. This is due to the proportional relationship between the pneumatic trail and aligning moment. As load increases the contact area increases approximately proportionally [21] and as most of the increase occurs along the length rather than width of the contact patch due to the construction of the tire, the pneumatic trail increases almost proportionately with load. **Fig. 2.20** and **Fig. 2.21** indicate the effects of load on the lateral force and aligning moment vs. slip angle curves respectively. As a note, with reference to **Fig. 2.22**, is that it is possible for the aligning moment to be negative i.e. at high slip angles and lower loads, the onset of the lateral slip region in the contact patch can actually move forward of the tire-ground contact centre causing the tire to tend to want to self steer into a turn rather than out of it.

Speed has much less of an influence on the generation of a lateral force and aligning moment in the general regions of operation of a tire. This according to reference [21] is due to the kinematic nature of the force and moment generation. At low speed small radius turns however the aligning moment generated is large and here again increases proportionally with load [21].

There is nothing in the literature that would suggest that the above effects of load and basic shapes of the lateral force and aligning torque versus slip angles would not be true for the large off road tires as found on the BELL ADT. In fact due to the larger tread blocks and harder hence stiffer tire material, larger load and tires hence larger contact patches and pneumatic trails, the effects would be even larger.

Another contribution to lateral force is camber. Camber angle notation was described in § 2.1.2. Basically camber is a tilting of the tire spin plane from the perpendicular to the ground. The pure definition of the tilt is known as inclination angle (γ) and camber angle, the more dominantly used term in vehicle dynamics parlances, is described slightly differently in terms of its sign (see § 2.1.2).

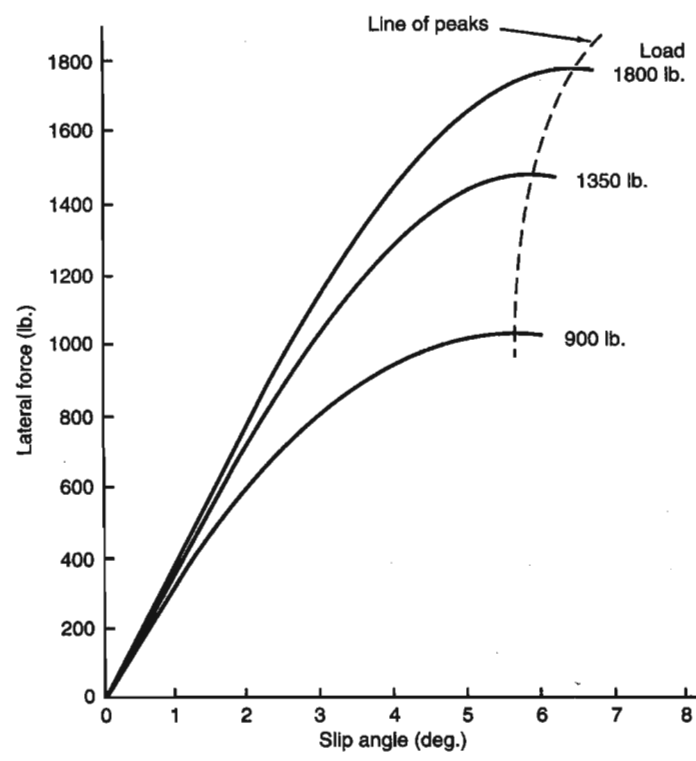


Fig. 2.20 Lateral Force vs. Slip Angle curve for a racing car tire showing dependency on load [40]

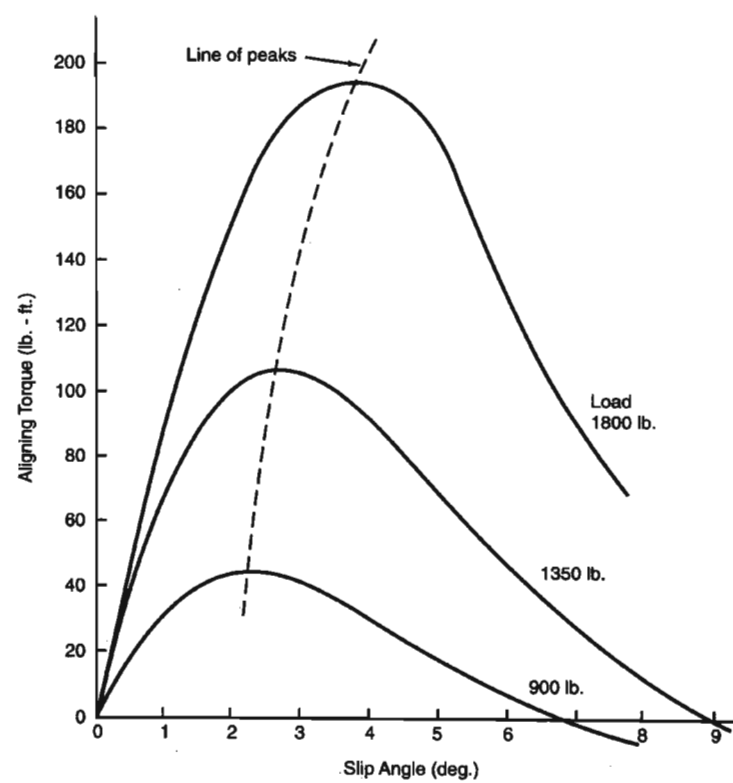


Fig. 2.21 Aligning Moment vs. Slip Angle curve for a racing car tire showing dependency on load [40]

A camber angle will generate a force in the direction of the angle of tilt (of the top of the tire) and is known as camber thrust ($F_{\gamma\gamma}$) [87]. It is additive to the lateral force due to slip angle alone ($F_{y\alpha}$) for small angles γ and the effect decreases at higher angles. The camber angle thus acts to raise the F_y vs. α curve for a tire leaning into a turn and lower the curve for a tire leaning out of a turn. Reference [53] presents results of camber angle verse lateral force that show for large width street racing radial-ply tires, the effect of camber falls off at camber angles greater than 5° . This suggests that camber effects on large width radial-ply tires such as used on the BELL ADT, are minimal. Camber effects though are useful in motorcycle tyres (narrow, bias-ply) up to 50° . For equivalent values of slip angle, much less lateral force is generated by camber effects than by slip angle effects. The effect of camber is also larger for bias-ply than for radial-ply (approximately one-fifth the effect of equivalent slip angle for bias-ply tires and much smaller for radial-ply [87]). References [87], [46] give brief introductory explanations of the reasons for the above effects. As with other tyre forces, camber thrust is affected by load. The optimal camber angle for a given tire design, that acts to increase the lateral force, increases with load [46]. Reference [46] also indicates that the camber thrust acts ahead of the tire-ground contact-centre and acts to steer the wheel into a turn (opposite effect to aligning moment) however this effect is negligible. High camber angles also promote excessive wear on a tire [87].

It will be noticed in actual tire test data from certain tires that plots of F_y and M_z vs. α that the forces and torques are not zero, at zero slip angle. For example the data obtained from Michelin for the BELL ADT tire [44] display this effect. This is due to tolerances in the manufacturing process and actual tire imperfections. The effects are known as conicity and ply-steer. The definitions are as follows:

“Conicity – When the manufacturing process results in a tire that has the shape of a truncated cone when viewed from head on. This will result in the tire wanting to steer in the direction of the apex of the cone (for $\alpha, \gamma = 0$) no matter which direction it is rolled in.” [46]

“Ply Steer – Caused by the direction of the ply’s (in the carcass and the crown) wanting to self-steer the tire from its intended straight line course (for $\alpha, \gamma = 0$). The direction of the lateral steering force thus generated changes direction with change of direction of rolling.” [46]

It should be noted that these effects can actually be designed into a tire to produce the desired effects and not necessarily be that of manufacturing imperfections.

A concluding consideration on out-of-plane steady-state tire dynamics is the overturning moment (M_z). Reference [46] presents a diagram that is reproduced in **Fig. 2.22** which best explains how this moment is generated. The axes directions are according to the SAE axes system with R_l being the tire loaded radius and ϵ being the offset of the vertical load on the tire from the tire-road reaction force on the tire.

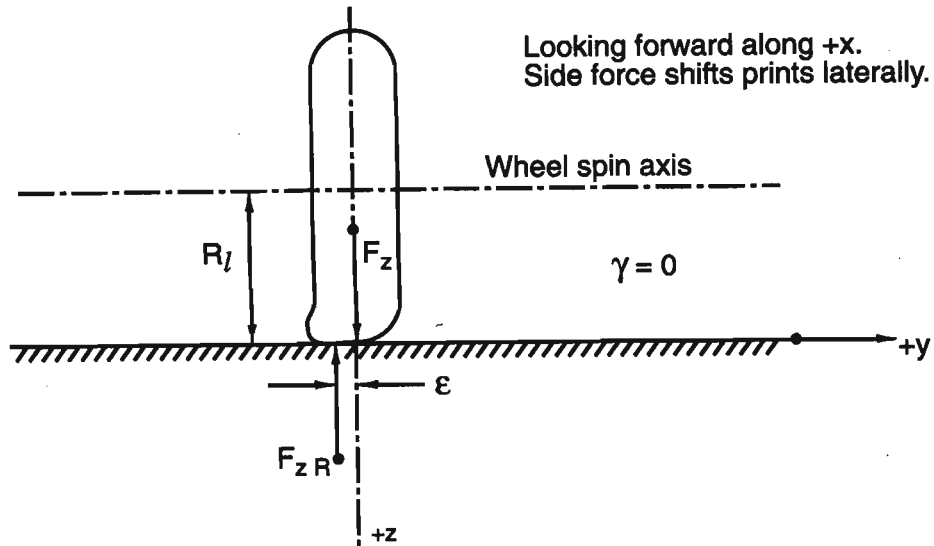


Fig. 2.22 Overturning moment caused by offset of vertical load and vertical reaction force on a tire [46]

An overturning moment is essentially created whenever the vertical load and the road reaction force ($-F_z$ according to the SAE convention) from the tire contact patch are not collinear. Its effect is more pronounced in wide tires that are operating at close to rated speed in high lateral acceleration cornering.

2.1.5.3 Combined slip and non-stationary behaviour

So far in the above discussion on tire forces, only the steady state forces have been discussed and in the lateral and longitudinal directions separately. The reality though is that the tire often operates in a transient region for example in an accident avoidance manoeuvre [11] or with lateral and longitudinal forces acting simultaneously as when a vehicle is braked in a corner [87].

In considering combined longitudinal and lateral force behaviour, it turns out that the limits of tire force generation in the individual lateral and longitudinal force directions are reduced in combined longitudinal and lateral slip situations. At low values of tractive effort (i.e. longitudinal braking and forward acceleration), the decrease in lateral force that the tire is able to sustain, is due to the reduction in cornering stiffness, which contributes to the lateral force

formation due to tire strain in the lateral direction [87]. Reference [21] reports though that for certain intermediate slip angles the lateral force that can be developed can actually increase slightly for moderate braking. References [87], [11] also present data to support this phenomenon and add that while the cornering force available in braking or driving conditions is approximately equal for radial ply tires, this is not the case with bias-ply tires which exhibit a slight increase in cornering force under moderate braking for slip angles in the range 2° and 4° .

For higher values of slip angles and tractive slip, the available force for cornering (lateral) and traction (longitudinal) is limited by the available frictional force at the contact patch [87]. The friction force basically has to be shared between the longitudinal force and lateral force acting on a tire. For a tire on the friction limit, increasing the lateral force means a decrease of the longitudinal force if the tire is to be prevented from sliding and vice versa. **Fig. 2.23** presents a family of curves for the normalised longitudinal/lateral forces (F_v representing vertical load in the figure) in combined slip conditions for a radial ply passenger car tire.

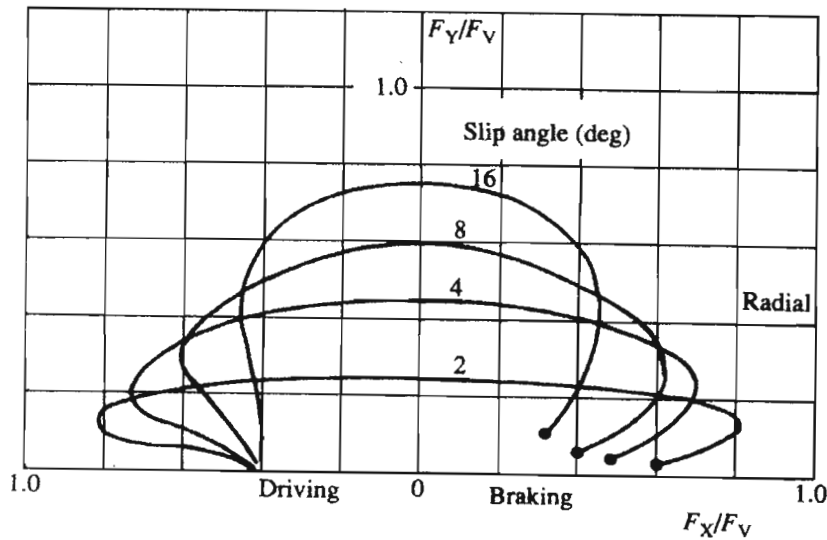


Fig. 2.23 Combined slip curves for a radial play passenger car tire [11]

If an envelope is drawn around the curves, a curve approximating an ellipse is formed [87] and represents the limiting area of available friction force for longitudinal and lateral forces available to a particular tire. The friction ellipse concept indicates that the tire will begin to slide along the ground if the vector sum of the longitudinal and lateral forces reaches the ellipse proper, which is defined, by the coefficient of local friction and the vertical load. The friction ellipse is represented graphically in **Fig. 2.24**. Reference [87] also presents an empirical method and semi-empirical theory to define the combined slip operation of a tire.

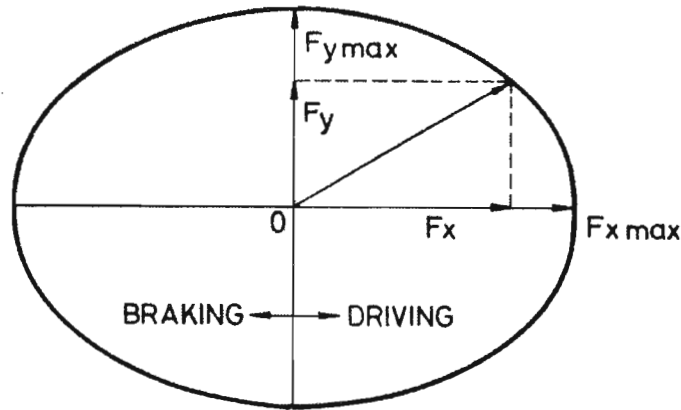


Fig. 2.24 Friction ellipse representing combined maximum lateral and longitudinal force limits [87]

Reference [11] indicates that more accuracy can be introduced into such theories of combined slip behaviour by considering the effect of speed of travel on the frictional coefficient. The friction ellipse concept is sometimes also referred to erroneously as the friction circle. It must be noted that hardly a tire exists that has such a perfect locus of limit friction behaviour. In fact even the friction ellipse can fail to completely define a tires limit friction forces as many tires including heavy truck tires [87] have asymmetrical combined slip behaviour as regards limit lateral force generation w.r.t. full wheel lock and full wheel longitudinal slip [11].

In addition to combined slip behaviour a vehicle very often undergoes dynamic manoeuvres whereby the assumption of steady state force development cannot hold true. For example sudden accident avoidance manoeuvres involving large amplitude steering inputs as well as high frequency steering motions dictate the inclusion of transient effects in a model of a tire. Such manoeuvres affect the dynamics of the tire not just in the road plane but in the vertical tire direction as well. Sudden steering manoeuvres involve vertical and longitudinal load transfer and if the vehicle is being braked or accelerated and is being driven over a rough surface for example, it can be seen that the tire dynamics are very complex indeed.

Perhaps the best way to explain the effects of tire transient behaviour is to say that the tire does not respond immediately to inputs (steering, traction and braking) and that if the input frequency is increased, there will be critical frequencies above which the steady state force that the tire is able to develop will diminish or in extreme situations cease to exist.

In general then there will be a lag in response to inputs of lateral and longitudinal slip. The reason this occurs is largely due to the compliance of the tire carcass (the compliance of the

tread being assumed to be such that it contributes negligibly to the lag effect) [53], [56], [30]. In order to begin to quantify the effects of carcass compliance on transient behaviour the concept of relaxation length is introduced [56]. The relaxation length is the distance from the initial time of input that a tire must roll to develop 63.2% of its steady state value and has a value equal to approximately one tire radius [11]. References [87], [29] describe methods to determine the relation length from testing. The standard representation of the relaxation length in the literature is the symbol (σ) with the subscripts x, y, z indicating the direction in which the effect is being considered according to the SAE axis system. Many authors model the relaxation length effect by introducing or fitting a first order delay element to their equations of motion for the tire [53], [79], [11]. This works well only for low frequencies and amplitudes of slip-angle oscillation and long wavelength undulations in the road. This is because the tire behaves linearly only over a small region. Analytical models of tires developed consider linear stiffness of the tire as relates the longitudinal, lateral and vertical forces and moments, and linear methods of analysis (such as state space methods) are use to investigate the model behaviour [30]. Additionally, above certain frequencies the rigid mode behaviour of the tire belt about the wheel rim must be considered as well [56]. **Fig 2.25** indicates the failure of the delay fitting method to completely track the actual lateral force response to a step change in slip angle of moderate amplitude. Reference [30] indicates that the frequency range to be considered for transient effects on lateral dynamics is 1-10Hz while that for transient vertical dynamics extends to 25Hz. Reference [56] presents a model that includes transient behaviour but recommends its use for steering oscillations well below the first natural frequency of the tire (\approx 0-15Hz range) and for wavelengths of road undulations much greater than the tire contact length (\approx 1.5m undulations). This gives an idea of the frequency range that must be considered when modelling a tire for vehicle handling investigation.

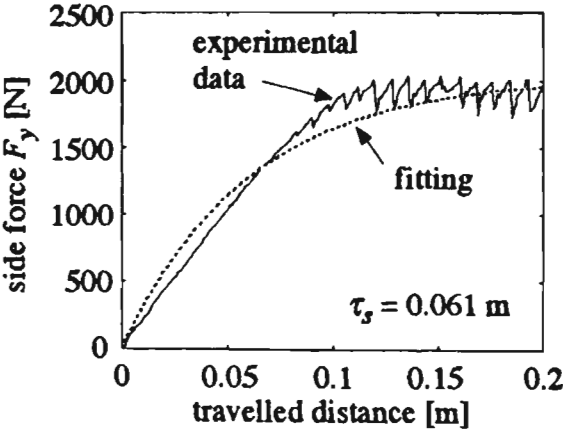


Fig. 2.25 Failure of delay fitting procedure to model transient tire behaviour [56]

The effects of transient tire behaviour are significant. For example the loss in cornering ability of a tire with varying vertical load (e.g. cornering on a road with short wavelength undulations)

is depicted in **Fig. 2.26**. The μF_z curve represents the total frictional force available for cornering. As can be seen even at quasi-steady state values of vertical load (F_z) variation the lateral force (F_y) able to be developed is reduced and at 8Hz the average cornering force available is drastically reduced. **Fig. 2.27a / 2.27b** shows the influence of slip angle frequency on lateral force development for slip angles up to about 2Hz (linear lateral stiffness range). As is evident the tyre loses cornering stiffness and the phase difference (i.e. delay) increases with an increase in frequency of oscillation of slip angle. Reference [30] also presents data for higher wheel speeds, which confirm the trend that at higher speeds the changes in tire lateral stiffness and phase are reduced.

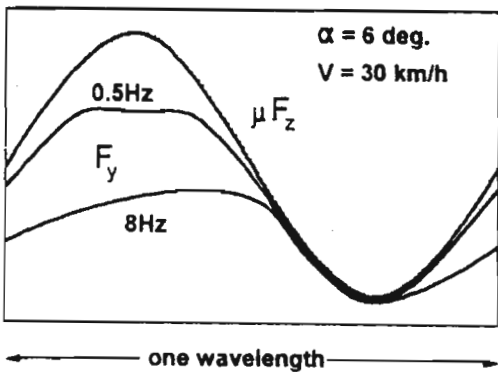


Fig. 2.26 Reduction in lateral force with increasing freq. of vertical load variation [53]

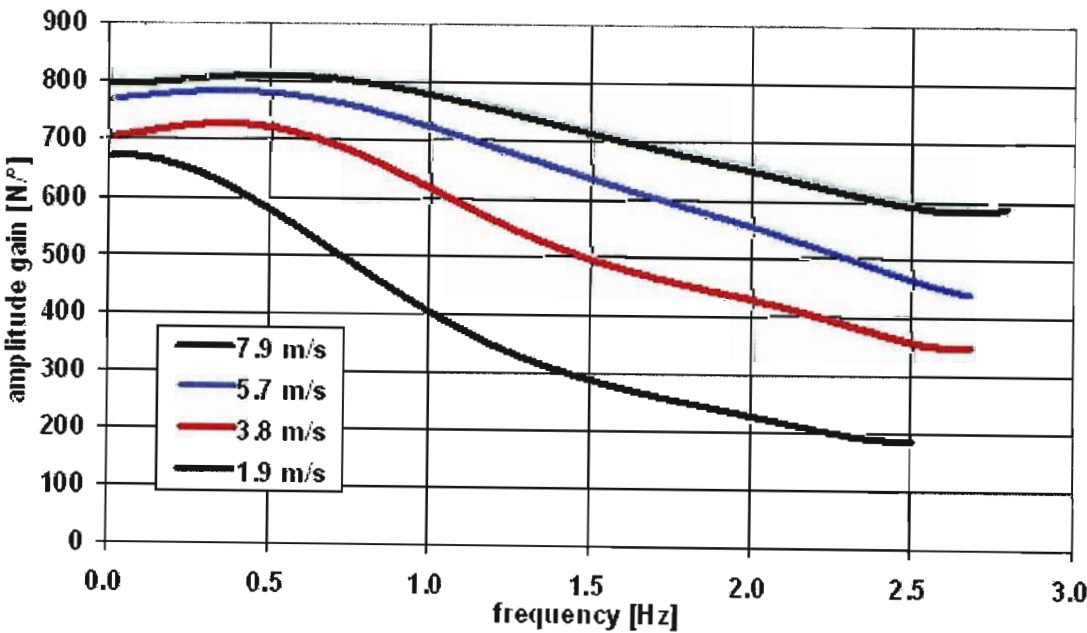


Fig. 2.27(a) Reduction in lateral force with increasing frequency slip angle variation for different wheel speeds [30]

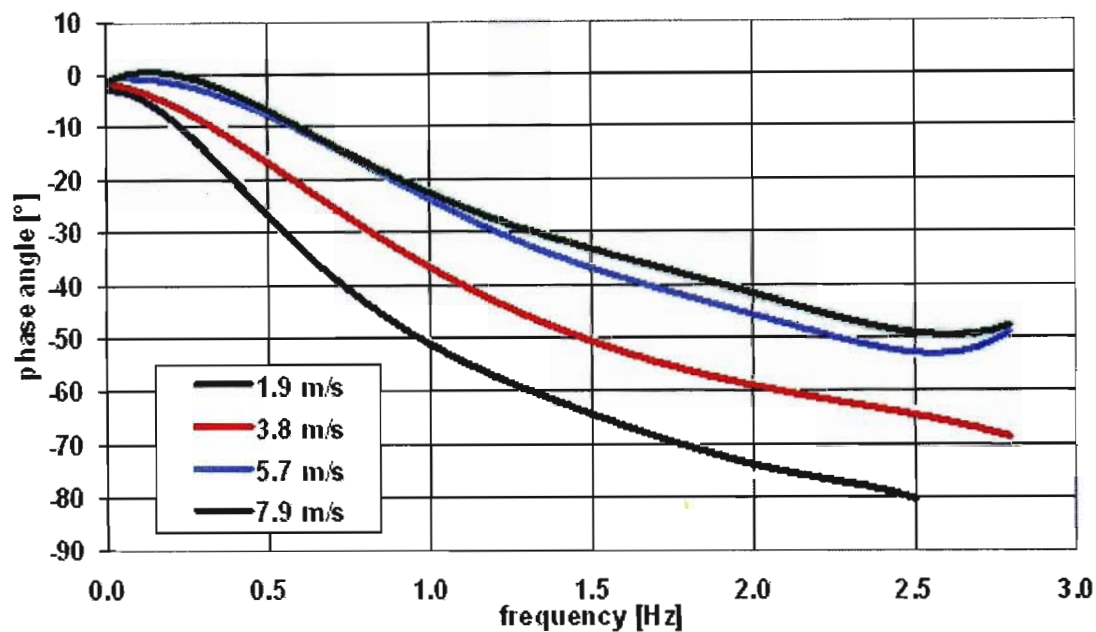


Fig. 2.27(b) Lateral force phase drop showing increasing delay with increasing frequency of slip angle variation for different wheel speeds [30]

Fig. 2.28 is a graphical representation of a simulation neglecting transient behaviour in a model of a tire. The figure indicates the final positions of a car in a simulation of a double lane change manoeuvre, with the car on the left utilizing only a stationary tire model and the car on the right using a tire model with transient characteristics. The authors of the reference [66] states that in neglecting transient characteristics no conclusions can be made about the stability of a vehicle tire system.

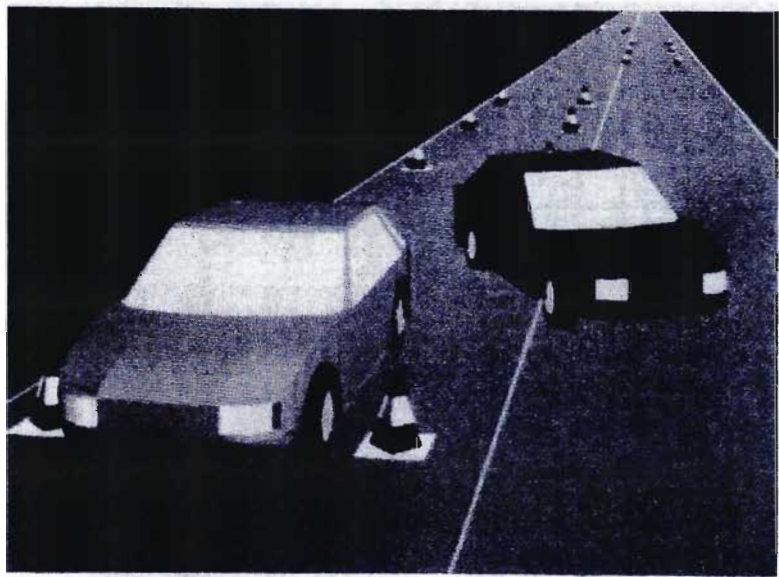


Fig. 2.28 Multi-body simulation highlighting effect of neglecting transient tire behaviour on vehicle handling and stability [66]

2.1.6 Tire modelling for vehicle dynamics simulation

Due to the complexity of the tire as a system, application specific approaches have been adopted by researchers and engineers for modelling the physical behaviour of the pneumatic tire. Four broad types of tire models exist, each varying in degrees of complexity, accuracy and computational efficiency. Further the tire models can be identified as being either analytical or empirical in nature.

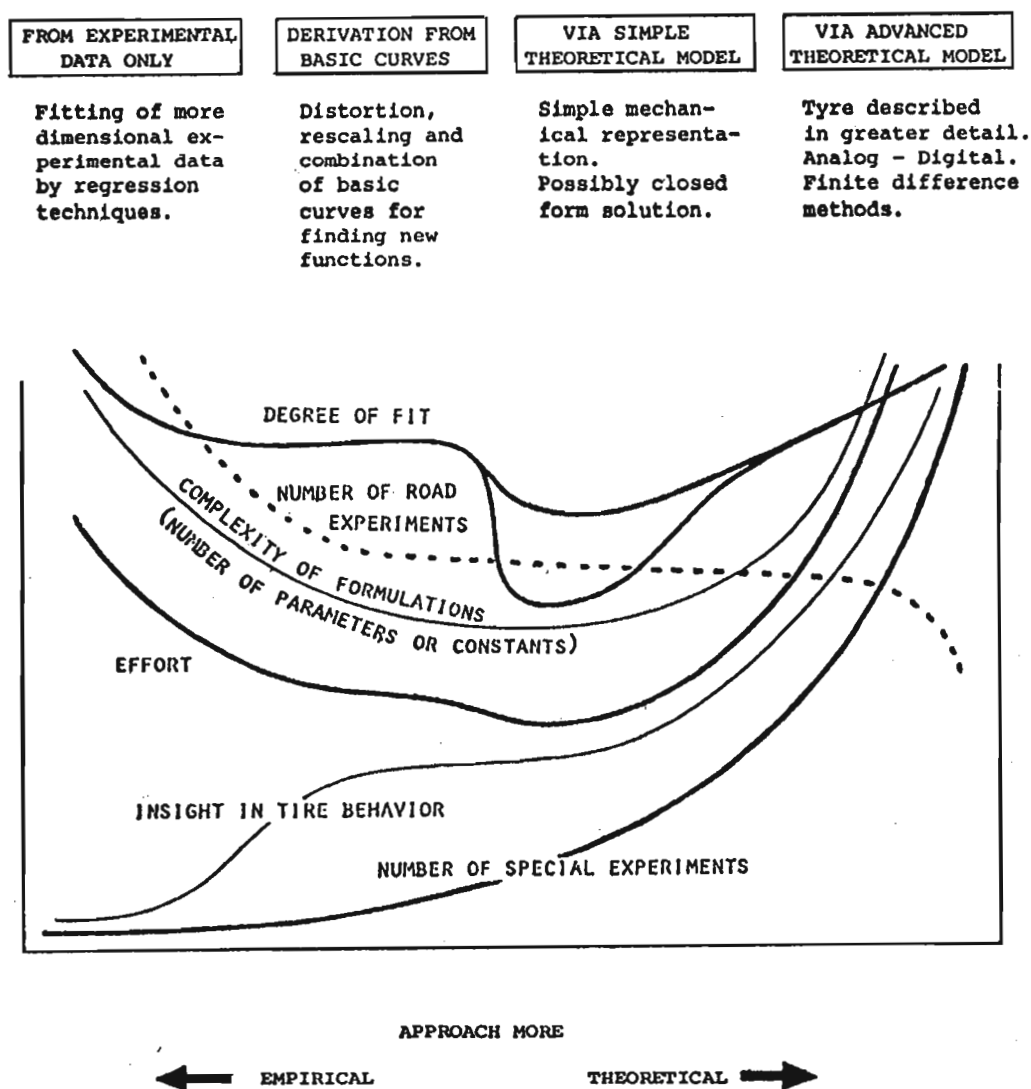


Fig. 2.29 Four types of tire models in use for vehicle dynamics simulation [54]

Perhaps most simple are the analytical models that use mechanical analogues to determine the physical principles of operation, and often closed form solutions are sought. Of course these models can only be considered simple at a first approximation stage where for example linear steady state operating regimes are considered and forces and moments in the various tire axes are considered uncoupled and other further simplifying assumptions are made. These models though can be developed to be quite complete in the general case. Another analytical method

of modelling tires is via the finite element method where the well-established technique is used to determine tire stresses developed from discrete impacts or disturbances. The FEM technique is also useful in determine mode shapes and high frequency vibratory behaviour of the tire. The technique is useful for large deformation type modelling and has been used to model such effects as the standing wave phenomena [13] and tire tread and water interaction with a fluid dynamics finite element code [50].

More empirical type tire models adopt the black-box approach whereby replication of actual comprehensive test data is the objective rather than physical understanding of the process that generates the forces and moments in a tire. Two approaches to empirical tyre models can be identified, non-dimensionalisation and auto-regression techniques. Voluminous data can be made available to the engineer in search of definition of a particular tire's behaviour. Many sets of tests of slip angle verses aligning torque and lateral force (and in turn these relationships verses load) can be conducted. In fact tests where various tire parameters are varied in turn can be accomplished. The question then arises of what to do with all this data. To use the raw data as look up tables and to try to interpolate between values for particular state variable conditions, is cumbersome and will be a huge burden on finite computing time. Non-dimensionalisation in effect attempts to compress this data by defining single curves for multiple tyre tests, for example by defining a curve for lateral force verses slip angle as a function of load. Reference [46] presents a non-dimensionalisation technique. Another more popular empirical method is that of reducing the tire data to functional expressions that relate one tire parameter directly to another, via auto-regression techniques [10]. This has proven to be very accurate in determining tire forces and moments. In particular, a formulation known as the "Magic Formula" has become the most recommended model for vehicle dynamics analysis where comprehensive tire test data is available.

The vehicle dynamics engineer has to consider the best choice of model for his application. Certain models such as finite element method (FEM) models are not particularly suited for vehicle dynamics modelling. The computational effort required automatically precludes its use. A robust computationally efficient model is sought for vehicle dynamics modelling. In addition the FEM model is useful at accurately predicting strains in the tire model. More analytical effort must be expended in determining the boundary conditions and the development of the kinematic input parameters such as slip ratios and angles still needs consideration. The FEM model is thus more suited to tire structural development. On the other hand a very simple analytical model that might prove to be qualitatively correct might prove useless as a design tool where accuracy is sought. And while an empirical model might seem attractive because of its accuracy it has drawbacks in that comprehensive tire data might not be

available. In addition while empirical models work exceptionally well for large amplitude non-linear type tire behaviour they tend to be limited to steady state conditions. As models need to become more accurate the vehicle dynamics engineer might even need to consider combinations of model types. A summary of considerations for the modelling of tires for vehicle dynamics modelling as indicated by [53] is reproduced below: -

- Larger magnitudes of wheel slip and slip angles require a non-linear representation
- Combined slip conditions as opposed to pure lateral and longitudinal slip
- Wheel camber and turn-slip (rate of change of path curvature)
- Conditions when the frictional coefficient independence no longer holds true such as on wet or icy roads
- Transient wheel motions where steady state theories no longer apply
- High frequency inputs and high speeds require consideration of tire inertia properties
- Short wavelength wheel oscillations and road irregularities that require detailed consideration of the contact line i.e. the line that the tire central plane forms in contact with the ground and which is considered non-deformed for flat roads and steady to quasi-steady state conditions
- Simulations starting from and ending at standstill.

Brief description of tire models used in vehicle dynamics modelling

In developing analytical models of tires, researchers use various analogies to develop their models. The brush, stretched string, beam, multi-spoke and rigid ring analogies have found most common use, with authors modifying the basic principles of the analogous representations to include particular effects of tire behaviour depending on the models particular application. The brush model, beam and stretched string models are similar in their approach in that flexible elements are considered attached to a rigid rim. The rim is considered constrained with respect to the flexible elements and the stresses in the flexible elements at the tire contact patch are related to the tire kinematics states such as vector velocities, slip-angles and slip-ratios. Arising from this the output forces are determined for given tire input states. Qualitatively these represent the steady state forces at the tire contact patch well, however more model refinement is necessary if accuracy of prediction is sought. For example to introduce the effects of the carcass compliance and damping in the longitudinal vertical and wheel rotational directions, the rim onto which the flexible elements are attached is assumed to move w.r.t. to the tire centre, with the associated stiffness and damping. Better frictional models can also be included

showing a dependency of frictional coefficient on speed. **Fig. 2.30** indicates the basic physical realisations of the analogous stretched string and beam models. The brush model is very similar to the stretched string model in its approach in that discontinuities in the slope of the lateral and longitudinal force distribution curves are permitted [87], [3]. This leads to more accuracy as the shape of the lateral and longitudinal force curve is in reality discontinuous about the point of transition where the vertical force distribution starts to decrease. The beam model, on which the ADAMS FIALA tire model is based, does not allow discontinuities. The force distributions in the vertical, lateral and longitudinal directions are often parabolic for beam models. These models also cease to be accurate in determining lateral forces when the assumption of small slip angles is violated, as the model is a linear approximation [87]. Also it must be noted that the wheel rim as indicated in **Fig. 2.30** is considered linear and fixed and constitutes the tire centre line (around the circumference), which is undeflected. For steady state and large curvature turns this assumption is valid but as soon as large tire slip angles are required and the frequency of steering oscillation increases, the centre line will deflect requiring model modification. Here the concept of turn-slip or the tire yaw rate is important and reference [52] makes use of this in a stretched string type model to include transient effects.

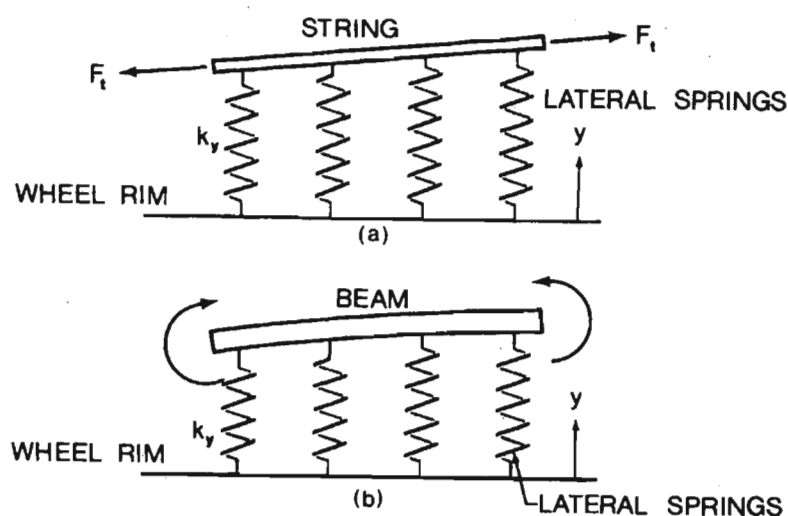


Fig. 2.30 Physical analogies of the stretched string and beam type tire models [87]

Two other prominent analytical models are the rigid-ring and radial spoke models. These models add more accuracy in the vertical and longitudinal directions. The rigid ring model is so named because it uses an analogy of a rigid ring representing the tire tread about a hub which is restrained by rotational and linear spring dampers. This model is able to model the motion of the tire in the frequency ranges that encompass the first few natural modes of vibration of a rotating tire. The radial spoke model consists of spring dampers that extend radially outward from the tire centre to the circumference. This model attempts to capture the

enveloping nature of the tire as it rolls over obstacles. The analogous representations of the rigid ring model and the radial spoke model are shown in **Fig. 2.31** and **Fig. 2.32**.

Perhaps the most accurate model for vehicle dynamics simulation that exists in common usage today is the empirical tire model known as the ‘Magic Formula’. It has been shown to have greater than 99% correlation with the measured data it represents [10] and because the model converts voluminous amounts of tire data into neat trigonometrical expressions, it is rapidly implementable in computer numerical algorithms. It is available in many proprietary as well as popular commercial vehicle specific multi-body codes such as ADAMS and DADS as the techniques used to develop the model have been published in the general literature. The model is attributed to Prof. Hans B. Pacejka of the University of Delft, Netherlands but has been worked on and modified by many authors. Essentially a steady state model for the determination of lateral forces, longitudinal forces and aligning torques as a function of the kinematic states of the tire, it has been used in conjunction with other analytical models to extend its use to transient and combined slip conditions. Pacejka [52], [56] has used the turn-slip and relaxation length concepts to modify a stretched string tire model which predicts tire transient response and coupled this with the steady state response of the magic formula model. Researchers at Michelin [56] have developed a purely empirical technique that employs weighting functions to determine the interactive effects of κ on F_y and α on F_x for combined slip conditions. Thus the model is accurate for a large variety of vehicle manoeuvres and is the recommended first choice for vehicle dynamics simulations [10].

The reader is referred to the literature for detailed descriptions of the various models described above. The brush model is treated by [52] while the stretched string model is adequately covered by [52], [87]. Reference [90] describes the rigid ring type model well, while the multi-spoke model is elaborated upon in [48]. The Magic Formula model development, implementation and use in vehicle dynamic models is covered in depth by [52], [55], [80], [37], [10].

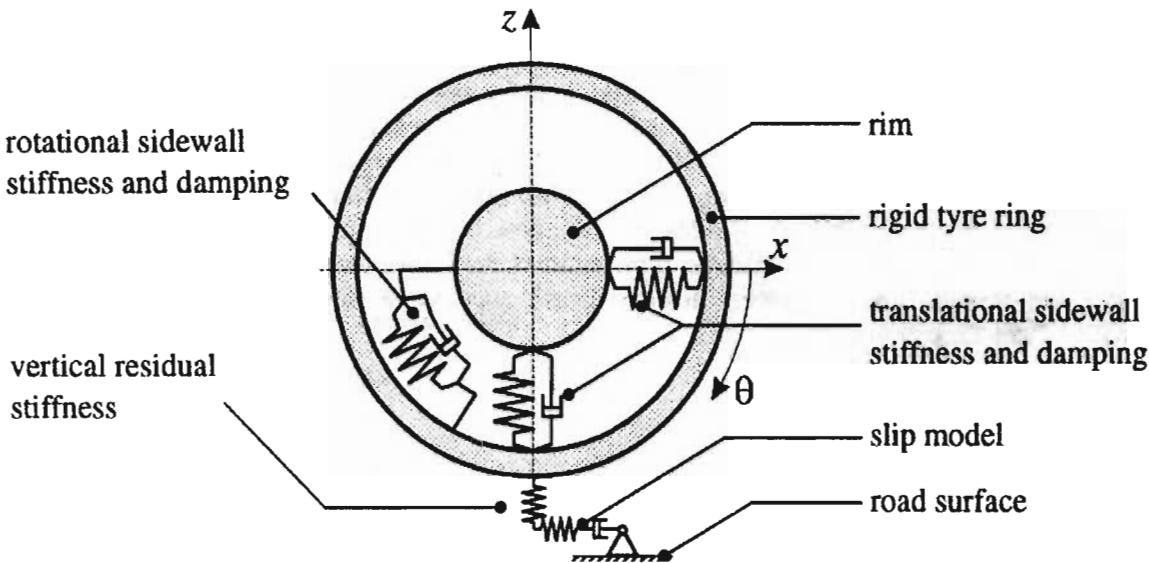


Fig. 2.31 Analogous representation of the Rigid Ring Tire Model [90]

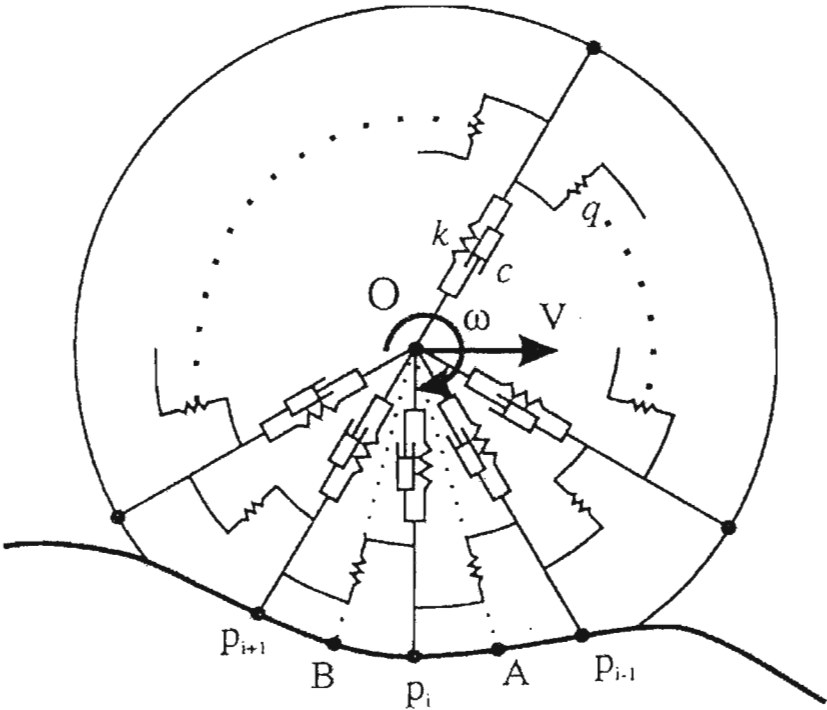


Fig. 2.32 Analogous representation of the Radial Spoke Tire Model [48]

2.2 Approaches to Modelling of Compliant suspension components in MBS codes

In vehicle dynamics modelling, perhaps the largest complications in modelling the dynamics of the rigid body vehicle system are the joints that connect the rigid members. While kinematically it is easy to idealise the joints as those that permit relative degrees of freedom in certain directions while restricting freedom in others, in reality it is not as simple. Real joints do not behave as ideal joints in terms of ideally restricting or allowing relative motion. They have internal friction i.e. energy loss mechanisms, approximated by a coulomb friction and viscous friction or damping, and finite stiffness as well. It may in some modelling applications be acceptable to neglect the effects of joint stiffness and friction, for example when the structure has low friction and high stiffness joints. However when the typical 'joints' used in the automotive industry are considered such as rubber suspension bushes, gas struts and shock absorbers it becomes apparent that the simple approximation of these joints by idealised kinematic constraints will yield incorrect results when full vehicle handling models are attempted. This is because in reality these joints need to be modelled as dynamic or force elements.

While MBS software packages such as ADAMS may be successful at modelling the motion of many interconnected rigid bodies, once the respective connections have been well defined, it is the actual modelling of the connections that present a problem. If the connections can be kinematically defined using idealised joints, the MBS software easily handles this. If the connections can be represented by simple force relationships dependant on a few motion state variables, this can also be easily implemented in the MBS software. The situation becomes problematic when the connections between the bodies in a MBS require complicated models in their own right. Two approaches to modelling physical systems can be considered, whitebox and blackbox modelling. Whitebox modelling adopts an analytical approach and considers the detailed physics of the relationships between the various state variables and outputs of a system. This results in complex differential algebraic equations that require considerable effort in terms of developing the model and solution, using numerical techniques [5]. Blackbox modelling is less concerned with the inner workings of the system but rather with the functional relationship of the inputs and outputs. Thus experimental data is obtained for inputs and outputs of the system under consideration and splines or polynomial functions are fitted to the data to represent the input output relationship. Whitebox techniques remain adjustable due to the physics of interaction between the states variable being well understood. Thus changes in the variables that define the system can be accommodated. Blackbox models on the other hand exist only for the specific system under consideration. Changes to variables necessitate a complete new model or the functional relationship has to be re-established.

The question of when to use a blackbox or whitebox model depends on accuracy, complexity and focus of the model. The analytical techniques for the synthesis and solution of MBS for example are well established and their accuracy in solving a large class of engineering problems are proven [35]. Thus it makes a sense to use such whitebox modelling techniques to model a MBS such as a vehicle. On the other hand modelling vehicle suspension compliant components such as rubber bushes and dampers may be better accomplished as blackbox models. They are very often not the focus of engineering development in considering full vehicle handling models. If the objective of the modelling project is to optimise the design of the bushing or damper then of course whitebox or analytical models of the component have to be considered to understand the influence of the state variables on the behaviour of the component. However if the handling behaviour of various suspension configurations or vehicle system arrangements is to be modelled, it is beneficial not to expend effort on characterising the internal behaviour of the bushes or dampers, but rather to represent their input-output behaviour as blackbox models derived from experimental data. In addition due to the complexity of the physical behaviour of components such as bushes and dampers they are difficult to model analytically. Efforts have been made to model rubber automotive components analytically (whitebox) [7], [70], [71], [72] but even then restrictions on their use for maintaining accuracy are made. For automotive dampers, principles from fluid mechanics can be used to model the energy conserved and lost in the system. But even this requires extensive knowledge of the internal construction of the system and also significant effort in developing a whitebox model. It would thus seem that for a virtual prototyping project that is concerned with the behaviour of the entire vehicle system, it would be prudent to utilise blackbox methods for characterisation of the force and motion behaviour of compliant suspension components.

Blackbox modelling of compliant suspension components has shortcomings over and above issues of adjustability of the model however. Systems such as rubber bushes and dampers have significant non-linearity and also display frequency dependency. It is possible to model the system having only amplitude dependency or frequency dependency, but not both, using conventional blackbox modelling techniques. Non-linearity is displayed when the output doesn't scale by the same factor as the input. This behaviour can however be represented by splines of experimental data or polynomial functions that can be fitted to the data using auto-regression techniques for example. If this behaviour changes with frequency of input though, this type of blackbox model cannot accommodate this requirement. In addition if the system is not a simple single input, single output system then more spline curves or polynomial functions must be considered and interpolated between to arrive at an output. Thus the functional relationship between the output and various inputs is represented by a surface in three dimensions for two input states. If the relationship has to consider more input states, this type

of modelling increases in complexity and the ability to visualise the model is lost [5]. For systems with frequency dependency, the output depends on the change in the frequency of the input and the system is modelled using frequency response functions (FRF's). With a frequency dependent system the output changes phase and amplitude with a change in frequency of the input. The FRF's can be developed from experimental data and using methods such as Laplace transforms [5]. A critical requirement of such frequency modelling techniques though is that the system behaviour is linear.

It can be thus seen that modelling compliant automotive components presents a significant challenge. Analytical techniques are either inadequate or require significant investment in time for components that are strictly not the focus of the vehicle dynamics modelling project. In addition blackbox modelling techniques are not capable of capturing the full amplitude and frequency dependant characteristics of the compliant components. Despite this it is still possible to model these components using blackbox models. Recently developments in the application of neural networks to model systems with non-linearity and frequency dependency as well as multiple input systems have been made. These neural network models have been applied to automotive component such as bushings and dampers and have been shown to accurately capture the entire range of behaviour of such systems [5]. This is however beyond the scope of this work. It is still possible however, using conventional blackbox modelling techniques, to represent the realistic behaviour of automotive compliant components. This is accomplished by considering the range of operation that is to be modelled and consequently to make restrictions on the types of inputs or the type of system that is to be considered. For example if it is only the NVH characteristics of a vehicle that is to be considered, where the inputs are usually small (and in a linear range centred around some equilibrium position), then linear FRF's can be used. For the case of vehicle handling and manoeuvring where the amplitudes of motion are high but the frequency of motion is confined to the quasi-static frequency range then [5] and [7] suggest that non-linear splines or polynomial functions can be utilised. It is this approach that is adopted in the modelling of the BELL EQ. ADT in this work.

2.3 General vehicle dynamics fundamentals

The study of the motion, response and stability of land bound vehicles falls under the broader category of vehicle dynamics. While strictly this study encompasses all the forces that are present in a vehicle system that cause it to change or maintain its current state of motion, including higher frequency vibrations, vehicle dynamics is generally assumed to be the study that encompasses the large-scale motions of a vehicle. The study of vehicle dynamics has come to the fore since the start of the 20th century with the advent of the motorised vehicle [11], [21]. This has led to detailed study of the various arrangements of suspension and sprung and unsprung masses that constitute land-based vehicles, mostly those vehicles that traverse prepared surfaces, or on-road vehicles. This section however does not purport to be a detailed study of the kinematics and kinetics of the BELL EQ. ADT. Instead it presents some general ideas from the literature on fundamentals of vehicle dynamics that encompass the low frequency large motion behaviour vehicle. Of necessity due to the lack of analytic literature available in the public domain on vehicles such as the ADT, many of the principles have been derived from the study of more typical road going vehicles. This is not to say that such an overview is of no value in the study of a dedicated off-road vehicle of the size and configuration as the ADT. In fact a brief overview of certain key principles of road going vehicles present ideas on the behaviour and testing of land based vehicles in general. This offers an entry point into understanding the specific behaviour of a vehicle such as the ADT and offers a project such as this insight into what sort of tests and simulations should be run in order to begin characterising the ADT. Certain principles from road going vehicles that are common to the ADT are mentioned. These include the behaviour of solid axles, which are still present on many cars and road-going light and heavy commercial trucks as well as principles of road going articulated vehicles such as tractor semi-trailers. Behaviour of road going vehicle configurations such as independent suspensions with little or no relevance to the dynamics of the ADT have not been discussed. The section is broken down into sections that constitute the vertical, longitudinal and lateral motions of a vehicle and the rotations about these axes. While the motions about and in these principle axes are essentially coupled, there are cases when the motions can be considered decoupled and a study of the motion in each principle axis separately makes for a better understanding of the overall behaviour of a vehicle. The vehicle axis system is shown in **Fig 2.33**.

The ride behaviour of a vehicle is considered to be the response of the vehicle in the vertical or x-z plane. In general this is composed of the vertical translation of the vehicle along the vehicle z-axis and the pitch of the vehicle about the y-axis. Due to the relative dimensions of

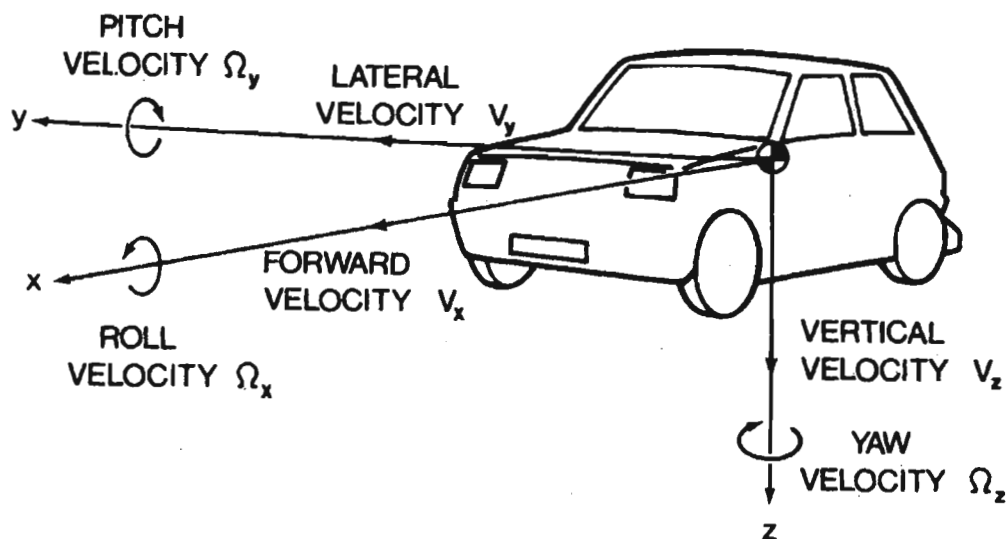


Fig. 2.33 Vehicle axis system [87]

the wheelbase of a vehicle to the track as well as the angle of incidence of road obstacles acting first on the front then on the rear of a vehicle (rather than from side to side) it is the pitch rotation that is more of a concern than roll about the x-axis. Ride is broken up into three distinct frequency regimes: primary ride, secondary ride and harshness. Primary ride encompasses the motion of the sprung mass in bounce and pitch while secondary ride concerns those frequencies between the primary ride frequencies to the wheel-hop frequencies. Harshness is defined as the vibrations induced in the vehicle that are much higher than the secondary ride frequencies. Harshness however will not be considered in this discussion.

To gain a better understanding of the actual frequency ranges of interest one must first consider the desired relationship between sprung and unsprung mass. The sprung mass is that part of the vehicle which exists above the vehicle suspension i.e. that part of the vehicle which is suspended by the suspension. The unsprung mass is the suspension and moving parts (hub, axle drive gear in a driven solid axle) supported by the stiffness of the tire alone. The desired ratio of unsprung mass to the part of the mass carried by a wheel (sprung mass per wheel) is 0.1% for non-driven axles and 0.15% for driven axles [21]. Insofar as the ratio of unsprung mass to sprung mass, together with the suspension and tire stiffness' and damping, influence the primary and secondary ride frequencies, this ratio gives a primary ride frequency around 1Hz and wheel hop frequencies (secondary ride limit) of 10Hz for passenger cars [4], [21]. For heavy trucks such as road going tractor semi-trailers the higher stiffness' of the suspension result in bounce and pitch frequencies (primary ride) of 2.5 – 3 Hz [21]. In a study of a 19 DOF model of a commercial articulated vehicle with a two-axle tractor and two-axle semi-trailer, with a gross

vehicle weight of 26 tons the tractor bounce resonant frequency occurred at 1.4 Hz with the tractor pitch resonance occurring at 2.33Hz. The trailer pitch resonance occurred at 1.4Hz [2].

In explaining the wheel hop frequency which determines the secondary ride frequency boundary, a two degree of freedom quarter car model is used that includes the two masses (sprung and unsprung) with the tire stiffness and damping acting between the road profile (which acts as the input to the system) and the suspension stiffness and damping between the two masses. The wheel hop frequency is thus the second (higher) natural undamped frequency of the two mass system. This manifests itself as a bouncing mode of the tire/wheel assembly against the sprung mass which remains stationary during wheel hop [21]. The frequency range from the primary bounce and pitch mode of the sprung mass and the wheel hop frequency is referred to as secondary ride. Road inputs as well as powertrain rigid body motions and tire non-uniformities resulting in imbalance forces act in this secondary ride range. Harshness falls in the frequency range beyond the secondary ride range and manifests itself as noise and a qualitatively defined “rough” ride. This is due primarily to random fluctuations in the road profile. The study of random vibrations involving spectral information and linear transfer functions of the road-vehicle system is used to define the behaviour of the vehicle in this higher frequency range. As it does not influence the handling and gross body motions of the vehicle it has been ignored for the purposes of this study.

While the two-degree of freedom quarter car model is useful in describing the primary bounce and wheel hop resonance, it is not able to fully capture the primary vehicle response behaviour in pitch and bounce, as this is coupled behaviour [21]. For this motion to be uncoupled the product of the front spring rate and the distance to the centre of gravity from the front axle must equal the product of the rear spring rate and the distance to the centre of gravity from the rear axle [87]. This has been found to produce bad ride however. Thus the pitch and bounce motion is to be considered coupled. In determining the solutions to the 2 DOF model (with coupled pitch and bounce) used to study the pitch/bounce motion of a vehicle, the concept of oscillation centres arises [87]. For the 2 DOF model each natural frequency of the system is associated with an oscillation centre, which is defined as being a distance relative to the centre of gravity. One oscillation centre in general will fall to the right and outside of the wheelbase of a car moving to the left viewed from the side. This is known as the bounce oscillation centre as the overriding perception of a passenger will be one of the vehicle bouncing. The other oscillation centre will fall to the left of the centre of gravity and within the wheelbase of the vehicle. This is known as the pitch oscillation centre. Thus any disturbance of the front or rear axle will create a motion about both centres thus causing the vehicle to pitch and bounce and the overall motion will be a sum of the oscillation about both centres [21], [87]. The reason for introducing

the concept of oscillation centres from the literature here, is because it is used in designing good ride quality in vehicles. From [87], the most undesirable location of the oscillation centres will be at infinity to the right of the vehicle and at the centre of gravity. This results in an uncoupled pitch and bounce motion with conditions as described above. The optimal position of the oscillation centres occur when the radius of gyration about the vehicle y-axis (see **Fig. 2.33**) squared is equal to the product of the distances from the centre of gravity from the front and rear axles respectively. This is the most desirable configuration as input at either axle causes no motion at the other. In practice though this is not achievable and designers try to meet this criterion as closely as is possible [87]. Another consideration in the primary ride regime is the ratio of front spring rate to rear spring rate. Reference [4] indicates that in order to attain “flat ride” the front springs must be softer than the rear. A vehicle’s rear axle will encounter the same perturbation in the road as the front axle only delayed in time. This causes a pitching motion of the vehicle. With respect to **Fig. 2.34**, if the front springs are softer than the rear the vertical oscillation curves merge after about one cycle. This results in an overall bounce motion. As pitch motion is more objectionable to humans than bounce [4], [11], [21], [87], this is considered desirable. Reference [4] presents an empirically derived optimal ratio of overall rear to front spring rate (i.e. suspension stiffness and tire stiffness in series):-

$$K_{rear} = 1.21 * K_{front}$$

where K_{rear} = overall rear suspension stiffness

K_{front} = overall front suspension stiffness

While the above discussion pertains to a two-axle vehicle, it is applicable to the ADT, which can be reduced to a two-axle system. The articulated joint can be considered rigid in bending for the purposes of the above analysis and the load equalised arrangement of the rear axles via the walking beam means that the twin axle arrangement at the rear can be simplified to one axle with the load acting at the walking beam pivot.

Due to vibration of a vehicle in the vertical direction, the normal loads on the tires fluctuate. In addition due to the relaxation length effect of the tire as discussed in § 2.1.5.3, a tire is not able to recover to the steady state force immediately. Thus the average vertical force on a tire is reduced and if the oscillations of the vertical force are at sufficiently high frequencies such as near the wheel hop frequency the vertical contact force between tire and road may not be able to recover at all and the wheel might actually lift off the road resulting in a near zero average

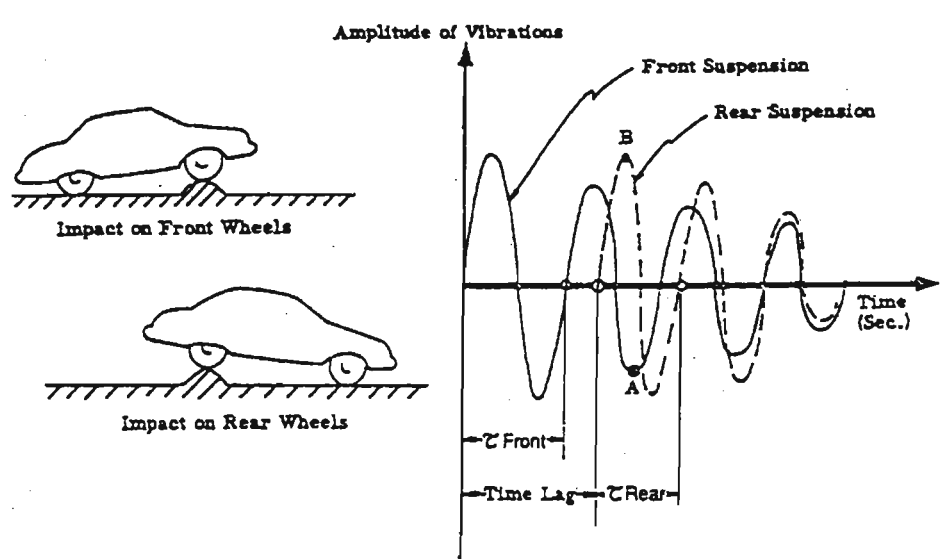


Fig. 2.34 Ride-Flat Tuning by having softer front springs [4]

vertical contact force. As detailed in § 2.1.5, the change in vertical load of a tire impacts greatly on the longitudinal and lateral forces that it is able to sustain. Thus the ride motion is coupled to the handling of a vehicle by the vertical force on the tires. Reference [87] presents a frequency analysis of a quarter-car 2 DOF model that shows how ride affects handling over the primary and secondary ride bandwidth as three critical parameters, unsprung mass to sprung mass ratio, tire stiffness to suspension stiffness ratio and suspension damping ratio. **Figs. 2.35 – 2.37** represent the frequency response of the dynamic tire deflection as a ratio of the sinusoidal input displacement of the road profile. For example the vertical axis (logarithmic scale) represents the gain in motion of the unsprung mass and hence the decrease in tire deflection) as a function of the input road displacement. Thus for example at a gain of 2 if the road displacement is 1cm the decrease in the static deflection of the tire would be 2cm. If the road profile amplitude as well as the gain is such that the tire is allowed to fully release its static deflection, it is on the verge of bouncing off the road and hence cannot support a vertical contact force with the road [87]. Of course this is an undesirable situation, as the tire cannot then support any external lateral forces applied to the vehicle. Practically this situation is likely to occur on a bumpy road surface while a vehicle is cornering.

Examining the effect of unsprung mass on the dynamic tire deflection in **Fig. 2.35** one can observe that there is no influence on the dynamic tire deflection close to the primary ride frequency. However a lighter unsprung mass pushes the wheel hop natural frequency higher as well as reduces the loss in the static deflection of the tire so a lighter unsprung mass is desirable for road holding. It however has some adverse effects on harshness of ride at frequencies above wheel hop frequency [21]. **Fig. 2.36** indicates the loss in static deflection of a tire as the suspension spring stiffness increases in relation to the tire stiffness. Here it is evident that a

stiffer spring will result in a greater loss of static tire deflection at the primary ride resonance but is beneficial at the wheel hop frequency at which the loss in static deflection is more critical. The effect of suspension damping is indicated in Fig. 2.37. As is evident a higher damping is beneficial for road holding at the primary ride and wheel hop frequencies while a lower damping is beneficial in the region in between. It can be seen from the above discussion that there is a trade-off between overall ride quality and road holding capability of a vehicle.

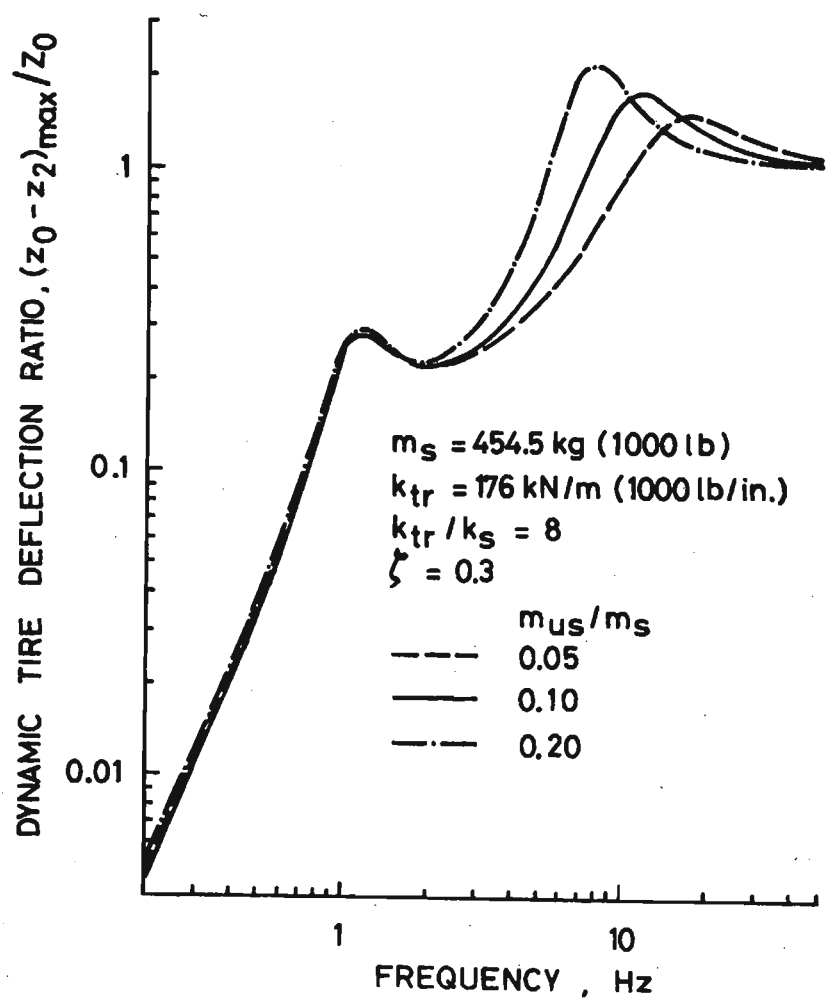


Fig. 2.35 Effect of unsprung mass on ride as indicated by dynamic tire deflection [87]

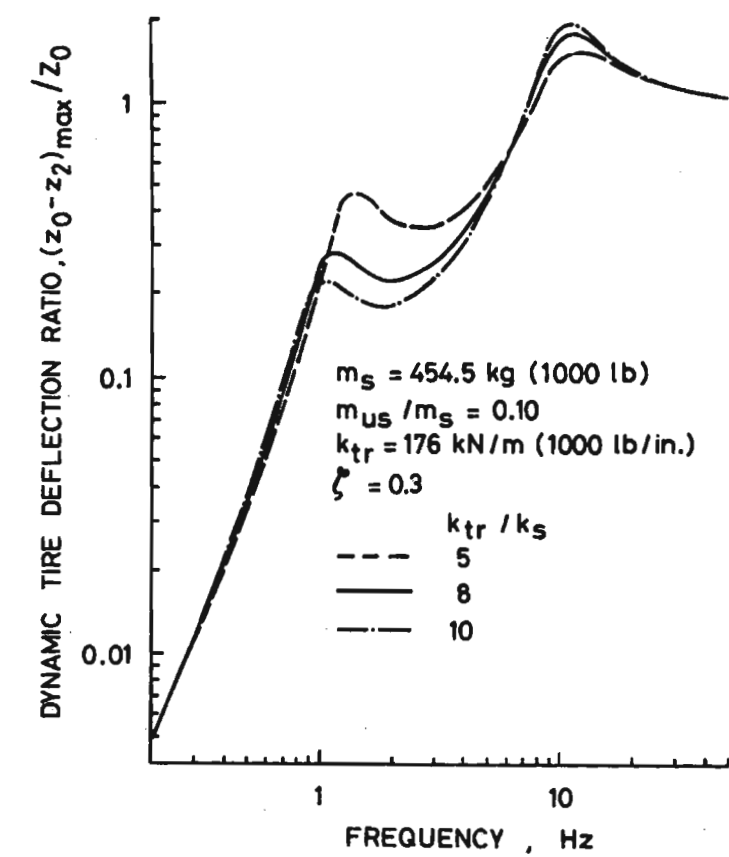


Fig. 2.36 Effect of relative tire and suspension spring stiffness on ride as indicated by dynamic tire deflection [87]

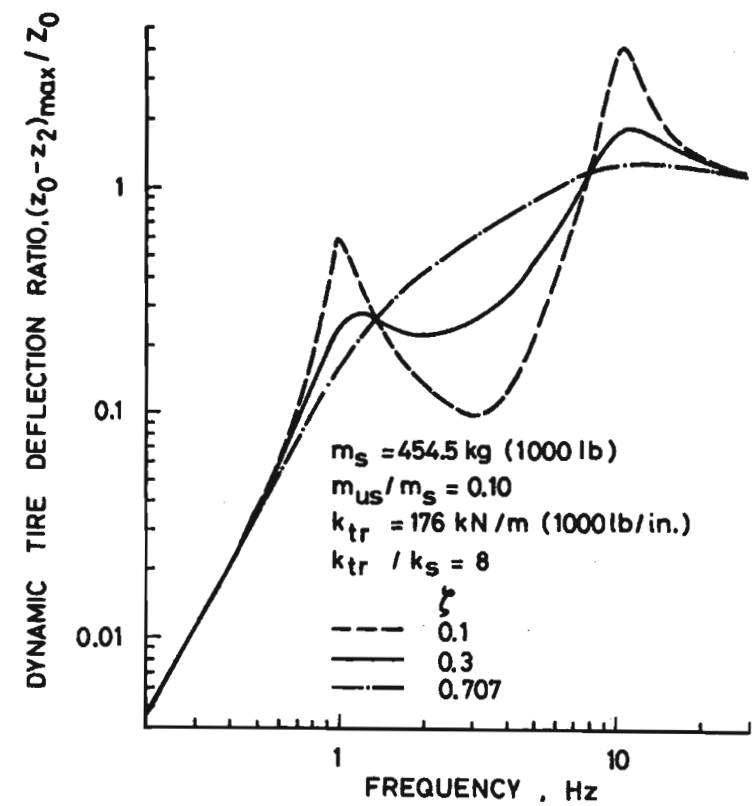


Fig. 2.37 Effect of damping ratio on ride as indicated by dynamic tire deflection [87]

3. VEHICLE TESTING AND DATA ANALYSIS

The actual physical system can be looked upon as the most accurate model of all. Thus testing of the system under investigation gives vital information about the characteristics of the system and vehicle testing is no different. Testing can occur in a variety of environments and during various stages in a traditional system design cycle and beyond. The system under investigation can be tested in a laboratory or in actual working environments. Testing of different concepts could be conducted even before design parameters for the new system can be set while testing of sub-components of a system might be necessary to define input parameters for the system. Various prototypes of the system will then be tested in the process of developing the design. Ultimately the final design will be tested in real operating conditions to prove the validity of the design in meeting the defining criteria for the system. It may also be that further tests are conducted during the life cycle of the produced system to maintain competitiveness or improve on the original design.

Thus it can be seen that testing of the physical system is the final authority in the confirmation of a systems validity. Testing though is typically a recursive and expensive exercise. With modern analytical techniques becoming more powerful and the computing hardware and software required to implement them increasing in efficiency and speed the testing cycle can be drastically reduced with fewer prototypes having to be built in the design process. Thus due to modern analytical method's increasing ability to predict reality, prototypes are becoming virtual in nature, existing via the analytical techniques implemented on computers hence the concept of virtual prototyping. Virtual prototyping cannot replace testing however as final testing of a physical prototype of a new design must remain the definitive confirmation of a design's validity. However the concepts of physical and virtual prototypes cannot be considered to be mutually exclusive. Testing can help validate a virtual prototype and the virtual prototype can ensure fewer actual prototypes are needed and hence fewer tests.

For the purposes of this study, testing assumes the role of validation of the physical prototype. A physical system exists and will be used to investigate the validity of a virtual prototype and hence indicate the virtual prototype's usefulness in future design cycles. Thus the scope of testing in this study is restricted to validation of the virtual prototype. There are of course various considerations in the testing of a system such as a large off-road vehicle. These issues as well the procedures finally adopted for this particular testing exercise are discussed in this chapter. The analysis of data from the tests is also be discussed.

3.1 Vehicle tests

With the question of “Why test?” having been clarified, attention must be turned to how and what to test. With the stated aim of this project being vehicle dynamics a narrower field of testing requirements presents itself. Even then however, one has to consider that an off-road vehicle and a vehicle confined to prepared road surfaces have different operating requirements and hence require different testing procedures. This situation becomes more obvious when one has to consider the difference between a road going passenger car and a 40-ton load capacity off-road articulated dump truck. The scope of the study however must dictate what sort of tests need to be conducted. In addition the available testing facilities and testing hardware play a pivotal role in the decisions taken as relates to a testing program.

This project has certain parameters. It is a first attempt at implementing the technology of virtual prototyping at BELL Equipment. Thus it cannot be considered to be a full design cycle requiring all the detailed testing that accompanies such a process. Deformable road surface modelling must be considered essential to the modelling of an off-road vehicle in its element; however this was not part of the scope of this project. In addition a finite budget impacts on what types of measurement equipment can be acquired. Despite this many concepts of vehicle dynamics are common to all types of land vehicles. The ADT does traverse terrain that can be assumed to be rigid ground. Questions about its stability in various modes of operation are the same as those asked of various dedicated road-going vehicles. Finally a validated rigid road vehicle model can be used as a starting point to model the deformable road (soft-soil) vehicle interaction. Thus vehicle tests that have been developed through years of testing and which have been reported on in the general literature have been considered as starting points for this project’s testing program for the ADT. As the tests are not specifically intended to determine the characteristics of the existing vehicle but rather to validate the virtual model, the tests are modified according to the available resources. To validate the virtual model similar boundary conditions can be specified, with these being easier to control in the virtual model then having to replicate the boundary conditions specified by testing standards in reality.

Vehicle dynamics encompasses handling and ride as discussed in § 2.3. The focus of this study is biased toward handling. Ride however does sometimes fall within the frequency regime of handling and it is considered where applicable to the aims of the project. A discussion of the tests performed which relate to these two operating regimes is presented. Vehicle handling deals primarily with the horizontal (X-Y) plane. The vehicles ability to change direction as well as its stability in maintaining a chosen path needs to be studied. Effects that occur in other planes under certain operating conditions affect the vehicles behaviour in the horizontal plane, for e.g. longitudinal load transfer during braking and lateral load transfer during cornering

impact on the forces available at the tires to maintain stability or change direction. Ride deals with the vertical response of the sprung mass of a vehicle as experienced by a person in the vehicle due to inputs from the road surface. While it can incorporate high frequency content due to the spectral density of the road surface, this analysis will be restricted to primary and secondary ride effects in the low frequency regime. This can identify the susceptibility of a vehicle to unwanted vertical motion on flat road with very little disturbing input as well as the vehicle response to discrete road events such as bumps.

3.1.1 Steady state track lapping

This test involved manoeuvring the BELL Equipment ADT around the approximately oval test track of BELL Equipment at Richards Bay in Kwa-Zulu Natal, South Africa. The track is represented in Fig. 3.1 below.

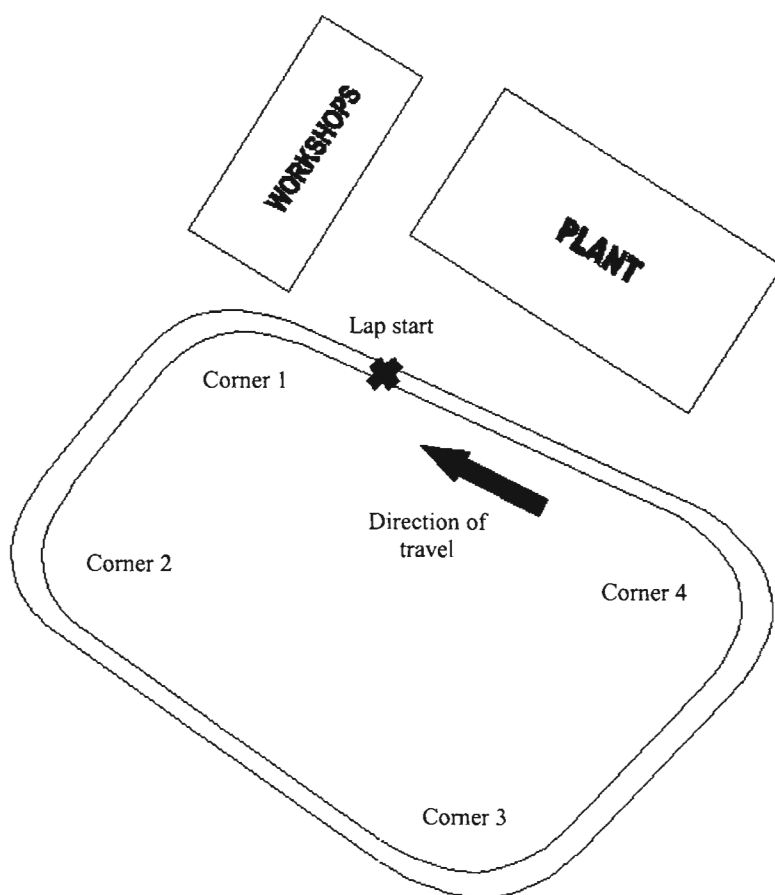


Fig. 3.1 Layout of BELL Equipment test track in Richards Bay

The track has a length of 740m and the corner radii can be approximated to be constant in the range 60 m to 70m. The centre of the track was marked along the length of the track and the driver kept the centre of the nose of the ADT (from the drivers' seat position) pointed along this line. The ADT was driven around the track at constant speeds in loaded and unloaded conditions for speeds of 20, 35 and 50km/h. The data acquisition was started once a constant

speed was reached and the ADT passed the lap start point as indicated in **Fig. 3.1**, and stopped once the ADT reached the lap start point again. Steady state tests give an indication of the steady cornering behaviour of a vehicle and allow conclusions about the understeer or oversteer behaviour of the vehicle under test to be made. Standards such as [62] indicate that corners with radii in a range 30 –300m must be used and that the steady state cornering condition must exist for at least 3 seconds. The tests as conducted attempted to comply with the standard in this regard. Were the testing conditions differ from the standard is in the camber of the track. The track is inwardly cambered with the outer perimeter of the track being higher in elevation than the inner perimeter. The camber is most severe at the corners. Due to the lack of other suitable test facilities this had to be accepted. This did not prove to be a major impediment to the testing program however as the tests being conducted were to be used to validate the virtual prototype. To achieve similarity of boundary conditions in the virtual prototype, the test track including the camber was modelled in ADAMS.

3.1.2 Single lane change tests

The single lane change test is conducted to assess the vehicles transient open loop characteristics i.e. fixed input with no feedback action trying to return the vehicle to its original line. Ideally there would be a fixed path which the vehicle would have travel with the complete change of lanes occurring in a fixed distance. The single lane change manoeuvre would then be attempted at increasing speeds up to a point of instability with vehicle lateral acceleration, steer angle and yaw stability being monitored. However it was not known at the time of testing, at what speed and minimum distance the lane change test could be performed without adversely affect safety. Rollover or spinout situations were not to be considered part of the testing program. The road and safe run-off area available also did not allow large deviations from intended paths even if spinout and rollover situations were avoided. The driver thus performed practise runs to determine a safe distance that the lane change manoeuvre could be performed in while still maintaining absolute control of the vehicle. This distance (40m) was clearly marked on the road surface as well as a distance of 60m. The driver then performed the lane change at 50km/h over a distance of 40m and 60m. The schematic of the test performed is indicated in **Fig. 3.2** below. It must be highlighted that the manoeuvre performed does not represent the limits of the ADT, but rather the limits of safety as adjudged by the driver of the ADT. The width of the available road space was 9.5m. This was divided into two lanes of 4.5m in width and the ADT traversed a path such that it was always in the centre of either lane at the start and end of the test. The driver aimed to complete the tests such that vehicle was just about in the straight ahead position (i.e. no articulation) as the nose of the vehicle pass the marked distance i.e. 40m or 60m. The test was conducted in the loaded and unloaded conditions.

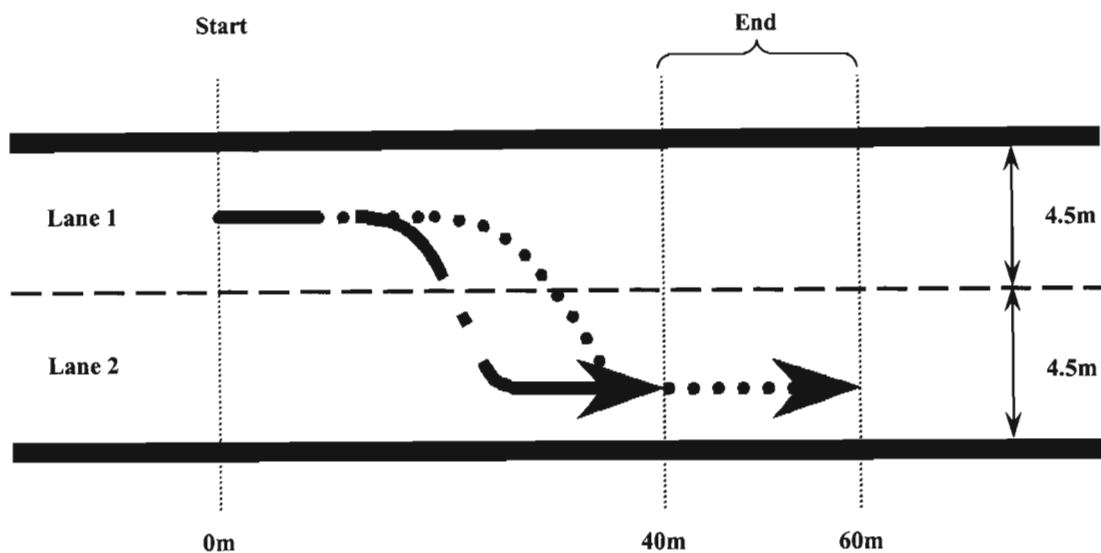


Fig. 3.2 Lane change test (— • —) ADT path over 40m at 50km/h
(.....) ADT path over 60m at 50km/h

3.1.3 Straight-line acceleration and brake tests

This test was conducted to simulate the longitudinal load transfer along the x-axis of the vehicle. The ADT was accelerated from standstill to a maximum speed (dictated by the length of the test surface) and then braked to a standstill. The distance from the start to end was marked and measured. In the unladen condition the ADT reached a speed of 50km/h and was braked to standstill in an overall distance from the start of 239m. With the ADT laden, a maximum speed of 45km/h was reached and braked to standstill over a distance of 276m. While the acceleration and braking was done under conditions of maximum throttle and maximum braking, neither engine torque or brake pressure was monitored. The longitudinal acceleration on the rear and front chassis was recorded. This would allow some correlation with the virtual prototype.

3.1.4 Bump test

The bump test was carried out to obtain a measure of the vertical transfer characteristics of the ADT when traversing discrete large-scale (in comparison to rough road irregularities) obstacles in its path. The vertical accelerations at the axles (at each wheel) as well as at the approximate centre of gravities of the rear and front chassis and the cab were recorded. The longitudinal pitch and lateral roll of the front and rear chassis were also recorded. The obstacle used was of a trapezoidal shape and 0.12m in height as shown in **Fig. 3.3**. Two such obstacles were used to obstruct the entire track of the vehicle. The vehicle was driven in its entirety over the obstacles. The obstacles were of steel construction and were not fixed to the test surface. The ADT was driven over the obstacles at 10 km/h. It was decided not to test the vehicle at a speed higher than this as the vertical accelerations to the cab was sufficient at a speed of 10km/h to cause

sufficient discomfort to the driver and passenger operating the measurement equipment as well as to cause large scale movement of the data acquisition system attached to the ADT. The vehicle was tested in a laden condition only.

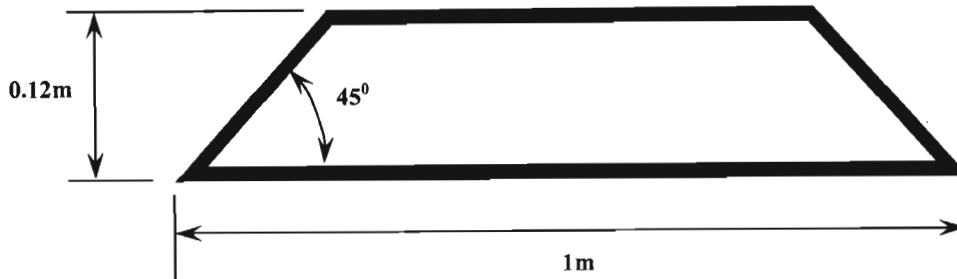


Fig. 3.3 Side view of obstacle used for bump test

3.2 Measurement equipment and sensors

The data acquisition (DAQ) system used was the IOtech® Wavebook 516. The DAQ system was chosen due to its flexibility, upgradability and ability to interface with a wide variety of common voltage output sensors. The system had a 1MHz aggregate sampling rate capability as well as a 16-bit analogue to digital converter (ADC) offering high resolution. The system has a variety of modules that add extra channels to the base system as well as providing different signal conditioning needs. The modules used were the 8-channel base Wavebook module with limited signal conditioning as well as the WBK16 module, which added an extra 8 channels to the system, as well as allowing higher order user customisable low pass filters as well as the ability to supply the excitation voltage needed for certain sensors via a composite cable terminating in a DB-9 pin adaptor at the DAQ end. A full report [22] was submitted to BELL Equipment detailing the choice of the DAQ system over other competitor systems.

For vehicle dynamics testing various parameters need to be measured. Prominent among them are accelerations in each of the three vehicle axes. For vehicle dynamics application these are steady to quasi steady state accelerations. For ride vibration and other vibratory behaviour in the longitudinal and lateral directions the accelerations fall in the low frequency domain. In addition when a vehicle traverses a discrete obstacle larger frequency shock vibrations are transmitted to various parts of the vehicle. Thus the acceleration transducers needed to be robust in a sense that they had to be able to measure down to a true DC or steady state value as well as have sufficient frequency response to capture higher frequency vibrations. In addition while typical handling accelerations (longitudinal and lateral) are relatively low (in the order of 1g for all vehicles but racing cars) the transducers must have sufficient amplitude ranges to capture higher accelerations due to the traversing of discrete obstacles as well as not be damaged by over-range events. They must also be robust in terms of packaging as especially

for measurements on off-road type vehicles they are liable to be fouled by higher temperatures and water and sand.

Equally important in vehicle dynamics testing is the need to measure angular rate or angular displacement of the vehicle about each of the principle vehicle axes. Typically pitch, roll and yaw of the chassis need to be recorded to get a better picture of the dynamics of the vehicle. Traditionally these angular displacements were measured using liquid level inclinometers; however these tended to be cumbersome, fragile and expensive. In addition the frequency response is limited to sub 1 Hz performance. With the advances in solid state devices it has become possible to measure angular displacement under dynamic conditions using smaller more accurate devices which in addition to being more robust and cheaper, offer greater frequency responses making them excellent under dynamic conditions. These sensors measure angular tilt about an axis parallel to the true horizontal using the acceleration of gravity as a reference. The error in angle output is thus a function of sine. Even though this error could be corrected via post-processing these devices are accurate up to a range of 15 degrees. It is thus possible to measure pitch and roll. It is not possible to measure yaw with this type of sensor however as the gravity force reference cannot be used as yaw occurs about an axis that is perpendicular to the horizontal. Yaw is measured using angular rate gyros. The yaw angle can then be obtained by integration, however yaw rate is often the desired parameter of interest. Angular rate gyros are typically very expensive.

Other parameters that typically are of interest are road speed, steering wheel angle and articulation angle for articulated vehicles. In addition parameters such as engine rpm and torque, throttle position as well as brake pressure and wheel forces are sometimes measured depending on the goals of the test personnel. With this in mind and taking into consideration budgetary constraints the following sensors were chosen:-

Single axis accelerometers

Eight single axis ICSensor® accelerometers were procured. These were of the solid-state piezoresistive type that allows accelerations down to true DC values (0 Hz) to be measured. The frequency response upper limit is 1kHz. The acceleration range is 0 – 100g and the sensitivity was 20mV/g. These were used primarily to measure vertical inputs to the ADT at the axles. Calibration was done using the actual rated sensitivity from the calibration chart for each sensor.

Tri-axis accelerometers

Two tri-axis accelerometers were used to measure the acceleration of the centre of gravities of 'the front and rear chassis'. These were also of the solid-state type with true DC response. The frequency response upper limit was 100Hz. The rated sensitivity was 1V/g. This sensor provided excellent response for the low level accelerations experienced in the horizontal vehicle plane, providing large voltage outputs for small physical parameter (acceleration) values that provided excellent signal to noise ratio in the presence of DAQ measurement chain induced random noise. Calibration was done using gravity as a 1g reference in all axes.

Two-axis tilt sensors

Two Crossbow® two-axis tilt sensors were purchased to record the roll and pitch of the rear and front chassis' respectively. These were of the solid-state micro-machined silicon type. Each sensor could measure angular displacement in each of two axes parallel to the horizontal independently. Cross axis sensitivity is typically 5% of full-scale output. The sensors have a frequency response of DC – 125Hz. The sensitivity is 35 mV/° with a 0.05° resolution and the output is linear in the range $\pm 20^\circ$. The sensors were calibrated using the rated sensitivity for each sensor using the actual calibration charts supplied with the sensors. The sensors displayed 'zero angle temperature drift' during testing. The zero angle drift is typically 0.2° per degree centigrade. The outputs were zeroed at the start of tests via the WaveBook software to overcome this effect.

Velocity transducer

To measure the forward speed of the ADT, a DATRON® microwave based velocity sensor was used to record the instantaneous speed. The transducer functions by emitting microwaves aimed at the moving surface (the ground) and uses phase and amplitude information from the reflected waves to determine the ground speed of the vehicle. The device can be set to output a simple voltage, which can be calibrated to give the ground speed. As the exact calibration value was not known, the ADT with the DATRON sensor attached was driven around the BELL Equipment test track at a constant speed and timed over one lap. The resultant speed was compared to the output of the DATRON and the calibration constant modified to match the calculated constant test speed. The device is accurate to within 1km/h.

Articulation angle transducer (DWT)

Due to budgetary considerations and ease of use with the WaveBook DAQ system, use was made of a SIKO® string potentiometer or draw wire transducer (DWT). It had its own signal-conditioning module, which required a 20-28VDC supply, which was taken off the 28V ADT battery. The output could be easily selected via the signal-conditioning module as a simple

voltage. The transducer was mounted on the articulation joint on the front chassis side and the free end of the wire (string) was attached to the rear chassis side via a post with a magnetic base at a height that allowed the wire to be level with the horizontal and for clearance of moving parts. The transducer was calibrated by measuring the voltage outputs at full articulation right to left and using the knowledge that the B40C ADT full articulation was 42° either side of centre (straight ahead). The slope and y-intercept of the linear equation thus formed was used to calibrate the transducer directly to degrees of articulation. The sensor responds accurately to changes in length as long as the draw wire speed does not exceed 3m/s which is way above the speed generated by the articulation steering turning manoeuvres performed under tests.

3.3 Test set-up

In performing the tests set out in § 3.1, the sensors had to be mounted in different configurations to capture useful data. In addition various parameters had to be modified both on the DAQ side and on the ADT as well. This section aims to present the basic testing parameters.

There were two basic sensor configurations, one that was used to capture data from the steady state and transient handling manoeuvres and one to capture the vertical response of the ADT. In addition the sampling frequency had to be varied if test time was of such a length that the throughput and data storage rate of the DAQ system was exceeded. The low pass analogue filters available on the two modules of the Wavebook used had cut-off frequencies of 20KHz and 1kHz. The module with a 1kHz LPF cut-off can be modified to have lower cut-off frequencies by changing resistors on the module, however it was not possible to obtain these high precision resistors in time for the tests. From noise tests done on the sensors prior to the tests at Richards Bay, the single axis accelerometers proved to be the most sensitive to noise effects. The ratio of noise to full-scale output was 80dB, i.e. a *useful* resolvable range of the *entire* measurement chain involving the single axis accelerometers of 80dB as compared to the Wavebook resolvable range of 104dB. Using this as a reference and assuming the Wavebook module used had the 1kHz LPF cut-off, the minimum sampling rate to prevent *all* aliasing would be 11.9kHz [31]. This is already a high sampling rate that would place a burden on the DAQ system resources as the channel count increased. If the sensors were used on the module with a LPF of 20kHz the sampling rate to prevent all aliasing would have to have been much higher.

All of this assumes that there is sufficient noise energy higher than twice the sampling frequency that can be resolved by the ADC of the WaveBook. Noise tests on all the channels (with the ADT switched on to simulate any ADT based electrical disturbances), done prior to the actual tests, at frequencies of 10, 15, and 20kHz resulted in almost the exact frequency

spectrums, which meant that there minimal (if none at all) aliasing present in the ADT operating environment for the sampling frequencies chosen. It was thus decided to sample as high above 10kHz as was permitted by the DAQ system for each test. The data was then successfully post filtered secure in the knowledge that no aliased energy was present in the signal. The two sensor configurations are indicated in **Figs. 3.4 & 3.5** with reference to **Table 3.1 & 3.2**.

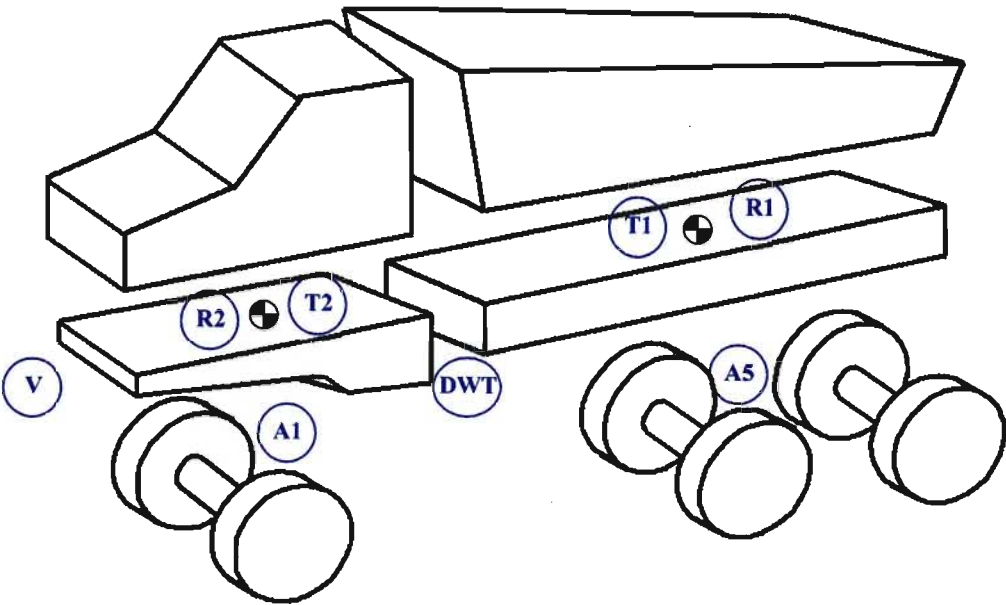


Fig. 3.4 Sensor configuration for the steady state and transient handling tests
(Configuration 1)

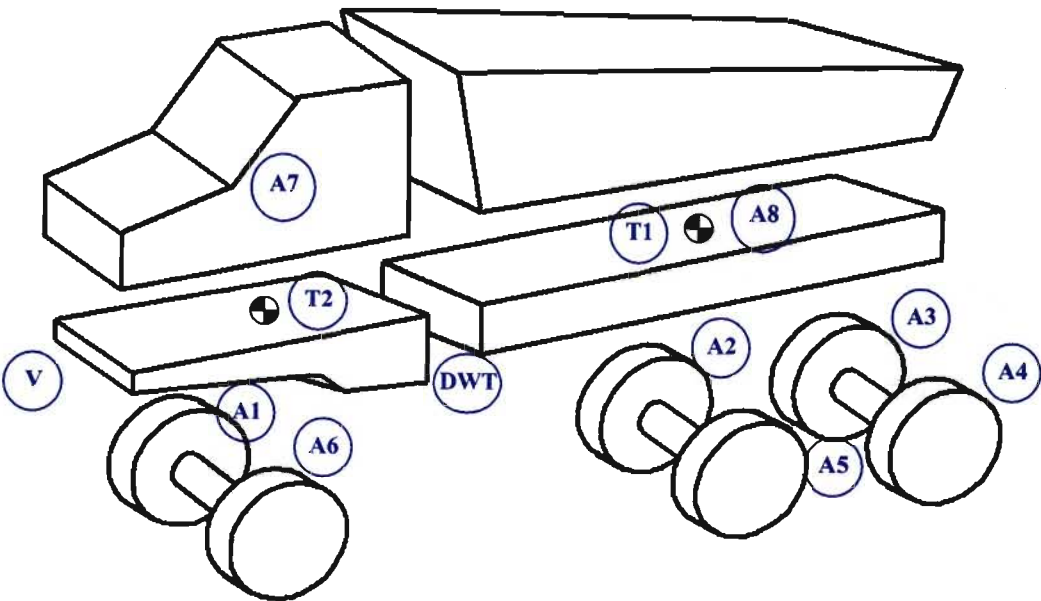


Fig. 3.5 Sensor configuration for the vertical response tests
(Configuration 2)

Sensor Symbol	Sensor type	Measured parameter description	Wavebook channel	Matlab data file column number
T1-X	Tilt	Rear Chassis roll	CH 0-2	1
T1-Y	Tilt	Rear Chassis pitch	CH 0-3	2
T2-X	Tilt	Front Chassis roll	CH 0-4	3
T2-Y	Tilt	Front chassis pitch	CH 0-5	4
DWT	String Pot.	Articulation angle	CH 0-6	5
V	Velocity	ADT ground speed	CH 0-7	6
R2-Z	Tri-Ax. Accel.	Front chassis vertical acceleration	CH 1-1	7
R2-X	Tri-Ax. Accel.	Front chassis longitudinal acceleration	CH 1-2	8
R2-Y	Tri-Ax. Accel.	Front chassis lateral acceleration	CH 1-3	9
R1-Z	Tri-Ax. Accel.	Rear chassis vertical acceleration	CH 1-4	10
R1-X	Tri-Ax. Accel.	Rear chassis longitudinal acceleration	CH 1-5	11
R1-Y	Tri-Ax. Accel.	Rear chassis lateral acceleration	CH 1-6	12
A1	Single Ax. Accel	Front axle vertical acceleration	CH 1-7	13
A5	Single Ax. Accel	Middle axle vertical acceleration	CH 1-8	14

Table 3.1 Sensor configuration 1 – handling tests

Sensor Symbol	Sensor type	Measured parameter description	Wavebook channel	Matlab data file column number
T1-X	Tilt	Rear Chassis roll	CH 0-2	1
T1-Y	Tilt	Rear Chassis pitch	CH 0-3	2
T2-X	Tilt	Front Chassis roll	CH 0-4	3
T2-Y	Tilt	Front chassis pitch	CH 0-5	4
DWT	String Pot.	Articulation angle	CH 0-6	5
V	Velocity	ADT ground speed	CH 0-7	6
A7	Single Ax. Accel	Cab vertical acceleration	CH 1-1	7
A1	Single Ax. Accel	RHS front wheel - axle vertical accel.	CH 1-2	8
A6	Single Ax. Accel	LHS front wheel - axle vertical accel.	CH 1-3	9
A8	Single Ax. Accel	Rear chassis vertical acceleration	CH 1-4	10
A2	Single Ax. Accel	RHS middle wheel - axle vertical accel.	CH 1-5	11
A5	Single Ax. Accel	LHS middle wheel - axle vertical accel.	CH 1-6	12
A3	Single Ax. Accel	RHS rear wheel - axle vertical accel.	CH 1-7	13
A4	Single Ax. Accel	LHS rear wheel - axle vertical accel.	CH 1-8	14

Table 3.2 Sensor configuration 2 – vertical response tests

In addition to the configuration changes for the handling and vertical response tests, the mass of the ADT were changed to assess the effect of payload changes on vehicle response to similar manoeuvres. The sampling rate was also varied to allow the maximum permissible sampling rate (dictated to by the DAQ system transfer rates and storage capacity) for each particular test. **Table 3.3** lists the ADT parameter changes for the loaded an unloaded conditions, while **Table 3.4** lists the sampling rates for each test.

Condition	Axle mass [kg]			Total mass	Tire Pressures [bar]		
	Front	Middle	Rear		Front axle	Middle Axle	Rear Axle
Unloaded	13 940	7 540	7350	28 830	3.00	3.75	3.75
Loaded	18 730	19 830	19 490	58 050	3.30	4.00	4.00

Table 3.3 Loaded and unloaded parameters of ADT during testing

Load condition	Test Type	Test Run	Sampling Rate [kHz]
Unloaded	Steady state track lapping	20 km/h	10
		30km/h	10
		50 km/h	10
	Acceleration brake tests	0 – 50 – 0 km/h	15
	Lane change	60m length	15
		40m length	15
Loaded	Steady state track lapping	20 km/h	12
		30km/h	12
		50 km/h	12
	Acceleration brake tests	0 – 50 – 0 km/h	12
	Lane change	60m length	12
		40m length	12
Loaded	Bump test	10km/h	12

Table 3.4 Sampling rates for various tests performed

3.4 Test Results

The test data was analysed using the engineering data manipulation software package, MATLAB®. The raw data from the tests were converted from binary files to a convenient MATLAB® format using the built-in data conversion software of the WaveBook. The discrete recorded time history of each sensor used in the tests was stored per column in matrix format. Knowing which Wavebook channel the sensor was plugged into allowed one to correlate the sensor with a column in the data matrix of each test run. As the sensor channels were deliberately oversampled to prevent aliasing effects from distorting the data captured, there was more frequency information than that which was needed in the discrete time histories. Thus the signals needed to be digitally post filtered. In addition some spectrum analysis had to be conducted to investigate the frequency content of the signals. Toward this end the graphical signal processing tool in MATLAB® known as SPTOOL was used. This was much more user friendly and intuitive to use than having to write large amounts of MATLAB® script to accomplish the task of filtering and spectral analysis. This section presents some key results of the testing program conducted on the BELL EQ. B40C ADT.

3.4.1 Steady-state handling tests

The results presented here are the roll angles as well as the lateral accelerations of the front and rear chassis'. As with all the results presented here, the data was filtered at with a LPF cut-off of 3 Hz as suggested by [11], using a Chebyshev Type 2 IIR filter as designed graphically in MATLAB® using the SPTOOL graphical user interface. The passband attenuation was set to 65dB as this allowed for a stable and reasonable filter with a flat passband. The phase angle was linear in the passband.

Fig 3.7 and **Fig 3.8** show the lateral acceleration of the ADT front and rear chassis' over one lap of the test track as indicated in **Fig 3.1** for a constant speed of 50km/h in the loaded and unloaded conditions respectively. The data acquisition was started as the ADT passed the marked lap-start position as indicated in **Fig 3.1** and stopped once the ADT reached the lap-start position after one lap. As the trigger was manual, some discrepancy exists in the total time for each lap as well as in correlating an exact event (e.g. exact start of a corner) between different tests runs. The various corners are indicated in the figures.

As the three-axis accelerometer was set up with its positive y axis facing to the left of the ADT (from a driver forward position), a left hand corner is indicated by a negative lateral acceleration. As the direction of travel was counter-clockwise around the track, all the corners as experienced by the ADT during the steady state testing were left hand corners. Thus whenever the plot is negative, the ADT was in a corner. It must be noted that the BELL EQ.

test track is inwardly cambered. Thus even on the straights the lateral acceleration showed an approximately +0.05g offset. In addition the camber angle differed along the length of the track especially on the corners and between the corners themselves. The offset is due to a steady state gravity component of acceleration that resolves itself along the lateral acceleration axis of the accelerometer as explained in Fig. 3.6.

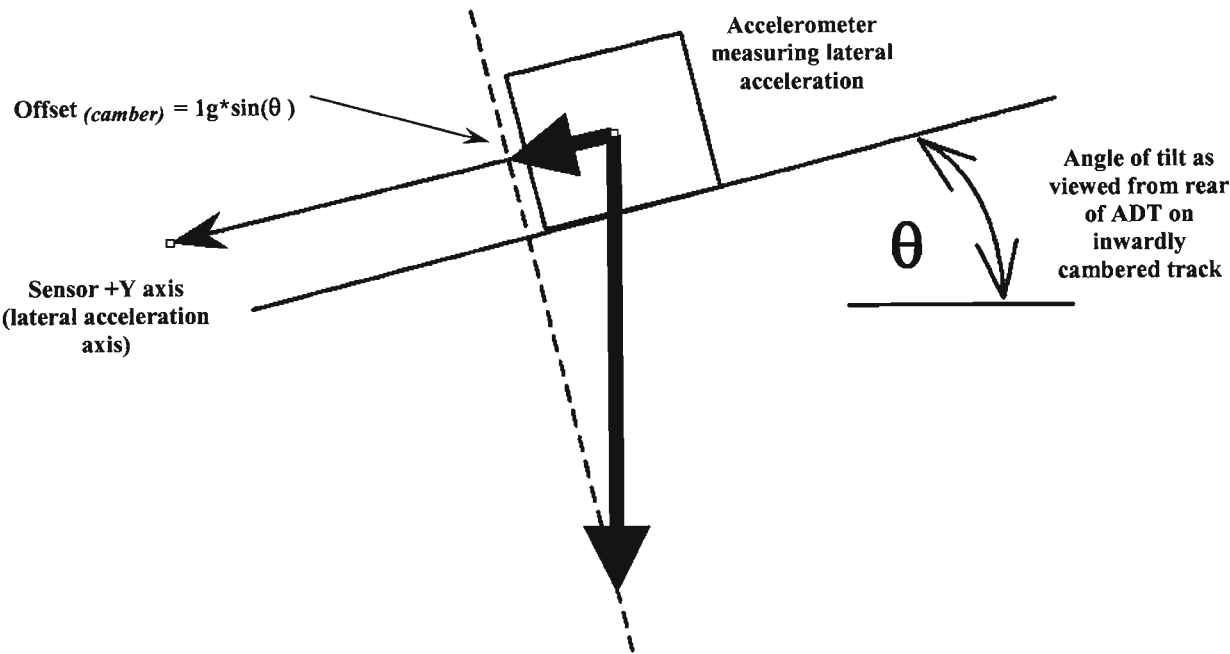
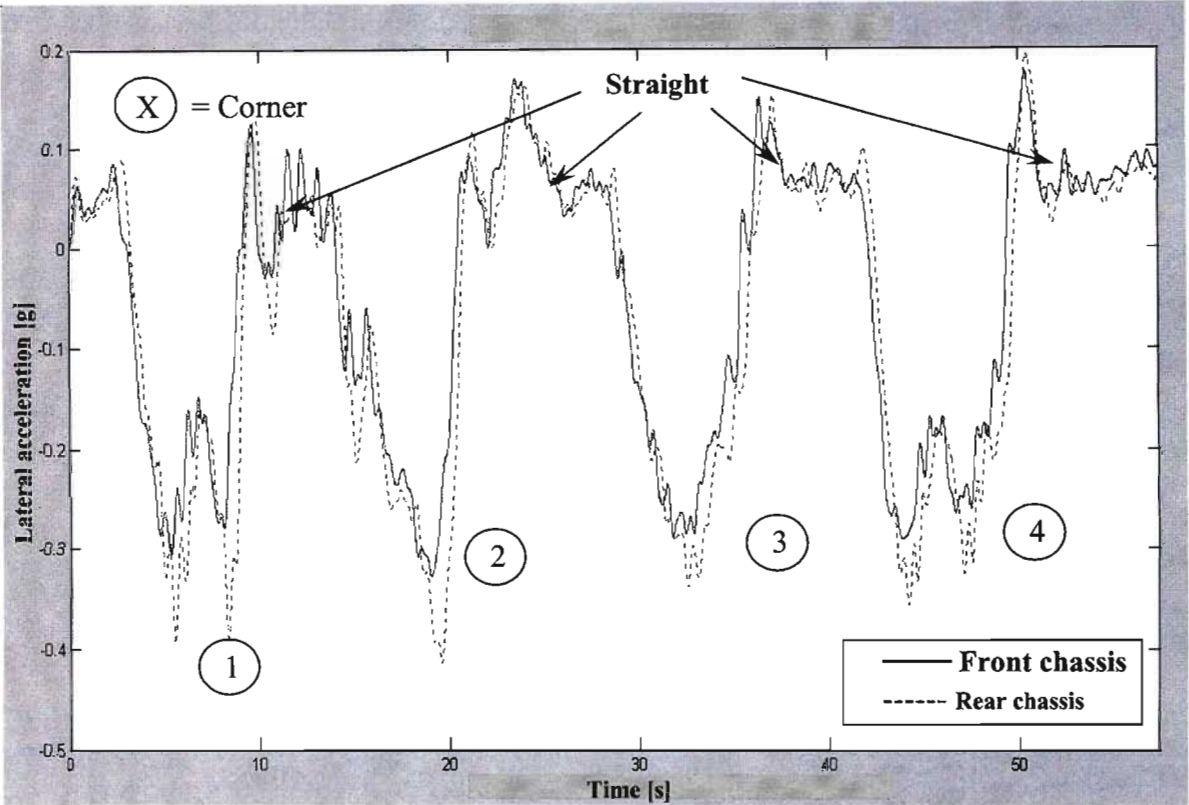


Fig. 3.6 Lateral acceleration offset due to track camber

The offset cannot be zeroed out as the camber is not constant and changes along the length of the track. It is possible to remove the offset knowing the angle of tilt, at each instant in time, of the surface that the accelerometer is mounted on. This information (as a time history) is available from the tilt sensor. Both time histories can be used to correct each other (the tilt sensor displays a similar angular offset due to lateral acceleration). This was not done however.

Even though this was essentially a steady state test, the lateral acceleration time histories were erratic even at the conditions under which the ADT was in a steady state condition (i.e. corners and straights). This could be attributed to the fact that the speed and direction control was done by a human driver. Especially at higher ADT speeds the vehicle was difficult to drive smoothly, requiring many corrections by the driver. In addition as can be noted from the plots (especially at corners two and three) the radius of curvature is not constant through the corners



**Fig. 3.7 Lateral acceleration of rear and front chassis at 50km/h around BELL
Equipment test track (LOADED)**

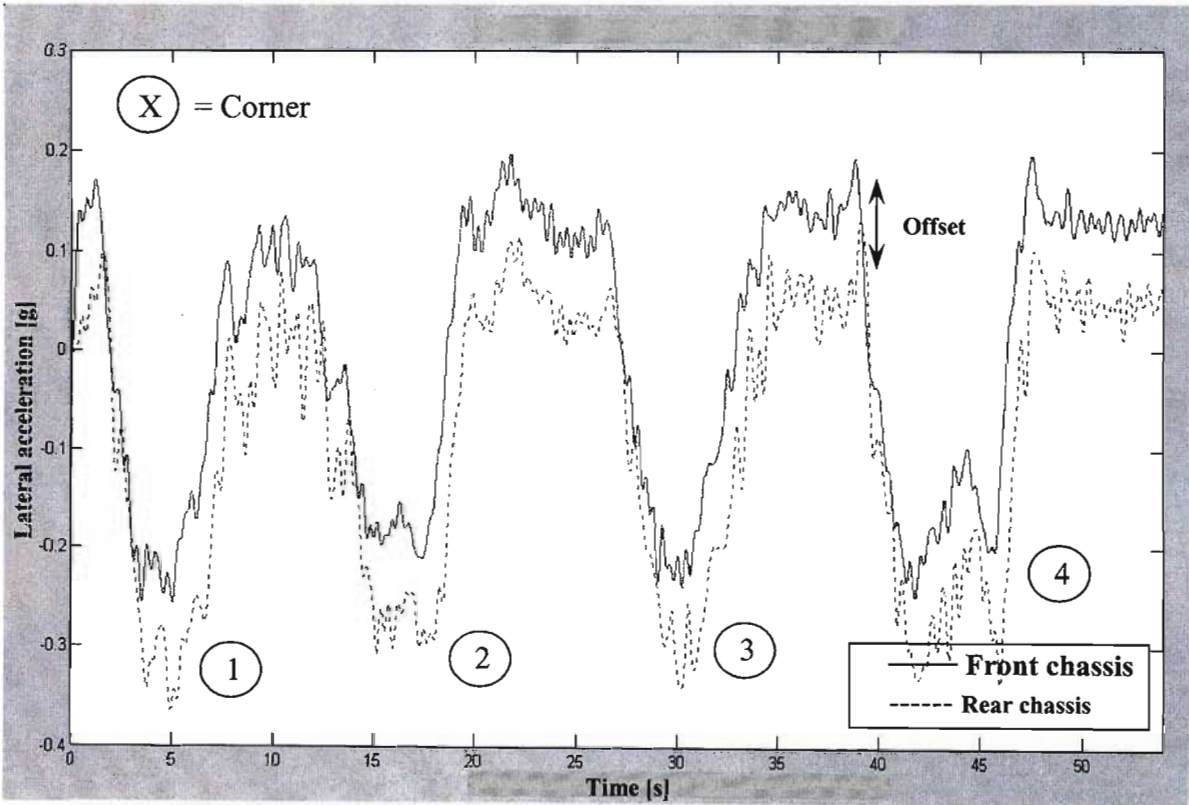


**Fig. 3.8 Lateral acceleration of rear and front chassis at 50km/h around BELL
Equipment test track (UNLOADED)**

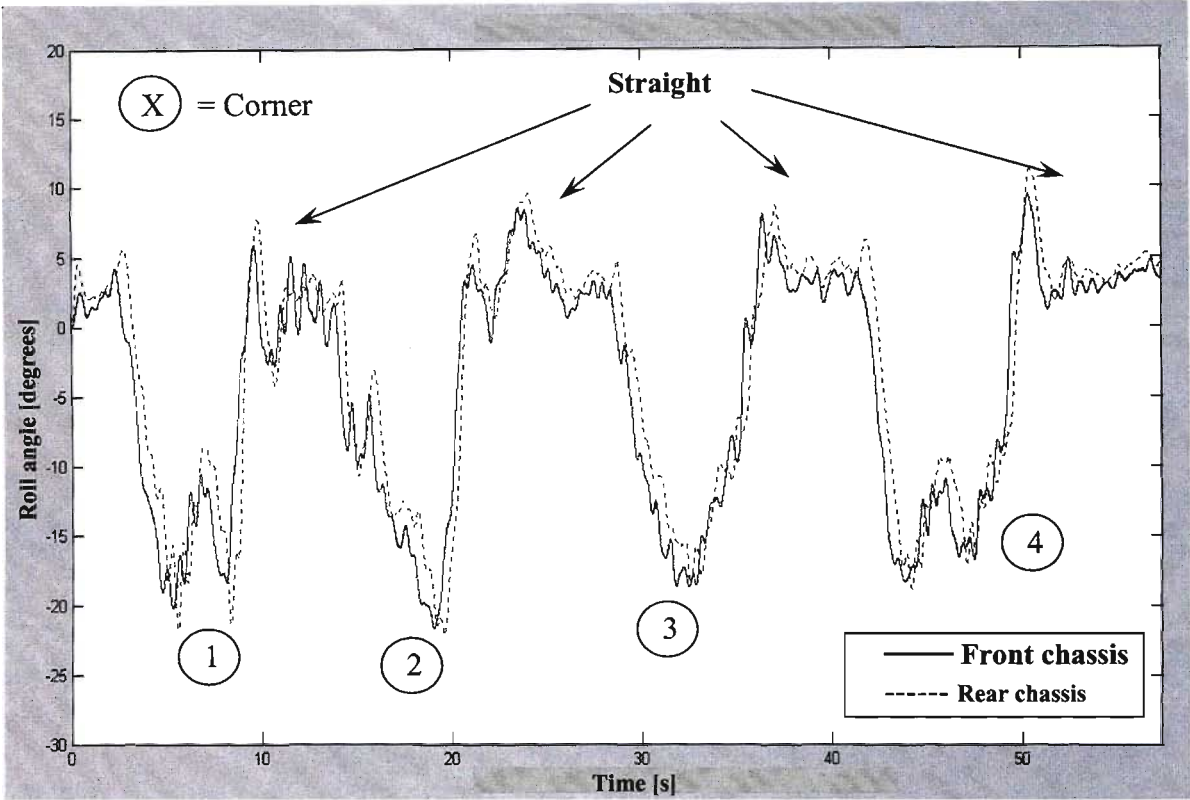


Fig. 3.9 Roll angle of rear and front chassis at 50km/h around BELL Equipment test track (LOADED)

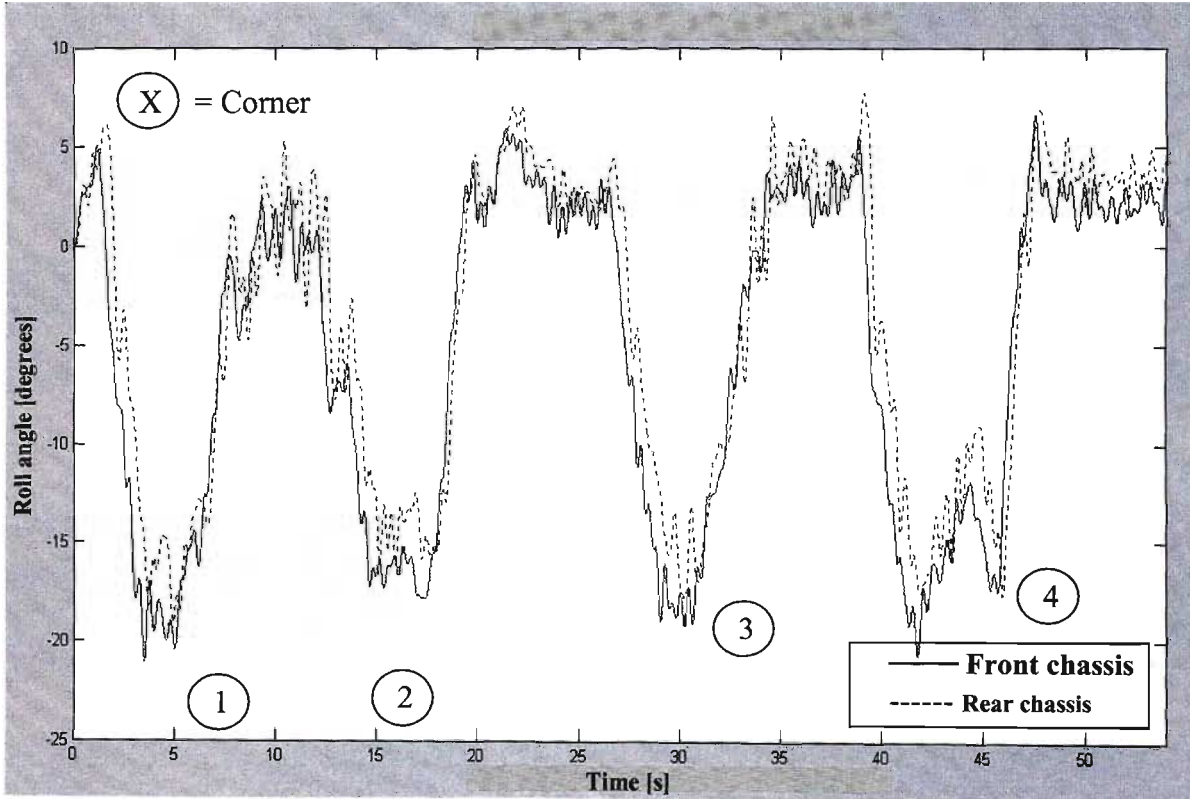


Fig 3.10 Roll angle of rear and front chassis at 50km/h around BELL Equipment test track (UNLOADED)

of the test track. In addition there were long wavelength imperfections in the test track with the camber not being constant along the width of the track in some cases. All of this made it difficult to achieve pure steady state conditions for a sufficient length of time. The lateral acceleration of the rear of the chassis lags that of the front chassis and the shape of the plots mimic each other to an extent that is to be expected. The large discrepancy (almost 0.1g) between the rear and front chassis lateral accelerations (see **Fig 3.8**) can be attributed to sensor drift, as the offset is constant throughout the time record. Some channels on the three-axis sensors were prone to temperature and time related drift. The steady state tests for the unloaded conditions were done after a series of pre alignment tests for the driver and other system checks. The measurement channels were not zeroed in between the last few tests for the unloaded tests. Thus there was sufficient time for some of the sensors to have drifted. As the rear chassis results are closer to the values of the loaded tests, it can be assumed that the front chassis lateral acceleration sensor was the one that drifted.

Fig. 3.9 and **Fig. 3.10** represent the roll of the rear and front chassis for the loaded and unloaded ADT respectively. The tilt sensors x –axis (i.e. around which roll was measured) was set up such that it measured a roll to the left (as determined from the drivers straight ahead position) as positive. Thus due to the camber even on the straights there was a positive tilt measurement of approximately 2.5 degrees. This positive value would increase around the corners, as the cambers angles were higher there. Around the corners the ADT did roll to the right as would be expected in left hand corners. Thus the readings of the tilt sensors were negative around the corners. These tilt angles should be greater by the angle of the track camber at that point, however this does not reflect on the plot. The rear chassis roll lags the front chassis as is expected although the front chassis seems to roll slightly more than the rear in most instances around corners for both the loaded and unloaded cases. This however can also be attributed to sensor drift as even on the straights, as is evident from **Fig 3.9** and **Fig 3.10**, the rear chassis roll angle is slightly higher indicating a constant offset not related to the camber angle of the track.

In addition even though the roll angles of the rear and front chassis have a high correlation as is to be expected, there is an even greater correlation (in terms of shape) between the roll angles of the individual chassis' and their respective lateral acceleration time histories. As the tilt sensors use the constant vertically downward gravitational acceleration as a reference to calculate an angular displacement from the horizontal, any increase in force experienced by the sensor in the gravitational acceleration direction will cause the angle reading to be exaggerated. As the ADT corners, and the lateral acceleration increases, the roll angle of the surface on which the tilt sensor is mounted will cause a component of the lateral acceleration to resolve itself into the vertical gravitational acceleration direction, hence exaggerating the angle of roll reading. This

is similar to the effect that the roll angle has on the lateral acceleration measurement discussed above. This explains why the correlation between the lateral acceleration and roll angle measurements is high. This effect can be corrected by knowing both the lateral acceleration and roll angle values at each instant in time.

3.4.2 Transient handling tests

To explore the transient handling behaviour of the ADT, the lane change manoeuvre as outlined in § 3.1 was conducted. Here again it was the lateral acceleration of the ADT and the subsequent roll angles that were of most concern. **Fig. 3.11** and **Fig. 3.12** shows the lateral acceleration time history of the rear and front chassis for the manoeuvre completed over 40m for the unloaded and loaded case respectively.

It can be seen that the acceleration levels are higher for the unloaded as compared to the loaded case. This was due to the fact that it was not possible to reach the 50km/h speed over the distance available prior to the start of the marked lane change area with the loaded ADT (the speed reached was approximately 45km/h). Thus with a lower entry speed the lateral accelerations had to be lower over the same marked distance. In addition the lateral accelerations for the initial articulation (i.e. to change lanes) is greater than that for the correction articulation to remain in the changed lane and return the ADT to the straight ahead position. This was because the actual path through the marked 40m region was not specified. The only criterion was that the driver attempt to enter and exit the 40m marked zone in the straight-ahead position. Thus the actual path curvature was greater at the lane change part of the event than was during the straight-ahead correction event. The road surface was approximately level and thus there was little offset to speak of. As the lane change manoeuvre involved an initial right hand turn, the lateral acceleration increased to a positive maximum value.

It can also be noted that the rise and fall of the lateral acceleration values for the loaded case (**Fig. 3.12**) are not as smooth as for the unloaded case (**Fig 3.11**). This was because it was very difficult to conduct smooth manoeuvres with the loaded ADT at higher speeds. The vehicle seemed unstable and required many steering corrections from the driver when conducting the lane change manoeuvre. The roll angles for the manoeuvre are depicted in **Fig. 3.13** and **Fig. 3.14** for the unloaded and loaded cases respectively. Once again the correlation between roll angle and lateral acceleration is high for reasons as discussed in § 3.4.1.

It is also noted that the correlation between the roll angles of the rear and front chassis is not as high as seen in the steady states tests. The roll angle time history of the rear chassis seems to have more peaks than the front chassis, indicating a higher natural roll frequency of the rear chassis as compared to the front.

The lateral acceleration and roll angle time histories for the lane change manoeuvre over 60m are shown in **Fig. 3.15** and **Fig. 3.16** respectively. As the ADT was loaded, the erratic nature of the time histories can be seen even when performing the manoeuvre over a longer distance. The obvious discrepancy between the lateral accelerations of the rear and front chassis in **Fig. 3.15** can be attributed to sensor drift, as the offset seems constant throughout the whole time history.

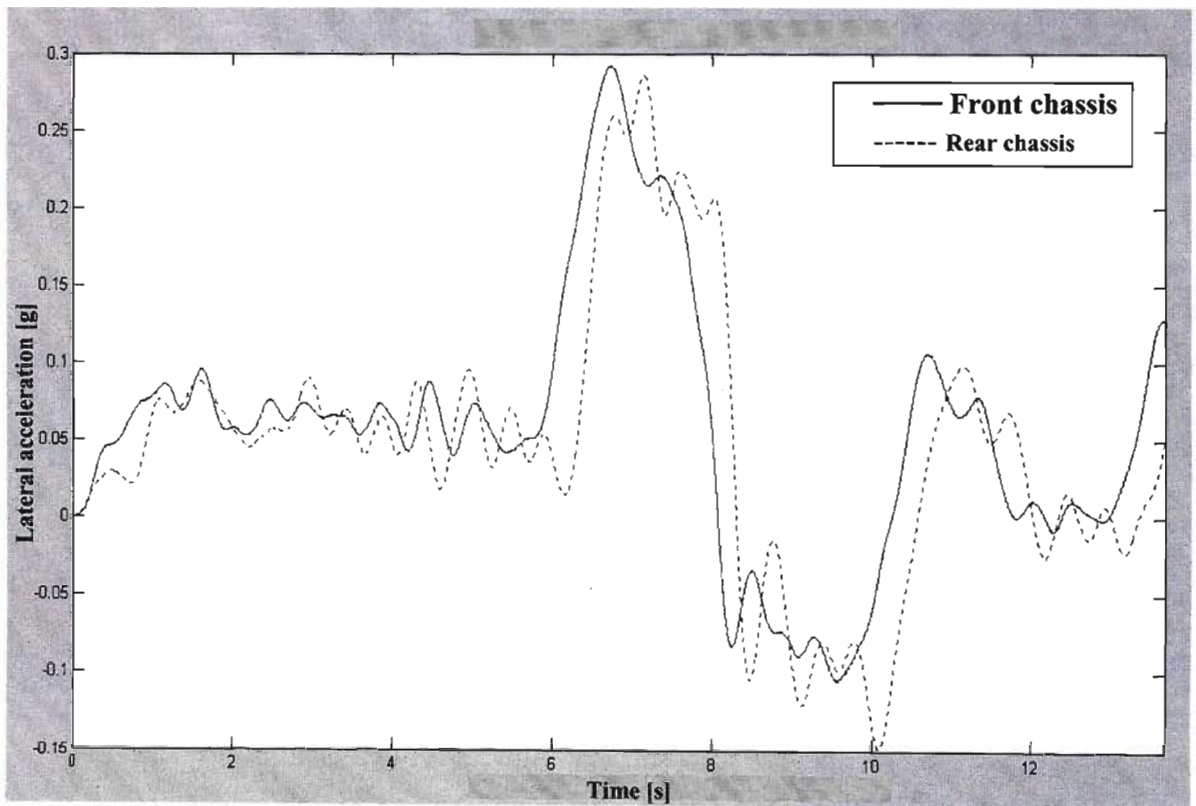


Fig. 3.11 Lateral acceleration of the rear and front chassis for the single lane change manoeuvre over 40m (UNLOADED)

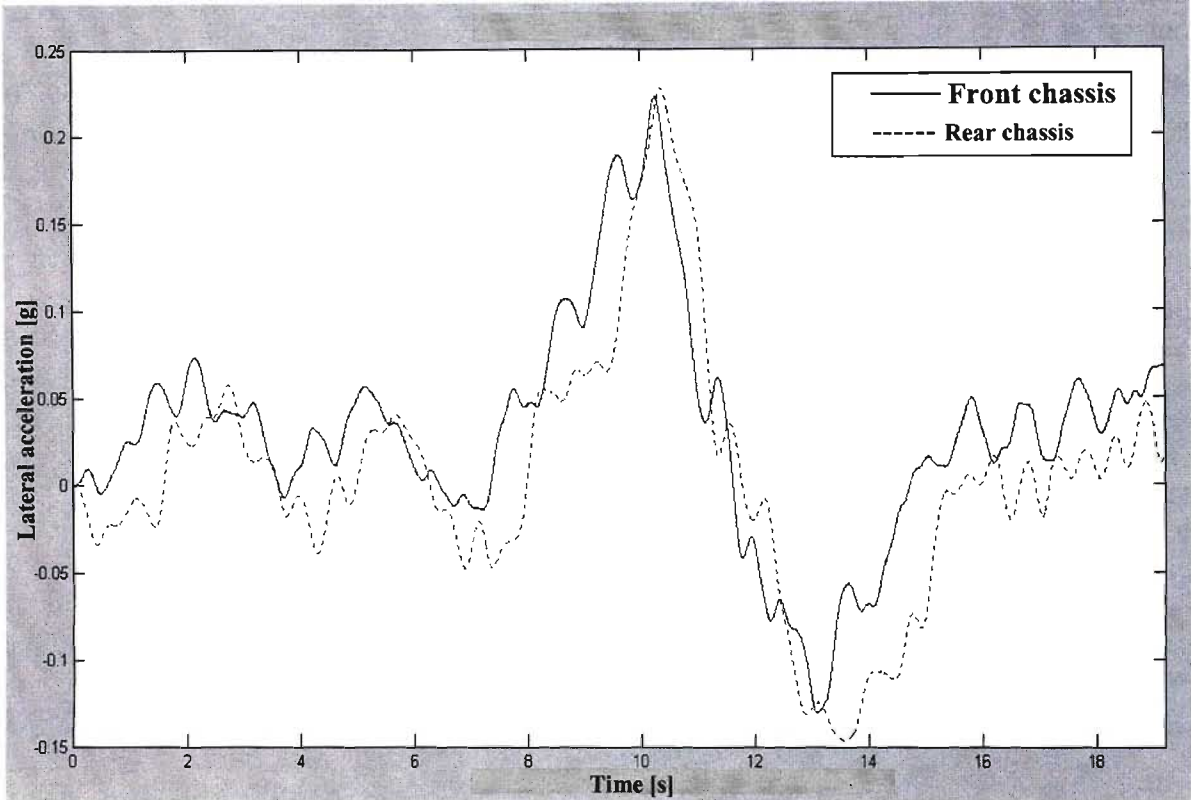


Fig. 3.12 Lateral acceleration of the rear and front chassis for the single lane change manoeuvre over 40m (LOADED)

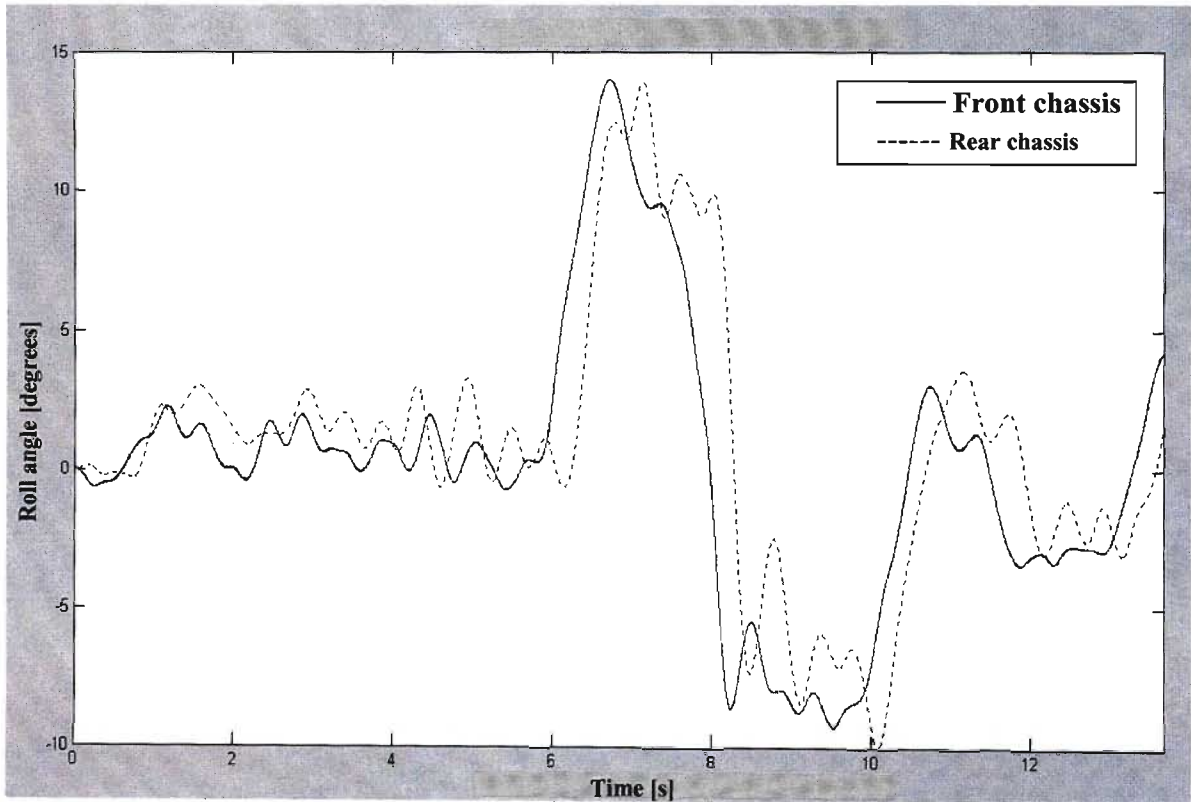


Fig. 3.13 Roll angle of the rear and front chassis for the single lane change manoeuvre over 40m (UNLOADED)

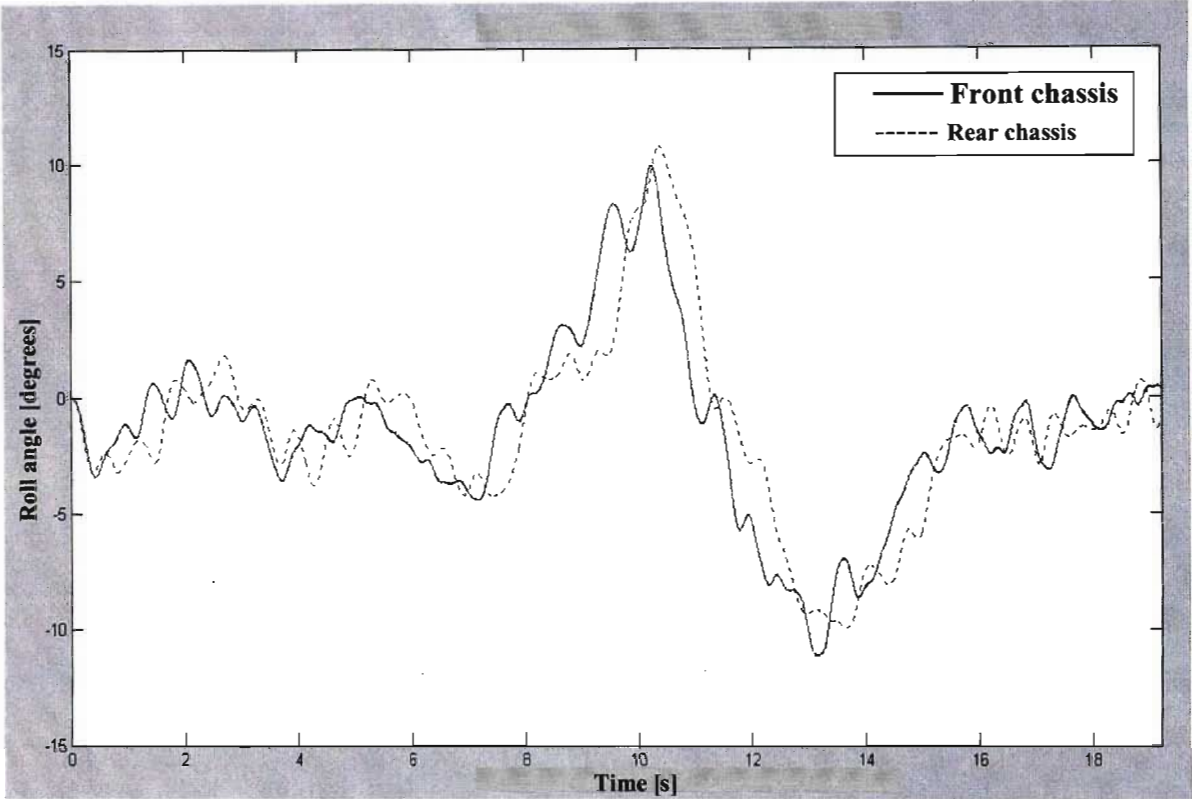


Fig. 3.14 Roll angle of the rear and front chassis for the single lane change manoeuvre over 40m (LOADED)

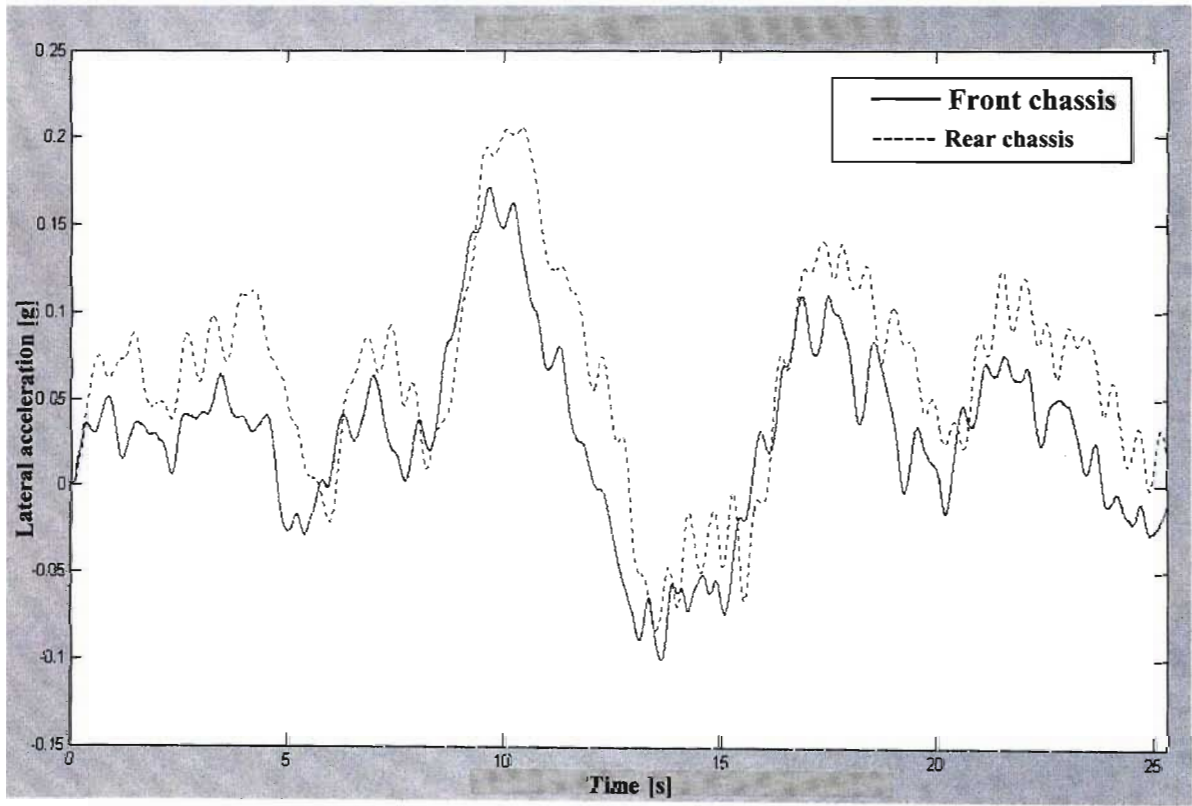


Fig. 3.15 Lateral acceleration of the rear and front chassis for the single lane change manoeuvre over 60m (LOADED)

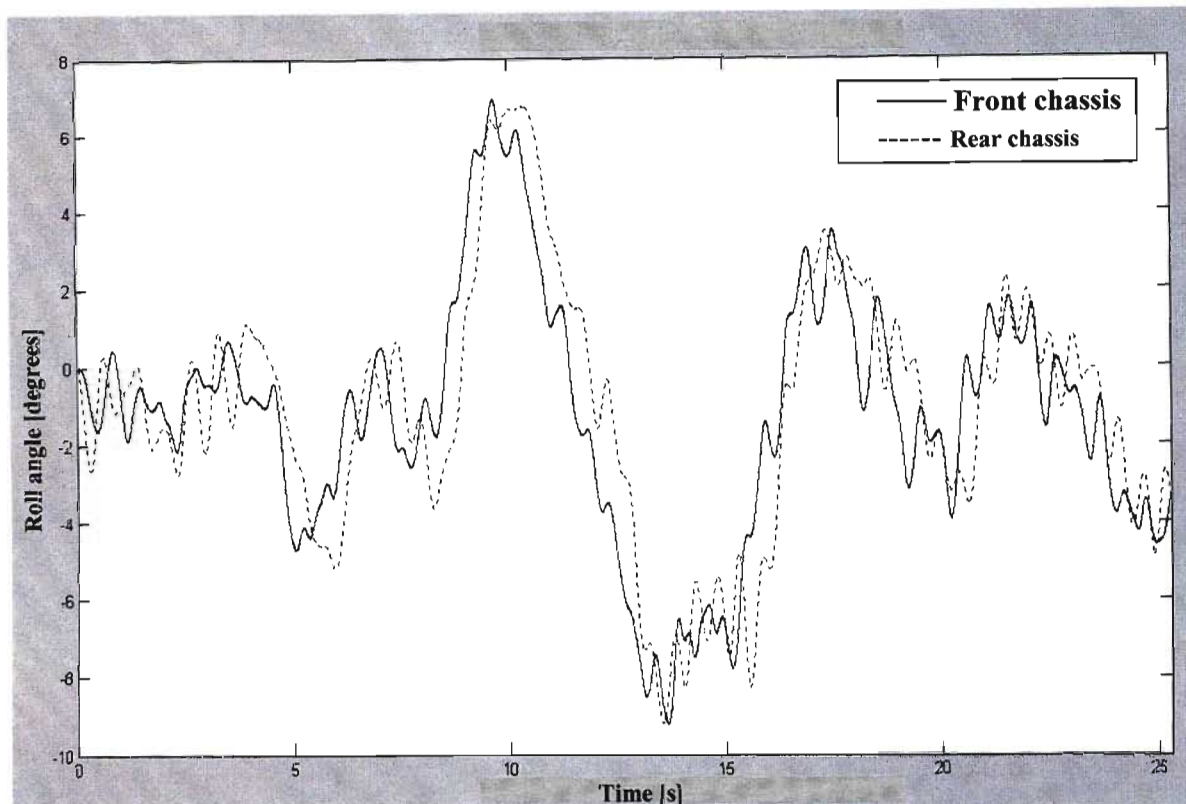


Fig. 3.16 Roll angle of the rear and front chassis for the single lane change manoeuvre over 60m (LOADED)

3.4.3 Vertical response tests

The vertical response test was conducted to have a true response to a discrete road event that could be correlated to the ADAMS model simulation. The test involved driving over an obstacle as described in § 3.1.4 at 10km/h. The vertical input to the system was measured at each wheel axle connection points and at the cab and the rear chassis. Examining the response at the cab and the rear chassis in conjunction with the inputs at the wheel/axle attachments would indicate the nature of the transfer through the front and rear suspensions. This when correlated with results from a similar simulation with the ADAMS model would indicate the validity of the force elements used to describe the various suspension connection compliances used to model the ADT in ADAMS. The time data histories were filtered digitally in MATLAB® (using SPTOOL) using a Chebyshev Type 2 IIR filter, with a LPF cut-off frequency of 100Hz. The passband attenuation was set to 70dB as this allowed for a stable and reasonable filter with a flat passband. The phase angle was linear in the passband.

Figs. 3.17, 3.18 & 3.19, represent the vertical acceleration of the front LHS (with respect to the driver forward seating position) wheel/axle attachment point, the front RHS wheel attachment

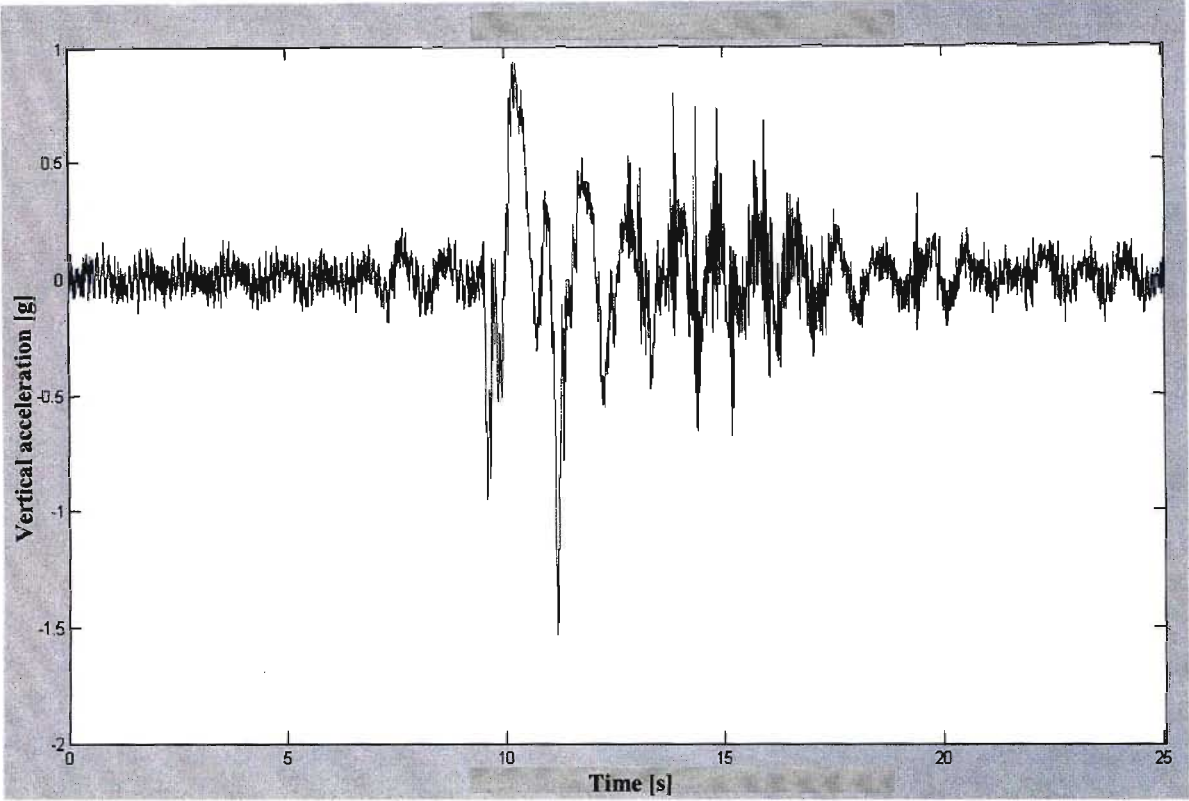


Fig. 3.17 Vertical acceleration of front LHS wheel/axle attachment point traversing a discrete profile at 10km/h (LOADED)

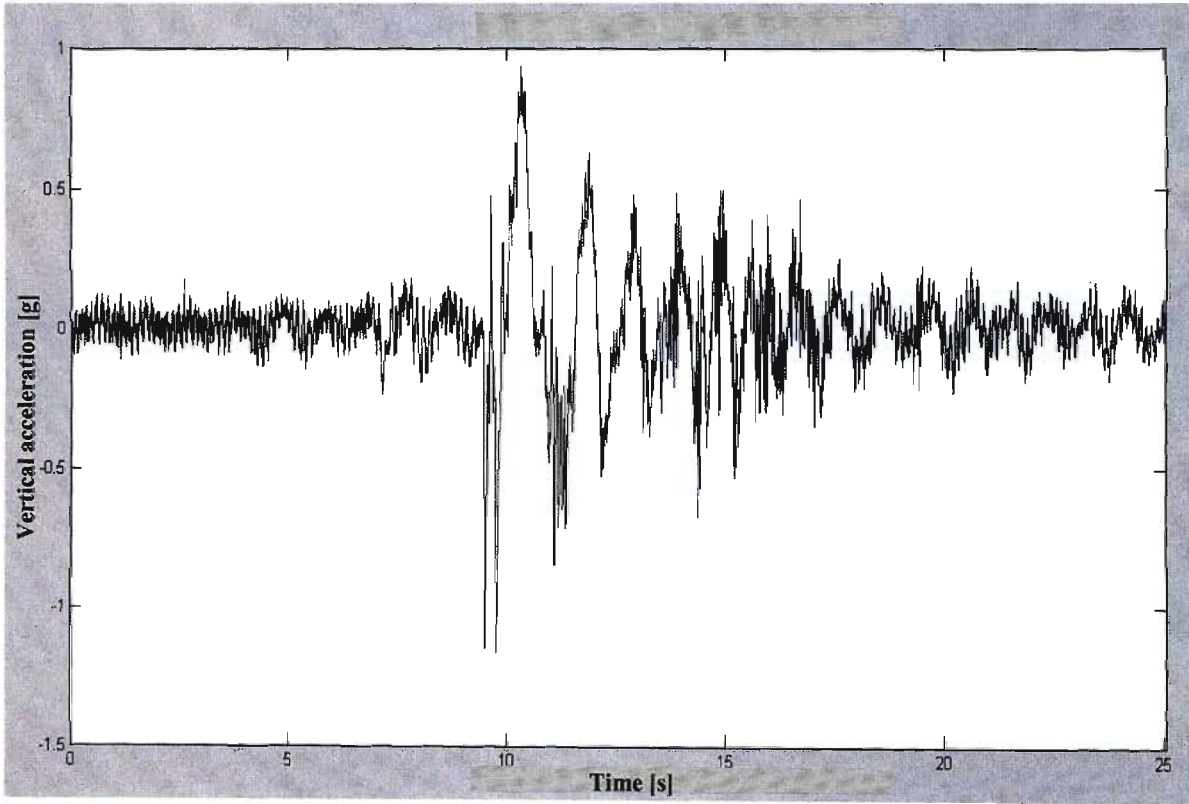


Fig. 3.18 Vertical acceleration of front RHS wheel/axle attachment point traversing a discrete profile at 10km/h (LOADED)

point and the cab respectively, in response to the discrete input. As can be seen the shape and the levels of the two front axle acceleration measurements are similar in waveform shape and level. The result for the cab-mounted accelerometer (**Fig. 3.19**) however shows a much higher acceleration level with high frequency peaks approaching 3g. With the peaks being very narrow, and not following the general shape of the base waveform, it could be speculated that some form of sensor resonance might be involved. The sensor was however mounted firmly via a threaded connector onto an aluminium block that was glued on with a very stiff special purpose mounting glue. In addition the single axis sensors used have a linear 0-1kHz response and a resonant frequency of 5kHz. They also have a large operating range (0-100g) and a high shock tolerance. It is possibly however that a resonance of the plate that forms the bottom of the cab had a resonance mode. The sensor was mounted onto a driver's seat-mounting bolt. The base waveform of the cab acceleration shows an approximately 1g peak in acceleration due to the impact with the discrete obstacle. There also does not appear to be a significant phase lag between the input at the wheel/axle attachment points and the response of the cab.

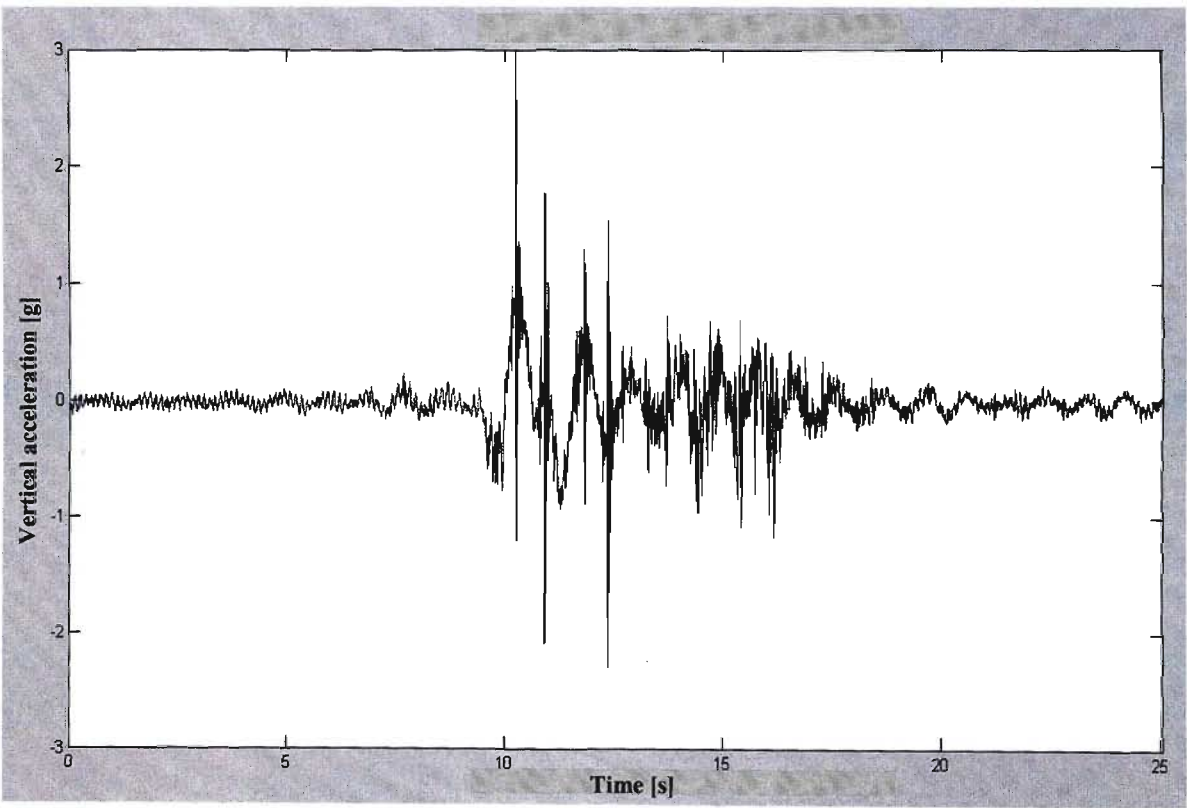


Fig. 3.19 Vertical acceleration of cab for ADT traversing a discrete profile at 10km/h (LOADED)

The vertical acceleration peaks of the middle and rear axles are shown in **Fig. 3.20** and **Fig. 3.21** (only the acceleration levels at the LHS wheel/axle attachment points are shown as the RHS acceleration levels are the same) expectedly delayed by about 2 seconds due to their distance from the front axle. The peak accelerations are higher than at the front wheel/axle mounting points. For the middle axle it goes down to a peak of $-4g$ while the rear axle has a maximum peak of approximately $2.5g$. This is probably due to the higher pressures on the rear tires (4bar) as compared to (3.3bar) on the front for loaded conditions. The acceleration measured on the rear chassis (see **Fig. 3.22**) has a peak acceleration of approximately $-1.5g$, which indicates that the rear suspension is effective in isolating high acceleration inputs to the wheel, from the rear of the ADT, although this could also be due to the added mass of the load acting to damp out the force input. Even though the rear chassis peak acceleration has no appreciable lag from the peak accelerations on the middle and rear axles, the start of the high acceleration response leads that of the rear and middle axles. This is due to the input from the front axle coupling via the oscillation joint assembly to the rear via a pitching motion of the ADT. The vertical bounce oscillations of the rear chassis actually lead the vertical oscillations the rear and middle axles after the discrete event. It can be seen that the oscillations of the rear chassis do not have a high level of damping as they continue long after the discrete bump event at a frequency of approximately 1.3Hz.

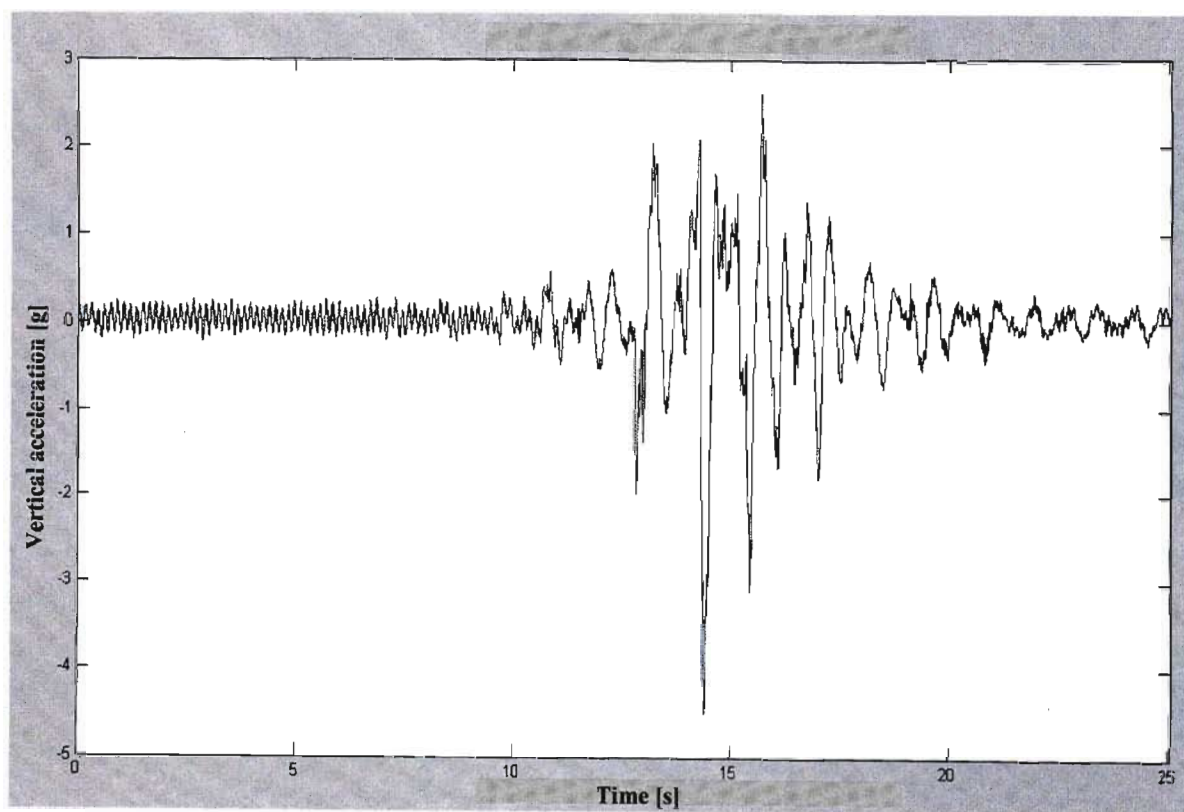


Fig. 3.20 Vertical acceleration of LHS middle-axle/wheel connection point for ADT traversing a discrete profile at 10km/h (LOADED)

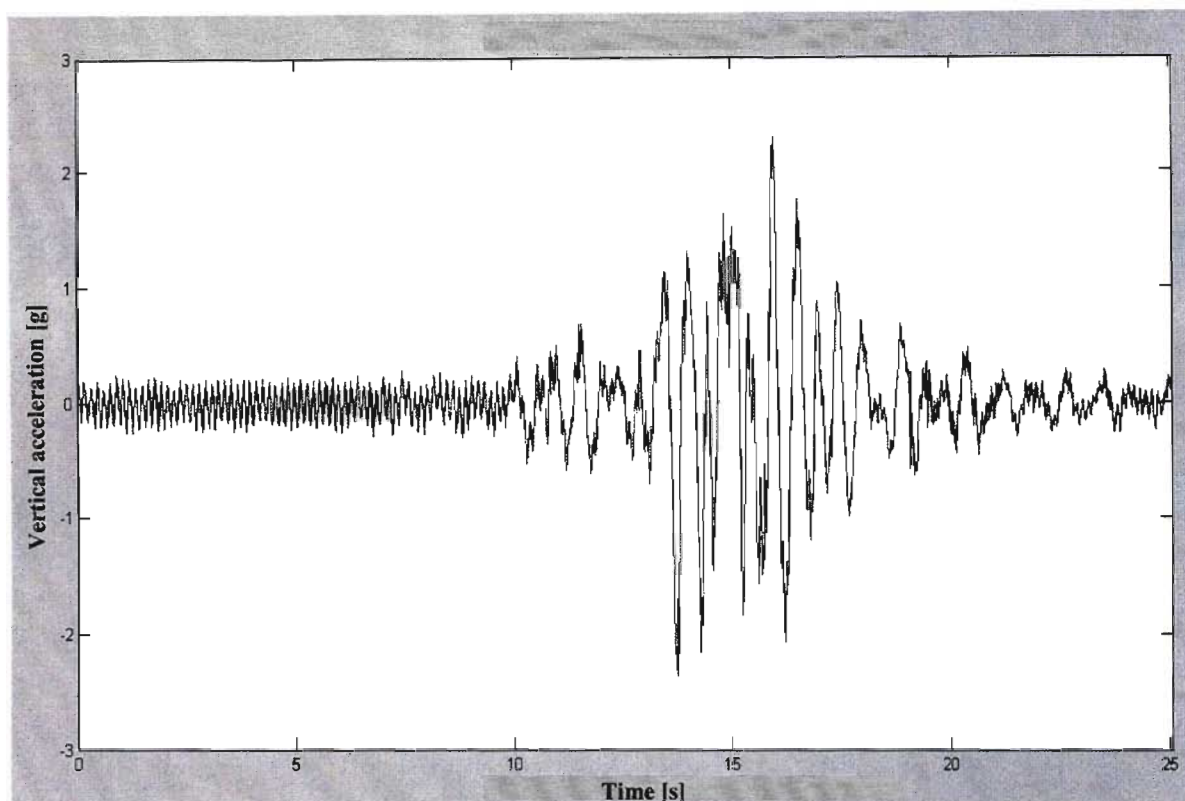


Fig. 3.21 Vertical acceleration of LHS rear-axle/wheel connection point for ADT traversing a discrete profile at 10km/h (LOADED)

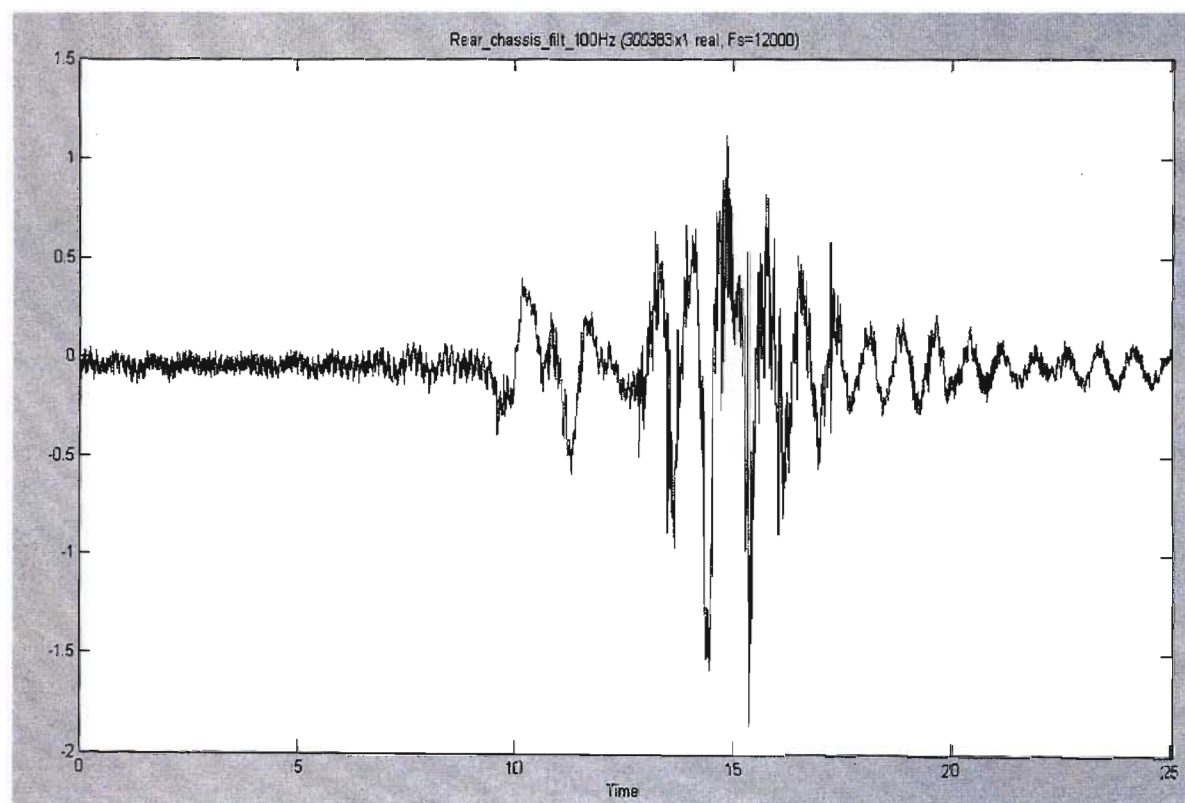


Fig. 3.22 Vertical acceleration of rear chassis for ADT traversing a discrete profile at 10km/h (LOADED)

4 ADAMS MODELLING

The modelling of multi-body systems in software environments such as ADAMS are made simpler by the graphical user interface and the graphical method of building in a virtual environment, the actual physical model of the mechanical system under consideration. While the construction of the rigid body parts, and connecting them with idealised joints may be a simple enough procedure once the necessary solid body modelling software skills have been mastered, it is the modelling of the highly non-linear and dynamic (frequency dependent) real world behaviour of the various joints and sub-systems such as the tires that prove to be the biggest challenge. This section proceeds then by discussing in brief the ADAMS software environment and the methodologies used to construct the rigid body model in the ADAMS. This is not intended to be a user manual of the program but rather to highlight issues faced in modelling the vehicle in this particular project. By far the most challenging aspects are the modelling of the compliant components viz. the suspension rubber components and the front shock struts and the tire. Progress made in understanding the problems associated with modelling such components are stated and recommendations are made as to the applicability of the model and restriction of simulations to certain operating regimes given the current level of information and tools available within this project.

4.1 ADAMS modelling principles

The ADAMS software package is built around the very powerful ADAMS/Solver module which contains numerical solver routines particularly suited to the synthesis and solution of the equations of motion for multi-body systems. While one can create an ADAMS command set (.adm file) containing all the necessary information about one's particular model such as number of parts inertia properties, masses locations and connection via joints in the ADAMS command file syntax, it is typically an elaborate process prone to error. While knowledge of the underlying command set structure that is submitted to the solver can be useful when debugging difficult problems with the simulation, it is best handled by an expert user. A much simpler approach that has become part of the latest versions of the ADAMS software package is ADAMS/View.

The Graphical User Interface (GUI) of ADAMS/View is very similar to many Windows based general-purpose applications and allows one to graphically construct the mechanical system on a computer such that it displays virtually on the computer screen. From the geometry and user specified material type ADAMS/View calculates via the internal solver routines the appropriate mass, and inertial properties of the rigid object. The user is thus spared from having to calculate or measure and test for these inherent mass and inertial properties of his system. The

user then connects the rigid bodies via idealised joints, which restrain degrees of freedom in the translation and rotational axes of the rigid bodies relative to each other. If the model is constructed correctly geometrically and kinematically (i.e. it moves and is constrained as it would be in realty) the user can then either add constraint motions to the joints or parts and investigate resultant motions at different locations in the model and or resultant forces at the joints. Alternatively forces can be added to the model acting at specific points and the resultant motions of the different bodies can be determined. The effects of gravity are automatically factored in for force analysis although the gravity force field can be modified with regard to the gravitational constant of acceleration or switched off completely. The various rigid body geometries can be constructed from a library of links and simple geometric solids available in template form which is easily called up from the ADAMS/View Toolbar. Similarly, the various joints, forces and motions that form part of the model can be selected from templates in the toolbar. The results of the simulation can be viewed in the ADAMS/Postprocessor, an easy to use post-processing tool that lets a user immediately graph the outputs required from the model. **Fig. 4.1** shows the basic ADAMS/View window with the toolbox palette. **Fig. 4.2** shows an example of a four-bar mechanism as modelled in ADAMS while **Fig. 4.3** shows a few of the various idealised joints available in ADAMS

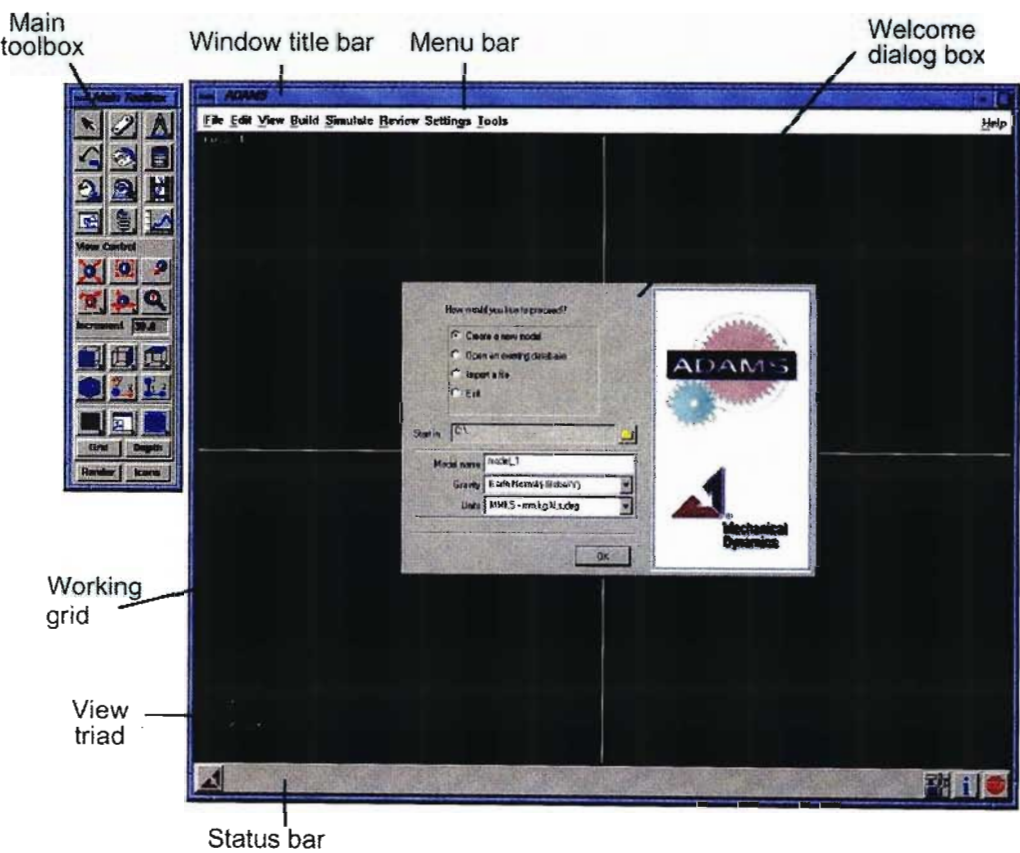


Fig. 4.1 Graphical user interface – ADAMS/View modelling environment

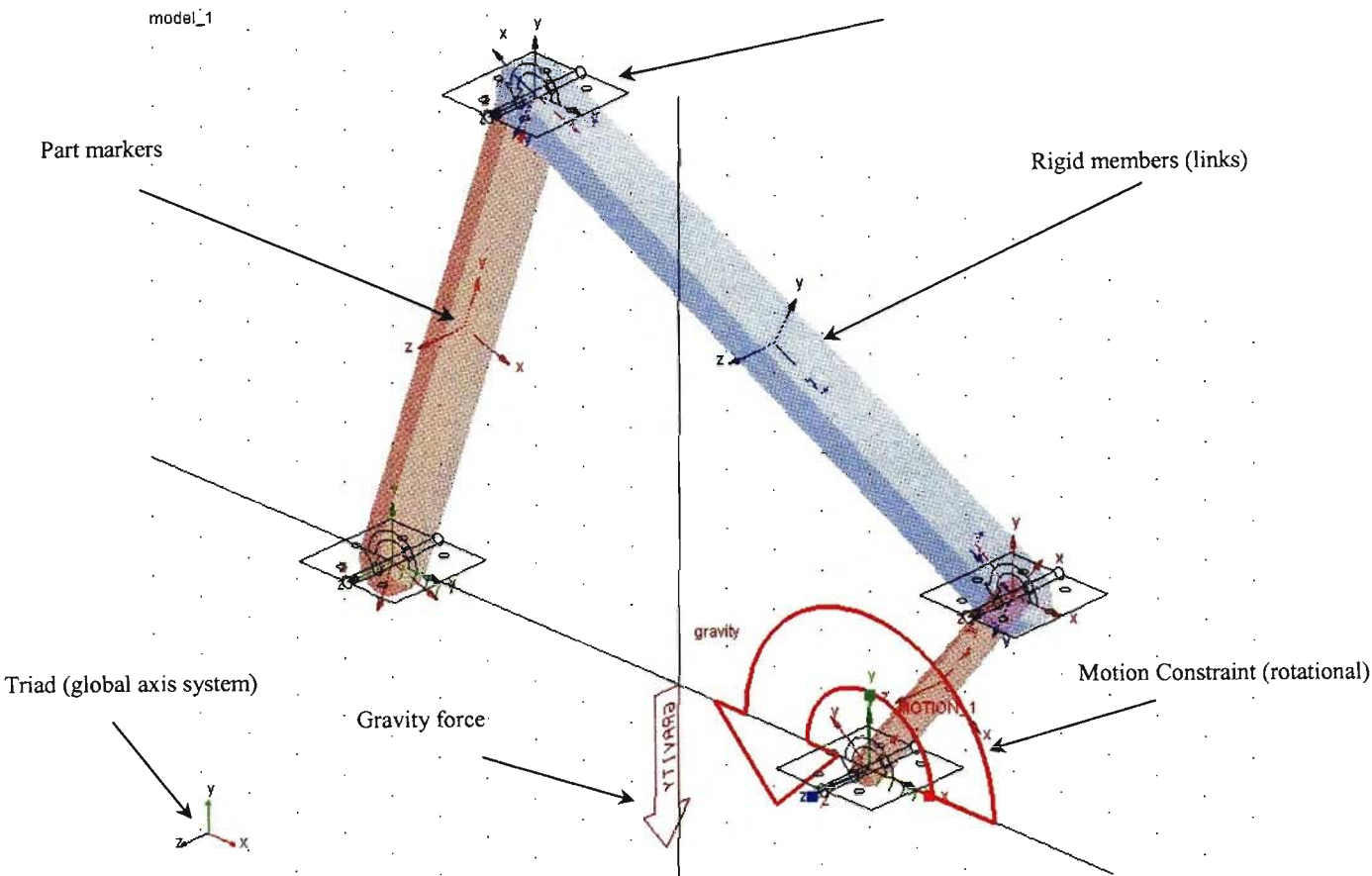
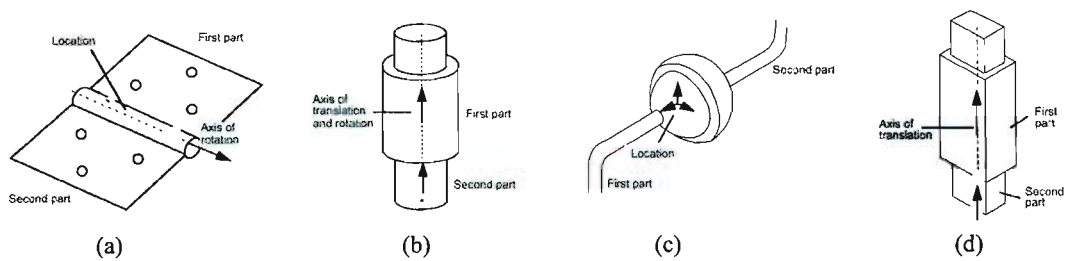


Fig. 4.2 Example of a 4-bar mechanism as modelled in ADAMS



**Fig. 4.3 Samples of idealised joints in ADAMS (a) Revolute
(b) Cylindrical (c) Spherical (d) Translational [42]**

Although the above model may be a simple well-studied mechanism the power of the ADAMS software tool can be easily seen. Traditionally with analytical techniques, even with a digital computer available, one would first need to determine the equations of motion using for example Lagrangian or Newtonian methods and then formulate the equations of motion that must be solved using a numerical algorithm encoded in software. If the number of bodies and degrees of freedom has to increase the actual formulation of the equations of motion can be prohibitive.

Of course the above discussion relates to a simplified first approximation of a model. What if for example the model did not have ideal joints, coulomb friction for example can act to increase the stiffness of the joints for low amplitude motions. What if the rigid members and even the joints cannot be assumed perfectly rigid for the system's particular application? There is also the question of flexible couplings and other external system-force models e.g. impact and contact between rigid (or flexible) bodies, tire models and aerodynamic forces. To model reality all of these types of situations need to be considered and if their omission impacts negatively on the accuracy of the model the specific effects have to be modelled. ADAMS fortunately is extremely versatile in its scope. Many of the effects can be modelled within the functional parameters of the standard ADAMS environment using sub-models that are available to the user in easy to use templates form. Once the analytical model underlying the template is known and understood by the user, it becomes a matter of filling in the various parameters, acquired from testing or theory, into the template. Such examples are the contact model, which has been improved to now handle cases of 3-dimensional solid-to-solid contact (Version 11), flexible couplings (bush and beam elements) and various tire models. If the functionality is not available as part of the standard ADAMS package, there are add on modules available for e.g. ADAMS/Flex which in conjunction with FEA packages such as MSC/Nastran® is used to accurately model flexible bodies. For cases where no analytical predictions in the ADAMS software suite exist for particular subsystems that constitute a model in addition to the multi-body dynamics, dedicated user definable subroutines exist in ADAMS for the user to implement a unique sub-system model. An example of such a subroutine is the TFSISO (Transfer Function Single Input Single Output) function, which allows a user to implement a system model using linear state space analysis methods.

Once a validated model has been constructed, the ADAMS model can be used as a design tool. Thus not only can the model be used to predict the results qualitatively to changes in parameters but it can also be used to optimise a design. ADAMS include tools whereby design of experiments can be accomplished such that those parameters that impact the most on a specific function of the system under investigation can be identified and systematically varied to find the optimal value. By way of example a particular hard point on a car independent suspension can be identified as having the most influence on say the toe angle of a tire-wheel assembly. The hard point can then be parameterised via a design variable and then systematically varied over an operating space on the chassis to trace out a minimised locus of toe angle verses suspension vertical travel (if that was to be the design criteria for the suspension system).

In addition to the above functionality the ADAMS software has various add-on modules that help define the entire system modelling process as relates to the multi-body dynamics in a more

detailed manner. Such modules are for example ADAMS/Controls, ADAMS/Hydraulics as well as specific ADAMS environments for particular industries, such as ADAMS/Car and ADAMS/Rail. These particular modules provide a software environment that is particularly suited to the tasks that engineers in these industries have to perform on a daily basis. Templates containing various suspension designs are available so that users can concentrate on particular issues such as running virtual experiments to determine an optimal spring rate for a particular vehicle application for example. Templates and company specific designs can be stored as part of a company specific database management system with various employees having access to commonly used designs and constructions such that it can become an effective tool in a company's core business on a daily basis rather than to only use the software for long time period research and development.

The environment that the BELL 40ton B40C ADT was modelled in is the ADAMS Full Simulation package. While it does not have the functionality that would have allowed quicker model development and access to more advanced tire models as ADAMS/Car would have, it has allowed a rigid body model of the truck to be built and simulated.

4.2 Constructing the rigid body model in the ADAMS environment

At the start of this project no three dimensional geometrical model was available of the B40C ADT in a format that could be readily imported into the ADAMS virtual environment. Models that were available from BELL Equipment in 3-D format were in AutoCAD® format, which could not be imported into ADAMS without additional object translation software, which was not available to this project. Attempts were made to import geometry in a non-propriety format, which ADAMS recognises, STEP. The AutoCAD® file of the 3-D geometry of an ADT rigid member was converted into STEP format via a geometry-handling tool of an FEA package that was available to the project and imported into ADAMS. This however proved to be unsuccessful. It was not possible for example for ADAMS to automatically calculate the mass and inertia properties of the rigid member and the geometry of the part (especially curved surfaces) was not replicated faithfully. In addition even when displayed in wireframe mode the geometry of the part in ADAMS had a multitude of surface 'speckles' that made manipulation of the object in the graphics environment of ADAMS/View inefficiently slow. Also it was not possible to snap to parts of the model such as centres of curves and edges of surfaces etc. The ability to snap to geometric features accurately makes the process of assembling a rigid body system with many parts in ADAMS/View simpler and less prone to co-ordinate placement errors.

It was thus decided to model the 3-D geometry in SolidEdge® which is a solid modelling software package based on the Parasolid® graphics kernel. As the graphics in ADAMS/View is based on the Parasolid® kernel as well, it makes for a simpler transfer of 3-D geometry into ADAMS/View. Detailed drawings of the individual ADT chassis and body components that comprise the BELL Equipment ADT were sourced from BELL Equipment. The components were then modelled in SolidEdge®. The choice of using SolidEdge® to construct the 3-D geometry of the ADT over the 3-D modelling tools available in ADAMS/View was necessary due to the simplicity of use of SolidEdge®. It is difficult to produce complex geometry in ADAMS/View. An oversight initially was to construct the solid geometry with too much detail. This placed a heavy burden on the computers processing time. Even though the animation capability can be turned off during simulation, manipulation of the model during construction and later during further modification work, was extremely inefficient. Ideally it would be best practice to use simple geometry to model a system in ADAMS/View and then input the measured and calculated mass and inertia properties for example using the tri-filar pendulum technique [11], [21]. However this requires large capacity in terms of manpower, equipment and time and was not within the scope of this project. Thus accurate geometry allows ADAMS to calculate accurate mass and inertia properties of rigid bodies, which would have been otherwise unavailable to this project.

The rigid body parts of the ADT were thus created in SolidEdge® and then imported into ADAMS. It was found that the following steps (with reference to **Fig. 4.4**) as outlined in the discussion below were necessary in importing the geometry into ADAMS/View.

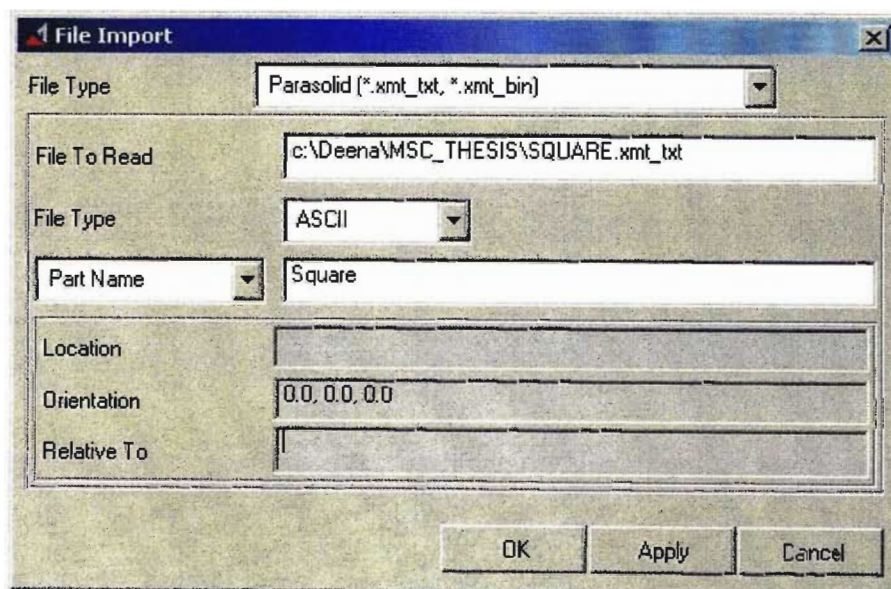


Fig. 4.4 Import dialogue box in ADAMS/View

It was first necessary to change the Parasolid file extensions of the rigid bodies created in SolidEdge® from < .x_t > to < .xmt_txt > before the geometry files could be imported into ADAMS. In the import dialogue box (**Fig. 4.4**) it was necessary to select the option 'Part Name' in the third dropdown menu and assign unique names for each rigid part being imported into the model. It is also important not to modify the greyed out fields in the dialogue box. Changing these fields in an attempt to import a rigid part to a specific location and orientation moves and orientates the centre of mass marker and not the solid geometry itself. So while a user might connect and assemble a model according to the position of the geometry in ADAMS/View, the centre of mass marker is not coincident with the geometry of the rigid body. This will lead to errors in the output of the simulation as ADAMS uses the centre of mass markers of parts in the synthesis and simulation of the equations of motion for the assembled multibody system.

Once the rigid part has been imported via the file import dialogue box, it was still not visible to the user. This is because rigid part geometry created by importing is only assigned at run-time (i.e. once a simulation has been run). Thus a mock simulation must be run (which will fail due to the mass of the system having no defined mass as it creates a singularity in the mass matrix of the simulated system) to have the part geometry defined. The part is then visible to the user who must then modify the part by defining its mass and inertia properties for it to be a valid rigid body in ADAMS. This can be done by either inputting the mass and moments of inertia directly or as is more convenient, if the geometry of the part is accurate, by specifying the engineering material the part is made from and letting ADAMS calculate the inertia properties. The user then moves and rotates the rigid part to whatever point in the 3-D space its position is in the actual real system, using object manipulation tools available from the toolbox in ADAMS/View. In such a manner then, the entire ADT rigid body system was imported into ADAMS and assembled using idealised joints. **Fig. 4.5** shows examples of the 3-D rigid body parts of the ADT as imported into ADAMS.

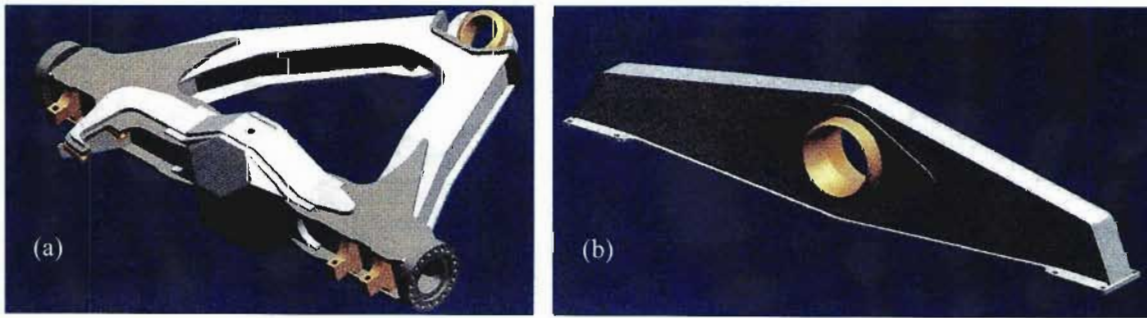


Fig. 4.5 Examples of rigid body geometry as imported into ADAMS
(a) Front axle with A-Frame (b) Walking Beam

The part topography of the rigid bodies in the ADT model in ADAMS is indicated in **Fig. 4.6**.

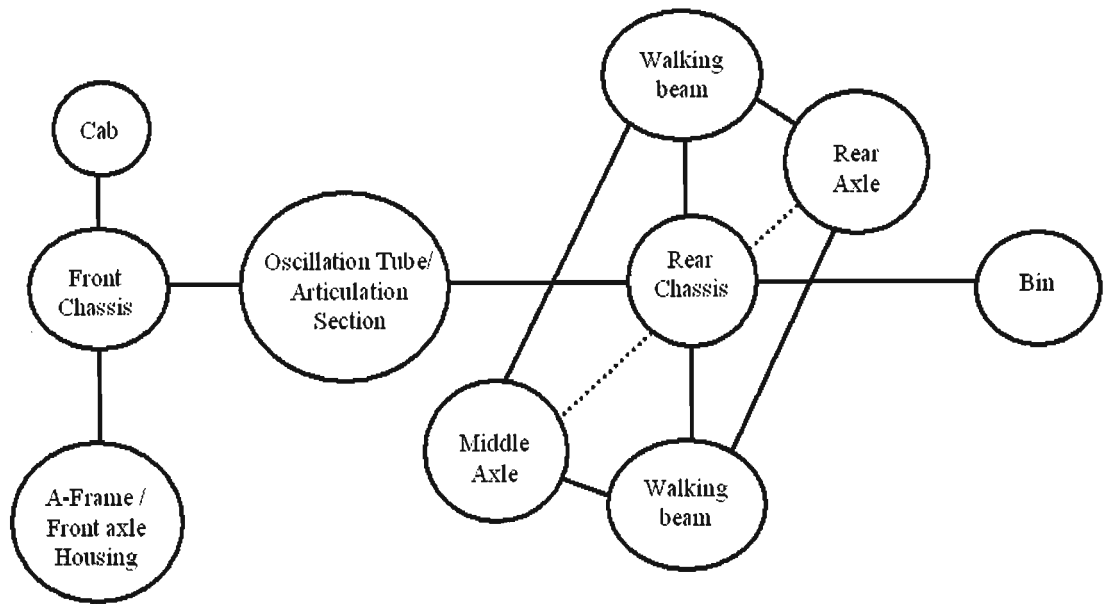


Fig. 4.6 Part topology of the rigid body parts of the ADT model in ADAMS

The front chassis part consisted of the front chassis, all the front body parts such as the tanks and fenders, wheel housings and the bonnet. Rectangular blocks having the approximate mass of the engine and the transmission drop box were also added to the front chassis part as part of the chassis i.e. they have no additional degrees of freedom with respect to the chassis. Thus these components constitute the rigid part indicated as the front chassis in **Fig. 4.6**. The cab proved difficult to model accurately due to a large number of panels that constitute it plus the interior trim and strengthening frame add to its mass. As it is not necessary to model the geometry in such detail if the inertia properties are known, the cab outer structure was modelled. The cab part’s mass was then modified in ADAMS to reflect the actual measured mass of the cab. The level of accuracy of the centre of gravity as well as the moments of inertia about the principle axes would need to be confirmed however. The cab was connected to the front chassis via four linear springs during the assembly (later modified to G-Forces) with very stiff linear springs to represent its connection to the front chassis via asymmetrical rubber bushes as on the actual ADT.

The A-frame/Front Axle housing is linked to the front chassis via a panhard link, the A-frame pivot and two strut dampers as shown in **Fig. 4.7**.

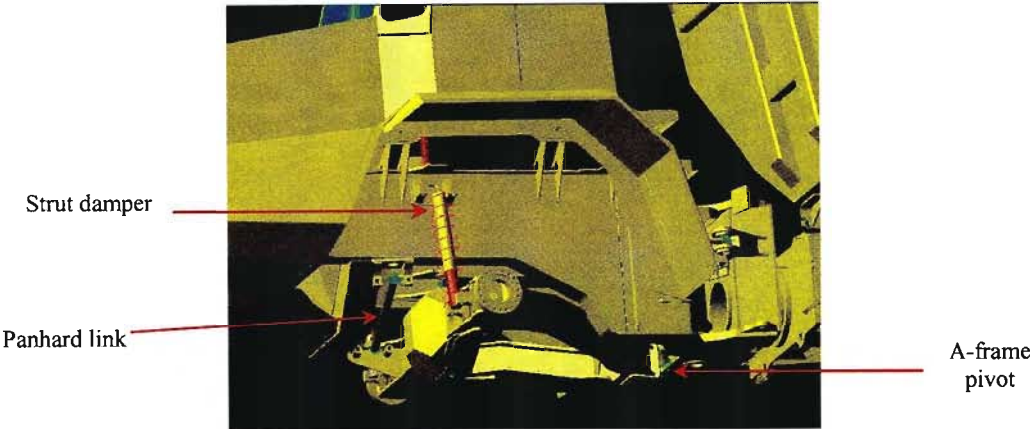


Fig. 4.7 Relative constraints between A-frame/front axle and front chassis

The strut dampers were modelled via stiff spring-damper elements. The panhard link had its connections to the A-frame/front axle and the front chassis modelled as a spherical joint as was the direct connection to the two rigid bodies (i.e. at the A-frame pivot). This idealised joint was chosen as in reality the actual joint moves kinematically in a spherical part space.

The rear chassis is connected to the middle and rear axles via panhard and drag links as well as two walking beams. The walking beams are connected to the rear chassis directly via the walking beam pivot as indicated in **Fig. 4.8**. The walking beams are linked to both the rear and middle axles via a sandwich box, which is a stiff compliant member (see **Fig. 4.9**). Each walking beam is connected to the middle axle at the front and the rear axle at the back. Single panhard links connect each axle to the rear chassis (see **Fig. 4.10**) as well as three drag links per axle, one above (see **Fig 4.8**) and two below (see **Fig. 4.10**). The sandwich boxes are modelled as stiff linear springs and the various links are connected at each end to the axles and the rear chassis via spherical joints. The walking beam is connected at the walking beam pivot to the rear chassis via a revolute joint.

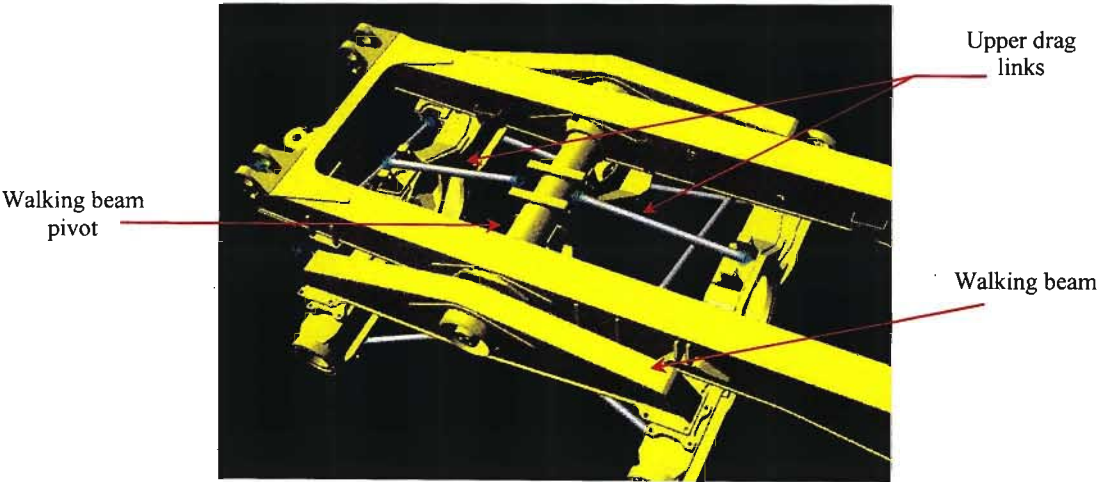


Fig. 4.8 Rear suspension arrangement showing upper drag links, walking beams and pivot and the rear and middle axles

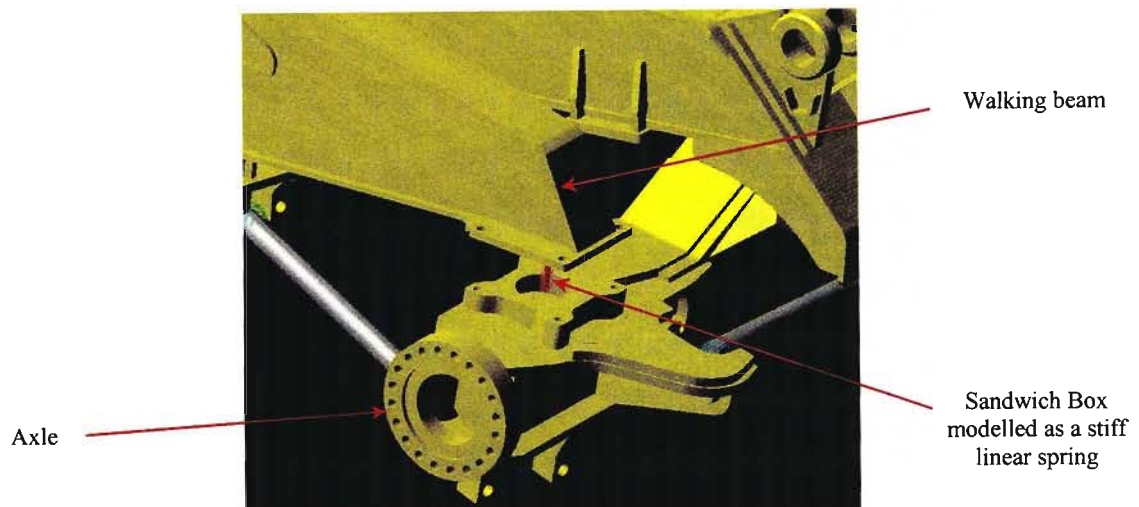


Fig 4.9 Axle to walking beam connection via sandwich box

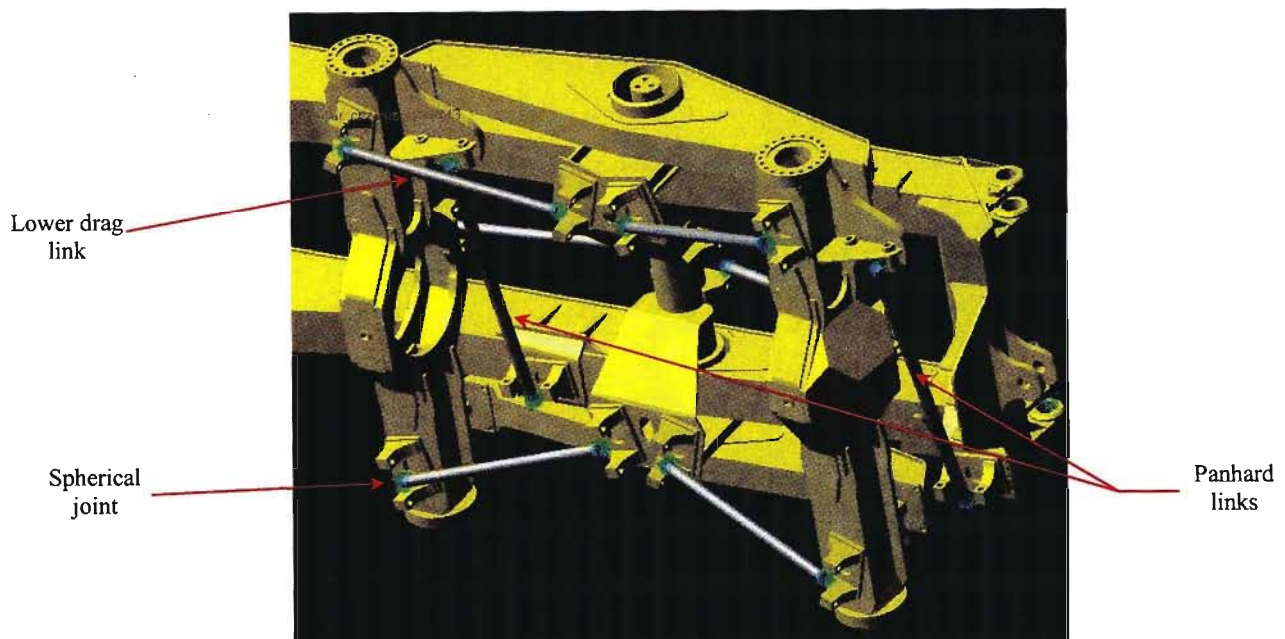


Fig 4.10 Rear ADT suspension indicating lower drag and panhard links

The bin was connected to the rear chassis via a locked joint. In reality the bin is hinged at the rear of the chassis. In addition two hydraulic cylinders connect the bin to the rear chassis. The connectors are spherelastastic bearings, which are compliant members. The hydraulic cylinders when operated act to lift and lower the bin to tip off loads. When not in use the hydraulic cylinders act to hold the bin firmly in its fully lowered position. It was decided not to add a relative degree of freedom between the bin and the rear chassis as the bin is firmly held down when not being tipped. To include the rotational degree of freedom would mean having to specify the force function of the hydraulic cylinders. Any force variation would have to have

been a function of the hydraulic system (the modelling of which was beyond the scope of this project) and would typically be very small amplitude high frequency motion and would not affect the ride and handling frequency regime of the ADT. For all intents and purposes the bin would not move relative to the chassis other than when it was explicitly powered to tip. The hydraulic cylinders were modelled as rigid parts and fixed to the rear chassis with fixed joints (no degrees of freedom) so as to include the approximate mass of the cylinders to the model.

To connect the front and rear of the ADT an articulation-oscillation assembly is used. This is unique as compared to a commercial road going semi-trailer as it permits a yaw as well as roll degree of freedom between the tractor and the trailer where as the semi-trailer has only a yaw degree of freedom at the fifth wheel (hitch point). The oscillation tube / articulation joint assembly is slid into the rear chassis and locked into place as shown in **Fig. 4.11**. Thus the assembly is allowed to rotate (roll) relative to the rear chassis and is modelled in ADAMS via a revolute joint. The front part of the assembly is then hitched to the front chassis via two pivots such that the front chassis can yaw relative to the rear. The yaw degree of freedom was modelled via a revolute joint oriented to allow the degree of freedom in the yaw plane. **Fig. 4.11** indicates how this was achieved in ADAMS.

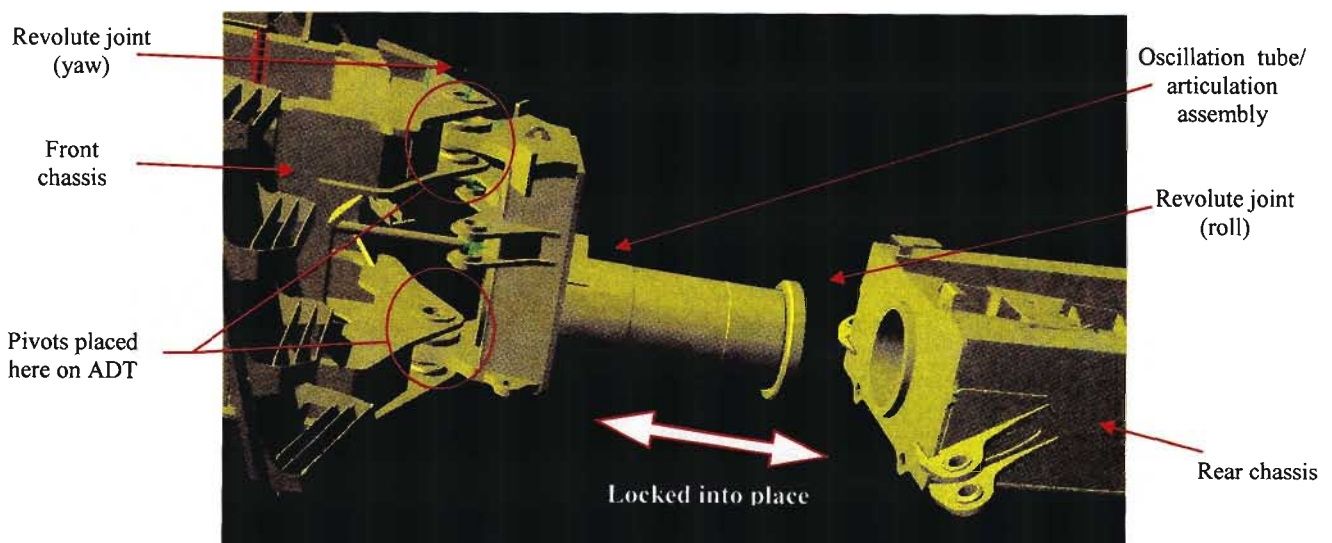


Fig 4.11 ADAMS model assembly at the articulation oscillation joint

In order to turn the vehicle the ADT is equipped with two hydraulic steering cylinders on either side of the vehicle with one end connected to the oscillation tube / articulation assembly and the other on the front chassis. Increasing the pressure in one cylinder and decreasing the pressure in the other causes the front chassis to yaw relative to the rear chassis about the articulation joint.

Since the front/rear tire relative slip angles now increase, the vehicle steers. **Fig. 4.12** shows how this steering mechanism was modelled in ADAMS.

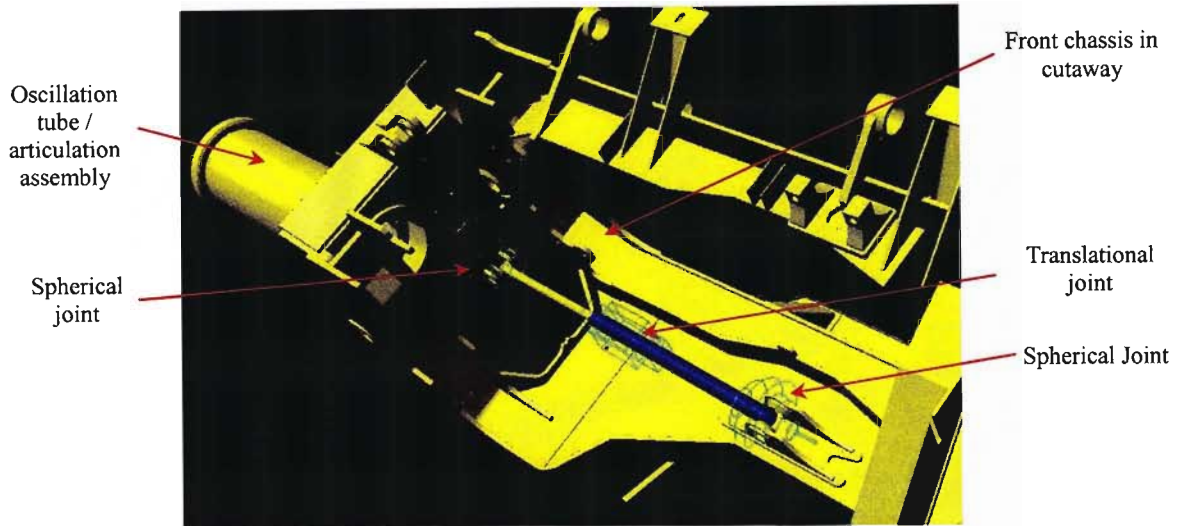


Fig. 4.12 Cutaway section through front chassis showing steering mechanism of ADT as modelled in ADAMS

The ends of the hydraulic cylinders are joined to the ADT via spherelastic bushes so it makes sense to model the attachment as a spherical bearing. The translational joint that links the two cylinders that represents the steering hydraulic piston-cylinder arrangement allows a translational degree of freedom between the piston and the cylinder. Thus by prescribing a motion constraint at the joint or a force relationship between the piston and cylinder, the articulation of the ADAMS ADT model can be achieved.

Once the model was constructed the kinematic assembly of the model needed to be checked. To achieve this, vertical translational joints were fixed between the axle-hub wheel attachment points and ground. In addition linear springs approximating the vertical static stiffness of the tires were attached between these points as well. Static equilibrium simulations were conducted to check for model lock-up occurrences and correctness of the assembly. In this way a functioning kinematic assembly of the ADT was obtained in the ADAMS simulation environment.

The next step was to replace the idealised joint constraints by real force constraints that more realistically modelled the rigid body connections of the various rigid bodies that constitute the ADT multibody system. Thus key joints such as the spherelastic bearings connecting the suspension links to the chassis and axles, the sandwich blocks, asymmetric bearings of the cab attachment points, the A-frame to front chassis joint as well as the front suspension struts had to be replaced by compliant force restraints. This is discussed next.

4.3 Compliant suspension components

The discussion of the modelling effort in ADAMS so far has focussed on the geometrical assembly and the kinematic relations of the various rigid bodies that constitute the ADT. However as discussed in § 2.2 the actual behaviour of the MBS under dynamic conditions is highly dependent on the various compliances in the system. This means that the idealised joints used to construct the model need to be replaced by ‘real’ restrictions on the relative degrees of freedom between rigid bodies in the model. As an illustration of why this is needed one can consider two links joined by an ideal spherical joint. The two links thus have rotational degrees of freedom about any axis that passes through the actual joint centre. This means that the two links can traverse the full spherical space relative to each other as the ideal spherical joint allows them to. In reality this may not be so. A trivial restriction is that the two rigid parts cannot occupy the same space at the same time as is allowed to happen in the MBS environment of ADAMS. More realistically the actual joint could be a rubber bush with finite stiffness and energy loss mechanisms such as dry friction and viscous damping. Thus while the ideal joint will allow any motion in the free directions between two rigid bodies, the reality is that such motions might result in a real force that is too large for the real system to handle resulting in failure (e.g. of the bush) or there may just not be sufficient force in the system to cause the required motion. It thus becomes imperative to replace the ideal joints by force relations involving stiffness and damping where the compliance of the real joint is of such an order as to significantly differ from an ideal joint under real operation conditions.

In the limit behaviour of the system where the forces are high, even the rigid bodies themselves must be considered as compliant members [65]. However for this study this was not considered as part of the modelling exercise. Only the compliance of the joints due to the use of rubber in their construction was considered. Of course the tire is a highly compliant part of the MBS, a compliance which if not properly accounted for will cause the MBS model to be inaccurate. The physics of tire behaviour was discussed in § 2.1. This section deals with, the spherelastic bearing, A-frame bearing, asymmetric bearing, sandwich box and the front suspension strut and the various force relations used to describe these compliant joints in the ADAMS model of the ADT. In order to understand and better characterise the behaviour of these compliant components under dynamic conditions an undergraduate project was instituted to test these components under varying amplitudes and frequencies of operation. Section 2.2 highlighted the difficulty of accurately modelling compliant components across the entire frequency and amplitude range of operation. Thus the results from the characterisation tests on the compliant suspension components were studied to understand the nature of the dependency on amplitude and frequency with a view to simplifying the behaviour of the components for implementation into the MBS model of the ADT in ADAMS. As the aim of this study was to use the MBS

model in ADAMS to model the vehicle dynamics i.e. handling and low frequency ride behaviour of the ADT, this simplification primarily resulted in the use of the information gathered on the low frequency, large amplitude behaviour of the compliant components as these are the operating conditions that encompass the ride and handling regime of a vehicle [7].

4.3.1 Determining the damping and stiffness values

Section 2.2 highlighted the various difficulties that arise in modelling the compliant suspension components of an automobile. In reality, these components display behaviour that is both highly non-linear as well as frequency dependant. Analytical models of these suspension components can be a significant individual study in their own right. Also when one chooses to characterise these systems in terms of their energy restoring (stiffness) and energy loss (damping) mechanisms empirically from extensive testing, it could, and very often does, give rise to behaviour which is difficult to capture in such a black-box model. To use non-linear splines or polynomial fitted functional expressions to capture the non linearity precludes the modelling of frequency dependant behaviour and vice-versa using frequency response functions to capture the frequency dependant behaviour must assume linearity.

In order to proceed with the modelling effort in the face of these conflicting parameters, the question must be asked of the vehicle engineer attempting a virtual prototype, “Which dynamic regime are you most concerned with?” A NVH engineer would obviously be concerned with the higher frequency low amplitude behaviour of his system. This would then suggest that frequency response functions be used to capture the frequency response assuming linearity and small amplitudes of motion. The vehicle ride and handling engineer would be better served by using non linear splines or polynomial functions to capture the non-linearity that arises with the large scale motions involved during the low frequency or quasi static ride and handling regime. Having established that the latter forms the primary focus of this work the next step was to actually test the various components and then calculate their stiffness and damping characteristics across the working range of operation.

In order to characterise the dynamic characteristics of the compliant suspension components of the ADT a series of tests were carried out on a MTS[®] dynamic test rig by an undergraduate team at the University of Natal [61]. This involved building interfaces for the various suspension components to the MTS[®] dynamic testing rig. The MTS[®] rig is a set-up that includes a hydraulic actuator that is mounted to the bottom of a vertical frame. A sliding cross-member can be fixed at any height vertically on the frame. This forms the ‘ground’ point, which resists the force applied to the component. An interface then connects the component to be tested to the cross member and the hydraulic actuator. The MTS[®] rig has a hydraulic servo-control

system to control the force or displacement according to the input criteria via a calibrated load cell and integrated LVDT. The particular system available at the University of Natal is able to generate forces up to amplitudes of 100kN. The various components were then tested at varying loads and frequencies. Due to the design of the MTS® rig available at the University of Natal, component excitation could only be achieved along a single axis in translation only. Thus dynamic stiffness and damping characterisation tests of the compliant suspension components were only conducted in translation along the principle axes of the components. No rotational excitations about the principle axes were attempted. More information describing the test procedures and rig set-up can be obtained from the unpublished project report for the dynamic testing of the BELL Equipment ADT suspension components [61].

With the substantial amount of force and displacement data obtained for the various compliant suspension components from the testing described above, the effort then focuses on extracting useful information from the above data. The undergraduate team responsible for the testing of the components attempted to perform the analysis of the data. The resulting stiffness and damping values obtained though seemed too high upon first inspection. Upon investigating their methods of determining the stiffness and damping values from the above force and displacement data, using a single degree of freedom mass-spring damper model with known coefficients, it was found that the methodology used over-estimated the damping value of the system by as much as three orders of magnitude. While it was difficult to pinpoint the exact failings of the methodology used, it would have nevertheless been incorrect to proceed with the modelling of the ADT using these values. The undergraduate team methodology is presented in Appendix A.

Thus at a late stage in the project it became necessary to re-evaluate the stiffness and damping of the compliant suspension components. In a discussion in August 2002 with Mr. Hans Heltmann (BMW AG - Department EG-32 “Schwingungen und Akustik”) [27] a new approach was suggested. Given the force and displacement time histories from the tests conducted on the MTS® test rig at a particular constant frequency of excitation, with linear behaviour at the frequency of excitation, the graph in **Fig. 4.13** can be generated.

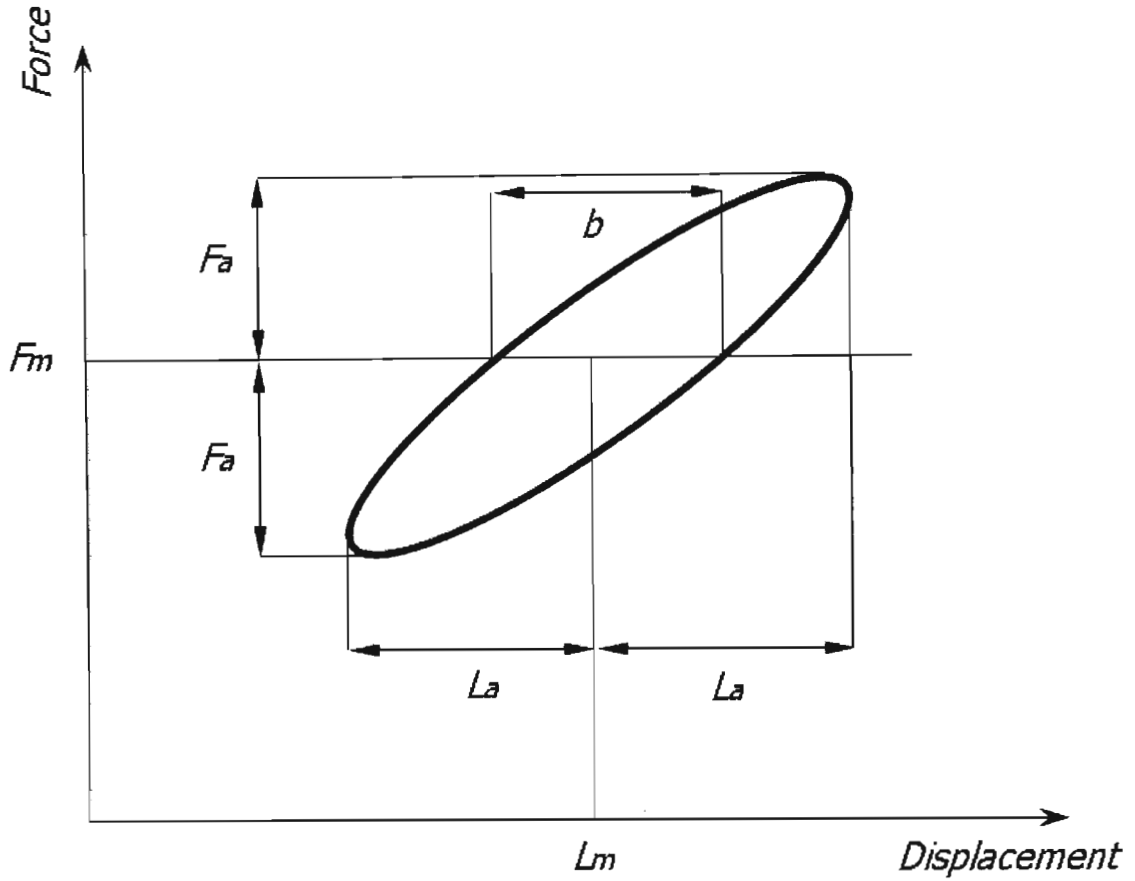


Fig. 4.13 Graph of Force versus Displacement for linear behaviour of compliant suspension component at a single frequency of excitation [27]

In addition from [7],[70] it is possible to write for the dynamic stiffness relationship incorporating the energy restoring elastic stiffness and the energy dissipating damping 'stiffness':-

$$K_{dyn} = K_{elastic} + K_{non-conservative}$$

Now with K_{dyn} being the measured stiffness of the system and using complex numbers one can write the above dynamic stiffness equation in the form:-

$$k_{meas} = k + j\omega c$$

where $k_{meas} = K_{dyn}$
 $k = K_{elastic}$
 $j\omega c = K_{non-conservative}$

The stiffness vector triangle displayed below in **Fig. 4.14** shows how the above stiffness equation translates into vector components.

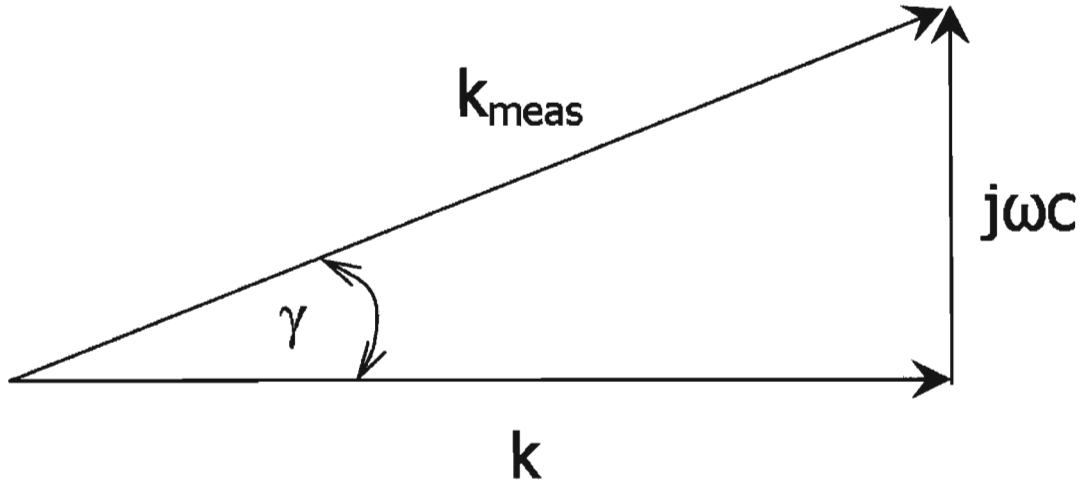


Fig. 4.14 Stiffness vector triangle showing the measured dynamic stiffness having components of elastic stiffness and complex stiffness due to damping [27]

The angle γ represents the loss angle and is the parameter which characterises the energy lost in the system while k represents the real static stiffness and c the real damping in the system. From **Fig. 4.14** it is possible to write the following trigonometric relationship:-

$$j\omega c = k_{meas} \times \sin(\gamma)$$

Ignoring the complex operator, to obtain the real linear damping coefficient, the above equation can be rewritten as:-

$$c = \frac{k_{meas} \times \sin(\gamma)}{\omega}$$

with ω being the frequency of excitation of the component under test in [rad/s].

The parameter k_{meas} can be approximated from the test data for the linear system under consideration as:-

$$k_{meas} = \frac{Force}{Displacement}$$

while $\sin(\gamma)$ is, with reference to **Fig. 4.13**, given by :-

$$\sin(\gamma) = \frac{b/2}{L}$$

In **Fig. 4.13** F_m is the mean force and L_m is the mean displacement while F_a and L_a are the maximum amplitudes of force and displacement for each test respectively. The above methodology was then successfully used to calculate the stiffness and damping coefficients from the force and displacement input-output data of a known single degree of freedom spring-mass-damper system. With the methodology proven for linear systems, a MATLAB® script file was compiled to handle the reading in of the raw time data from the tests, the conditioning and processing of the data as well as to implement the above methodology for calculating the stiffness and damping. The MATLAB® script file is reproduced in Appendix B and with it being well documented, is not discussed further here.

It is important to note that the graph depicted in **Fig. 4.13** will only be of the ellipsoid shape shown if the system under test (in this case our compliant suspension components) behaves linearly at the frequency and amplitude of excitation. If this is not the case, the shape will deviate from the ellipsoid shape and lack symmetry. Thus the methodology described above to obtain the stiffness and damping parameters would be inaccurate and tend to a greater inaccuracy with an increasing deviation of the force displacement graph from the ellipsoid shape. At this stage in the project it was decided only to apply the method to the low frequency large amplitude tests conducted on each component, with this being the characteristic dynamic regime of vehicle handling behaviour [7]. Within this dynamic regime, an examination of the data collected showed that the force displacement relationships approximated the ellipsoid curves closely and that the compliant components could reasonably be assumed to be linear for each test amplitude of excitation in the low frequency regime. Of course the components were non-linear with respect to damping and stiffness across the amplitude range of operation as can be evidenced from the ensuing plots of damping and stiffness, but for each test with a specific amplitude at low frequencies, the ellipsoid approximation of the force-displacement curves allowed the method presented above, to be used with confidence to approximate the stiffness and damping values of the compliant suspension components tested.

4.3.2 Spherelastic bearing

The spherelastic bearing is the compliant joint that is used most commonly to link the various suspension components in the ADT. For example the suspension links that act as constraints on the axles relative to the chassis are connected using spherelastic bearings. It has a function that is similar to the annular rubber bush as found in many production-car suspensions, however it differs in construction. **Fig. 4.15** below shows the spherelastic bearing while **Fig. 4.16** shows the exploded view of the bearing.

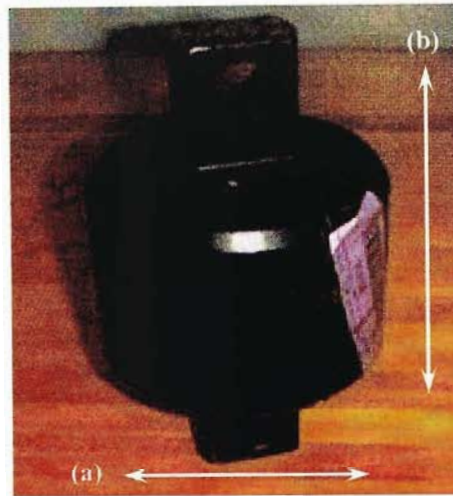


Fig. 4.15 Spherelastic bearing (a) radial direction (b) axial direction

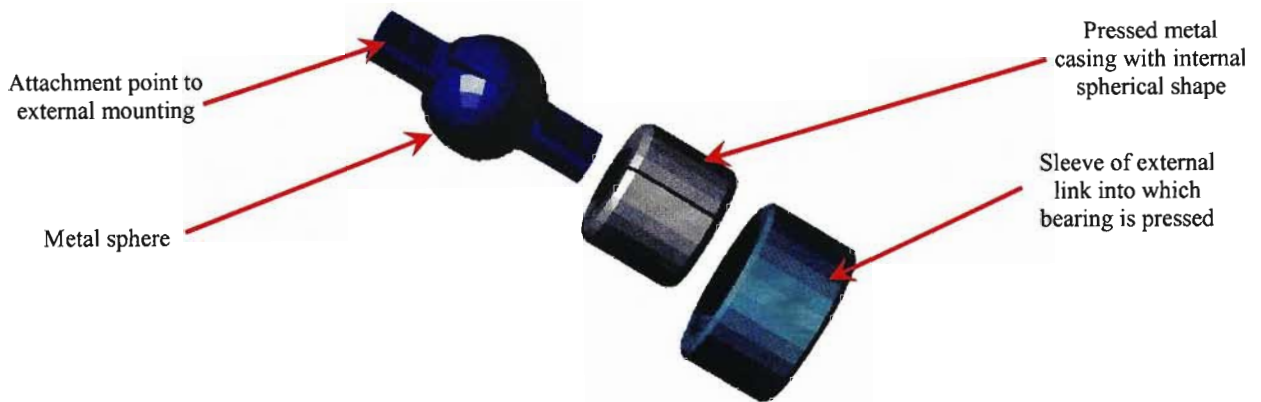


Fig. 4.16 Spherelastic bearing – exploded view

A metal casing with a concave spherical internal shape and divided into thirds, is pressed around the spherical metal ball with its external mounting attachment points. In between is a rubber compound, which acts to separate the metal surfaces of the spherical ball and the casing. Thus with the entire spherelastic bearing pressed into a sleeve of an adjoining link and attached to an external mounting point, the bearing allows the link freedom in a spherical part space (limited by the stiffness effects of the rubber in the bearing) relative to the attachment point.

Unfortunately due to the limited time available to the undergraduate student team, tests on the spherelastic bearing were conducted only along the radial direction (as indicated in Fig. 4.15 above). The tests were conducted for frequencies of 5, 10 and 15Hz. The data at 1Hz was unreliable. Thus the lowest frequency tested that would thus give an indication of the low frequency high amplitude behaviour is at 5Hz. Table 4.1 presents the maximum forces and displacement amplitudes for each test at 5Hz as well as the calculated stiffness' and damping from the methodology presented in § 4.3.1., while Fig. 4.17 and Fig. 4.18 present the plots of stiffness and damping versus force in the radial direction. For the axial direction, studying the more comprehensive results from the similarly constructed A-frame bearing can lead to useful approximations of the damping behaviour.

FORCE_max [N]	FORCE_min [N]	FORCE P-P [N]	DISP_max [m]	DISP_min [m]	DISP P-P [m]	STIFFNESS [N/m]	DAMPING [N.s/m]
4306.6	-964.0262	5270.6262	-0.022369	-0.02244	7.1E-05	73.978E+6	23982
9322	-1015.9	10337.9	-0.022306	-0.022438	0.000132	78.183E+6	59071
14500	-1011.8	15511.8	-0.022234	-0.022435	0.000201	77.421E+6	55080
19645	-952.02	2.06E+04	-0.022158	-0.022427	0.000269	76.664E+6	60384
24685	-955.41	25640.41	-0.022088	-0.022423	0.000335	76.663E+6	58697
29817	-1022.3	30839.3	-0.022018	-0.022417	0.000399	77.391E+6	83653
34934	-877.31	35811.31	-0.021947	-0.022408	0.000461	77.694E+6	69839
39832	-996.84	40828.84	-0.021883	-0.022405	0.000522	78.243E+6	100670
44882	-1039.8	45921.8	-0.021814	-0.0224	0.000586	78.424E+6	96022
50156	-971.54	51127.54	-0.021741	-0.022399	0.000658	77.756E+6	82848
60393	-906.65	61299.65	-0.021595	-0.022386	0.000791	77.509E+6	73035
80721	-710.99	81431.99	-0.021319	-0.022357	0.001038	78.459E+6	82485
99889	-1056.5	100945.5	-0.020998	-0.022305	0.001307	77.250E+6	120300

Table 4.1 Results of testing of Spherelastic bearings in the radial direction at 5Hz

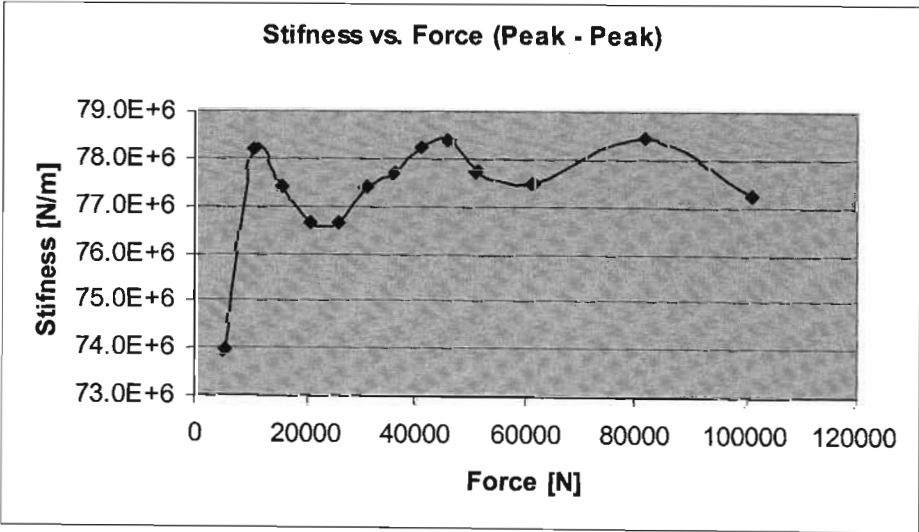


Fig. 4.17 Stiffness vs. Force for the Spherelastic bearings in the radial direction at 5Hz

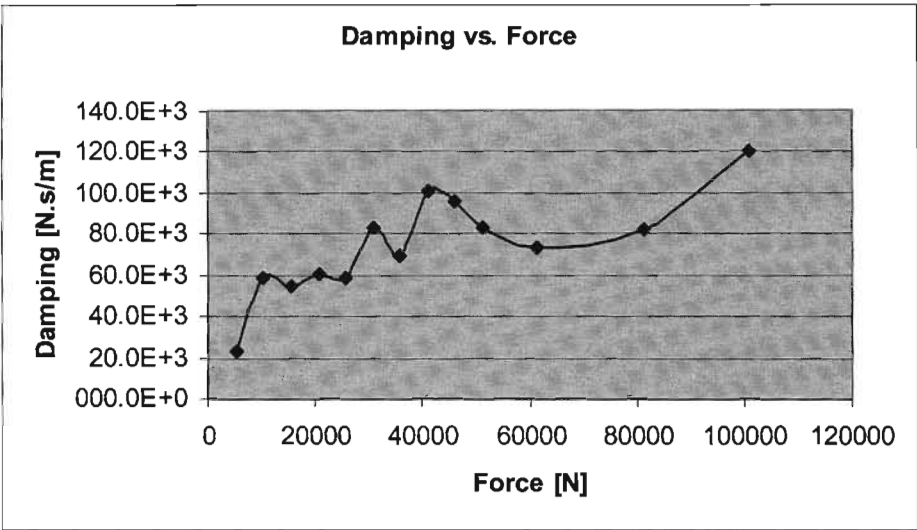
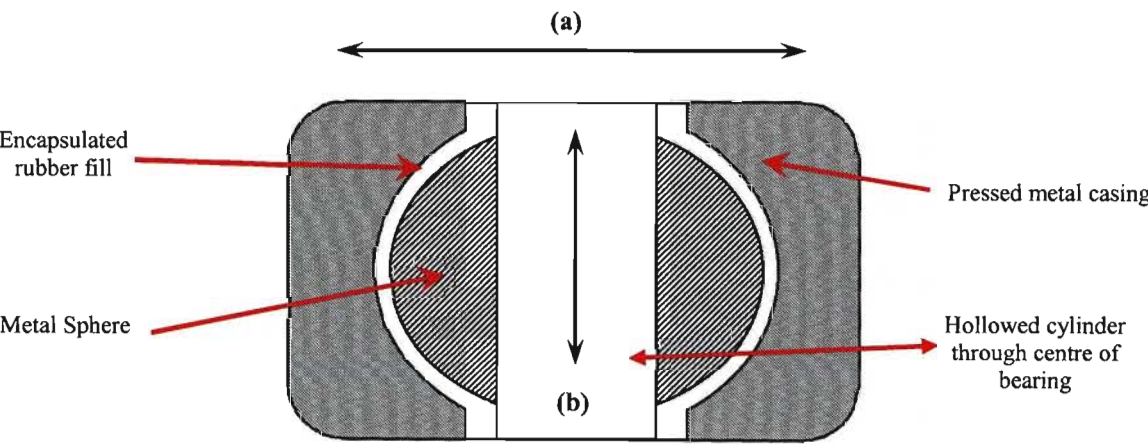


Fig. 4.18 Damping vs. Force for the Spherelastic bearings in the radial direction at 5Hz

4.3.3 A-Frame bearing

The A-frame bearing connects the front axle / A-frame assembly to the front chassis and is similar in construction to the spherelastic bearing. Its primary difference is that the metal sphere as indicated in **Fig. 4.16** above does not have external attachment points and has a cylindrical portion removed from its centre as indicated by the cross-sectional view in **Fig. 4.19** below.



**Fig. 4.19 Cross section of A-frame bearing (a) radial direction
(b) axial direction**

The A-frame bearing is then pressed into a cylindrical sleeve at the apex of the A-frame assembly. The apex of the A-frame is then attached to a bracket that is part of the front chassis. A metal pin is then inserted through the bracket and the A-frame bearing, through its hollow cylindrical centre, locking the apex of the A-frame to the front chassis via the stiff but flexible A-frame bearing. This arrangement is indicated in the assembly stage of the ADT in **Fig. 4.20**.



Fig. 4.20 Connection of the A-Frame to the front chassis via the A-frame bearing

The A-frame Bearing was tested in the radial and axial directions on the MTS test rig. For static compression tests up to 100kN the following stiffness' were obtained [61]: -

$$K_{\text{rad}} = 54.4 \text{ kN/mm}$$

$$K_{\text{axial}} = 15.9 \text{ kN/mm}$$

Dynamic tests were conducted in the radial directions for frequencies of 1, 5, 10 and 15Hz and in the axial direction at 1 and 5Hz. At each frequency, various force and displacement amplitudes were used to characterise the component over a wider force operating range. As in § 4.3.2 only the analysis of the data to obtain the stiffness and damping effects in the low frequency range are presented, in this case being the results from the tests at 1Hz. **Table 4.2** and **Table 4.3** present the maximum forces and displacement amplitudes for each test at 1Hz as well as the calculated stiffness' and damping from the methodology presented in § 4.3.1 in the radial and axial directions respectively. **Fig. 4.21** and **Fig. 4.22** present the plots of stiffness and damping versus force in the radial direction while **Fig. 4.23** and **Fig. 4.24** present the plots of stiffness and damping versus force in the axial direction.

FORCE_max [N]	FORCE_min [N]	FORCE P-P [N]	DISP_max [m]	DISP_min [m]	DISP P-P [m]	STIFFNESS [N/m]	DAMPING [N.s/m]
8528.8	103.87	8424.9	-0.0007473	-0.0009495	0.00020222	41.663E+6	863.220E+3
18679	80.901	18598	-0.0005425	-0.0009158	0.00037327	49.825E+6	553.860E+3
28777	88.788	28689	-0.0003742	-0.0009135	0.0005393	53.196E+6	791.980E+3
38978	85.491	38892	-0.0001961	-0.0008726	0.00067654	57.487E+6	228.060E+3
49061	88.51	48973	-3.17E-05	-0.000877	0.00084532	57.934E+6	324.450E+3
59172	71.062	59101	0.00013773	-0.0008567	0.00099439	59.435E+6	354.570E+3
69332	47.816	69284	0.00030434	-0.0008457	0.00115	60.248E+6	194.350E+3
79461	10.59	79450	0.00046526	-0.0008486	0.0013139	60.470E+6	603.300E+3
89576	76.635	89499	0.00062575	-0.0008126	0.0014384	62.223E+6	115.050E+3

Table 4.2 Results of testing of A-Frame bearing in the radial direction at 1Hz

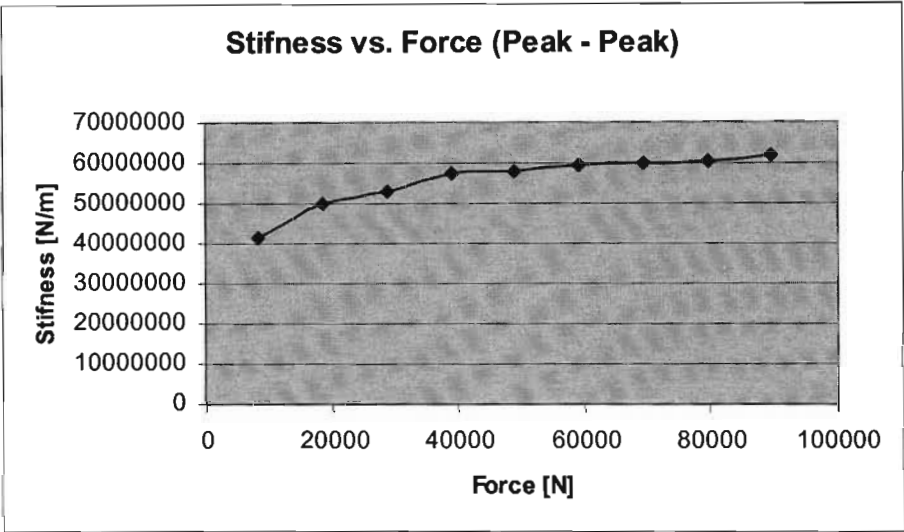


Fig. 4.21 Stiffness vs. Force for the A-Frame bearing in the radial direction at 1Hz

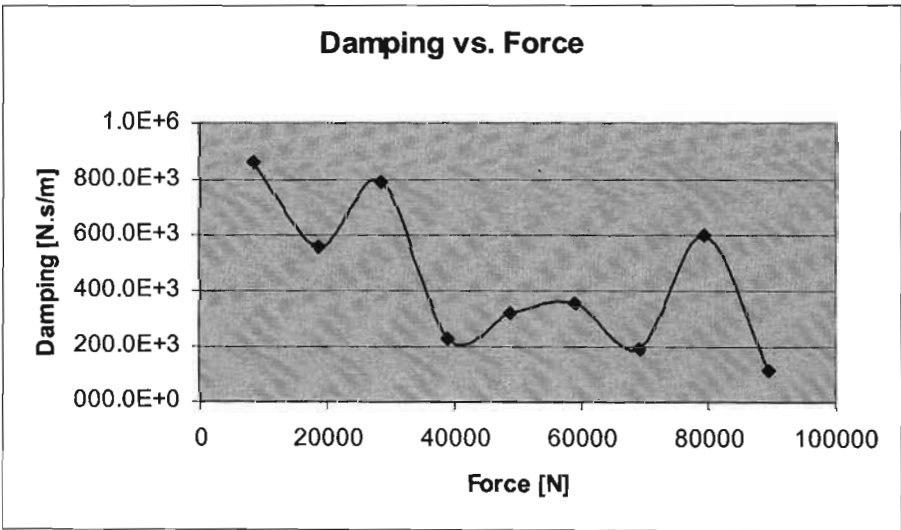


Fig. 4.22 Damping vs. Force for the A-Frame bearing in the radial direction at 1Hz

FORCE_max [N]	FORCE_min [N]	FORCE P-P [N]	DISP_max [m]	DISP_min [m]	DISP P-P [m]	STIFFNESS [N/m]	DAMPING [N.s/m]
3440.2	152.59	3287.6	0.0015284	0.0013968	0.00013166	24.970E+6	213.850E+3
8558.8	175.74	8383	0.0018434	0.0014204	0.000423	19.818E+6	272.110E+3
18660	186.73	18473	0.0025242	0.0014915	0.0010327	17.889E+6	287.730E+3
29761	-766.26	30528	0.0032388	0.0014903	0.0017485	17.459E+6	277.400E+3
39915	-677.71	40593	0.0038887	0.0015224	0.0023663	17.155E+6	242.080E+3
50026	-651.56	50678	0.0045527	0.001582	0.0029708	17.059E+6	268.430E+3
60131	-722.41	60854	0.0052417	0.0016115	0.0036302	16.763E+6	236.750E+3
70294	-633.33	70928	0.0058566	0.0016657	0.0041909	16.924E+6	245.210E+3
80351	-671.43	81022	0.0064337	0.0016677	0.004766	17.000E+6	229.700E+3
90371	-669.21	91040	0.0069953	0.0016804	0.0053149	17.129E+6	249.940E+3

Table 4.3 Results of testing of A-Frame bearing in the axial direction at 1Hz

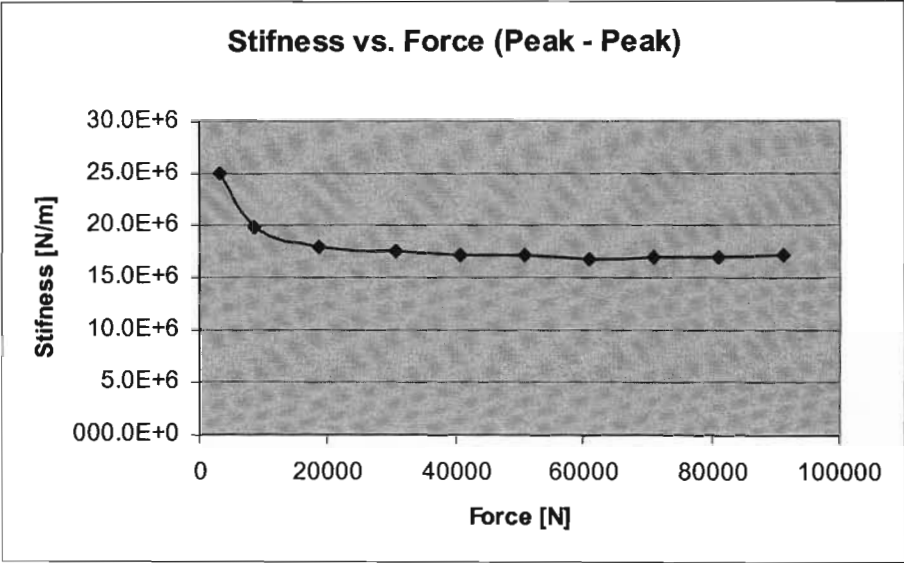


Fig. 4.23 Stiffness vs. Force for the A-Frame bearing in the axial direction at 1Hz

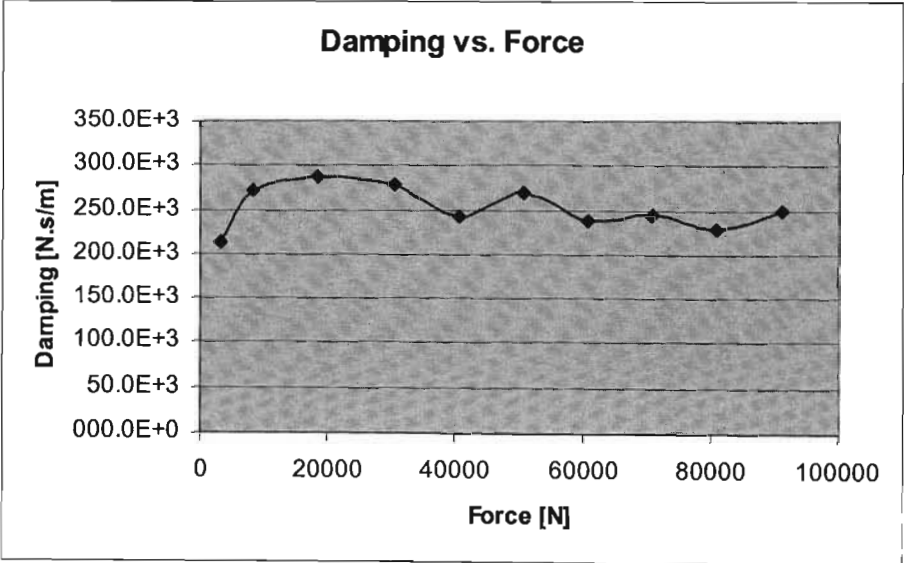


Fig. 4.24 Damping vs. Force for the A-Frame bearing in the axial direction at 1Hz

As can be seen the A-frame bearing has a hardening spring type behaviour in the radial direction and a softening type behaviour in the axial direction. The damping for the A-frame bearing varies significantly in the radial direction while the damping in the axial direction remained fairly constant.

4.3.4 Sandwich block

The sandwich block is an essentially rubber component that connects the walking beams to the middle and rear axles and is composed of alternating layers of steel plates and rubber which are bonded to form one unit as shown in **Fig. 4.25**. The sandwich block was tested only in the vertical or axial direction (see (a) in **Fig. 4.25**) and here again the results of the data analysis are presented only for the 1Hz response. In addition the sandwich box was tested without a preload and with a preload of approximately 50kN. As can be seen in the results presented below, the resultant stiffness and damping values differ significantly.

Table 4.4 & **Table 4.5** present the maximum forces and displacement amplitudes for each test at 1Hz of the sandwich block, as well as the calculated stiffness' and damping from the methodology presented in § 4.3.1 in the axial direction with and without preload force respectively. **Fig 4.26** and **Fig 4.27** present the plots of stiffness and damping versus force in the axial direction with preload force while **Fig 4.28** and **Fig 4.29** present the plots of stiffness and damping versus force in the axial direction excluding the preload force.



Fig. 4.25 Sandwich block (a) vertical direction

FORCE_max [N]	FORCE_min [N]	MAX AMP FROM P-LOAD	FORCE P-P [N]	DISP_max [m]	DISP_min [m]	DISP P-P [m]	STIFFNESS [N/m]	DAMPING [N.s/m]
53672	48547	2572	5125.8	0.030073	-0.0002434	0.030317	1.69E+05	295.97
56155	46041	5055	10114	0.030776	-0.0009711	0.031747	3.19E+05	729.21
58663	43506	7563	15157	0.031489	-0.001696	0.033185	4.57E+05	1053.1
61178	40985	10078	20193	0.032203	-0.0024201	0.034623	5.83E+05	1323.3
66193	36020	15093	30174	0.033659	-0.0038276	0.037486	8.05E+05	2119.2
71210	31000	20110	40210	0.035055	-0.0052874	0.040343	9.97E+05	2514.4
76236	26003	25136	50233	0.036506	-0.0067073	0.043213	1.16E+06	3201.9
81192	21009	30092	60183	0.037926	-0.0081522	0.046078	1.31E+06	3546.4
86145	16095	35045	70050	0.039353	-0.0095557	0.048909	1.43E+06	3944.7
91064	11141	39964	79922	0.040711	-0.010953	0.051664	1.55E+06	4214.4
95980	6181.9	44880	89799	0.042204	-0.012393	0.054598	1.64E+06	4074.5

Table 4.4 Results of testing of Sandwich Block in the axial direction at 1Hz (Preload)

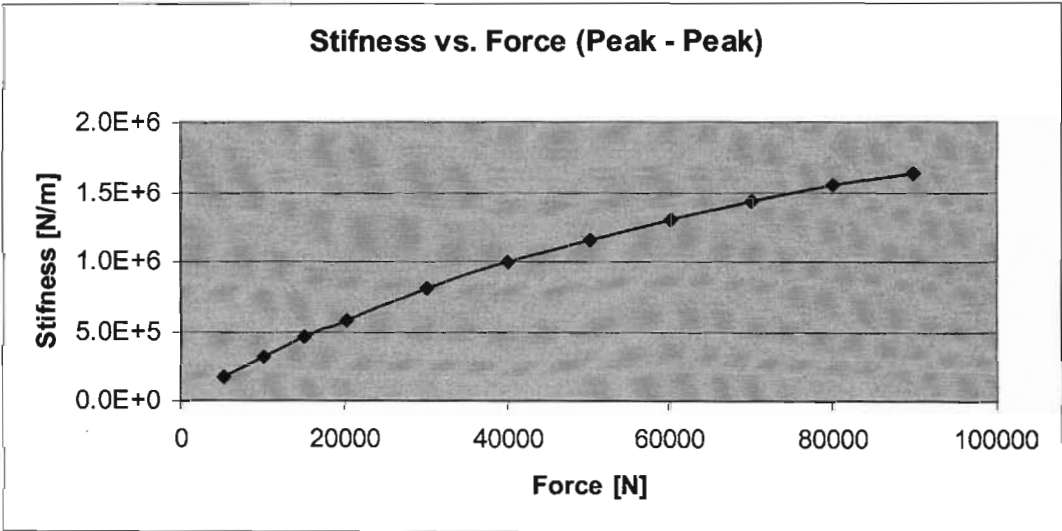


Fig. 4.26 Stiffness vs. Force for the Sandwich Block in the axial direction at 1Hz (Preload)

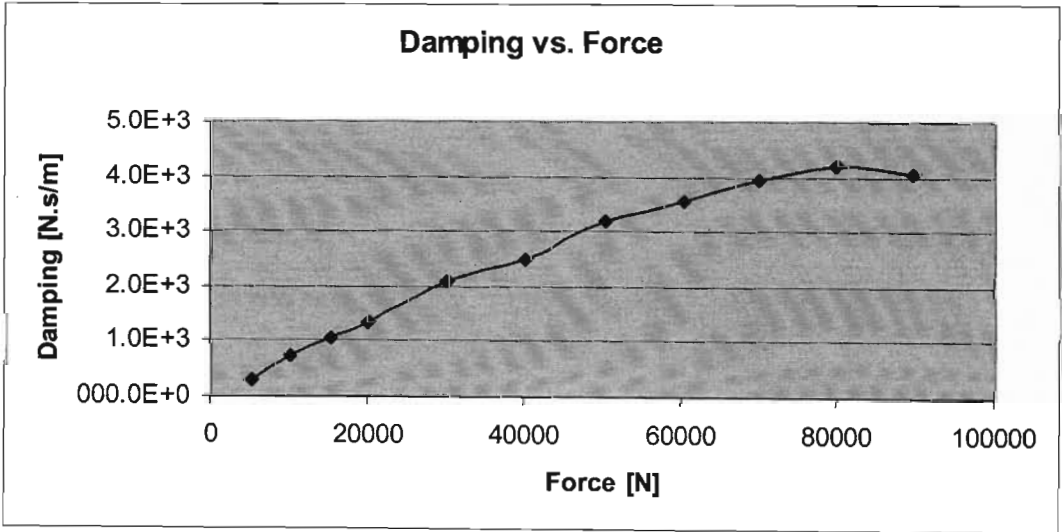


Fig. 4.27 Damping vs. Force for the Sandwich Block in the axial direction at 1Hz (Preload)

FORCE_max [N]	FORCE_min [N]	FORCE P-P [N]	DISP_max [m]	DISP_min [m]	DISP P-P [m]	STIFNESS [N/m]	DAMPING [N.s/m]
4898	-247.54	5145.5	0.017707	0.017214	0.00049318	10433000	121.850E+3
10004	-182.94	10187	0.018336	0.017268	0.0010677	9.541E+6	142.400E+3
20163	-20.883	20184	0.019928	0.017446	0.0024822	8.131E+6	137.550E+3
30257	77.249	30180	0.021653	0.017596	0.0040563	7.440E+6	125.730E+3
40425	208.28	40216	0.023421	0.017739	0.0056814	7.079E+6	116.610E+3
50542	265.87	50276	0.025072	0.017825	0.0072466	6.938E+6	110.190E+3
60632	332.92	60299	0.026765	0.017923	0.0088425	6.819E+6	105.630E+3
70660	482.01	70178	0.028399	0.01805	0.010349	6.781E+6	100.740E+3
80761	564.15	80197	0.02995	0.018114	0.011836	6.775E+6	97.922E+3
90807	641.89	90165	0.031419	0.018195	0.013224	6.818E+6	99.642E+3
1.01E+05	721.79	99807	0.032847	0.018204	0.014644	6.816E+6	93.731E+3

Table 4.5 Results of testing of Sandwich Block – axial direction at 1Hz (No preload)

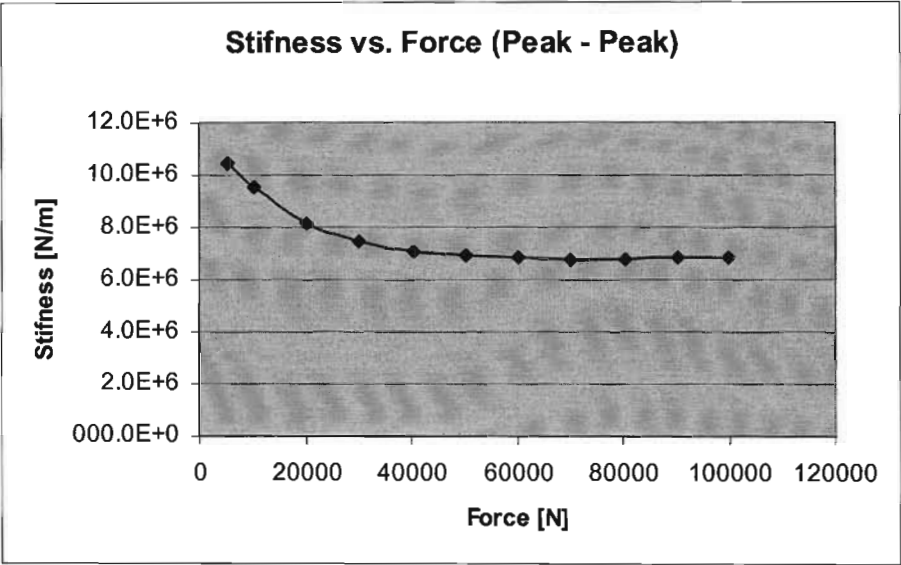


Fig. 4.28 Stiffness vs. Force for the Sandwich Block – axial direction at 1Hz (No preload)

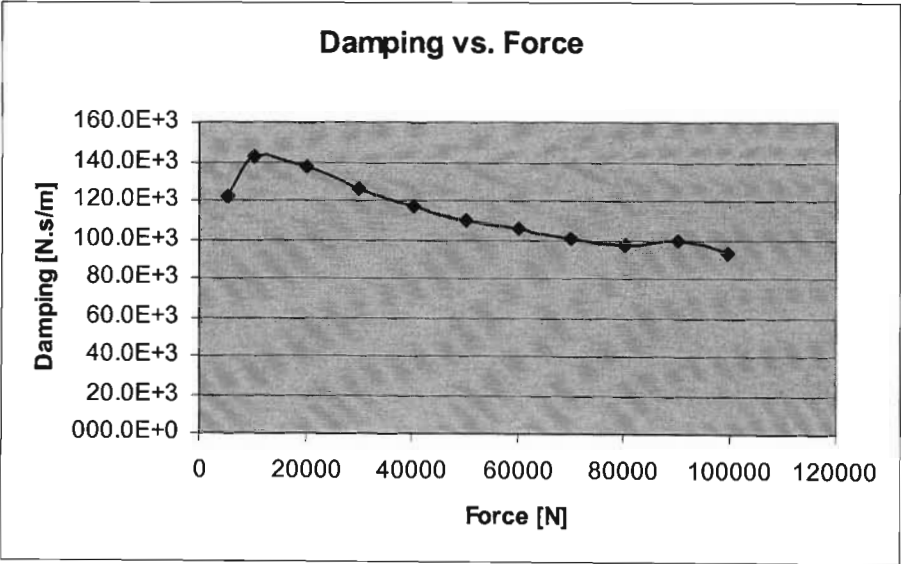


Fig. 4.29 Damping vs. Force for the Sandwich Block – axial direction at 1Hz (No preload)

4.3.5 Asymmetric Bearing

The asymmetric bearing is essentially an annular rubber bush with an offset centre. It is used to mount the cab to the front chassis at each of the four corners. **Fig. 4.30** shows where the asymmetric bearing is assembled in the ADT in relation to the cab and chassis while **Fig. 4.31** shows the construction of the bearing indicating the offset of the centre mounting point.

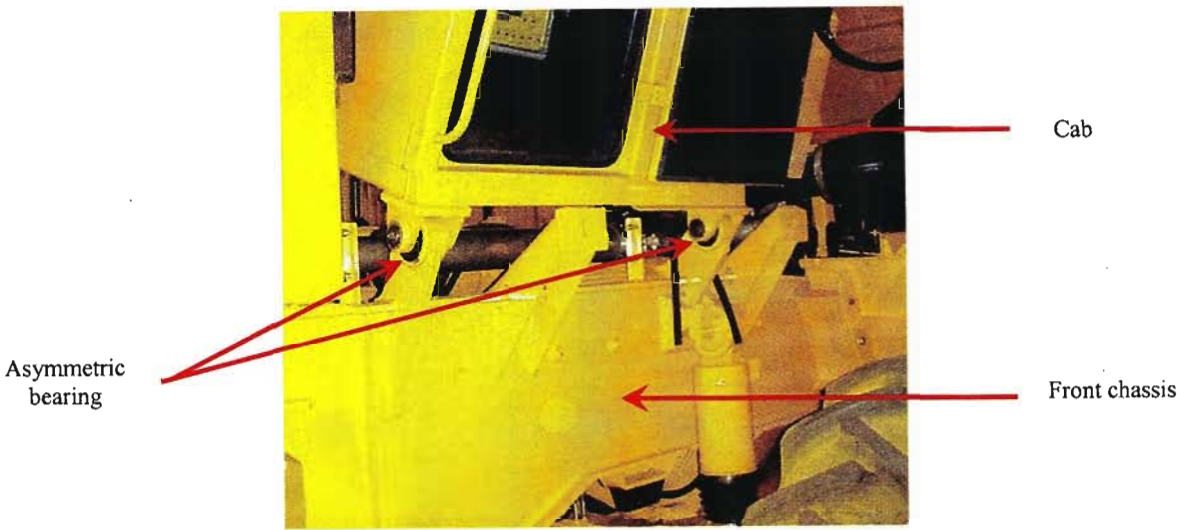


Fig. 4.30 Asymmetric bearing assembly position

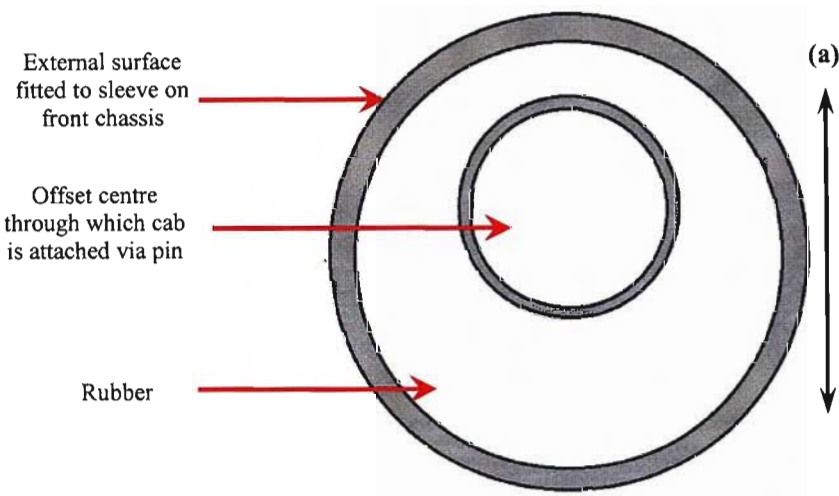


Fig. 4.31 Construction of asymmetric bearing (a) radial direction

The asymmetric bearing was tested on the MTS test rig in the radial direction only. Unfortunately it was only possible to test the asymmetric bearing at a frequency of 1HZ up to a force amplitude of 80kN as it failed at this point. Still the data gathered in the low frequency regime represents the data that is desired for handling analysis. The fact that the asymmetric bearing failed at a force amplitude of approximately 80kN indicates that this could be the designed strength capability with the actual or real loading conditions not exceeding this value. Thus the data collected would suffice for the current requirements of the ADAMS model.

Table 4.6 presents the maximum forces and displacement amplitudes for each test at 1Hz as well as the calculated stiffness' and damping from the methodology presented in § 4.3.1., while **Fig. 4.32** and **Fig. 4.33** present the plots of stiffness and damping versus force in the radial direction. It was however not possible to get an indication of how the component would behave at higher frequencies of operation or in the axial direction.

FORCE_max [N]	FORCE_min [N]	FORCE P-P [N]	DISP_max [m]	DISP_min [m]	DISP P-P [m]	STIFNESS [N/m]	DAMPING [N.s/m]
8815.5	-398.78	9214.3	-0.038276	-0.043661	0.0053852	1711100	25.965E+3
18633	-0.45422	18634	-0.033125	-0.042815	0.0096906	1.923E+6	37.826E+3
28674	18.037	28656	-0.029427	-0.042256	0.012829	2.234E+6	41.223E+3
39599	302.55	39296	-0.026386	-0.041059	0.014673	2.678E+6	64.947E+3
49005	884.77	48120	-0.024053	-0.040233	0.01618	2.974E+6	85.517E+3
58790	205.24	58585	-0.022496	-0.039472	0.016976	3.451E+6	91.467E+3
68339	572.02	67767	-0.020358	-0.037996	0.017639	3.842E+6	118.360E+3
78733	826.59	77907	-0.01926	-0.037358	0.018098	4.305E+6	141.740E+3

Table 4.6 Results of testing of Asymmetric bearing in the radial direction at 1Hz

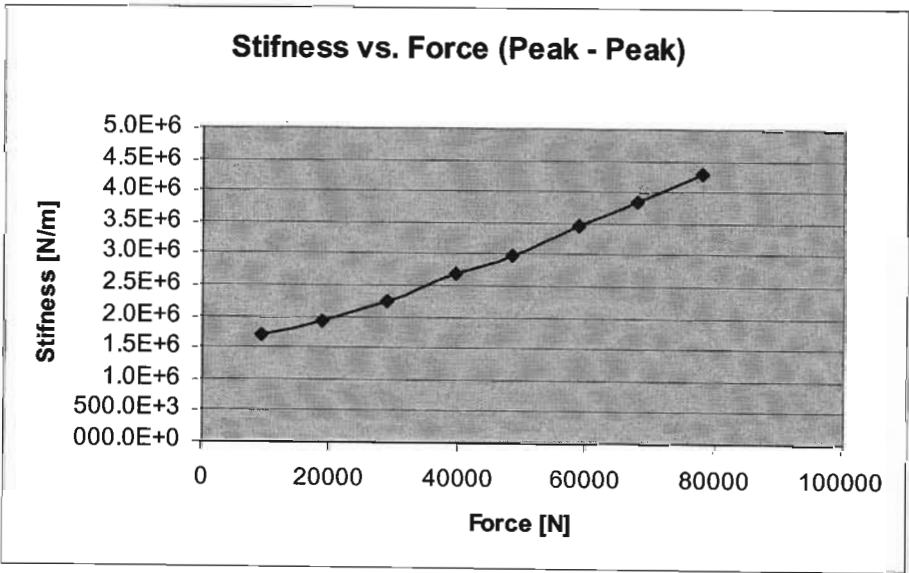


Fig. 4.32 Stiffness vs. Force for the Asymmetric bearing in the radial direction at 1Hz

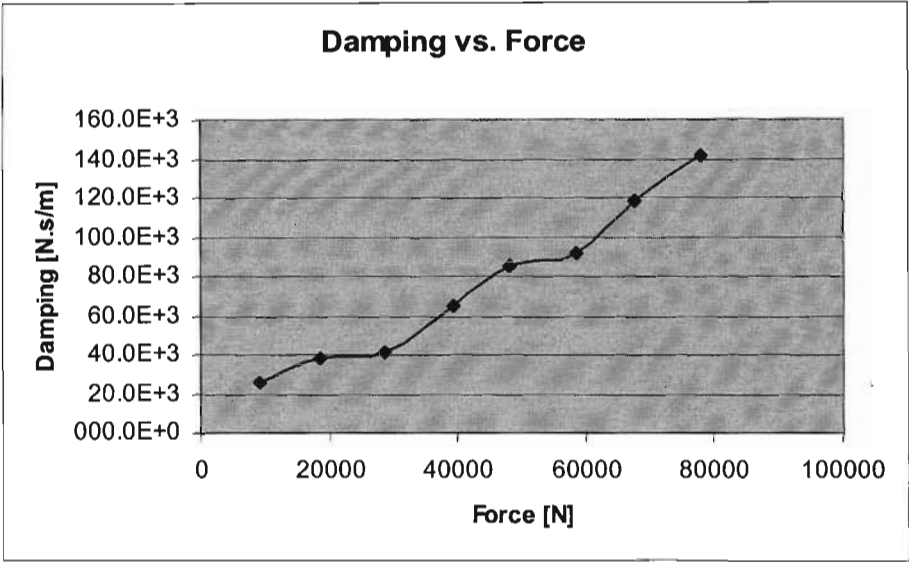


Fig. 4.33 Damping vs. Force for the Asymmetric bearing in the radial direction at 1Hz

4.3.6 Suspension strut

The suspension strut was the final compliant suspension component tested on the MTS machine. There are two suspension struts on the ADT and its purpose is to define the relative vertical motion between the front axle / A-frame assembly and the front chassis. **Fig. 4.34** shows a 3-D CAD solid representation of the strut.

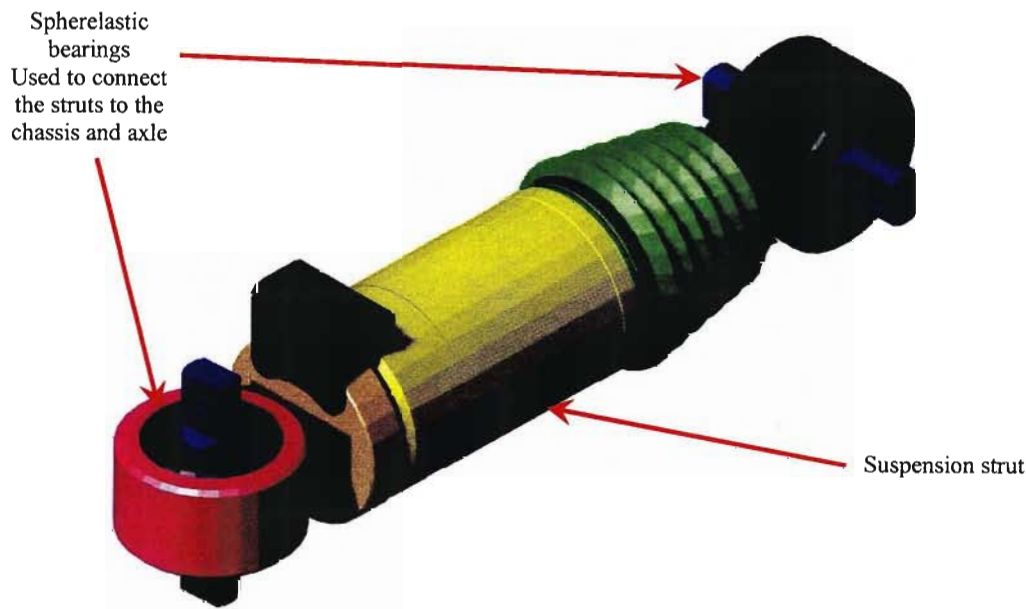


Fig. 4.34 Front suspension strut [61]

The strut operation however differs from the dynamic rubber mechanics as found on the other compliant components discussed above. The strut is essentially a pressurised gas load-bearing device with damping characteristics as found in an ordinary automotive shock absorber. It is thus bound to have varying stiffness' across its displacement range of operation (due to the increase in stiffness as the gas is pressurised) as well as differing damping characteristics in jounce (compression) and rebound (extension). The internal structure was not studied in detail. Rather it was the actual behaviour under load conditions that was investigated. It is known that the strut is pressurised with nitrogen gas such that it exerts a force (preload) acting to extend the strut up to its end stops. The strut in its natural state is fully extended with a preload force determined by the pressure of the gas in the strut. Static load tests to determine the static stiffness behaviour of the strut were performed up to the 100kN capability of the MTS test rig. The strut was tested with both the spherelastic bearings used to connect it to the front chassis and the front axle / A-frame assembly in place. The static load behaviour is displayed in **Fig. 4.35**, which indicates two distinct stiffness regions. Up to the preload value, which for this particular test specimen was approximately 50kN [61], the stiffness of the strut is determined largely by the radial stiffness' of the two spherelastic bearings in series. Once the preload force value is exceeded the stiffness changes drastically. Some hysteresis behaviour is evident which for the static case can be attributed to the effect of the spherelastic bearings and the internal gas compression/decompression behaviour.

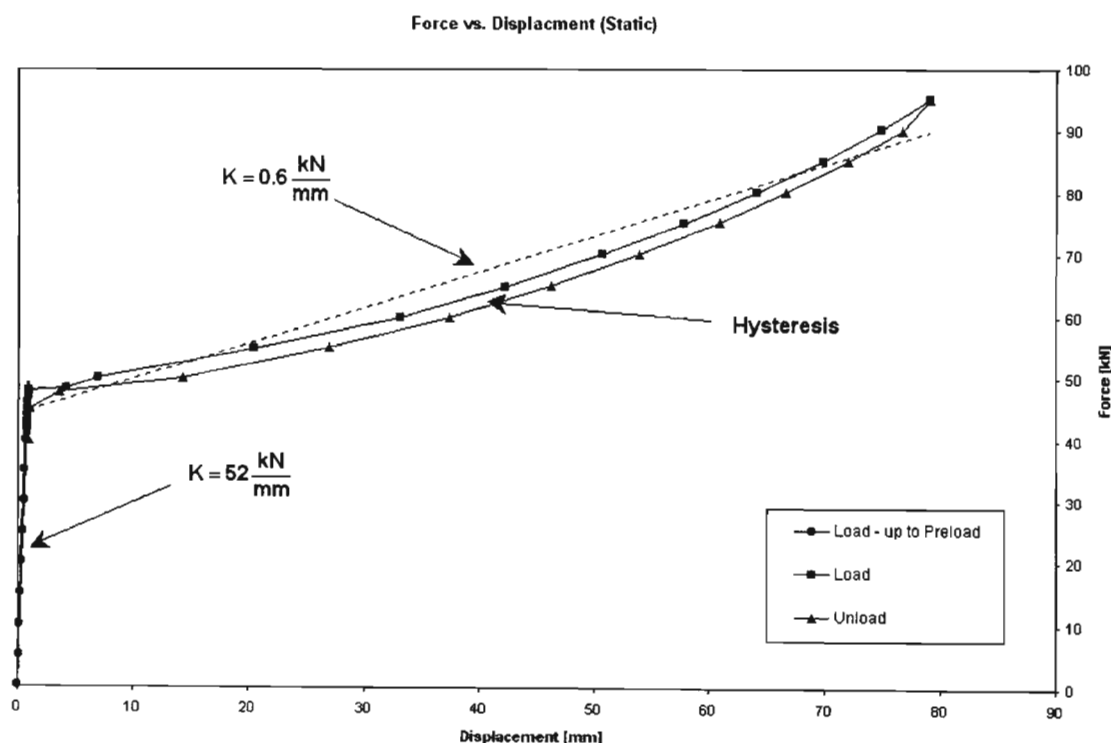


Fig. 4.35 Static stiffness behaviour of the suspension strut with Spherelastic bearings [61]

As mentioned above, the stiffness of the strut past the preload value is much lower than that prior to the pre-load value being exceeded. To counteract this, the damping in the strut past this preload value is determined by the flow of oil through the strut's internal flow restriction mechanisms and is very high even for low velocities. The strut was tested dynamically at frequencies of 1, 3, 5 and 8Hz across the load capability of the MTS test rig (0 – 100kN). Above 8Hz the load control on the MTS controller had become unstable due to the large forces and amplitudes involved. **Fig. 4.36** shows the force-displacement plot for one cycle of loading and unloading of the strut at a frequency of 1 Hz. The large hysteresis area indicates large energy dissipation and hence large damping. The damping calculations performed by the undergraduate team however involved the overall damping for one cycle [61] using their methodology discussed in § 4.3.1. In addition to this being incorrect for reasons discussed in § 4.3.1 the approach of calculating the damping for the entire load cycle was also incorrect. While this may have been sufficient for the rubber components which have a linear damping for small motions at low frequencies in compression and extension, it is not so for the suspension struts. This is due to the strut having three distinct regions where the damping is different. Up to the preload force, (approximately 50kN for the specimen tested) the damping (and stiffness) is determined in most part by the spherelastic bearings, as there is little relative motion between the ends of the strut. Past this point of loading the damping force increases dramatically and is different for loading (bounce or jounce) and unloading (rebound) as is expected from an automotive strut damper [11] and as is evident from the slopes of the loading and unloading curves in **Fig 4.36**.

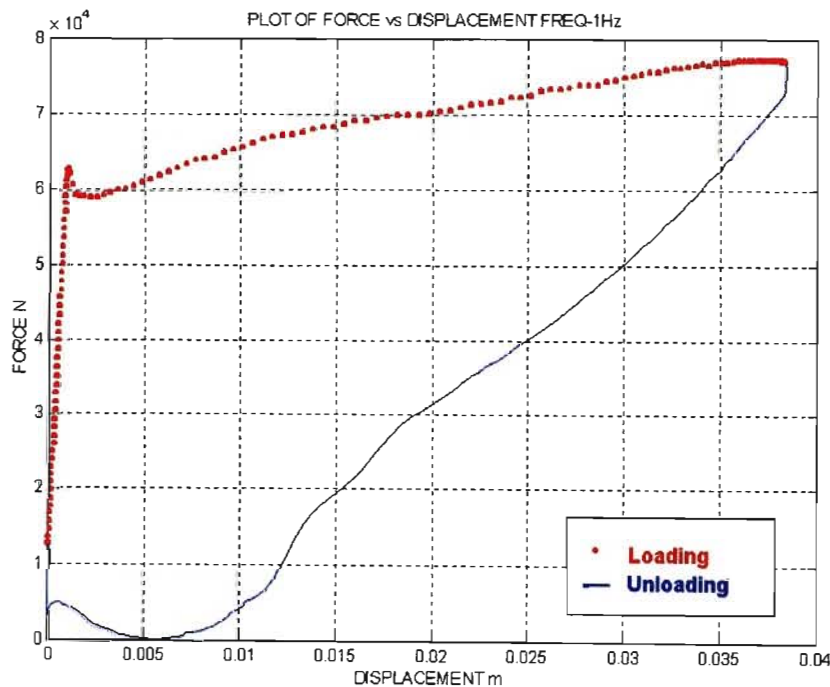


Fig. 4.36 Force displacement plot of loading and unloading cycle of suspension strut at a frequency of 1Hz [61]

Reference [46] presents a classical method for determining the damping properties of a damper in bounce and rebound. The damper under test is subjected to a sinusoidal motion of constant amplitude. The frequency of excitation is then changed with the amplitude being held constant each time. This produces a series of *carding loops* as depicted in Fig. 4.37 [46]. For sinusoidal motion the maximum velocity obtained is at the point of zero displacement and is given by:-

$$Velocity = 2\pi \times \omega \times amplitude$$

This point of maximum velocity is also the point of maximum force obtained for each of the rebound and compression directions of motion. Fig. 4.38 [46] shows how the rebound and compression forces are read from the carding loops for each maximum velocity arising from each test frequency. A graph similar to that shown in Fig 4.39 [40] can then be plotted of force versus velocity for each of the rebound and compression directions. It is a generally found that automotive dampers have differing damping curves in compression and rebound with the damping in rebound being approximately twice that of the damping in compression [11].

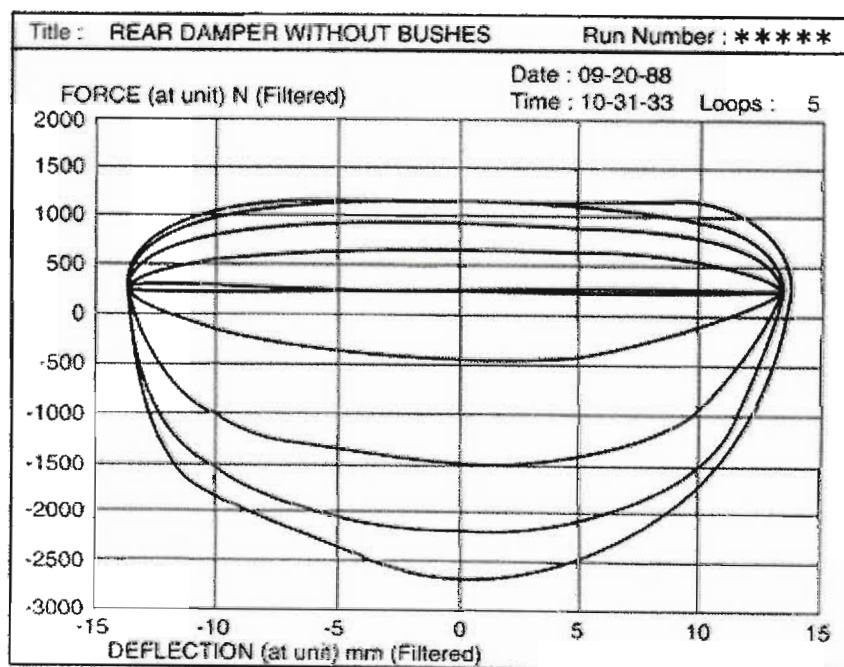


Fig. 4.37 An example of the result of a classical damper characterisation test showing carding loops [46]

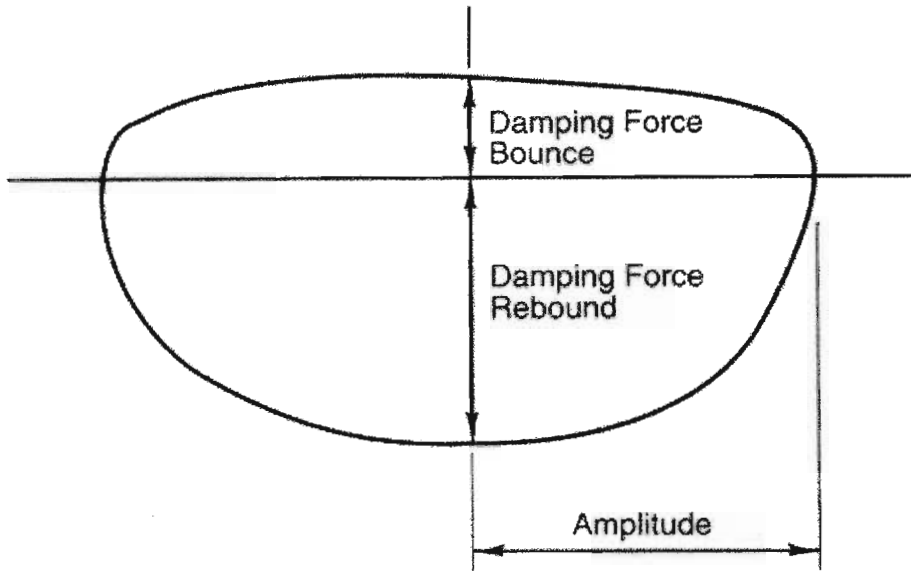


Fig. 4.38 Determination of the maximum compression (bounce) and rebound force from each carding loop at a specific frequency [46]

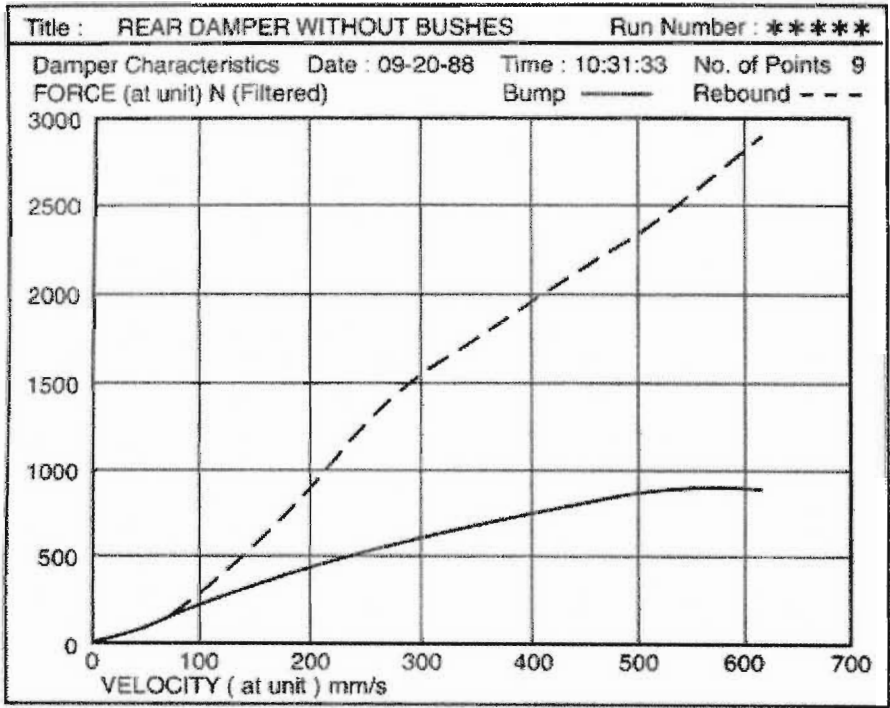


Fig. 4.39 Typical result of a carding loop test, quantifying a damper’s behaviour in compression (bump) and rebound [46]

An exact carding loop analysis could not be conducted on the suspension strut of the BELL EQ. B40C ADT however as firstly the testing of the strut was done at a constant force for each frequency rather than a constant displacement and secondly the strut is not a pure damper but a strut-damper i.e. a component having stiffness as well as damping. This leads to the strut having a finite force at maximum displacement (i.e. zero velocity) in a carding loop due to the stiffness of the compressed gas and hence it is not possible to determine the effect of the damping action on its own.

In order to get a principle approximation of the damping forces involved, it was decided to re-examine the raw force-displacement data obtained from the testing of the strut at all forces at the frequency of 1Hz i.e. the low frequency range. From the time data of the applied force it was noted that the struts were excited sinusoidally above the preload of approximately 50kN at various loads up to 100kN. Thus the average of all the exciting forces at 1Hz lay in a range of 50-75kN. **Fig. 4.40** and **Fig. 4.41** represent the zeroed time data of the force and displacement results form the testing of the strut at 1Hz.

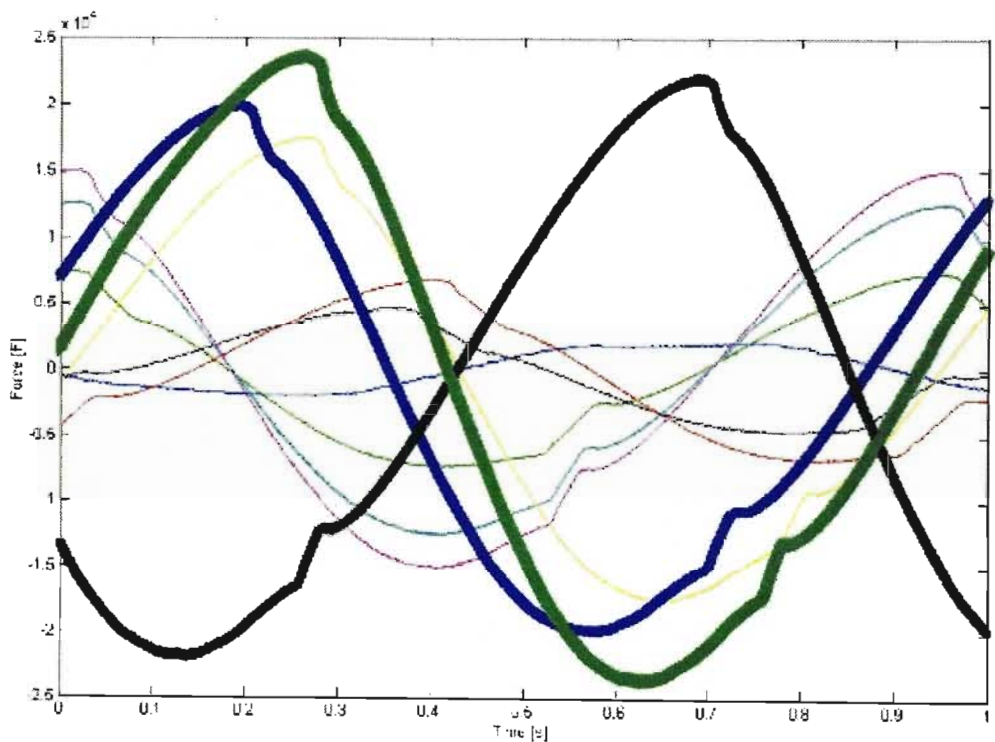


Fig. 4.40 Zeroed force vs. time data for the suspension strut tested at 1Hz and varying loads

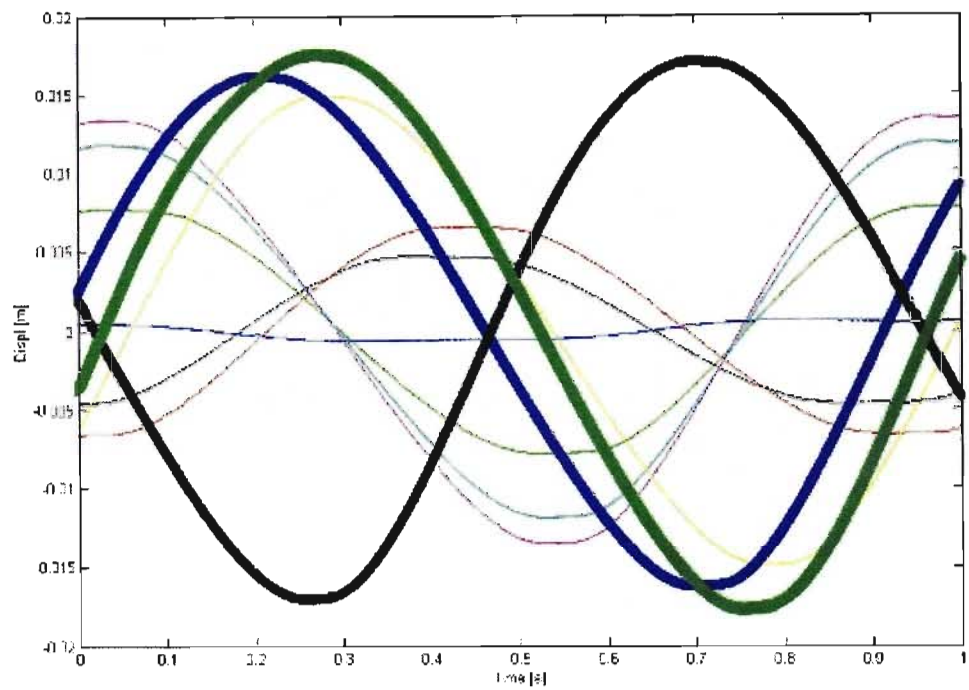


Fig. 4.41 Zeroed displacement vs. time data for the suspension strut tested at 1Hz and varying loads

It can be seen from **Fig 4.40** and **Fig 4.41** that the absolute value of maximum force coincides with the absolute value of displacement in the compression stroke only and lags the absolute value of displacement in rebound. The force versus displacement relationship for the strut tested at 1Hz at various load is shown in **Fig. 4.42**.

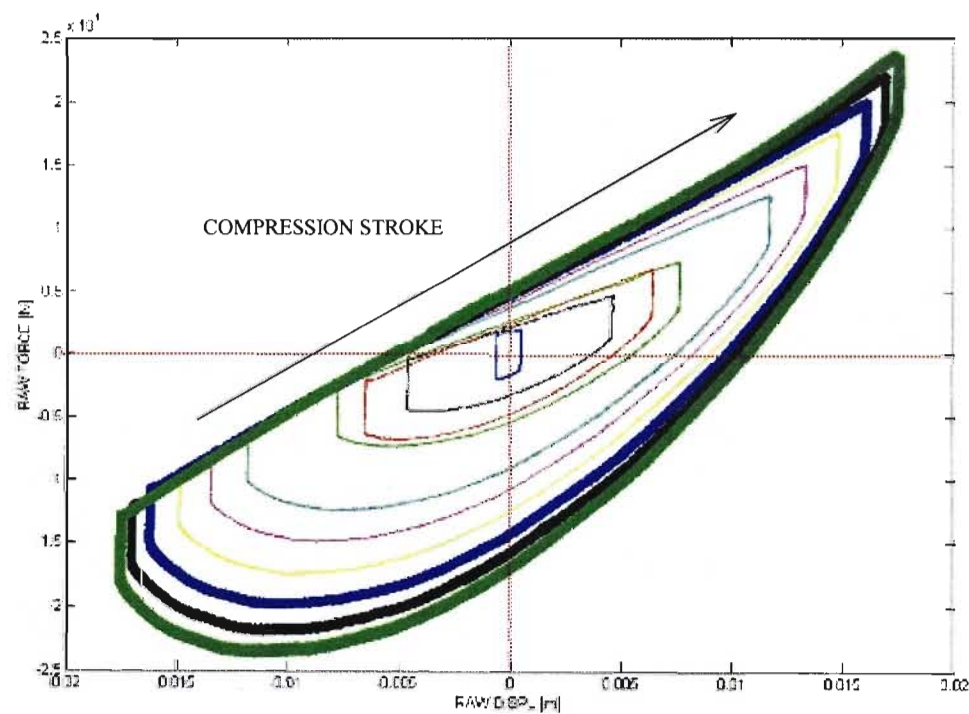


Fig. 4.42 Zeroed force vs. displacement relationship for the suspension strut tested at 1Hz and varying loads

Here again the non-ideal damper behaviour can be seen in that at positions of absolute maximum displacement (i.e. zero velocity) there is a finite force and that the absolute maximum forces in rebound and compression do not occur at the point of maximum velocity (i.e. zero displacement), this being due to the stiffness effect of the compressed nitrogen gas in the strut. For small motions of the strut, the damping effect is not largely different in compression and rebound and the force-displacement curves tend toward symmetry. As the strut travel increases however the asymmetry becomes more pronounced.

It was still considered instructive however to examine the force at the absolute maximum velocities in rebound and compression to get an indication of the damping force present in the strut as the damping forces would dominate the strut behaviour at points of maximum velocity, especially for large forces and displacements. This is presented in Fig. 4.43.

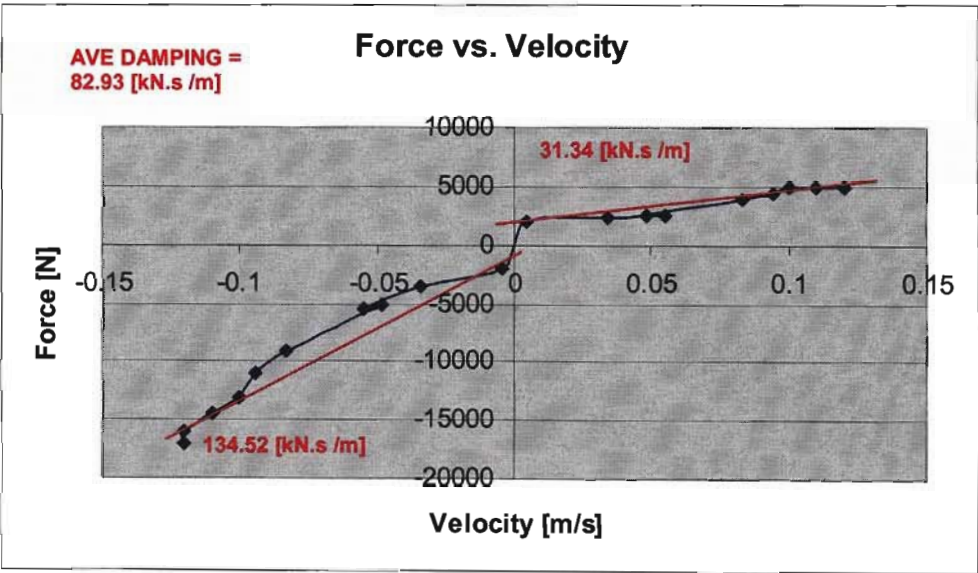


Fig. 4.43 Force vs. maximum velocity per cycle for the suspension strut tested at 1Hz and varying loads in compression and rebound

In Fig. 4.43 the linear curve fitting shows that the “approximate damping” in compression is 31.43 [kN.s/m] and that in rebound is 134.52 [kN.s/m] with the average being 82.93 [kN.s/m]. It must be stated that the above representation does not strictly represent the damping in the strut as the force measured at the absolute maximum velocities consists of a stiffness as well as damping force. Due to the complex stiffness relationship during non-static actuation of the strut it was not possible to separate the two components of force with just the non-optimal test results available from the undergraduate student project.

The stiffness of the strut was simplified as well to be the stiffness of the strut at large displacements. As the high stiffness area of operation is in the low displacement range (i.e. < 0.001m from **Fig. 4.35**) below the preload, and because the large displacement behaviour is of interest the strut stiffness was taken to be 0.6 [MN/m]. Thus as a first approximation of the strut behaviour the following force relationship was defined for the strut:-

$$F = -k(x_1 - x_2) - c(\dot{x}_1 - \dot{x}_2) + F_o$$

where k = linear stiffness
 c = linear approximate damping
 F_o = preload

$(x_1 - x_2)$ = relative strut end displacement

$(\dot{x}_1 - \dot{x}_2)$ = relative strut end velocity

4.3.7 Discussion of Test Results for Compliant Suspension Components

It can be seen from the above that the analysis of the test results proceeded with non-ideal test data at hand. A record of the breaking-in procedures for each component as well as the temperatures at which they were tested was not kept, two factors which can greatly influence the behaviour of the compliant components. Many components were also not tested with any preloads applied to the components. This can of course give rise to different values of stiffness and damping than that obtained. Preload values were however not known at the time of component testing and could be in future be obtained by direct measurement on the actual vehicle or by examining a multibody model at static equilibrium using simplified suspension joints. In addition an examination of the time data for the various test cycles for each component showed that the force control was sometimes erratic as well as prone to set-point drift. In some instances the results of the force-displacement relationship differed from the first cycles of the test to the last. This could also be attributed to the breaking-in effect of rubber [25]. In addition the erratic non-monotonic variation in stiffness and damping obtained for some components above could also be due to the components having been tested beyond operating conditions with the construction (minimal rubber separating metal connectors) not allowing significant flexing of the rubber at higher forces.

Thus while the methods of analysis presented above still remain applicable, more testing of the components is necessary for the model to proceed past the first approximation stage. The above results though form an important part of this work as it allowed an approximation of the

stiffness and damping values to be established for use in the multibody dynamic model of the ADT, which were not available in the general literature for this class of vehicle. **Table 4.7** presents the average linear values of stiffness and damping used in the ADAMS ADT model for each compliant suspension component tested which resulted from the above analysis presented in § 4.3.

Component	Stiffness [MN/m]		Damping [kN.s/m]	
	Radial	Axial	Radial	Axial
Spherelastic Bearing	76	30.4	72	36
A-Frame Bearing	52	21	489	251
Sandwich Box (no preload)	4.3	8.6	59	118
Asymmetric Bearing	3	1.5	84	42
	Stiffness [MN/m]	Damping [kN.s/m]	Preload [kN]	
Suspension Strut	0.6	83	50	

Table 4.7 Damping and stiffness values obtained and used for the various compliant suspension components in the ADT model from sinusoidal tests conducted at 1Hz



Due to the absence of test data for the spherelastic bearing in the axial direction, the value used in the axial direction was approximated from the ratio of axial to radial stiffness and damping obtained from the A-Frame bearing. This assumption was made due to the similarity in construction of the spherelastic bearing and the A-Frame bearing. In addition the sandwich box stiffness and damping in the “radial” direction was assumed to be half of that in the axial direction. This assumption was made due to the “radial” direction of excitation corresponding to shear of the sandwich block. Reference [25] states that for rubber compound in shear the strength is usually half that in compression in the linear range of operation. With no test data available for the axial direction of the asymmetric bearing the values for stiffness and damping were assumed to be half of that in the radial direction

4.3.8 Implementation of the Compliance Force Effects in ADAMS

The results presented above of the dynamic behaviour of the compliant suspension components stems from the need to replace the idealised joints in the MBS model of the ADT in ADAMS with actual dynamic force relationships as defined by the real joints in the ADT. In order to define these force relationships within the ADAMS/View environment the ADAMS constructs VFORCE and GFORCE are used. These constructs define a force / reaction force relationship between two bodies. This force relationship can take any functional form as defined by the user. As discussed above the force relationship between two points connected via a compliant joint can be defined according to the relative displacement and velocity of the two points if the stiffness and damping are known, as well as any preload or constant force that exists between them for zero displacement. Thus the force relationship between two points connected via a compliant joint can be expressed as follows [43]:-

$$F = -k(x_1 - x_2) - c(\dot{x}_1 - \dot{x}_2) + F_0$$

- where k = stiffness coefficient
- c = damping coefficient
- $(x_1 - x_2)$ = relative displacement between two points
- $(\dot{x}_1 - \dot{x}_2)$ = relative velocity between two points
- F_0 = preload

The stiffness and damping coefficients can be constants or any algebraic function. The VFORCE and GFORCE constructs are well suited to creating the force relationship represented above. To implement the constructs, the user has to use the VFORCE  or GFORCE  buttons from the forces pallet in the main toolbox of the ADAMS/View window. Basically the above constructs allows the user to define a functional force relationship along each of the three Cartesian coordinates of the markers that define the connection points of the two bodies. The icons that represent each of the constructs is shown in Fig. 4.44 below.

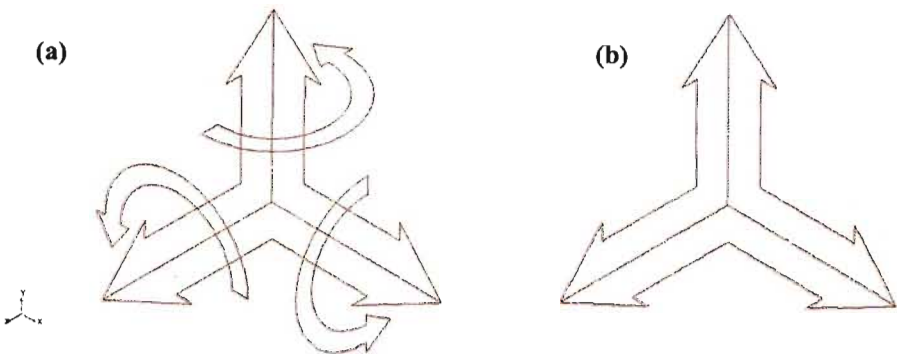


Fig. 4.44 (a) GFORCE and (b) VFORCE icons

As can be seen from **Fig. 4.44** the VFORCE is a simplified form of the GFORCE. While the VFORCE requires a force relationship to be defined along each cartesian direction vector, the GFORCE requires in addition that the rotational moment or torque relationships be defined about the cartesian direction vectors. As the form of implementation and operation of the VFORCE and GFORCE are functionally similar, only the GFORCE will be discussed further. **Fig. 4.45** shows the dialogue box for the GFORCE in ADAMS/View.

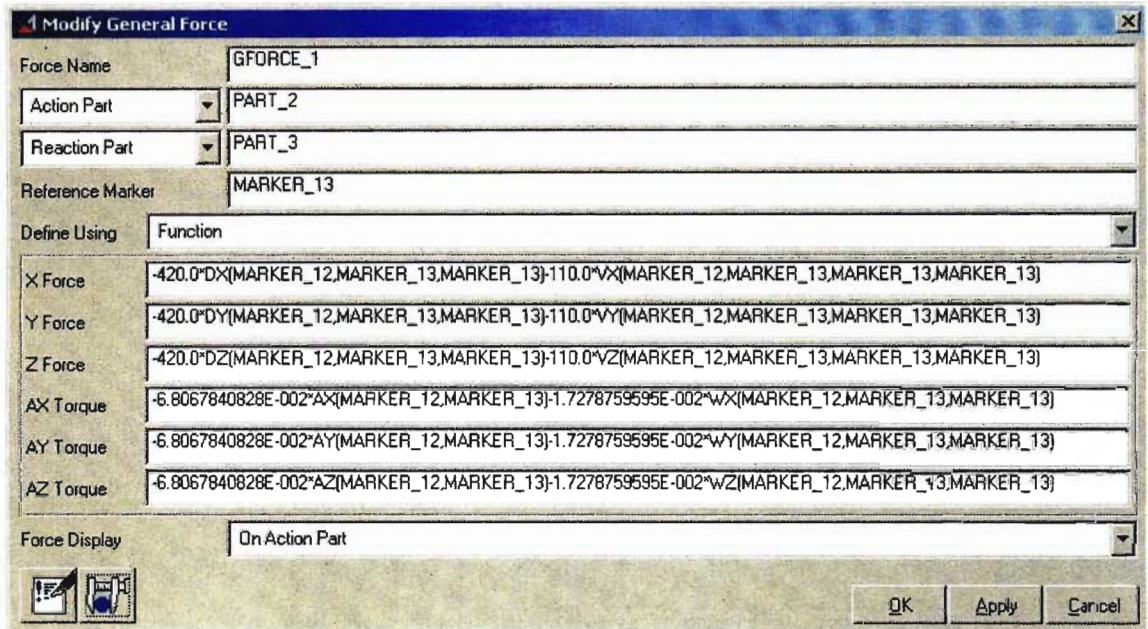


Fig. 4.45 Dialogue box for GFORCE in ADAMS/View

The dialogue box makes it intuitive to implement a GFORCE in a simple chronological manner. First the action and reaction parts are chosen; representing the two bodies between which the functional force relationship will exist. The reference marker can be any marker chosen in space within a moving or fixed frame of reference. However as the force relationship is defined according to the relative motion of the two connecting points, either one of the markers representing the connecting points of the two bodies must be chosen as the reference marker. As can be seen from the functions representing the force relationships along and about the connection marker's Cartesian direction vectors, a special syntax is used in ADAMS/View to represent the force relationship as functions of relative displacements and velocities. **Table 4.8** summarises the syntax for the ADAMS representation of the relative the relative displacements and velocities between two bodies in the translational and rotational directions. Marker1 represents the point of connection on the reaction body, Marker2 represents the point of connection on the reaction body while Marker3 is the reference marker (either Marker1 or Marker2 in this case) about which the relative displacements and velocities are measured.

Translational displacement	DX (Marker1, Marker2, Marker3)
Translational velocity	VX (Marker1, Marker2, Marker3)
Rotational displacement	AX (Marker1, Marker2, Marker3)
Rotational velocity	WX (Marker1, Marker2, Marker3)

**Table 4.8 ADAMS syntax for relative displacements and velocities
along and about the x –axis**

The syntax as represented in **Table 4.8** is specific to relative displacements and velocities along and about the x-axis. To represent the forces and torques about other axes all that is required is that DX change to DY or DX, VX change to VY or VZ etc. The marker convention as discussed above stays the same.

It can be noted from **Fig. 4.45** that the stiffness and damping values are constant. While it may be sufficient to model the force relationships with linear functions (as in the case of this project) it is possible, using the VFORCE and GFORCE constructs, to introduce non-linear stiffness and damping into the force relationships. The non-linear stiffness and damping could take the form of closed form algebraic functions of model state variables such as temperature or in this case displacement and velocity. It is also possible to use actual test data in the form of a spline to represent the functional relationship. As it is difficult to fit an algebraic model to the test data obtained from compliant suspension components, it is easier to use the actual data in the form of a spline.

In order to use a spline of the data the test data must first be imported as a spline (and given a name) via the import function from the ADAMS/View main menu bar. In order to reference a spline in any functional statement in ADAMS/View, the spline name must be called in conjunction with one of the following functions; CUBSPL (cubic spline fitting method), AKISPL (Akima fitting method) or CURVE (B-Spline fitting method). For relationships involving displacements and velocities the Akima spline fitting method is recommended [42]. The syntax for the AKISPL function is given below:-

$$\text{AKISPL (INDEP_VAR, NUM1, SPLINE_NAME, NUM2)}$$

where INDEP_VAR = the independent spline variable which would be DX (Marker1, Marker2, Marker3) for relative translational displacement or VX (...) for relative velocity etc

NUM1	=	AKISPL function modifier (default = 0)
SPLINE_NAME	=	Name of spline of test data
NUM2	=	AKISPL function modifier (default = 0)

In the complex case of using a GFORCE in order to define a force relationship between two points as a function of relative translational and rotational displacements and velocities using non-linear stiffness' and damping modelled as spline functions of displacement and damping, the syntax (along one catersian direction vector) would be:-

- [AKISPL (DX(Marker1, Marker2, Marker3), 0, SPLINE_Stiffness, 0)

* DX (Marker1, Marker2, Marker3)]

- [AKISPL (VX(Marker1, Marker2, Marker3), 0, SPLINE_Damping, 0)

* VX (Marker1, Marker2, Marker3)]

+ F0

Stiffness force

Damping force

Preload

The syntax for a similarly non-linear representation of the force relationship along and about other cartesian direction vectors would be similar in form. An important note to consider is that while it is possible to introduce non-linear effects with the G- and VFORCE constructs, it is not possible to account for the effects of frequency on the stiffness and damping using them. Frequency effects can be modelled using user written subroutines and the transfer function ADAMS construct, TFSISO (Transfer Function Single Input Single Output). The TFSISO function however is based on linear system state theory, which requires an assumption of linearity.

It is also important to note that for a displacement or velocity vector, not aligned with the primary axes of the markers used to signify the attachment points of the two bodies upon which the G- or VFORCE acts, the G- or VFORCE then reduces the displacement and velocity vector to its components along the primary axis of the reference marker. The subsequent stiffness and damping forces along each of the axes are then vectorally added to give the resultant force along the original displacement and velocity vector. Reference [19] makes the point that this is not strictly true for rubber suspension components and tends to a larger inaccuracy with increasing loads and displacements.

4.4 Modelling the Tire and Road

The tire represents one of the most important compliant components in the MBS modelling of vehicle dynamics. The forces generated at the contact patch of a tire in effect determine whether a vehicle is stable or not and whether it will follow the intended path or not. It also determines the forces transmitted to the rest of the vehicle due to the road surface. Section 2.1 discussed in some detail the behaviour of the tire, the effect of various tire parameters and the various approaches that have been adopted in modelling tires for multi-body simulation of vehicle dynamics. This section will focus on the tire model actually used in this project, its implementation and the determination of various parameters used in the tire model. In addition the modelling of the road upon which the tire travels is discussed as it forms the second half the implementation of the tire model in ADAMS.

Tire models available within the ADAMS modelling environment vary in complexity. In essence a choice must be made between a handling or durability tire model and for either, a choice must also be made between an analytical tire model or an experimental or empirical tire model. The handling tire models as the name suggests are particularly suited to the modelling of the handling characteristics of the vehicle i.e. concerned with the dynamics of the vehicle based mostly in the yaw or horizontal plane. The durability tire models are models used for the modelling of vehicle behaviour when contacting discrete road events such as potholes and bumps, and is used to investigate behaviour primarily in the vertical plane.

The further choice of experimental or analytical tire models depends on what tire data is available to the engineer and also what the focus of the model is. The experimental models are based on the results of auto-regression analysis of voluminous tire data generated from tests of specimen tires under varying conditions of key tire parameters such as load, slip and camber angle and braking and/or tractive forces. Typically this would be of the form of the Pacejka "Magic Formula" model discussed briefly in § 2.1.6. The analytical models on the other hand use basic tire properties which are then used in the analytical functions of the deformations parameters of the tire developed by the authors of the models. While the experimental models are more accurate (in some cases capturing to a very high accuracy the behaviour of the forces at the tire contact patch under specific steady state conditions), the analytical models are more general in nature. The tire model chosen thus becomes a trade-off between the above concerns. If the focus is the handling of the vehicle, then the handling tire is the most obvious, however if the higher frequency dynamics of tire-road-vehicle interaction is sought then the durability tire becomes the tire model of choice. Also the choice is impacted upon by the actual data available to the engineer. In many cases access to data from proper and exhaustive testing of the tire to be used is difficult to obtain and the engineer then has only very basic data, or the focus of the

model might be the tire itself. The focus is then, given an accepted new vehicle configuration, the broad ranging parameters that will govern the design of the new tire. In this case the analytical tire model might prove to be more useful as various parameters can be made the objects of the study. In the more “black-box” experimental models these parameters and their effects on tire behaviour are “hidden” in the fitted input-output tire curves that constitute these models.

Finally another factor affecting the choice is that some models are more, or less, accurate than others. **Table 4.9** shows the various tire models available within the ADAMS environment.

Tire Type	Data Required	Applicability
Simple equation and equivalent plane ⁽¹⁾	Basic tire properties	<ul style="list-style-type: none"> ▪ Durability analysis ▪ Pure slip
Interpolation and point follower ⁽¹⁾	Extensive tire test data	<ul style="list-style-type: none"> ▪ Handling analysis ▪ Pure slip
Fiala (default)	Basic tire properties	<ul style="list-style-type: none"> ▪ Handling analysis ▪ Comprehensive slip
University of Arizona (UA) ⁽¹⁾	Basic tire properties	<ul style="list-style-type: none"> ▪ Handling analysis ▪ Comprehensive slip
Smithers ⁽¹⁾	Coefficients from fitted tire test data	<ul style="list-style-type: none"> ▪ Handling analysis ▪ Pure slip
Delft ⁽¹⁾	Coefficients from fitted tire test data	<ul style="list-style-type: none"> ▪ Handling analysis ▪ Comprehensive slip
⁽¹⁾ Requires the purchase of the ADAMS\Tire option		


Table 4.9 Overview of the various ADAMS tire models [41]

Of the models, the University of Arizona is the most comprehensive analytical tire model available within the ADAMS environment and the Delft tire model the most comprehensive experimental model. As can be seen the use of the more sophisticated tire models requires the purchase of the ADAMS/Tire option. As this was not available within the ADAMS Full Simulation Package available to this project, the only other option was to use the default FIALA tire model. It was considered beyond the scope of this work to develop a new tire model as it would require significant effort outside the boundaries of this work and would have been a subject for research in its own right. In addition it was not possible to obtain extensive tire data from the manufacturer. The only data available was proprietary basic data provided by

Michelin [44], one of the manufacturers of the BELL EQ. ADT tires (not reproduced here in whole for secrecy restrictions), as well as data gathered from the general literature.

4.4.1 The Fiala Tire Model in ADAMS

The default ADAMS Tire model is an analytical one based on the work done by E. Fiala (1964). The model provides reasonable results for simple manoeuvres where inclination angle is neglected and the effects of longitudinal and lateral slip are considered unrelated i.e. the effect of comprehensive slip is not modelled [41]. In addition the default Fiala model does not consider the lag effects of tire dynamic reaction to step inputs of slip angle and/or longitudinal slip. Other assumptions are that the tire contact patch is rectangular and the pressure distribution is uniform across the contact patch. Despite the above shortcomings it was still considered instructive to use the Fiala model for the first approximation of the MBS model of the BELL EQ. B40C ADT and this work proceeded along this route.

Within the ADAMS/View environment, one first calls up the tire statement by depressing the tire icon  from the forces palette in the main ADAMS\View toolbar. The tire dialogue box is shown in Fig. 4.46. The various fields in the tire dialogue box are described in Table 4.10.

In order to calculate the complete wheel mass and mass moments of inertia (MOI) about the principle wheel axes a nominal construction of the cross sectional tire profile was used to create a 3-D CAD model of the tire. Using a density of hard rubber of 1190kg/m^3 the CAD model produced a calculated mass and MOI about the wheel spin axis very close to the given nominal values by the tire manufacturer [44]. With confidence that the CAD model of the tire closely resembles the actual mass inertia properties of the ADT tire, the ratio of the mass moments of inertia along the radial axes to that of the spin axis, from the 3-D CAD model, was found to be 0.62 and was thus used to calculate the mass MOI about the radial axes using the given mass MOI about the wheel spin axes from Michelin [44]. In addition a nominal hub design, fitting the general tire geometry, was also constructed as a 3-D CAD model using the density of steel (7801kg/m^3) and a nominal hub wall thickness of 20mm. This was done in the absence of data regarding the mass of the ADT wheel hub and mass MOI data. The hub mass and mass MOI thus obtained were used to determine the total wheel mass and mass MOI about the principle axes. From [45] the mass MOI of composite bodies are just the sum of the mass MOI of each body about the principle axes. Due to the symmetry of the wheel and the coincidence of the principle axes of the hub and tire, this was a simple summation. Table 4.11 details the individual and combined values of mass and mass MOI of the hub & tire wheel assembly thus calculated for use in the FIALA tire model.

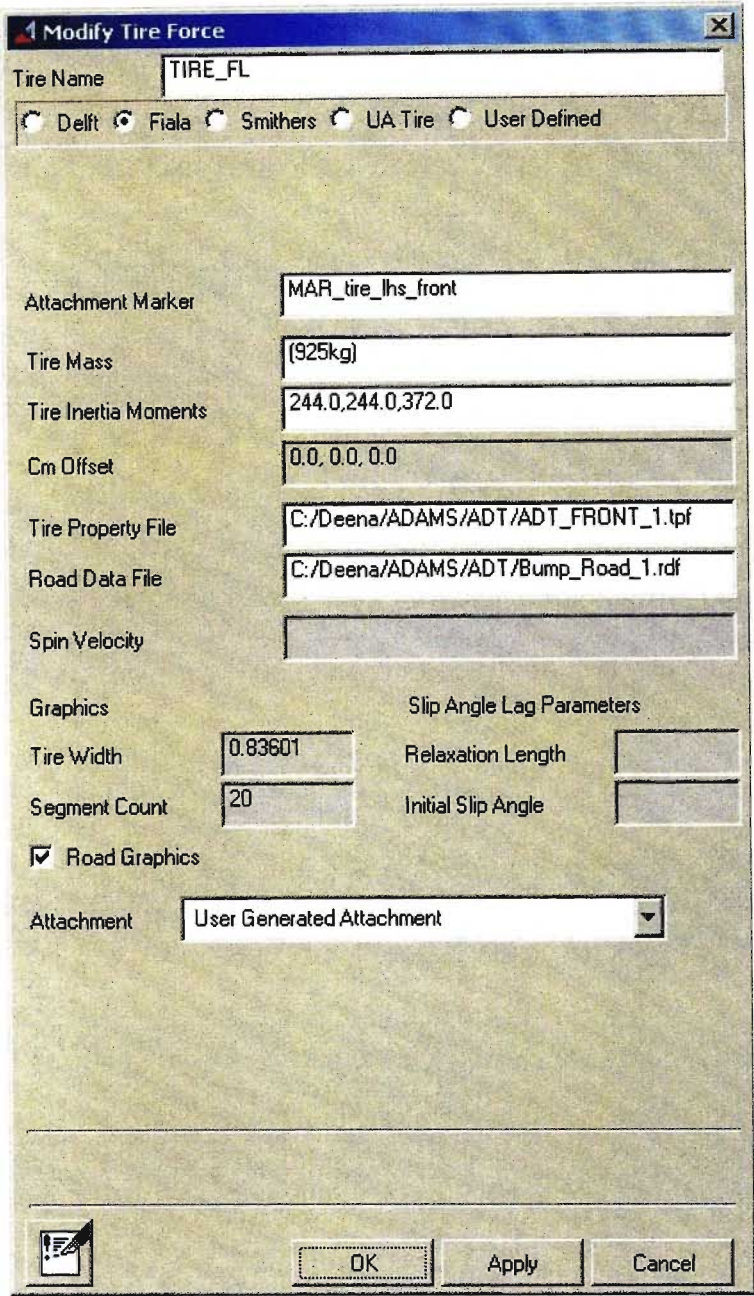


Fig. 4.46 Tire dialogue box in ADAMS/View

The heart of the tire model lies in the tire property file. **Fig. 4.47** shows a sample Fiala analytic tire property file. The tire property file is a simple text file with a specific format which can be constructed using any text editor. The file uses the exclamation mark as a comment line header. ADAMS/Solver upon reading the file ignores all comment lines. Each component of the tire property file (file extension .tpf) will be discussed in further detail along with the methodology

Field Name	Field Description	Comments
Tire Name	Tire name and tire model type selection	Only default Fiala model allowed in absence of ADAMS/Tire option
Attachment Marker	Tire attachment marker on body to which tire will be attached	Marker must have z-axis pointing in the direction of wheel spin axis
Tire Mass	Total mass of rotating wheel assembly	In this model only included mass of tire and hub. Other rotating components such as planetary gears not included
Tire Inertia Moments	Total mass moment of inertia of rotating wheel assembly about principle axes	In this model only includes mass MOI of tire and hub. Order of principal axes in the field – x,y,z with z being the spin axis
Cm Offset	Tire offset parameter in Cartesian coordinates from the tire attachment marker	Not used
Tire Property File	Path to file describing tire properties	-
Road Data File	Path to file describing road data	-
Spin Velocity	Initial spin velocity of tire	-
Tire Width	Tire width in units of length chosen for model for use in the graphic display of tire only	Has no influence on actual tire width which is given in the tire property file
Segment Count	Segments of toroid used to display default graphic of tire	-
Relaxation Length	Parameter used to model lag effects of tire response on more advanced tire models	Not applicable to default Fiala model
Initial Slip Angle	Parameter used to model lag effects of tire response on more advanced tire models	Not applicable to default Fiala model
Road Graphics	Checkbox to display the road surface as determined from road data file	Needs only be checked on one tire if all tires in model share the same road data file
Attachment	Attachment joint between tire and vehicle. Choice of user generated or default tire revolute joint	It is more practical to choose a user generated attachment and create the revolute joint relationship manually. This is so that the revolute joint is then visible and selectable by the user. This has a benefit in that one can then add motion and torques to the particular tire via the user defined revolute joint.

Table 4.10 Description of the fields in the ADAMS/View tire dialogue box

	Mass [kg]	$I_{xx}^{(1)}$ [kg.m ²]	$I_{yy}^{(1)}$ [kg.m ²]	$I_{zz}^{(2)}$ [kg.m ²]
Tire	593 ⁽³⁾	210 ⁽⁴⁾	210 ⁽⁴⁾	340 ⁽³⁾
Hub	332 ⁽⁵⁾	34 ⁽⁵⁾	34 ⁽⁵⁾	32 ⁽⁵⁾
Complete Wheel Assembly	925	244	244	372
⁽¹⁾ Wheel radial axis ⁽²⁾ Wheel spin axis ⁽³⁾ From nominal tire manufacturer data ⁽⁴⁾ Calculated as 0.62 of the nominal manufacturer data for mass MOI along spin axis ⁽⁵⁾ Calculated from 3D CAD estimation of hub				

Table 4.11 Estimation of the complete wheel assembly mass and mass MOI for the ADT Fiala tire model in ADAMS

used in calculating and obtaining representative values for each of the tire parameters in the tire property file for the BELL EQ. B40C ADT tire.

In general the analytical tire property file must proceed with the keyword MODEL and be set to “ANALYTICAL”. Ten keywords then follow, each representing key tire parameters that are used by the model to calculate the tire forces at the contact patch. For the default Fiala model available in the ADAMS full simulation package, nine keywords follow as the effects of camber angle are not modelled and hence the keyword CGAMMA can be omitted or will be ignored if included. For those keywords that require tire parameters that are not ratios but have units of measure associated with them, two arguments must be assigned to the keyword, one being the actual value of the parameter and the other being the multiplicative scaling factor that will make the parameter value consistent with the chosen units of measure being used in the ADAMS modelling environment. As all values were determined using units of measure that were consistent with the units used in the model of the ADT, (MKS – meters/ kilograms/ second) the first argument was always one

Undelected tire outside radius

The first keyword “R1” represents the parameter: undelected tire outside radius. **Fig. 4.48** details the representation of the tire geometry as used by the tire model. The value of R1 must be in a unit of length (consistent with the unit of length used in the ADAMS model). This value

was chosen to be **0.925m** as determined from the free tire diameter of 1.850m given by the manufacturer specifications of the tire [44].

```

! -----
! | TIRE_PROPERTY_FILE |
! -----

MODEL=
ANALYTICAL

! ANALYTICAL PARAMETERS BLOCK
! UNITS MKS (meters/kilograms/seconds)

! (undeflected outside tire radius)
R1
1.0 0.925

! (idealized toroidal cross section carcass radius)
R2
1.0 0.380

! (vertical stiffness at zero deflection)
CN
1.0 1140000

! (longitudinal stiffness at zero slip ratio)
CSLIP
1.0 3330

! (lateral stiffness due to slip angle at zero slip angle)
CALPHA
1.0 12000

! (lateral stiffness due to inclination angle at zero inclination
angle - not used in basic FIALA tire model)
CGAMMA
1.0 8000.0

! (rolling resistance moment coefficient)
CRR
1.0 0.01

! (radial/vertical damping ratio)
RDR
0.04

! (maximum friction coefficient, friction coefficient at zero slip)
U0
0.85

! (minimum friction coefficient, friction coefficient at full slip)
U1
0.55

```

Fig. 4.47 Example Fiala analytical tire property file

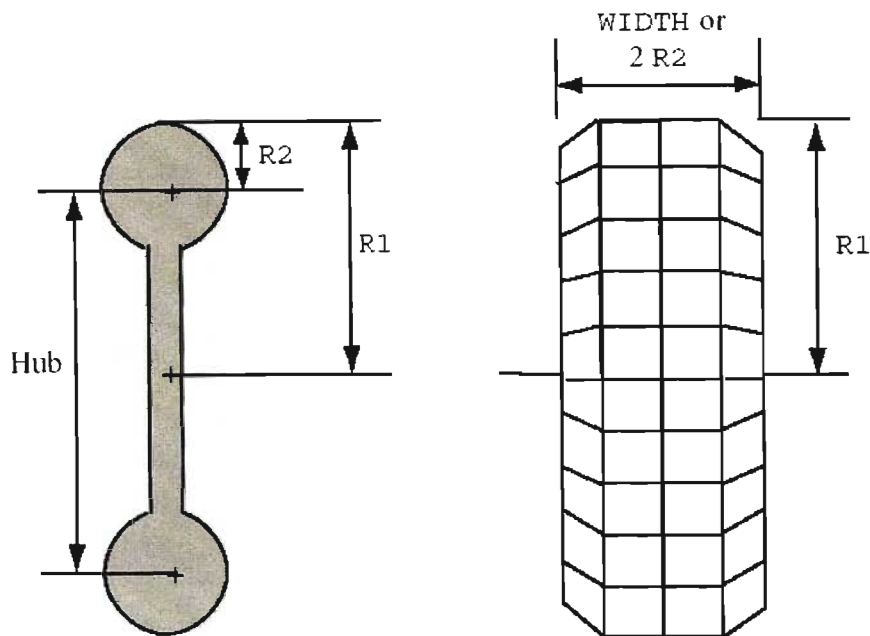


Fig. 4.48 Tire schematic showing ADAMS analytical tire property file geometry parameters [41]

Idealised tire cross-sectional toriodal radius

As depicted in **Fig 4.48**, the keyword “R2” represents half of the distance from one sidewall to the other and is in effect the carcass radius of an idealised toroidal shaped tire. The unit must be a unit of length. ADAMS may also use the value of R2 graphically to represent the width of the tire in ADAMS/View if no width argument is present in the TIRE statement (introduced in the tire dialogue box in ADAMS/View). The value used was **0.3715m** given an overall tire width of 0.743m given by the manufacturer specifications of the tire [44].

Vertical stiffness at zero deflection

This parameter is represented by the keyword “CN” and represents the partial derivative of the vertical force (F_z) with regards to the vertical penetration of the tire evaluated at zero vertical penetration. This is in essence the vertical stiffness of the tire at zero deflection. The unit of measure must be in units of stiffness force per unit deflection. It is important to note that the tire vertical stiffness is influenced by vertical load, tire pressure and the combined effect of the influence, on two different mediums (rubber compound and enclosed gas), of environmental conditions chief among them being temperature. This leads to non- linear vertical stiffness across the operating range of the tire. From the above it is seen that the Fiala model considers the contribution to the vertical force from the stiffness of the tire to be linear.

From the graphs of deflection versus load for the ADT tire available from Michelin [44] it can be seen however that the stiffness is linear or approximately linear over a large load operating range. The influence of tire pressure can also be clearly seen. Thus while the values of stiffness can be used with confidence at each load and pressure (at least within the limitations of the default Fiala model) it necessitates a recalculation and hence a new tire file for each load and pressure condition of the tire.

For the simulations to be carried out it was decided that only the unloaded condition would be investigated. From the values obtained of measurements of axle loads and operating tire pressures during the vehicle testing and measurement program carried out at BELL EQ. during August 2001 and detailed in **Table 3.3** it can be seen that the loads on all tires in the unloaded case fall very much within the linear range of vertical stiffness. It can also be seen that with the load distribution between rear and middle axles being approximately 50:50 all tires on the rear chassis can be considered to have approximately the same vertical stiffness values. Thus two vertical stiffness values were calculated from readings from the graph of deflection versus load for a front tire load of approximately 7 tonnes @ 3 bar and a rear chassis tire load of approximately 3.7 tonnes @ 3.75 bar. Interpolating between the curves and using the equation,

$$Stiffness_{vert} = \frac{\Delta LOAD}{\Delta DEFLECTION} \quad \text{in units of} \quad \left[\frac{N}{m} \right]$$

the values obtained for vertical stiffness for the ADT tires at unloaded operating conditions are shown in **Table 4.12**.

	Load [tonne]	Pressure [bar]	Stiffness [N/m]
Front Tire	7	3	957 000
Rear Tire	3.7	3.75	1 226 250

Table 4.12 Vertical stiffness values used in the Fiala tire property file used in unloaded simulations of BELL EQ. ADT

Longitudinal stiffness at zero slip ratio

This tire parameter is the partial derivative of longitudinal force (F_x) with regard to longitudinal slip (κ) at zero longitudinal slip or the tire longitudinal slip stiffness at zero longitudinal slip. It determines in conjunction with the road/tire friction parameters (sliding and static) the tractability of a tire i.e. the tires ability to withstand/transmit brake and tractive forces. This parameter is represented by the keyword “CSLIP” in the tire property file. As will be shown below this parameter must have units of force.

The longitudinal force /longitudinal slip relationship is most often represented in the literature as a μ -slip curve. A typical μ -slip curve is shown in **Fig. 2.13**. Here attention must be brought to the three distinct regimes of the μ -slip curve:-

- The slope of the curve in the low slip (approximately linear) region
- The peak value of the tractive force (at approximately 20% slip)
- The value of the tractive force at 100% slip (full sliding)

As in **Fig 2.13** most μ -slip curves are represented in a normalised form i.e. a ratio of longitudinal force to vertical load (F_x/F_z) vs. longitudinal slip ratio (κ). It is important to note however that the μ -slip curve is modified by changes in vertical load and forward velocity of the tire. Reference [15] shows in tests conducted on commercial road going heavy truck and bus tires that higher velocity tends to make the slope of the μ -slip curve in the low slip region less steeper and decreases the peak and full sliding tractive forces. The influence of vertical load on the longitudinal tractive forces, while in general acting to increase the longitudinal tractive forces with an increase in vertical load (up to an optimal load after which further increases act to reduce the tractive force), affect radial ply and bias ply tyre differently, with the radial ply tire showing a greater tendency to be influenced by the vertical load. The normalised μ -slip curves then are most often presented for rated load conditions.

Fiala determines the longitudinal tractive force as a primary function of longitudinal slip by first considering the longitudinal tractive force behaviour in two regimes based on a calculated critical slip value. The calculation of the critical slip value is presented in the [41]. Below the critical slip value the longitudinal force is just the product of the CSLIP parameter and the instantaneous longitudinal slip while above the critical slip value the longitudinal force is based on a more complex algebraic expression involving the CSLIP parameter (also detailed in [41]). In both cases tractive or braking forces are determined by the sign of the longitudinal slip parameter.

In the subsequent determination of the CSLIP parameter the absence of real tire data from the manufacturer of the BELL EQ. ADT tire regarding longitudinal tractive properties proved to be a stumbling block. It was then decided to use representative values from the available literature. Unfortunately generic or actual data for such specialised off-road heavy tires such as that used on the BELL EQ. ADT is not readily available (if at all) in the general literature. Reference [15] does however present measured values of normalised longitudinal forces for various heavy on-road commercial tires.

In the determination of the linear portion of the μ -slip curve, reference [15] presents the value of F_x/F_z at 4% slip. This was due to inaccuracies obtained in measuring at 0% slip. This however gives a good indication of the CSLIP parameter at 0% slip from the μ -slip curve. Of the largest radial ribbed tires tested (20 – 22.5 inch internal diameter by 15 inch carcass width) the values of F_x/F_z obtained at 4% slip (tested at rated load) lie in a range of 0.43 to 0.49 [15]. The rated load and pressure conditions of 60psi and 7500lb (4.1bar & 3402kg) are similar to the load and pressure conditions of that of the BELL ADT tire in an unloaded ADT state. Thus it was considered instructive to use these results to approximate the values of CSLIP to be used for the tire property file.

Thus the value of F_x at 4% slip at rated load is determined from the above as:-

$$F_x = 0.49 \times \left(3402 \text{ kg} \times 9.81 \frac{\text{m}}{\text{s}^2} \right) = 16\,353 \text{ N}$$

and the longitudinal slip stiffness at zero longitudinal slip is :-

$$\left. \frac{\partial F_x}{\partial \kappa} \right|_{\text{Slip}=0} = \frac{16\,353 \text{ N}}{0.04} = 408\,826 \text{ N}$$

Therefore **CSLIP = 408 826 N**. This was the calculated value of slip from results presented in [15] and represents a first attempt at approximating the value of CSLIP in the absence of proper tire data for the BELL EQ. ADT tire. It will be seen later however that this value had to be modified during simulation due to large forces being generated at the tire contact patch particularly during start-up conditions.

Lateral stiffness due to slip angle at zero slip angle

Tire lateral stiffness due to slip angle is defined as the partial derivative of lateral force (F_y) with regard to slip angle (α) at zero slip angle. In essence this is the tire's cornering stiffness and is represented by the parameter CALPHA in the tire property file and must have units of force per unit angle which must be consistent with the units used in the ADAMS model.

This parameter is of prime importance in the determination of the handling characteristics of a vehicle as it determines the amount of lateral force that the vehicle can resist without sliding and hence determines to a large degree the ultimate controllability of a curved-path following vehicle. While the parameter CALPHA calls for the constant slope or gradient of the lateral force (F_y) vs. side slip angle (α) graph, it is important to note that the above relationship cannot be considered linear under most driving conditions (except for very small changes in slip angle) and more so is highly dependent on vertical load (F_z) and the coefficient of friction between tire and road (μ). This is especially critical when considering the lateral load transfer across a solid axle when cornering. Due to the non-linear change in lateral force for a constant slip angle with an increase in load, the total lateral force that a pair of wheels on a solid axle is able to resist is decreased as compared to if the relationship between lateral force and vertical load were linear.

Fiala takes the above two critical affects of vertical load and coefficient of friction into account when calculating the lateral force due to slip angle. Fiala first defines a critical lateral slip value in an analytical expression involving CALPHA, F_z and μ . Below this value the lateral force (F_y) is given by a third order function of CALPHA, F_z and μ , and at and above the value of critical lateral slip, F_y is given simply by the product of sliding friction and F_z [41].

In calculating the parameter CALPHA one needs to know the lateral force generated by the tire at various constant slip angles. This data was sourced from the BELL EQ. tire supplier Michelin. In Appendix C, graphs for lateral force versus slip angle (under differing tire loads) and lateral force versus vertical load (for various slip angles) are presented [44]. The affect of vertical load on the lateral force / slip angle relationship can be clearly seen. It is also quite evident that the affect of pressure becomes significant only at extremely high tire loads. The small negative force measured at zero slip angle can most probably be attributed to conicity and/or ply steer effects. In order to calculate CALPHA the slope of the lateral force vs. slip angle curve, at zero slip angle, must be determined using those curves that most closely match the vertical loading and pressures of the tires as experienced during the testing program carried out on the BELL EQ. ADT (detailed in Chapter 3).

For the unladen condition at which the BELL EQ. ADT model was simulated in ADAMS, the front and rear tire vertical loads and pressures are presented in **Table 4.12**. Seeing as pressure has a minimal effect on the lateral force / slip angle relationship in the low vertical load and low slip angle range it was decided to use the 3.5 bar pressure curves as representative of the tire pressure conditions of both the front and rear unladen BELL ADT tires (3bar and 3.75bar respectively) and interpolate (for force vertical load) between the $F_z = 83500\text{N}$, 3.5bar curve and the $F_z = 34000\text{N}$, 3.5bar curve at 0 and 2 degrees slip angle (the curves are approximately linear within this range) to obtain the gradients (at zero slip angle) that would give a CAPLHA parameter for the front and rear unladen BELL EQ. ADT tires. The interpolated values of lateral stiffness used as the CALPHA parameter in the FIALA tire model for the front and rear unladen BELL EQ. ADT are thus given in **Table 4.13**.

	Load [tonne]	Pressure [bar]	Lat. Stiffness [N/deg]
Front Tire	7	3	10 430
Rear Tire	3.7	3.75	6 977

Table 4.13 Lateral stiffness values used in the Fiala tire property file used in unloaded simulations of BELL EQ. ADT

Tire rolling resistance moment coefficient

This parameter determines the resistance to rolling that a tire experiences and is represented by the parameter CRR in the Fiala tire property file. The magnitude of the rolling resistance moment (M_r) is calculated as the product of CRR and the vertical tire force (F_z) and results from the shift in vertical tire pressure distribution along the contact length of the tire as explained in Chapter 2. As with all the Fiala tire property file parameters, CRR must be consistent with the units used in the ADAMS model and must have units of length.

The data given in **Table 4.14** gives the rolling resistance of the BELL EQ. ADT tire for specific conditions and was available from Michelin. In **Table 4.14**, rolling resistance is represented as a ratio of vertical load (F_r). The problem lay in relating F_r to CRR which had to have units of length. **Fig. 4.49** shows a schematic representation of the parameters of a free rolling wheel which helps to explain the method used to establish this relationship. From **Fig. 4.49** it is instructive to note that F_r is a ratio of the rolling resistance force, F_x in this case, to the vertical

load (F_z) and the rolling resistance moment (M_y) is the product of F_x and the effective rolling radius R_e .

MICHELIN 29.5 R25 XADN 200B		
RIM : 29 X 25.00 / 3.5"		
LOAD [kg]	SPEED [km/h]	Fr (± 0.2) [kg/tonne]
11200	10	14.52
11200	20	12.21
11200 ⁽⁵⁾	30 ⁽⁵⁾	11.56 ⁽⁵⁾
14000	10	12.38
14000	20	11.46
⁽¹⁾ Fr = longitudinal tire force resisting motion as a ratio of vertical load		
⁽²⁾ Test conducted at cold tire pressure of 4.5 bar		
⁽³⁾ Measurement began when tire temperature had stabilised		
⁽⁴⁾ Pressure was not regulated during the test		
⁽⁵⁾ Load condition used in calculation of representative value of CRR		

Table 4.14 Rolling resistance data of the Michelin BELL EQ. ADT as obtained from Michelin [44]

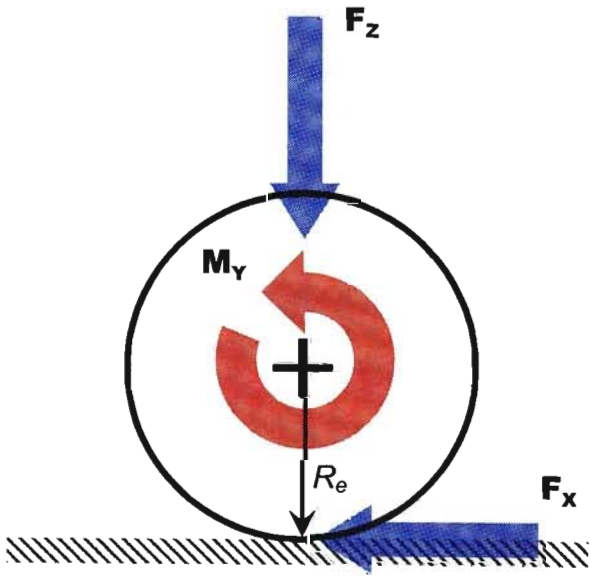


Fig. 4.49 Schematic representation of the parameters of a free rolling wheel used to establish the CRR parameter in the Fiala tire property file

The rolling resistance force determined from the rolling resistance ratio (F_r) given by Michelin in **Table 4.14** is :-

$$F_x = F_r \times F_z$$

The rolling resistance torque is calculated as follows [41] :-

$$M_y = CRR \times F_z$$

In order to calculate CRR, it was necessary to relate rolling resistance torque (M_y) to rolling resistance force (F_x). To do this the effective rolling radius (R_e) is required. Thus :-

$$\begin{aligned} M_y &= F_x \times R_e \\ CRR \times F_z &= (F_r \times F_z) \times R_e \\ CRR &= F_r \times R_e \end{aligned}$$

With data only available for higher loads as well as a higher pressure than for the unladen BELL EQ. ADT tested, the following calculation using the load condition indicated in **Table 4.14** serves to show the influence of the CRR parameter.

At a load of 11 200kg and 4.5 bar the deflection from the Michelin tire deflection chart [44] is 0.090m. This produces an effective rolling radius (R_e) of **0.835m**, given a free tire radius of 0.925m [44]. For this loading condition and at a vehicle speed of 30km/h, the rolling resistance coefficient given from **Table 4.14** is $\left(\frac{0.0097}{0.01} \right)$.

Thus for the above loading condition CRR is calculated to be 0.0097. CRR does not vary much from a value of 0.01 for all the values of (F_r) and loading conditions presented in **Table 4.14**. Even though the range of conditions for which rolling resistance data is available is limited CRR is unlikely to vary much from a nominal value of 0.01. Increased speed (up to about 55km/h) and decreased pressure (down to 3bar) would serve to increase the rolling resistance value but this would be offset by the lower loads experienced on the tire in the unladen ADT condition which would serve to decrease the rolling resistance. This in addition to the fact that the rolling resistance represents only 1 % of the vertical load on the tire resulted in the value of 0.01 being adopted for use as the CRR parameter in the Fiala tire property file.

Tire radial damping ratio

The radial damping ratio of the tire (ζ) is represented by the parameter RDR in the Fiala tire property file. This parameter is the ratio of tire damping to critical damping where a value of zero indicates no damping, a value of one indicates critical damping and a value greater than one indicates over-damping [41]. RDR is a ratio and hence has no units.

The parameter RDR is used in the determination of the vertical force (F_z) of the tire. Unfortunately no experimental data was available, neither from a tire supplier nor from the general literature for the specific type of tire used by the BELL EQ. ADT. Reference [52] however presents an analytical method of determining the tire damping from knowing the rolling resistance coefficient. As rolling resistance data was available from Michelin for the BELL EQ. ADT tire (albeit in a small tire load and speed range) it was decided to explore this method to arrive at an approximation for the vertical damping ratio that was representative of the BELL EQ. ADT tire.

The development of the analytic equations relating rolling resistance to vertical damping is left to the author of reference [52]. A section of reference [52] detailing the development of the equations to follow is however reproduced in Appendix D. The following key relationships result from the discussion reproduced in Appendix D. For the sake of clarity the nomenclature used in [52] is maintained in the following discussion in reference to tire parameters and differs in certain instances to that used in the rest of this dissertation :-

The author [52] begins by relating a rolling resistance force to vertical force via a rolling resistance coefficient as we know from the discussion on rolling resistance above.

Thus:-

$$F_r = A_r \times F_z$$

Developing integrations constructed from kinematic relationships of a rolling tire he arrives at the following analytical expressions:-

$$F_r \cong K \times \left(\frac{a}{r_f} \right)^2$$

and

$$k = \frac{(2 \times K)}{r \times \Omega}$$

where,

F_r	=	Rolling resistance force at the contact patch directed rearward
A_r	=	Rolling resistance coefficient
F_z	=	Vertical force acting on tire
K	=	Radially directed coulomb frictional force on tire per unit angle of revolution
$2 \cdot a$	=	Tire longitudinal contact patch length
r_f	=	Free tire radius
k	=	Tire damping coefficient
r	=	Axle height or tire deflected radius
Ω	=	Tire rotational velocity

In addition, to relate the damping coefficient thus determined to a damping ratio, the classical 1-degree of freedom spring-mass-damper system analytical relationship was assumed:-

$$\zeta = \frac{c}{(2 \times m) \times \omega}$$

where,

ζ	=	Damping ratio
c	=	Damping coefficient
m	=	Mass
ω	=	System natural frequency given by $\sqrt{k/m}$, where k = system stiffness and m = system mass

Rearranging the above expressions we arrive at the following for the damping ratio of a tire developed from the rolling resistance:-

$$\zeta = \frac{2 \left[F_r \times \left(\frac{r_f}{a} \right)^2 \right]}{(2 \times m) \times \sqrt{k/m}} \times [r \times \Omega]$$

The damping ratios calculated using the above derived expression and utilising the rolling resistance data available from Michelin for the specific tire loading and pressure conditions in **Table 4.14** are shown in **Table 4.15** below.

BELL ADT TIRE DAMPING RATIO CALULATION					
Tire vertical load [kg] ⁽¹⁾	11200	11200	11200	14000	14000
Cold tire pressure [bar] ⁽¹⁾	4.5	4.5	4.5	4.5	4.5
Tire velocity [km/h] ⁽¹⁾	10	20	30	10	20
Rolling resistance coefficient ⁽¹⁾	0.01452	0.01221	0.01156	0.01238	0.01146
Tire mass [kg] ⁽²⁾	925	925	925	925	925
Tire stiffness [N/m] ⁽³⁾	1308000	1308000	1308000	1635000	1635000
Rolling resistance force [N]	1595.341	1341.537	1270.120	1700.269	1573.916
Contact length [m] ⁽⁴⁾	0.540	0.540	0.607	0.607	0.607
Free tire radius [m] ⁽⁵⁾	0.925	0.925	0.925	0.925	0.925
Tire deflection [m] ⁽⁶⁾	0.090	0.090	0.090	0.108	0.108
Tire deflected radius [m]	0.835	0.835	0.835	0.818	0.818
Tire rotational velocity [rad/s]	3.327	6.653	9.980	3.398	6.796
Damping ratio (ζ)	0.194	0.081	0.041	0.146	0.068
⁽¹⁾ Load conditions for rolling resistance data supplied by Michelin (presented in Table 4.14)					
⁽²⁾ Total estimated mass of wheel assembly (tire plus rim) as detailed in Section 4.1., Table 4.11					
⁽³⁾ Calculated from readings off tire load-deflection graph from [44]					
⁽⁴⁾ Calculated from readings off tire load / contact patch length graph [44]					
⁽⁵⁾ Michelin tire spec sheet [44]					
⁽⁶⁾ Michelin tire load-deflection graph [44]					

Table 4.15 Damping ratios calculated from rolling resistance data supplied by Michelin and using damping ratio formula developed from reference [52]

Some restrictions must be noted in the acceptance of the above results. Firstly the tire loading and operating physical parameter choice (pressure / temperature) was assumed to be constant and as would be measured under static and cold conditions i.e. the load was taken to be the

static vertical tire load and the tire pressure indicated is the cold tire pressure. Michelin specifically state in the results presented (**Table 4.14**) that the rolling resistance tests were conducted after sufficient time had elapsed to ensure stabilised tire temperature. It is thus fair to assume that the tire pressures would then not have been that as measured cold. These two parameters (vertical load and pressure) would in turn affect other parameters such as vertical tire deflection, tire rotational velocity as well as contact patch length. The assumption is that these variations would be sufficiently small so as not to substantially influence the damping ratios calculated above.

Another concern would be the validity of the application of the formulas derived in [52] to determine the damping coefficient and the subsequent use of the classical 1-degree of freedom damping ratio calculation. A unit check performed on the final expression for damping ratio presented above, produced an unaccounted for radian squared unit of measure. As a radian is a dimensionless unit this was not considered indicative of an incorrect formula derivation. It must be stated though that no application of the above argument in deriving the formula for tire damping ratio from tire rolling resistance data was encountered in the literature available.

In summary though this approach led to values expected of the inherent damping of tires. Reference [74] indicates that a fair value to assume for the damping ratio of a rolling tire in general is of the order 10^{-2} as rolling tires have inherently low damping. Except for the very low speeds, the values obtained for damping ratio in **Table 4.15** above are of the order of 10^{-2} . The values of damping ratio calculated above however were calculated for those operating conditions that lie outside of the range of loading conditions experienced by the tires on an unladen BELL EQ. B40C ADT. Assuming a fairly constant rolling resistance co-efficient across the load range (of approximately an order of 2×10^{-2}) it would be fair to assume that at significantly lower tire vertical static loads (as experienced on the unladen BELL EQ ADT) the resultant rolling resistance force would be much lower and hence the damping ratio would be lower however the substantially decreased contact patch length at low vertical tire loads serves to counteract this expected decrease. Increasing speed also has a significant affect on the damping ratio calculation seeking to decrease the tire damping (as is also evident from the results presented in **Table 4.15**). Further calculations (assuming a fairly constant rolling resistance coefficient of the order of 2×10^{-2}) at a vehicle translational speed of 50km/h and under the tire load conditions of the unladen BELL EQ. ADT reveal that the damping ratio still remains of the order of 10^{-2} . Thus it was considered useful to use a **damping ratio parameter (RDR)** of **0.05** in both the front and rear tire property files for the simulations of the unladen BELL EQ. ADT simulations.

Maximum & minimum friction coefficient

The maximum and minimum friction coefficients (μ_{\max} & μ_{\min}) are represented by the parameters U0 and U1 respectively in the Fiala tire property file. They are used to determine the changing frictional coefficient as detailed below.

The maximum friction parameter is the theoretical maximum frictional coefficient of the tire-road interface at zero slip and represents the static friction coefficient. This is however is an unobtainable maximum as the there is always some slip within the tire footprint and hence is used in conjunction with the minimum friction coefficient which is the friction coefficient of the tire road interface at 100% slip or pure sliding. The exact frictional coefficient (μ) at any time is thus given by the linear relationship [41] :-

$$U(S_{s\alpha\gamma}) = U_0 - (U_0 - U_1) \times S_{s\alpha\gamma}$$

and as explained graphically in **Fig. 4.50** below.

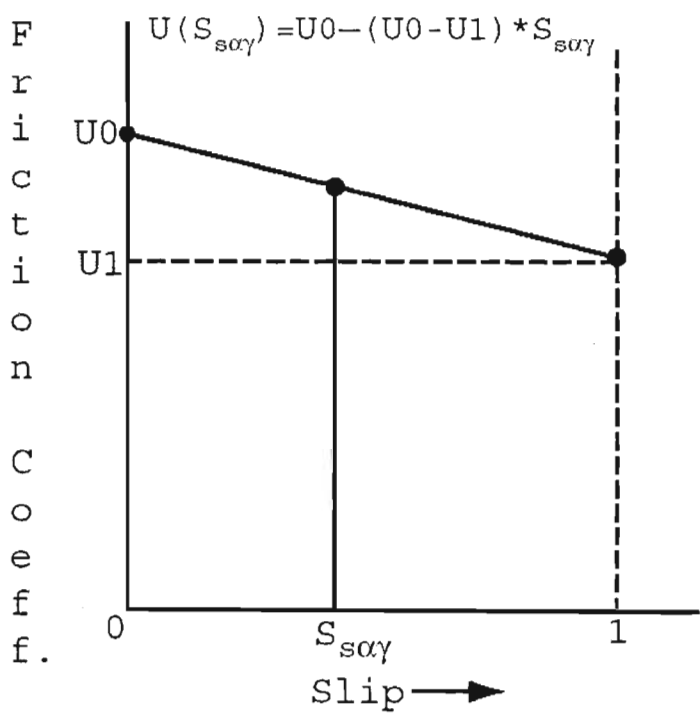


Fig. 4.50 Graphical representation of the calculation of the frictional coefficient in the FIALA tire model [41]

The parameter $S_{s\alpha\gamma}$ is the resultant slip ratio resulting from the combined effect of longitudinal slip ratio, slip angle and inclination angle (or comprehensive slip) conditions existing at the time. A detailed kinematical description of the calculation of this parameter is given in [41]. While other analytical models available within ADAMS allow for different frictional

coefficients in the longitudinal and lateral directions the Fiala model only allows for a single frictional coefficient valid for all directions of sliding. In addition it must be noted that the default Fiala tire model does not cater for comprehensive slip and does not consider the affects of inclination angle on the resultant lateral force or tire slip at the contact patch.

The frictional coefficients vary with many parameters – rubber compound, road surface material, road surface micro and macro roughness, road surface moisture level, tire tread as well as vehicle speed, tire pressure and surface temperature – in short a myriad of parameters. Even though semi-empirical testing of various combinations of materials have resulted in average or approximate values of frictional coefficients the determination of frictional coefficients would still require testing of in this case the tires to be used over the various surfaces to be simulated. As this test data was not available from the tire suppliers of the BELL EQ. ADT, available values from the general literature had to be used. Tire data for the type of tire used by the BELL ADT is not widely reported upon in the general literature however and here again it was decided to use data available from tests carried out on road going heavy commercial truck tires. **Table 4.16** tabulates average frictional coefficient data presented in [15] for heavy commercial road going truck tires.

Heavy duty commercial truck 20 inch radial tires		
Translational speed [miles/h]	Peak frictional coefficient [μ_{max}]	Sliding frictional coefficient [μ_{min}]
20	0.85	0.63
40	0.85	0.5
55	0.85	0.48

Table 4.16 Peak and sliding frictional coefficient data for heavy-duty road going commercial truck tires on dry concrete surfaces [15]

Depending on the speed to at which the simulations are to be carried out the parameters U_0 and U_1 can be set to those values which are applicable from **Table 4.16**.

4.4.2 The Road Model in ADAMS

The road or terrain model is the second constituent of the tire model in ADAMS that acts to determine the forces and moments generated at the contact patch. In essence the road model provides geometrical and frictional information to the tire about the terrain that the vehicle is traversing. The frictional information is used primarily to determine the slip state of the tire and the geometrical information provides a reference point for the deformable tire both of which allow the tire model to develop the forces being generated at the contact patch by the continually flexing and slipping tire.

The road model is similar in terms of intent to the role of a mesh in a finite element method (FEM) package; it provides a discrete representation of a continuous surface (surface and volume in FEM models). In fact a key approach to constructing a road model of a complex three dimensional road surface would be the use of a FEM meshing tool. As in the construction of a surface mesh in a FEM package, nodal points on the surface need to be defined and then the connectivity of the nodes needs to be established such that a series of adjacent, discrete patches or planes are created to approximate the three dimensional curvature of the surface. It follows then that the finer the mesh the more accurate the reproduction of the road surface, however it must be noted that this trend is offset by the subsequently increasing computational time in determining tire road contact forces.

Represented in **Fig. 4.51** is a sample of a nodal mesh representation of an ADAMS terrain representation. As can be seen there are six nodes that in turn define 4 discrete patches. In ADAMS the road patches or elements must be triangular. Each of the nodes will be defined by their x, y & z coordinates in the ADAMS global coordinate system. Connectivity is established to define each element such that for example in **Fig. 4.51** element A is created by the connectivity of nodes 1-2-3, while element D is created by the connectivity of nodes 3-5-6. The unit normal (\hat{U}_A , \hat{U}_B etc. in **Fig 4.51**) establishes the orientation of the surface to the tire with the unit normal vector for each element pointing toward the centre of the tire. As will be seen in the subsequent discussion of the road data file each element can have a unique frictional property associated with it. ADAMS uses a complex road-tire contact algorithm (explained in detail in [41]) to determine the contact of the tire with each element. Important is that the algorithm can detect no more than two simultaneous element contacts. Should more than two element contacts be detected, the rest are discarded with no weighting towards any particular element. This could mean that more important tire-element contacts are discarded while trivial contacts are accepted. It is thus important to avoid tires traversing areas, or avoid building such road models, as in the area around node three in **Fig. 4.51** where four elements converge.

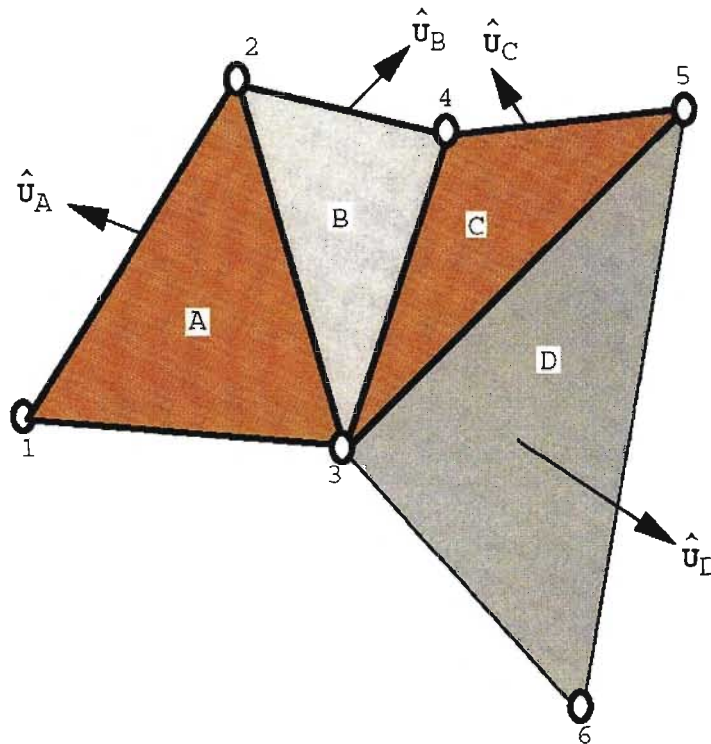


Fig. 4.51 Road terrain model as represented in ADAMS [41]

In order to implement the road model use is made of the road data file. This is the file (similar in function to the tire property file) that the ADAMS tire model calls upon in determining the tire forces at the contact patch. **Fig. 4.52** is an example of a road data file, the default flat road data file that consists of two large triangular elements forming a rectangular road surface. As with the ADAMS tire property file the road data file must follow a specific file convention, which can be edited with a normal text editor and consists of several keywords or parameters to which information is assigned in a particular format. The file proceeds with the keyword **METHOD** which must be set to “GENDATA”. This informs the ADAMS/Solver that the file provides information about the road in the general road profile format. The keywords that follow are detailed below.

X_SCALE, Y_SCALE, Z_SCALE

These keywords provide a convenient method of scaling the x-y-z coordinates of the road node points to be consistent with the units used in the ADAMS modelling environment or to scale the road by some specified amount. After multiplication by the scaling factor the coordinates of the nodes are assumed to be at distances consistent with the units of length in the ADAMS modelling environment.

```
! -----
! |          ROAD DATA FILE          |
! -----
!
METHOD
GENDATA
!
!   Conversion factors
!
X_SCALE
1.0
Y_SCALE
1.0
Z_SCALE
1.0
!
!Road origin is located at the following global coordinates in the
!data set.
!
ORIGIN
-10000 0 -250000
!
!Road coordinate system is oriented with respect to the global origin
!by the following transformation matrix.
!
ORIENTATION
1 0 0
0 0 1
0 1 0
!
!Coordinates for the node points on road
!
NODES
4
1 0.0 500000.0 0.0
2 0.0 0.0 0.0
3 500000.0 0.0 0.0
4 500000.0 500000.0 0.0
!
!Connectivity of node points defining the triangular element
!
ELEMENTS
2
1 2 3 0.95 0.7
1 3 4 0.95 0.7
```

Fig. 4.52 Example of a road data file in ADAMS

ORIGIN

This keyword defines the Cartesian coordinate displacement of the road profile origin to the global coordinate system origin. Here again the values are multiplied by the scaling factors in the x-y-z coordinate directions and after multiplication must be in units consistent with that in the ADAMS modelling environment.

ORIENTATION

The orientation keyword is used to orientate the road data file to the global coordinate system axes in the ADAMS modelling environment should the file have been constructed for a differently orientated road profile. A 3 x 3 matrix of real numbers is assigned to the ORIENTATION keyword. This can be used to rotate the road by a specific angle about the x, y and z axes, or swap axes under the assumption that the nodal Cartesian information as represented under the NODE keyword (to be introduced below) is in the order of x- then y- then z-coordinates. The identity 3 x 3 matrix (default if this keyword is not specified in the road data file) will not rotate the road profile and causes the road to be co-orientated with the global coordinate system in the ADAMS modelling environment.

NODES

This keyword is used to define the position of each node in the road profile triangular mesh. The input or assignment of data to this keyword follows the following format. In the line immediately after the keyword an integer value indicates the exact number of nodes in the mesh of the road profile. In the line immediately after that, four entries follow on the same line separated by a space. The first entry is a unique integer that identifies a specific node and the remaining three entries are real numbers that represent the x-y-z coordinates (in that order) of the node in question. Similarly the line immediately after that follows the definition in space of the second node and so on until all nodes are defined.

ELEMENTS

This keyword is used to define the connectivity of the nodes to determine individual triangular elements that constitute the triangular mesh of the road surface as well as the frictional properties of each element. In the line immediately after the keyword, follows an integer value of the number of elements. The following line has five entries each separated by a space. The first three entries are the three nodes that connect to define a unique triangular element, the fourth entry is the a real number representing the road/tire coefficient of friction under zero slip conditions and the fifth entry on the line is the tire/road coefficient of friction under full slip conditions. Each subsequent line then defines, in the above way, each element and individual element frictional properties. It will be recalled that the tire property file also has assigned in it, the frictional coefficients. The final static and sliding frictional coefficient for each element is the product of the static and sliding coefficients in the tire property file and the road data file. Thus the frictional coefficients can be defined either for the tire or road and depends on whichever is more convenient for a particular application. Additionally the advantage is that the road can be made to have different frictional properties for each element. If the frictional

properties are set in the tire property file (as in the case of this work) the frictional parameters under the ELEMENTS keyword in the road data file must be set to 1.0 and vice versa.

4.4.3 Discussion of the Various Methods of Constructing ADAMS Road Data Files

While the default road would be sufficient for the many common vehicle dynamics tests, additionally various terrain profiles may be needed to simulate vehicle dynamics with large scale terrain input. Such tests would include large scale (of the order of magnitude of the vehicle dimensions) sinusoidal and offset sinusoidal terrain undulations and the traversing of large obstacles to determine the shock-input behaviour of vehicle suspension systems. Additionally tests conducted on specific vehicle tracks with finite changes in elevation over the course and banked sections would require a triangular element mesh that would be difficult if not impossible to create manually. Toward this end the power of the meshing algorithms of finite element analysis packages can be used. The geometry of the terrain should be modelled in three dimensional modelling applications and this then exported in a compatible format to a finite element analysis package. The mesh node-element files can then be exported as a text file and the node-element relationship arrays can then be copied and pasted into an ADAMS road data file.

This was successfully accomplished for various irregular terrain examples (sinusoidal and continuously varying banked road sections) to prove this methodology. These were however not used in any full vehicle simulation with the BELL EQ. ADT model. A drawback of the method though was that in some instances especially around sharper changes in terrain profile but also occasionally in relatively flat planes, too many elements were created. This will have the effect (as discussed above) of causing the ADAMS tire to traverse sections where the tire patch was in contact with many triangular elements simultaneously, causing suboptimal element patches to be selected for the contact point calculation and slowing down the overall simulation considerably. It is obvious that a more intimate knowledge of three dimensional object meshing would need to be developed to work around this drawback.

In the case of this project, two non-flat terrain surfaces were considered for the purposes of simulation (arising from the actual physical tests conducted on the BELL EQ. ADT), a single bump and the BELL EQ. test track in Richards Bay, Kwa-Zulu Natal South Africa. The road data file to represent a single bump was meant to replicate the bump test as conducted on the actual vehicle and as described in § 3.1.4. The three dimensional road profile with the trapezoidal cross-sectional obstacle running along the width of the track and perpendicular to the oncoming vehicle was recreated by calculating using simple geometry and trigonometry, the points of the obstacle at its corners, from the cross sectional dimensions of the obstacle used in

the actual tests of the ADT. Thus the node positions in 3-dimensional space were obtained and each individual plane so formed was divided into two triangular elements.

As will be discussed later this method was abandoned as the simulation could not proceed beyond the first impact with the bump due to the sharp discontinuities in the bump profile. Thus a “smoother” bump was attempted by recreating a bump that had the same height dimension but with a smoother change in profile from flat road to maximum obstacle height using the 3-D modelling package SolidEdge® and meshing the 3-dimensional geometry in MSC/ NASTRAN®. These two road data files are reproduced in Appendix E-1 & E-2.

The most interesting challenge arising from defining a road terrain profile for simulation was presented by the construction of the BELL EQ. test track as a road data file in ADAMS/View. To attempt this, an accurate representation of the surface of the test track with changes in elevation and camber was needed. Thus an outside contractor was employed by BELL EQ. to survey the track. The drawings were presented as a scaled AutoCAD® file [84] which represented the track as a plan view contour map and as a cross-sectional elevation profile at chainage intervals perpendicular to the track centreline every 5 meters. From the plan view it was possible with some effort to establish the x-y coordinates (horizontal plane) of the track centreline, the track inner and outer perimeter at each 5 meter interval. To determine the elevation (z-coordinate) of the track centreline and the perimeter points (inner and outside track points viewed in cross section) it is first instructive to present a sample of the cross sectional elevation as presented by [84].

Fig. 4.53 represents a sample illustration of the scaled cross sectional track elevation drawing at each 5 meter chainage length along the track from [84]. The black curve in **Fig. 4.53** represents the actual cross sectional elevation profile. While most of the cross sectional profiles were linear some (as shown in **Fig 4.53**) depict a non linear variation in elevation across the width of the track. A first attempt at representing the three dimensional surface as an ADAMS road data file involved accurately capturing the x-y-z coordinates of each inside, center and outside points of the track along each 5m chainage interval. Thus with three, three-dimensional curves (inside track perimeter, track centreline and outside track perimeter) an attempt was made to reproduce the three-dimensional track surface by a surface extrusion-lofting process in a three-dimensional modelling package and then to mesh the resultant surface in a FEM modelling package. This was not however possible as the solid modelling package available to the project, SolidEdge®, was incapable of performing the procedure of generating the surface from the three curves. While this was later proven to be possible using a high end commercial version of the three dimensional modelling CAD package CATIA V5®, it was too late within the project timeframe

to then proceed with this method. For future reference however this methodology is noted to be indeed workable.

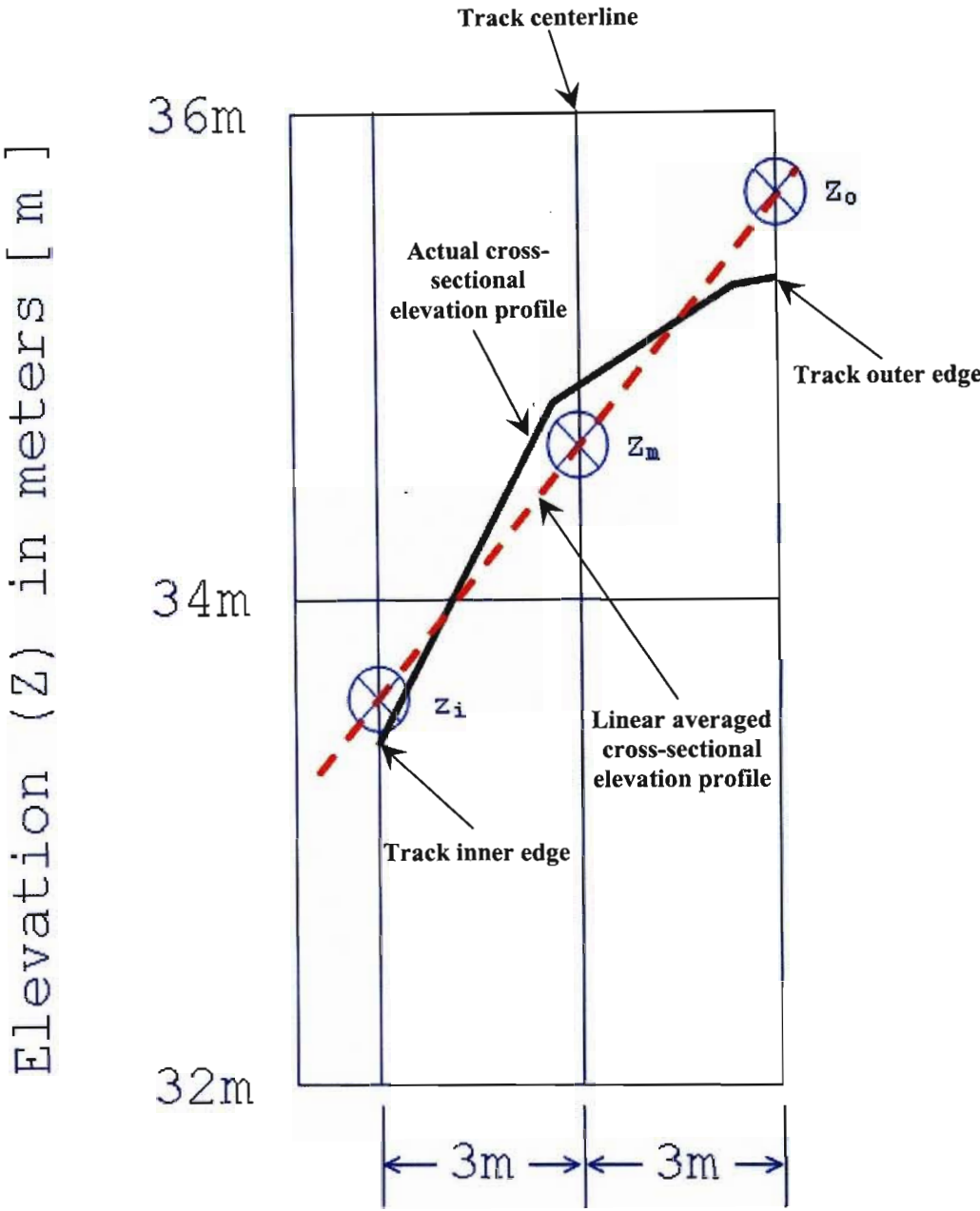


Fig. 4.53 Example of a cross-sectional track elevation profile along 5m chainage intervals perpendicular to the track centerline of BELL EQ. test track (from [84])

Thus in order to continue with the reproduction of the BELL EQ. test track as an ADAMS road data file a simplified approach was adopted. Reference [68] suggested that if the x-y-z coordinates of the track centerline, along with the camber angle and the track width at each centreline point respectively, were known then it would be possible to recreate the test track with an average camber angle at each centreline point. The method according to [68] was that

given the above information, the inner and outer track perimeter coordinates on the perpendicular to the centerline at each discrete centerline point could be calculated as follows:-

$$x_{inner} = x_{center} - [\sin(\alpha) \times (\text{track_width} / 2)]$$

$$x_{outer} = x_{center} + [\sin(\alpha) \times (\text{track_width} / 2)]$$

$$y_{inner} = y_{center} + [\cos(\alpha) \times (\text{track_width} / 2)]$$

$$y_{outer} = y_{center} - [\cos(\alpha) \times (\text{track_width} / 2)]$$

$$z_{inner} = z_{center} - [\sin(\text{camber_angle}) \times (\text{track_width} / 2)]$$

$$z_{outer} = z_{center} + [\sin(\text{camber_angle}) \times (\text{track_width} / 2)]$$

where,

α	=	Angle of tangent to track centerline at each discrete point in the horizontal plane (plan view)
track_width	=	Track width at each discrete centerline point respectively
camber_angle	=	Cross-sectional camber angle perpendicular to track at each discrete centerline point respectively

In order to simplify the process a linear averaged approximation of the change in cross sectional elevation (red dashed line in **Fig. 4.53**) was introduced with it intersecting the actual elevation change curves at approximate points where the BELL EQ. B40C ADT would have travelled along the track. This assumption of approximate wheel contact points on the cross sectional track profile was made due to the fact that the test was conducted by marking the centreline of the BELL EQ. test track and the test driver attempting to keep the centre of the nose of the truck along this centreline during the actual physical testing and the fact that the BELL EQ. B40C ADT has a track of approximately 3.4m. In addition this was carried out for a chainage interval of 10m rather than every 5m thus reducing the points that needed to be calculated by a factor of 2. Thus new centerline z-elevation coordinates were scaled off the drawing from point z_m in **Fig. 4.53** at each 10m chainage interval. Determining the new track inner (z_i) and track outer (z_o) cross-sectional elevations (also by scaling) allowed an “average” camber angle to be calculated for each track cross section at 10m intervals. The average track width was also calculated to be a constant 6.02 m to simplify further calculations. The range of deviation of the actual track width around the track was approximately $\pm 0.04\text{m}$.

The x-y-z coordinates of the track centerline established from the plan view and the cross-sectional elevations as discussed above, were then modified so as to coincide with the global (0,0,0) position of the ADAMS model. This was done by making the center of the track at the 620m chainage interval coincident with the global (0,0,0) reference position of the ADAMS ADT model. The 620m point was chosen as the ADAMS model reference point due to it being the approximate point where all physical tests involving lapping of the BELL EQ. test track were started and ended.

With the x-y-z coordinates of the centerline of the BELL EQ. test track in the global coordinate reference system of the ADAMS ADT model, the camber angle and track width now established it was possible to create points on the inner and outer perimeter of the test track at every 10m chainage interval as indicated by [68] and discussed above. Using these points as nodes it was then possible to create a triangular mesh as required by the ADAMS road data file. **Fig. 4.54** shows a plan view of the triangular mesh of the test track. The road data file representing the BELL EQ. test track is reproduced in Appendix E-3.

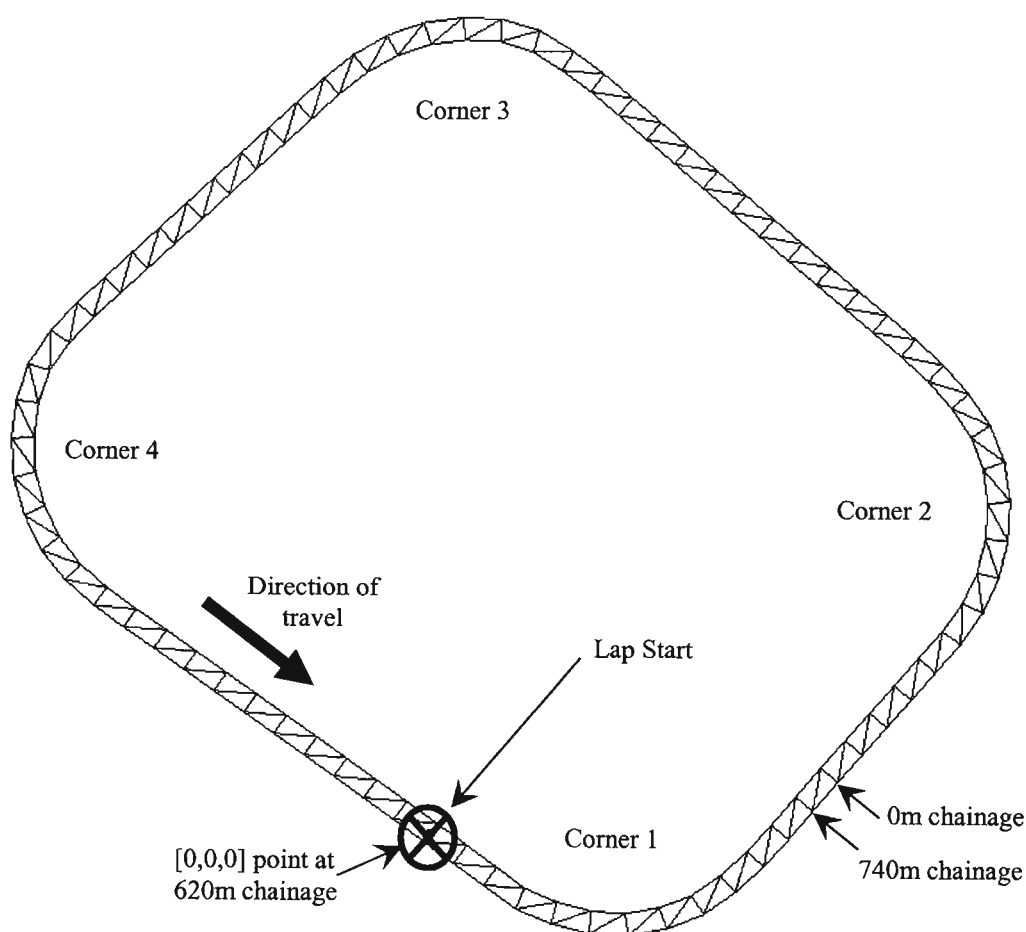


Fig. 4.54 Visual representation in plan view of the triangular mesh of the BELL EQ. test track as contained in the ADAMS road data file

4.5 Dynamic Controllers

In order for a vehicle model to be useful it must be able to simulate controlled and uncontrolled manoeuvres such as those the actual vehicle would be expected to undergo in reality. Controlled manoeuvres would involve a human driver in the loop for such scenarios such as path following while uncontrolled manoeuvres would be the vehicles response to a sudden change in input, for example a sudden steering input. The former would for example give indication of the controllability of the vehicle and the latter the inherent stability of the vehicle. As the primary aim of this project was to provide a validated vehicle model that correlated well to physical tests, the question of what to control and how to control was informed by the need to reproduce the manoeuvres conducted during physical testing in the ADAMS model of the BELL EQ. ADT.

In answering the question of what to control, it was quite obvious for the purposes of this project that the vehicle velocity and vehicle steering had to be controlled to enable a comparison of the ADAMS model to the physical tests conducted on the ADT. The question of how to control the above two parameters provoked a more serious interrogation of the stated aims of this project.

If one were to consider the human driver as the centre of the man-machine interface, as one must, control of the system then rests with the driver. The driver as controller of the system, with the aim of controlling speed and direction of the vehicle, has as inputs, steering angle and steering rate and throttle and brake position. The complexities of the control systems to translate those inputs into force actuators that accurately represent the real system (the actual physical vehicle being modelled) are high. Ultimately this would be the ideal solution to be aimed for. For example, performing a yet to be physically tested manoeuvre with a model might prove to require a steering rate of change too high for a human driver to reproduce. Unless the steering forces were related to a required rate of change of steer wheel angle, via a steering control system, the realisability of such a manoeuvre would be difficult to quantify. Also by way of another example, linking the force required to maintain a maximum cornering speed to actual torque at the wheels gives a better indication of the stability of a vehicle. A vehicle being “towed” around a corner at its maximum cornering speed has different stability characteristics to a vehicle providing its own tractive force via engine torque transmitted to its wheels, as the torque required at the wheels to maintain a set speed around a corner decreases the tires ability to withstand lateral acceleration (friction ellipse concept).

While designing a control system as discussed above would be optimal, the effort required to model such complex systems, which would include mechanical linkages with compliance and

hydraulic subcomponents, is a drawback. The project time-frame and obvious capacity constraints prevented such an approach.

Refocusing however on the project aim of validating a vehicle dynamics model with physical tests, it is evident that it is possible to accomplish the speed and direction control of the BELL EQ. ADT model using a simpler control strategy.

Two factors that counted in favour of a simpler control strategy were:-

1. The manoeuvres conducted during physical testing were far from the limit handling regime thus reducing the effect of torque at the wheels contributing to the cornering ability of the vehicle.
2. Real direction change manoeuvres during physical testing were well within the limits of operation of the driver implying that the manoeuvres to be modelled were achievable in reality.

Thus it was decided to build a velocity controller with the controlled parameter being a linear force “pulling” or “retarding” the vehicle to maintain a set velocity profile and a path following controller with the controlled parameter being a force applied to one of the articulation hydraulic cylinders (which articulates the front chassis relative to the rear) to maintain or follow a set path. These are described in more detail further on in this chapter. First however it is instructive to discuss the modelling of closed loop controllers within the ADAMS/View environment.

4.5.1 Modelling Controllers in ADAMS

There are many ways to devise control strategies and link these to the mechanical parameters that need to be controlled or those to drive a control system within ADAMS. The most basic control strategy is to implement a control law as a functional expression within ADAMS relating a forcing function to a desired value of a system output such as position or velocity etc. One can also create subroutines that are linked to the ADAMS model executable file. Thus one would be able to create a control law in FORTRAN or C programming language compile this as a self running executable linked to the ADAMS executable via forces and torques on the appropriate body or part in ADAMS. Co-simulation with other software packages such as MATLAB/Simulink®, Matrix-X® and EASY5® is also a very popular method of integrating control systems within an ADAMS mechanical model. The control system is constructed entirely within the external program and the two models, the control system and the ADAMS mechanical model, pass inputs and outputs between them. A strong advantage of this method is

that it leverages the inherent, individual strengths of the control system package and the mechanical simulation power of ADAMS. Each model is solved within its own environment with the control system numerical solver being particularly geared to solving control system differential equations and the ADAMS solver being adept at solving the differential equations resulting from a mechanical system. Finally one can implement a control system from right within ADAMS/View using the ADAMS/View Control Toolkit. The ADAMS /View user interface has a set of basic control elements such as gains, filters and PID controllers that interface with different forces and state variables of the system and allows the eventual control loop to be written as a set of differential equations which ADAMS/Solver then solves at run-time. It was this method that was adopted to create the control systems for the velocity and path following controllers.

In order to implement the control strategy using the ADAMS/View Controls Toolkit, it is imperative that one start out with a feedback control diagram. Without a well laid out schematic of the structure of the control system it is not possible to (except for simple cases) to proceed with constructing the control system using the toolkit. Using the controls toolkit then becomes a case of using the standard control blocks in ADAMS/View to replicate the blocks in the control system diagram and linking these blocks into a functioning control system. The controls toolkit is accessed from the main ADAMS/View menu bar as **BUILD → CONTROLS TOOLKIT → STANDARD CONTROLS BLOCKS**.

This will open up the “Create/Modify Controls Block” dialogue box as shown in **Fig. 4.55** which then lets one build the components of the control system. All control blocks with the exception of the “Input” block have inputs and outputs. Each of the inputs and outputs in a control block can be linked to force and motion elements in one's model as well as to other control blocks. In this way the “connecting” lines of one's control system are represented. The procedure as well as the actual functional representation coded into each of the control blocks making up the control system are discussed during the presentation of the steering and speed controller. New concepts are explained as they are encountered however not all individual steps are reproduced here due to their simplicity of implementation.

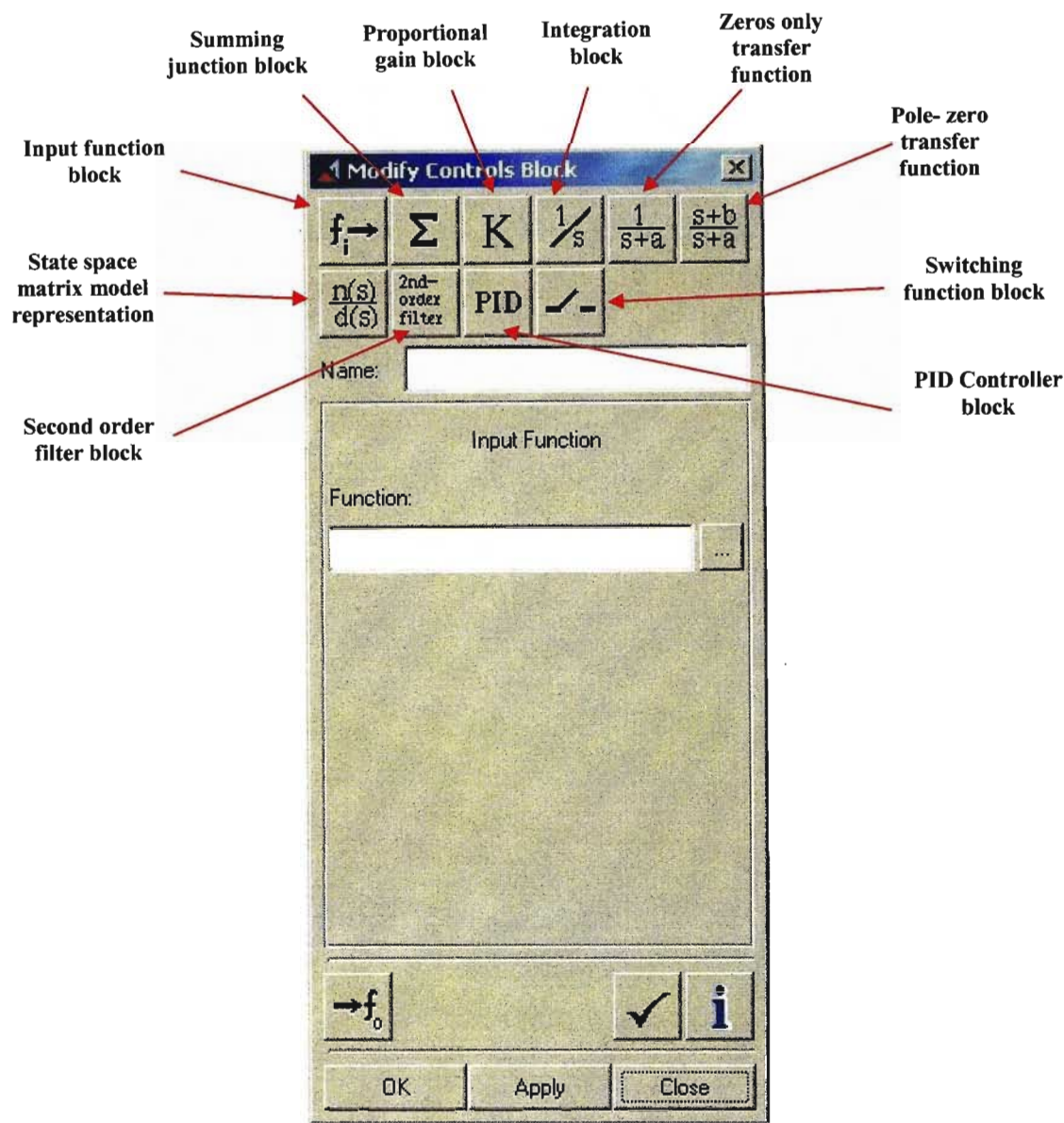


Fig. 4.55 The Create/Modify Controls dialogue box shown here for in the case for the input function block

4.5.2 The Speed Controller

First attempts at using a set motion to control the forward velocity resulted in simulation failures due to large tire slip ratios in response to the forcing motion constraint. Thus it was decided to control the forward speed of the ADAMS model of the ADT by building the speed control loop as shown in Fig. 4.56 in which the ADT model’s forward speed could be gradually brought up to the set speed via a steadily increasing force acting on the ADT front-chassis’ centre of gravity.

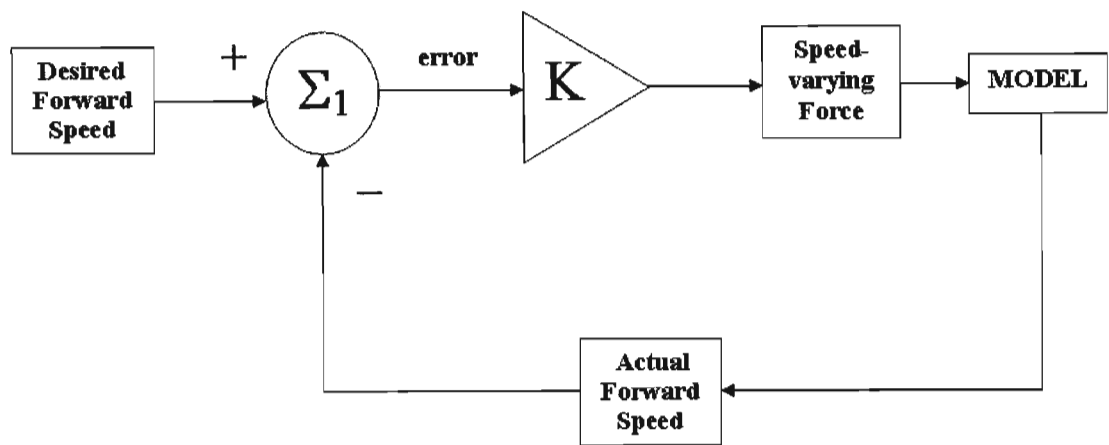


Fig. 4.56 Feedback control diagram for proportional speed control

Actual Forward Speed

In order to capture the actual forward speed an input function to the summing junction block had to be created. However first a state variable that captured the actual magnitude of the forward velocity of the center of gravity marker of the front chassis’ had to be created. The “Create/Modify State Variable” dialogue box (accessed via **BUILD → SYSTEM ELEMENTS → STATE VARIABLE → NEW**) is shown in Fig. 4.57

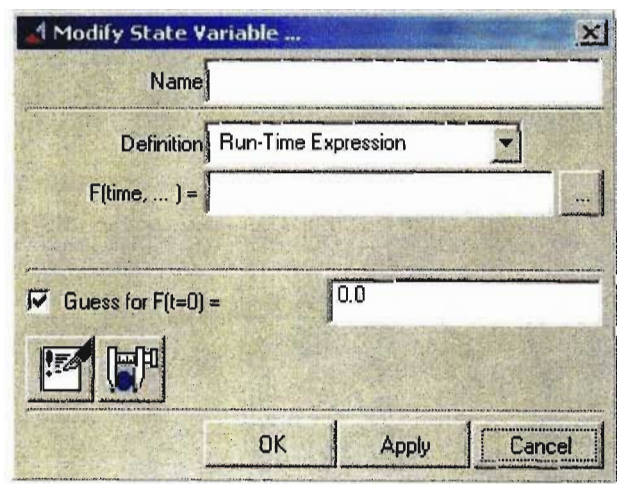


Fig. 4.57 The Create/Modify State Variable dialogue box

In the Create/Modify dialogue box the state variable must be given a name and the function of time associated with it can be defined. In this case the velocity magnitude function of the front chassis' center of gravity marker has the form **VM("COG marker name")**. Then the input function block (as shown in **Fig. 4.55** above) for the Actual Forward Speed is created. The input function has the form **VARVAL("State variable name for velocity magnitude")**, where the function VARVAL is used to return the current value of the state variable it references.

Desired Forward Speed

This parameter is an input to the control loop and is created using the input function box (as shown in **Fig. 4.55** above). The input function has the form **STEP(time, 0, 0, a, b)**. This acts to gradually increase the desired speed from a zero value to the final value (**b**) at a time (**a**).

Summing Junction (Σ)

The summing junction acts to sum the two inputs, desired speed and actual speed, and pass the error output on to the proportional gain block. **Fig. 4.58** shows the summing junction dialogue box.

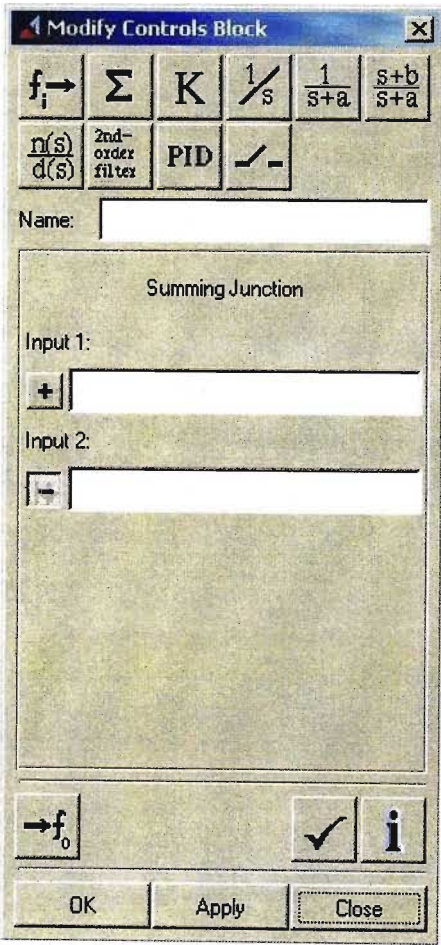


Fig. 4.58 The Summing Junction controls dialogue box

Proportional Gain (K)

The proportional gain block accepts the name of the summing junction block as input. In the proportional gain controls dialogue box (as shown in Fig. 4.59 below) a proportional gain constant must be set.

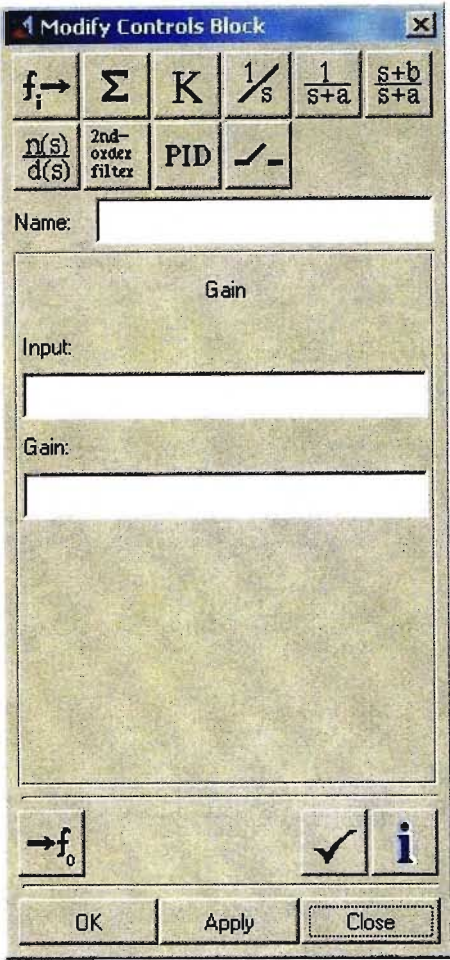


Fig. 4.59 The Proportional Gain controls dialogue box

In order to complete the loop the output of the proportional gain block must be linked to a force or torque element to be controlled in the ADAMS model. In this case for the speed controller the force to be controlled was the translational force applied to the ADT front-chassis' center of gravity marker. To link the output of the proportional gain control block to the translational force, the force had to be modified via **MODIFY → GETTING OBJECT DATA → MEASURES → RUNTIME MEASURES** and browsing for the name of the proportional gain controls block using the ADAMS/View Database Navigator. With this completed, the control loop was closed and could be tuned to produce the required result.

4.5.3 The Path-following Controller

The path following controller proved to be more complicated than the speed controller. Initial tests on a simpler four wheeled vehicle model with an articulating front axle showed that a simple proportional controller would be insufficient to control the ADT model. Thus a control strategy using Proportional-Integral-Derivative (PID) control was decided upon. As discussed above, the controlling force is a translational actuating force acting on a single articulation cylinder on the ADT model that acts to articulate the front chassis relative to the rear chassis in response to the path deviation error. **Fig. 4.61** shows the path-following feedback control system model implemented. The state variables X and Z in **Fig. 4.61** are the x- & z-coordinates of a fixed marker on the vehicle in the horizontal plane. The coordinates are related to each other according to the coordinate axes in the horizontal plane (as viewed from above) as shown in **Fig. 4.60**.

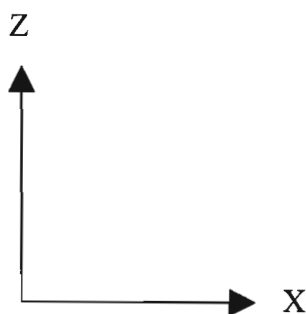


Fig. 4.60 ADAMS ADT model global coordinate system axes in the horizontal plane

The construction of each element or control block in the control system model for the path-following controller in **Fig. 4.61** is now discussed in detail.

Actual X & Actual Z

The driver does not control the vehicle's path by relating its center of gravity to the fixed path to be followed. Normally the driver will have a look-ahead point at which he would relate his vehicle's current position to the intended path and make the necessary adjustments to maintain the intended path. In this case the look ahead point was chosen to be the point at the tip of the nose of the ADT as the driver was required, during physical testing, to maintain the path by keeping the nose of the vehicle pointed along the intended path on the road. This is not strictly true as the look ahead point of the driver would vary with speed, terrain, type of vehicle and environmental conditions but it was considered instructive to use this as a starting point for the path following controller.

The actual x- and z- coordinates of the look-ahead marker on the nose of the ADT were inserted into the control system as input blocks (see **Fig. 4.55**). However as these inputs came from the

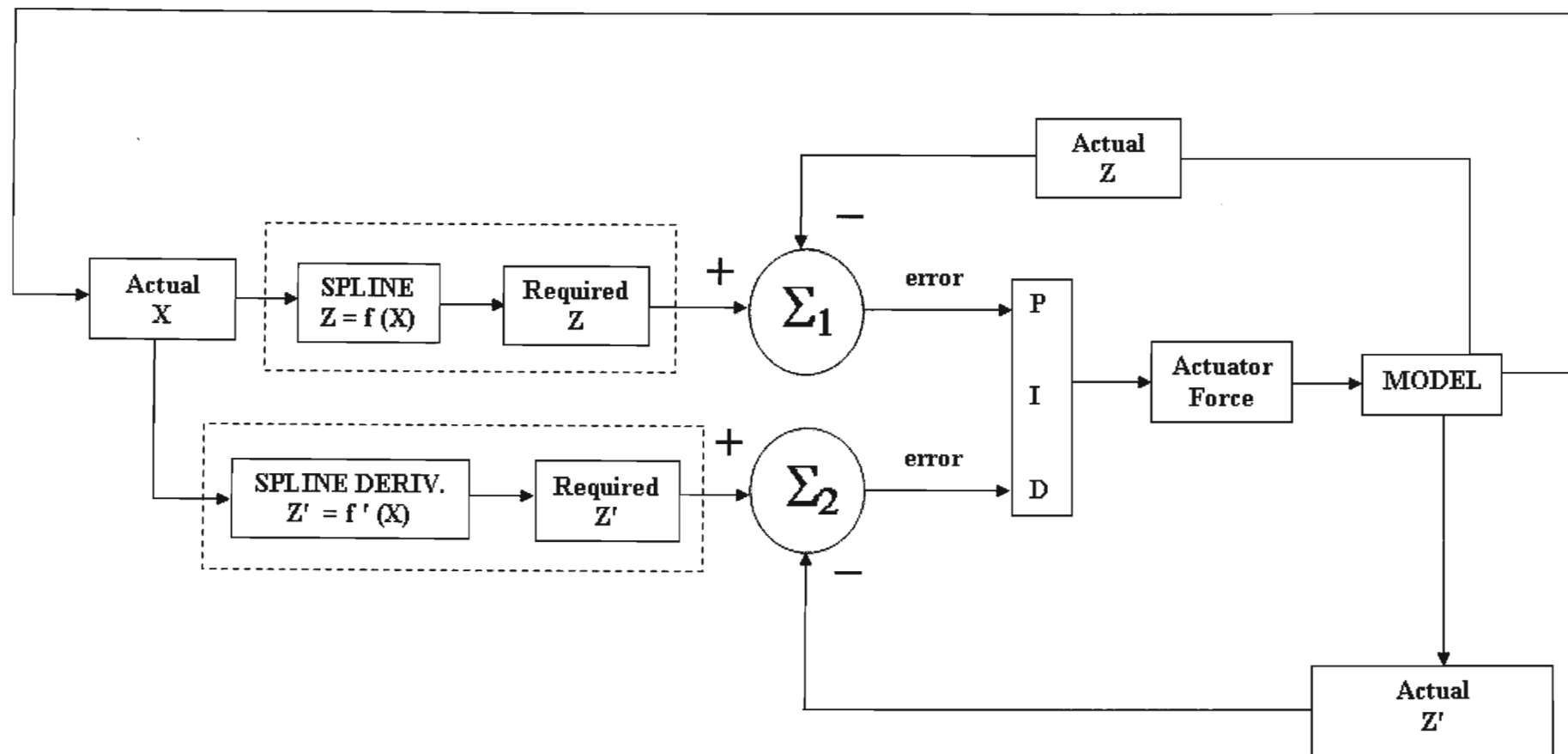


Fig. 4.61 Feedback control diagram for PID path-control

actual x-z position in the model itself, state variables had to be first created for the displacements (see **Fig. 4.57**). Thus the functional representation was as follows:-

State Variables: - "*Disp_X*" = **DX**("*Look ahead marker*")
 "*Disp_Z*" = **DZ**("*Look ahead marker*")

Controls Input Blocks: - "*Actual_X*" = **VARVAL**("*Disp_X*")
 "*Actual_Z*" = **VARVAL**("*Disp_Z*")

Required Z (Spline $Z = f(X)$)

In order to obtain the required z-displacement of the ADT a function had to be created which prescribes the desired x-z ADT displacement relationship. Thus given the actual or current x-displacement and the x-z displacement relationship, which defines the path to be followed, the required z-displacement is obtained. In defining the path it was decided to create the path as a spline ADAMS element using the spline editing tool in ADAMS/View. Thus the path defining x-z relationship was contained in a spline which could be referenced as a function via the spline elements name. The required z-displacement thus obtained would then be passed on as an input to the summing junction Σ_1 . This was implemented as a controls input function block (see **Fig. 4.55**) with the following functional relationship using the AKIMA spline function: -

$$"*Required_Z*" = \mathbf{AKISPL}("*Actual_X*", 0, "*Spline_name*", 0)$$

Required Z' (Spline $Z' = f'(X)$)

In addition to the required z-coordinate the required derivative of the z-coordinate with respect to the x-coordinate is also required for the derivative part of the PID controller. This was implemented as a controls input function block (see **Fig. 4.55**) similar to that for the required z-coordinate above. The "*Actual_X*" state variable is the input and the functional relationship is shown below: -

$$"*Required_Z_Prime*" = \mathbf{AKISPL}("*Actual_X*", 0, "*Spline_name*", 1)$$

were the last input parameter of the AKISPL function is changed from 0 to 1 to return the first derivative of the spline, dZ/dX . The output, the required derivative of the z-coordinate at the current or actual x-coordinate of the ADT, is then used as the input to the summing junction Σ_2 .

Actual derivative (Z')

Determining the actual or current derivative of the z-coordinate with respect to the x-coordinate proved to be more difficult. Performing even a time based derivative of a run-time variable in ADAM/View is not without drawbacks. A free differentiation is a numerically unstable process. In addition the accuracy of the process cannot be known in every case. ADAMS also cannot determine a derivative of a functional expression or run-time variable with respect to another run-time variable. There are however approaches to this problem that seek to get past these difficulties and will be discussed below.

It is possible to create an implicit differentiation function in ADAMS that returns the time derivative of a run-time variable. It is however a two step definition in ADAMS as the function references itself. For example given a run-time variable Y, the run-time derivative dY/dt is defined in ADAMS via the following functional expression [75]:-

$$"dY/dt" = \mathbf{DIF}("dY/dt") - \mathbf{VARVAL}("Y")$$

The function **DIF1**(" dY/dt ") then returns the derivative dY/dt .

In the case of the path-following controller a further issue is that the derivative required, dZ/dX , is the derivative of one run-time variable with respect to another run-time variable. This is not without further modification possible in ADAMS. The solution found entailed using the chain rule to reconstitute dZ/dX as a function of two implicit derivatives with respect to time [75] as described below :-

$$\begin{aligned} \frac{dZ}{dX} &= \frac{dZ}{dt} \times \frac{dt}{dX} \\ &= \frac{dZ}{dt} \div \frac{dX}{dt} \end{aligned}$$

and then to calculate the reconstituted derivative as a quotient of two implicit differentiation functions (with respect to time) as described above. There are a few issues to keep in mind however when attempting to calculate implicit derivatives as detailed above [47]: -

- The method doesn't work when using a coordinate partitioning method for dynamics solution i.e. the DIF1 function will always be zero if an integrator like ABAM solver is used

- It will not work for kinematics simulation
- There is no error control on the differentiated signal such that the accuracy of the answer cannot ever be ascertained beforehand. The only way to control the error is by controlling the step size.
- Feeding the differentiated signal back into the model can cause integration difficulties

In addition to the above it is important to ensure that the derivative that forms part of the divisor in the chain rule formulation above is never zero as this will cause the simulation to crash. A workaround established is to subtract a very small number, less than or equal to the error tolerance, from the divisor such that there is never a division by zero.

The actual derivative (Z') is modeled in the control system via a controls input block (see **Fig. 4.55**). First however the two implicit differential equations with respect to time had to be created via **BUILD → SYSTEM ELEMENTS → DIFFERENTIAL EQUATION → NEW**. This brings up the “Create/Modify Differential Equation” dialogue box as depicted in **Fig. 4.62** below.

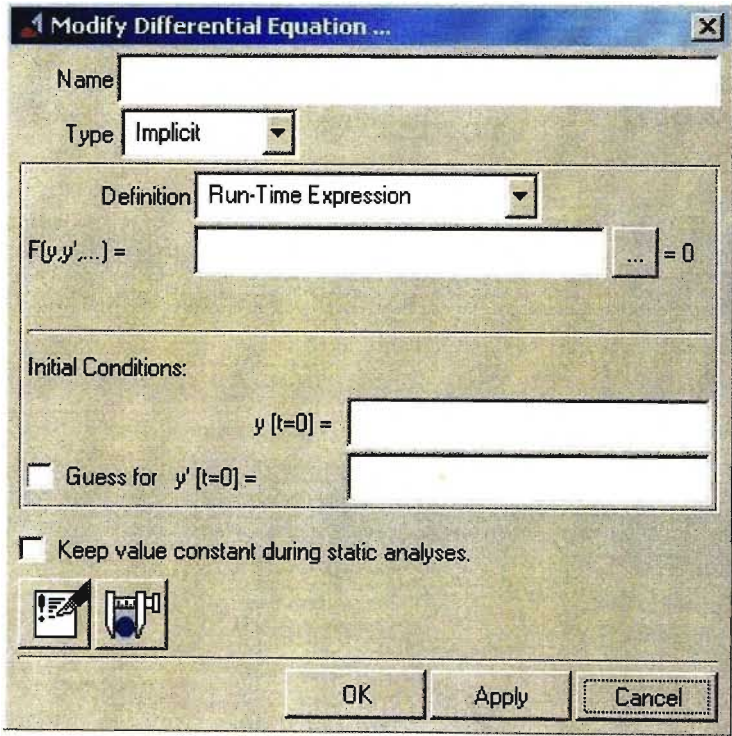


Fig. 4.62 The Create/Modify Differential Equation dialogue box

In addition to naming the differential equation (this is the name that will be self referenced in the defining function expression), the functional expression and the initial conditions must be defined. Checking the “Keep value constant during static analysis” is prudent if a static equilibrium analysis is to be performed. The functional expressions of the two differential

equations that need to be created in order to complete the actual derivative part of the path-following control loop are as follows: -

$$\begin{aligned} \text{"DX_DT"} &= \text{DIF} (\text{"DX_DT"}) - \text{VARVAL}(\text{"Disp_X"}) \\ \text{"DZ_DT"} &= \text{DIF} (\text{"DZ_DT"}) - \text{VARVAL}(\text{"Disp_Z"}) \end{aligned}$$

The actual derivate ($Z' = dZ/dX$) is then modeled as a controls input block (see **Fig. 4.55**) to the summing junction Σ_2 with the following functional expression: -

$$\text{"Actual_Z_Prime"} = \text{DIF1} (\text{"DZ_DT"}) / (\text{DIF1} (\text{"DX_DT"}) - 0.001)$$

Summing junctions (Σ_1 & Σ_2)

The summing junctions serve to calculate the error between the required and actual signal and to pass this on to the PID controller. The summing junction controls block (see **Fig. 5.58**) is used to insert these functions into the control loop. The functional expression for the summing junction Σ_1 is as follows: -

$$\text{"Error_Displacement"} = \text{"Required_Z"} - \text{"Actual_Z"}$$

and that for the summing junction Σ_2 , is as follows:-

$$\text{"Error_Derivative"} = \text{"Required_Z_Prime"} - \text{"Actual_Z_Prime"}$$

PID Controller Block

The PID controller block (see **Fig. 4.63**) introduces a compensating controlling actuation to correct the error of the actual signal to the required one. It is a linear control method and has the following input/output relationship (I/O) [12]:-

$$\frac{I(s)}{O(s)} = K_p + \frac{K_i}{s} + sK_d$$

were,

K_p	=	Proportional gain (controls the systems rise time or response)
K_i	=	Integral gain (controls the systems steady state accuracy)

K_d	=	Derivative gain (controls excessive oscillation)
$\frac{1}{s}$	=	Laplace transform representation of an integrator
s	=	Laplace transform representation of a differentiator

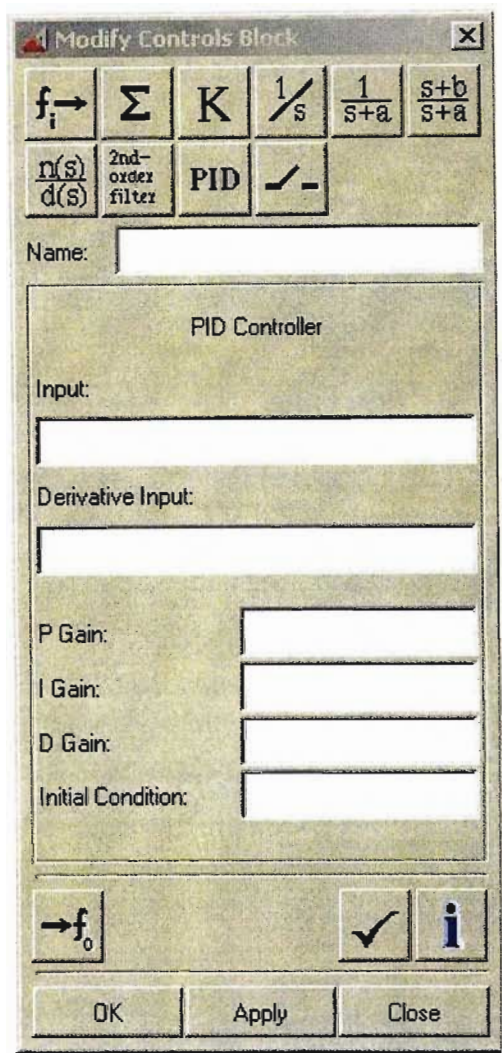


Fig. 4.63 The PID controller controls dialogue box

As can be seen in the path-following controller diagram in **Fig. 4.61**, the inputs to the PID controls bock are the outputs from the summing junctions Σ_1 & Σ_2 . The functional expression would then be:-

$$“PID_Ccontroller” = “Error_Displacement” + “Error_Derivative”$$

The various gain values are then set (or the controller is tuned) to enable the controller to accurately enable the ADAMS model of the ADT to follow the chosen path. In order to complete the path-following control loop, the output of the PID block must be linked to a force

or torque element to be controlled in the ADAMS model. In the case of the path-following controller the force to be controlled was the translational force applied between the cylinder and piston of a single articulation hydraulic cylinder linking the front & rear chassis (via the oscillation tube assembly). To link the output of the PID control block to the translational force, the above mention translational force had to be modified via **MODIFY → GETTING OBJECT DATA → MEASURES → RUNTIME MEASURES** and browsing for the name of the PID gain controls block using the ADAMS/View Database Navigator. With this completed, the control loop was closed and could then be tuned to produce the required result.

5. SIMULATION OF THE ADAMS ADT MODEL

Simulation of a complex multibody system such as a full vehicle does not proceed directly from construction of the model. Due to the complex interaction of the basic mechanical system (in itself complex with many degrees of freedom), and in this particular case the compliant joint connections, the tire model as well as the control system models, various parts of the model have to be tested and simulated in isolation. In effect many simplified models or assemblies have to be constructed to test the usability and accuracy of the various sub-components of the model. In this case many of the mechanical sub-systems were tested in isolation for kinematic realisability. The front and rear chassis' were tested separately without the tires and with idealised joints via kinematic simulations in ADAMS to prove the correctness of the mechanical assembly. The FIALA tire model was tested at first using a single wheeled, half axle model that could steer the wheel relative to the axle but with the free end of the axle constrained to move only in a vertical plane thus allowing the longitudinal and lateral vertical reaction forces to be determined due to slip angle and longitudinal slip ratio changes. The steering and velocity controllers were first tested on a simple single mass system constrained to move only in the horizontal plane. This typically illustrates the "crawl-walk-run" approach required to successfully complete a fully integrated multi-body system model in ADAMS.

The aim of this project was to prove the feasibility of such a model i.e. that it could be successfully built and simulated and that it would give realistic results. Given the time frame an exhaustive list of simulations could obviously not be carried out. It was thus decided that simulating the ADT single bump test, the lane change over 60m as well as a wheel imbalance simulation would satisfy the aims of this project. Simulating a single lap of the BELL EQ. test track proved at an advanced stage, to be not possible as the current path-following controller prevented this, due to the fact that a closed loop path would give rise to situations where a given x-displacement could correspond to more than one z-displacement in the horizontal plane. This was not possible to simulate without further modification to the control system model. To overcome this, a special subroutine written in external programming code to establish the exact path relationship would have to be written and was thus outside the scope of this project. **Fig 5.1** represents the lane change simulation while **Fig. 5.2** and **Fig. 5.3** show the bump test as simulated in ADAMS. In the following sections the simulations as well as challenges experienced with the simulation of the full vehicle model are discussed. In addition results of the simulations conducted are presented.

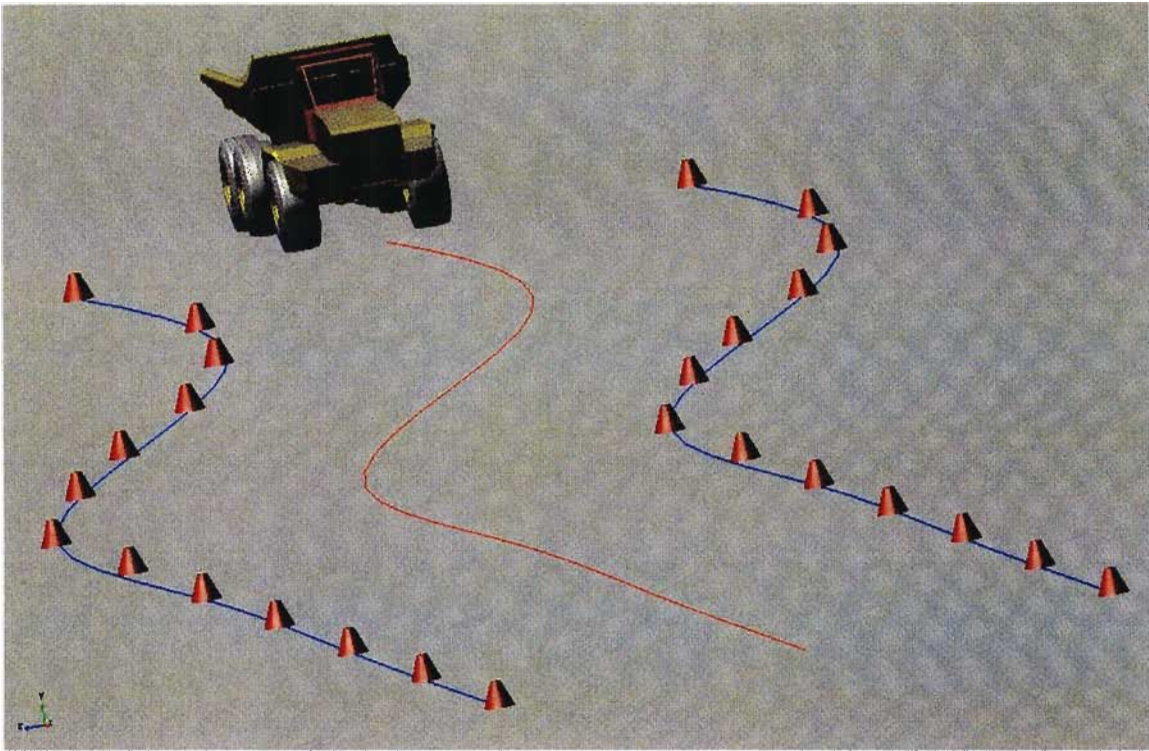


Fig. 5.1 Lane change simulation of the BELL EQ. 40 ton ADT in ADAMS

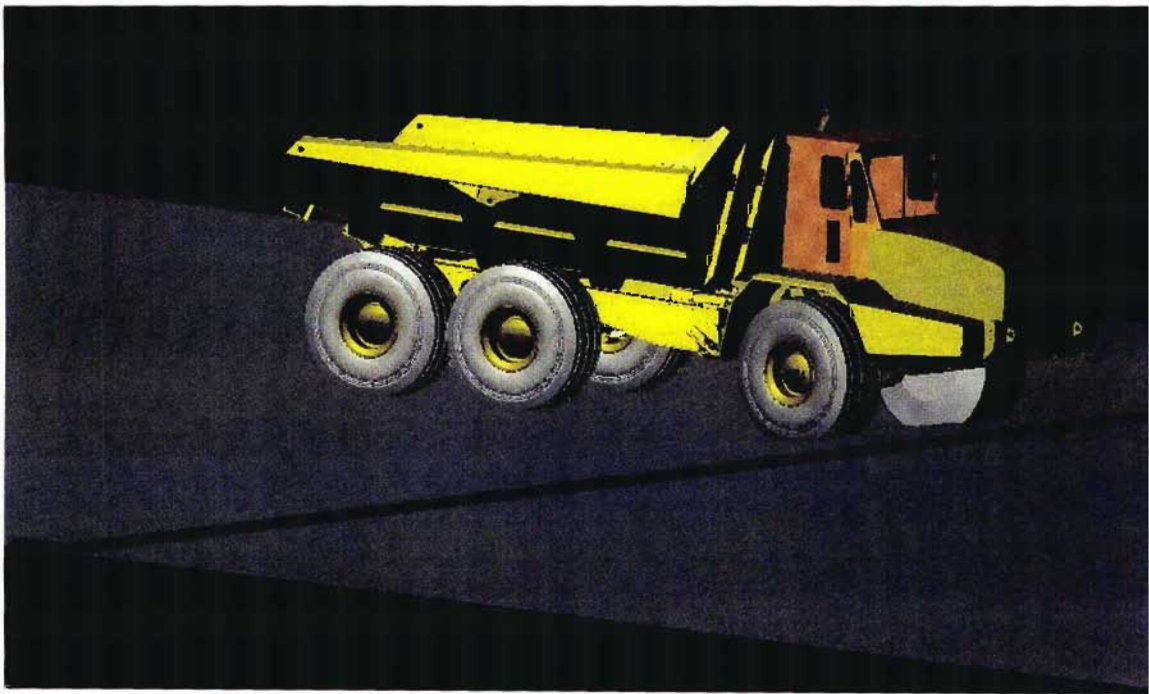


Fig. 5.2 Bump test simulation of the BELL EQ. 40 ton ADT in ADAMS – simulation with a trapezoidal cross-section bump



Fig. 5.3 Bump test simulation of the BELLE EQ. 40 ton ADT in ADAMS – simulation with a smooth bump

5.1 Simulating the ADAMS ADT model

As mentioned above, various parts of the final model were tested in isolation due to the complexities of assembling a large degree of freedom multibody system, with compliant connectors and a control system controlling the path to be followed and vehicle forward velocity. This model construction process was followed in order to aid in troubleshooting of the complete model. Upon initial simulation of the completely assembled model various simulation errors were encountered which prevented the actual running of the model. The more significant problems encountered and the methods adopted to solve these issues are presented below.

The first problem encountered upon simulation of the complete ADT model in ADAMS was 'lock-up' of the system. Lock-up in a mechanical simulation is encountered when the mechanical constraints result in an immovable system at some point in its intended space of motion, i.e. a system can no longer move without violating one or more of its constraints. With the ADT model this was encountered upon first performing an equilibrium simulation. The equilibrium simulation is important as this is the position of rest from which the assembled truck will be expected to perform any manoeuvre. The ADT model in ADAMS was assembled via the constraining geometry of the individual rigid body parts that make up the ADT. The position of the individual parts at assembly would not be that of the model at rest on horizontal ground and hence the equilibrium simulation was always performed before any further

simulation. An important point to note at this stage, for further model development and interpretation of results of simulations of the current model, is that a small percentage of the individual suspension linkages were not of the exact lengths of the actual linkages. This was a legacy from the early project stages of constructing the model. Keeping the linkages exact would have necessitated reworking large parts of the completed assembly in order to enable all the various mechanical assemblies to fit exactly and hence been very time consuming.

The ADAMS error reports of the lock-up condition indicated that the primary concern was the oscillation joint connecting the front chassis to the rear. As the first simulation of the assembled model was done using idealised joints, no flexing of any part of the model could take place to take up any large forces generated in the model. It is thus obvious that the oscillation tube assembly takes up large bending forces in reality, from the above scenario. Converting the idealised oscillation joint to a flexible joint (ADAMS Bushing element) helped avoid the lock-up scenario however too low a bushing stiffness resulted in large unrealistic relative motions and too high a stiffness resulted in large forces which would again cause simulation failure. Eventually this problem was overcome by modelling the various suspension joints as flexible force elements (except the oscillation joint) and also increasing the number of iterations permitted to achieve equilibrium from the default value of 25 to 1000.

ADAMS provides for many different types of mechanical systems simulations e.g. kinematic, dynamic, transient, equilibrium etc. The settings associated with each of these simulations types vary and affect the simulation of a model greatly in terms of the ability to complete a simulation, the speed and accuracy of the simulation. In order to control the simulation and vary settings, the simulation controls dialogue box shown in **Fig. 5.4** was used to control the parameters of the simulation as well as vary or change the various integrator-solver parameters as demanded by the type of system being simulated. Of concern during this project were the equilibrium and dynamics solvers. **Table 5.1** details the settings (accessed via the Simulation Settings button in the Simulation Controls dialogue box) used during the simulations performed as well as brief descriptions of the parameters [41].

The numerical techniques used to solve the EOM of such large DOF mechanical systems with complex force and constraint modifiers constitutes a large field of study with many pitfalls. If not approached with circumspection, numerical solutions may be difficult to achieve or worse still give results that are false. The many changes that can be made to the numerical integrators chosen to solve the system of differential equations representing the model are detailed in the ADAMS/Solver user guide [41] and are an invaluable reference for troubleshooting simulation problems.

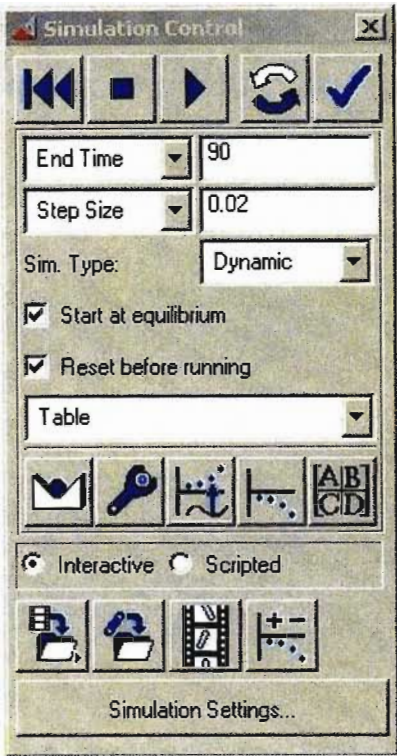


Fig. 5.4 Simulation Controls dialogue box in ADAMS/View

Maximum Equation Error				
Time	78.7581	Steps	8680	Iterations 25275
Type	DYN	Step Size	2.62e-013	Order 1
Rank	Element	Hits		Percent
1	input_PATH_DZ_DX_ACTUAL	input_PATH_DZ_DX_AC	24	96.0%
2	TIRE_RL	GFD17174529	1	4.0%
History Depth		25	Show	3
		Apply		Close

Fig. 5.5 ADAMS/View debug table

In addition to the numerical integrators, non-optimal modelling of the system or badly constrained systems with badly chosen system parameters can lead to simulation failures or simulation inaccuracies which can be difficult to pin-point. In this regard the ADAMS/View debug table is an invaluable tool (see **Fig. 5.5**). With the graphic output of measures of key variables and animations switched off during simulation to conserve CPU time, it is difficult to ascertain the causes of simulation failures. The debug table points to the specific elements in the model that are causing numerical difficulties. With this, one is able to determine via the step size (of variable step solvers), the order and number of iterations per step, as well as the rank of the different elements requiring additional iterations per step, the root cause as well as severity of numerical solver instabilities.

In the case of the ADT simulations initial problems stemmed from large tire forces being generated at the tire contact patch. High and non-realistic slip ratios were encountered which then led to large and sudden increases in forces at the tire. This led to simulation failures. It was found that reducing the tire longitudinal slip ratio by an order of magnitude of that calculated in § 4.4.1, allowed the simulation to run. In addition to this, slowly ramping up the speed of the vehicle to the desired speed level, instead of setting initial translational and rotation velocities to the required boundary conditions of the events being simulated, also aided in establishing numerical stability of the model.

The controllers were also the cause of many simulation problems. It is important to note that for the path controller containing DIF & DIF1 statements which create a differential equation of a system state variable and return the implicitly differentiated variable, the simulation type and type of integrator used is of utmost importance. ADAMS forces the differential equation to zero during all other analysis other than DYNAMIC so it is important to change the simulation type from DEFAULT to DYNAMIC as well as to make sure that a co-ordinate partitioning integrator such as ABAM is not used. In both the above cases the output of all DIF1 statements will be zero which will result in a non-functioning controller as well as (in the case of the path following controller) simulation failure due to a division by zero for the “*Actual_Z_Prime*” statement (see § 4.5.3) which is a non-time based derivative written as a division of one implicit time based derivate by another. With this particular formulation of the “*Actual_Z_Prime*” statement in cases where the divisor is zero the simulation will fail. In fact the simulation will fail at $t = 0$ without further modification, with a warning of a division by zero statement being encountered. Changing y' & y_0 to small non zero values at $t = 0$, in the “Modify Differential Equation” dialogue box had no effect. A work around to this problem was found to be the subtraction of a small non-zero value, of a few orders of magnitude smaller than the maximum allowable single step error of the integrator, from the divisor differential statement. While this

allowed the simulation to proceed with great success for the path controller controlling a simple block of the equivalent weight of the unladen ADT constrained to move in the horizontal plane, its absolute accuracy for the ADT path controller needs to be established. By far the biggest problem with the ADAMS ADT model in its current state, is the PID setting of the path controller. In addition, the cross controller interaction (i.e. speed controller force affects the path controller force and vice versa without any compensating terms in either controller) exacerbates the situation. While the speed controller, with a proportional gain setting of $1\text{E}+005$, copes adequately (with only slight fluctuations in steady state speed) the path controller is affected to a larger extent by the speed controlling force. While the path controller's overall design was proven by using it to control the path of a block part of the same mass as the unladen ADT on the required lane change path of the ADT, via trial and error modification of the PID settings, the self same settings ($P = 1\text{E}+007$, $T_i = 0.7$, $T_d = 0.175$ & I.C. = 0) on the path controller for the ADT produced undesirable results.

An attempt was made to use the Ziegler-Nicholls PID tuning method [12] using the above PID values as a starting point. This was unsuccessful for two reasons, the initial PID values were obviously not realistic for the ADT model and with ADAMS simulation times of approximately 1,5 hours for a 80 second lane change simulation on a Pentium 4, 1GHz machine with 256MB of RAM, it was not possible to converge to a solution within a realistic timeframe. Trying to shut down the speed controller with a step function close to the start of the lane change was also not successful as the ADT speed dropped off too quickly resulting in a sudden sharp turn of the ADT and simulation failure. It was also noticed that after the static equilibrium simulation, the z-position (lateral position of ADT in the horizontal plane) of the look-ahead marker (the marker upon which the position of the ADT was determined for path control purposes) was offset from the initial required path by 0.0516m. Correcting this condition, by offsetting the path spline by 0.0516 m to coincide with the look-ahead marker at $t = 0$, was also not successful.

Further experimentation with the PID settings revealed that the controller was not even allowing the ADT to reach a stable, straight ahead heading prior to the start of the lane change event. The ADT was deviating from the path with a steady state error as well as having too large oscillations that were not being damped out sufficiently quickly. Lengthening the ADT run-up prior to the lane change event, did little to help the controller force the ADT to the chosen path.

Reference [12] provides the following information on the effects of the PID terms:-

- Low proportional gain (P) results in a more stable system however a higher steady state error while a high P, results in an unstable system but with a lower steady state error.
- Integral term (I) output is a ramp and acts to reduce the steady state error but decreases stability. Thus for PI controller, one can have a lower P gain which acts to make the system more stable and the I action corrects the steady state error
- The derivative term responds to a rate of change of the system. It has no affect on the steady state error however it adds a large degree of damping to the system and acts to damp out overshoot and subsequent system oscillations in response to changes from steady state. It allows higher values of P and I gains to be used. It is however very susceptible to “noisy” control signals and quick changes making the system very unstable under these conditions.

Using the above guidelines the following PID parameters ($P = 100$, $T_i = 0$, $T_d = 2$ & I.C. = 0.075) resulted in the most stable system with the least overshoot along a straight ahead path however the ADT was still not able to perform the lane change adequately. It was later determined upon closer inspection of the controller outputs that the “*Actual_Z*” term in the path controller, which feeds the actual lateral position of the ADT in the horizontal plane into the controller, was constantly zero due to a possible syntax error in the function statement describing the term. In addition the derivative of the path generated by the AKISPL function differed from the derivative of the path when generated in the ADAMS/Postprocessor with the AKISPL statement producing a significantly smaller derivative for the lane change part of the required path. These problems were however not investigated further.

The above difficulties encountered with the tuning of a PID path controller for the ADAMS model of the BELL EQ. 40 ton ADT, indicates the difficult nature of the problem. If further attempts are to be made to control the path of ADT without using the purpose built path controllers for common dynamic manoeuvres in ADAMS packages such as ADAMS/Car, it would be prudent to tune the PID controller taking the ADAMS model into account from the start. While the overall design of the PID control structure as discussed in this section is reasonable, selecting the PID parameters should be done as part of a controller design that takes into account the ADAMS ADT system characteristics as well. A multi-input multi-output system with speed control as well as path control terms should be developed. The ADAMS state space model should be output to a program such as MATLAB and classical control system design techniques such as the root-locus method should be used to design the controller taking the inherent stability and controllability of the ADAMS ADT model into account.

SOLVER TYPE	Parameter	Settings	Description
EQUILIBRIUM	Eq. Type	Static	<i>Defines the type of equilibrium simulation. Static sets all inertia forces and velocities and accelerations to zero and considers only displacement and balancing forces</i>
	Error	0.1	<i>Maximum displacement error as factor of length units</i>
	T_limit	20.0	<i>Maximum translational iteration allowed to reach equilibrium. Too large a step can cause the solver not to reach a solution</i>
	A_limit	10.0	<i>Maximum angular (rad) iteration allowed to reach equilibrium. Too large a step can cause the solver not to reach a solution</i>
	Maxit	1000	<i>Specifies maximum number of solver iterations to reach equilibrium</i>
	Stability	1.0E-005	<i>Affects the rate of convergence to a solution by adding a fraction of the mass and damping matrices to the stiffness matrix. Does not affect the accuracy of the solution</i>
	Imbalance	1.0E-004	<i>Specifies the maximum force imbalance in the system. Change if the physical units of the problem are too large or too small</i>
DYNAMICS	Integrator	GSTIFF	<i>Selects the integrator type that numerically solves the set of differential equations generated by the model. This is a stiff system integrator</i>
	Formulation	SI2	<i>SI2 is a method of reducing the index of a set of DAE's while still maintaining the constraint conditions at small step sizes of the original DAE's. Makes the numerical solver much more robust.</i>
	Corrector	Original	<i>Specifies the form correct for the predictor-corrector numerical solver methodology</i>
	Error	0.1	<i>Defines the maximum error (function of the difference between predicted and corrected values, order of integrator and step size) allowed for each integration step</i>
	H_max	(none)	<i>Maximum time step the integrator is allowed to take</i>
	H_min	(none)	<i>Minimum time step the integrator is allowed to take</i>
	H_init	(none)	<i>Initial time step the integrator needs to take</i>
	Adaptivity	(none)	<i>Used to overcome corrector convergence difficulties in the integrator</i>
	Interpolate	No	<i>Specifies that the integrator not control step size to coincide with an output point</i>
	K_max	12	<i>Maximum order the integrator can use</i>
	Maxit	10	<i>Maximum iterations allowed before integrator can converge to a solution for each step</i>

Table 5.1 Simulation settings used in the running of the simulations reported on in this project

5.2 Simulation Results

The ADT model was simulated under three conditions, all in the unladen condition; an attempted lane change over 60m, a bump test and a simulated wheel imbalance test at 55km/h. The simulation results are presented below. First however it is instructive to review the axes of the ‘sensors’ used in the simulation as compared to the real sensors used on the physical ADT and how these axis choices translate into the direction of the dynamic parameter being measured.

Fig. 5.6 shows the axis orientations of both the real sensors used during physical testing and the ‘virtual sensors’ or measures used during the simulation. The virtual sensors were placed at the same positions on the ADAMS model as the real sensors were placed on the physical ADT. **Table 5.2** indicates the resultant sign convention for each parameter. For the simulation the accelerations are positive in the positive direction of the unit axes orientation and the rotations are positive about the unit axes according to the right hand screw rule. This measures the actual acceleration directions. Even though the real acceleration sensor axes are in the opposite directions to the simulation measures, the linear accelerations still have the same signs as the simulation measures. This is due to the fact that the real sensor measures the reaction force. The real sensor roll and pitch directions are as per the right hand screw rule.

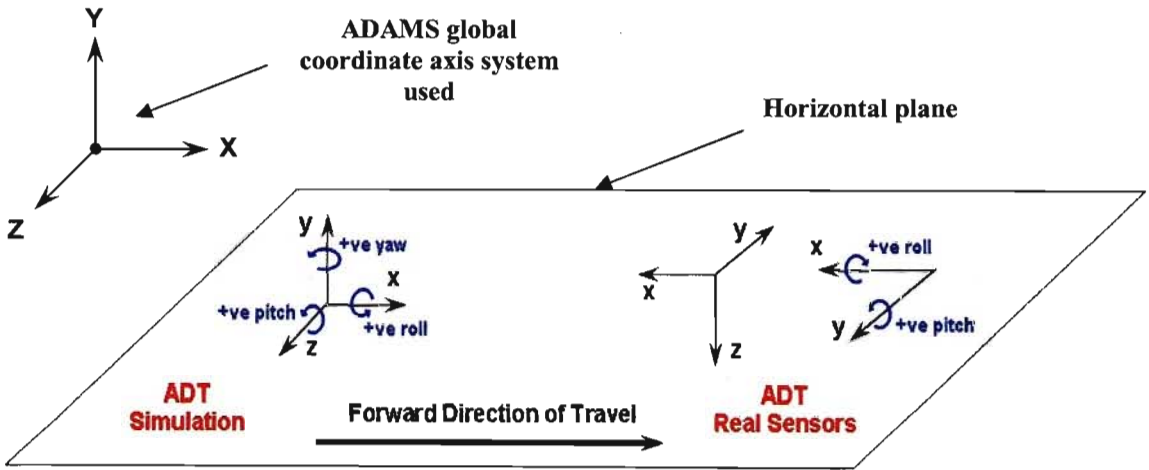


Fig. 5.6 Axes orientation of the parameter measures for the simulation and real sensors

Physical Parameter	Simulation	Physical Sensor
Longitudinal acceleration (forward)	+	+
Longitudinal acceleration (rearward)	-	-
Vertical acceleration (upward)	+	+
Vertical acceleration (downward)	-	-
Lateral acceleration (left turn)	-	-
Lateral acceleration (right turn)	+	+
Roll (right turn)	-	+
Roll (left turn)	+	-
Pitch (rearward)	+	+
Pitch (forward)	-	-
Yaw (counter-clockwise)	+	n/a
Yaw (clockwise)	-	n/a

Table 5.2 Sign convention for the measured physical parameters for the simulation and real sensors arising from choice of axes

Lane Change Simulation

The lane change simulation was not effective in terms of constraining the path of the ADT to that of the required lane change. This was due to the ineffectiveness in principle of the path PID controller due to non-optimal PID parameters. For a simulation run over 80 seconds with PID controller settings of ($P = 20$, $I = 0.25$, $D = 7$ & $IC = 0.075$) a step size of 0.02 sec and a velocity set-speed of 50km/h (13.88m/s) ramped up from zero by the velocity controller, the ADT simulation path shown in **Fig. 5.7** resulted.

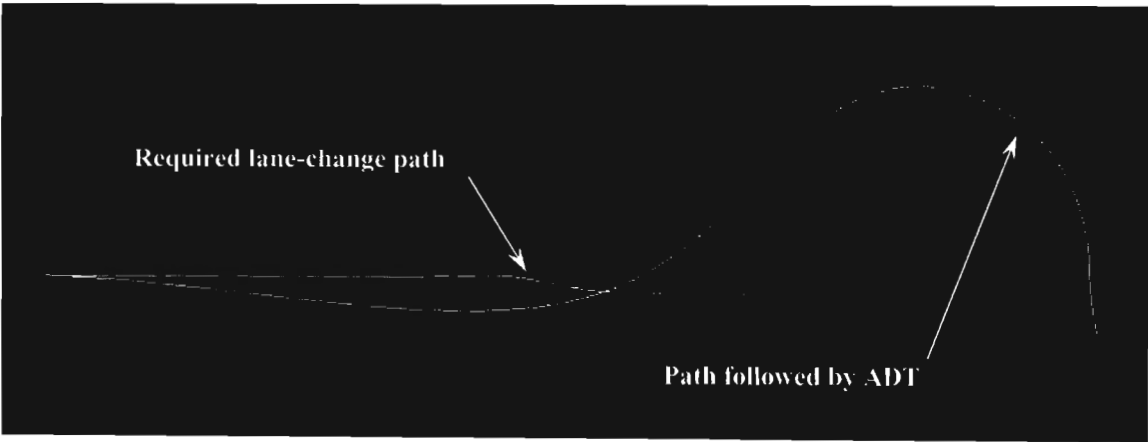


Fig. 5.7 Lane change simulation attempt over 60m with 9m lane width

Even though the lane change path was not followed, examining the results of the simulation is instructive in helping to understand the models viability. **Fig. 5.8** shows the actual speed of the ADT as compared to the set speed and that from 40 seconds onward the actual speed is 50km/h ($13.8\text{m/s} \pm 2.2\%$). In addition **Fig. 5.9** shows the path taken by the ADT as z-displacement (lateral) verses x-displacement (longitudinal). Also shown in **Fig. 5.9** are the approximate radii of the two the most significant curves and the duration time of approximately equal curvature.

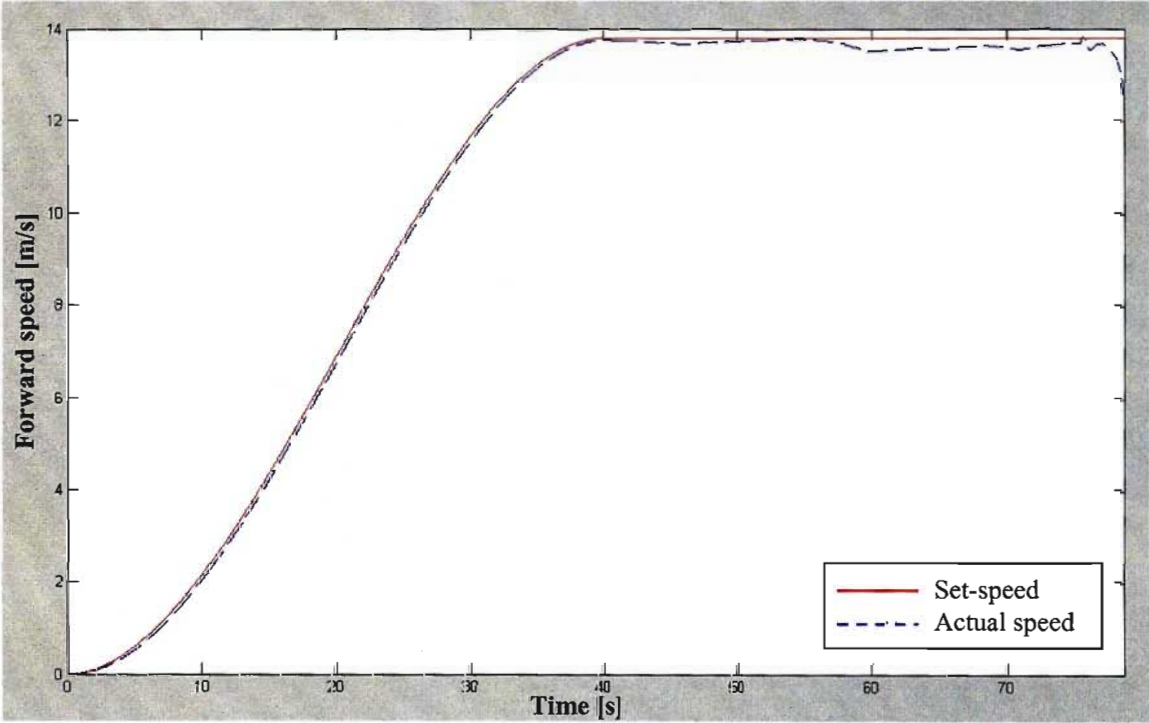


Fig. 5.8 Set speed and actual attained velocity of the ADT

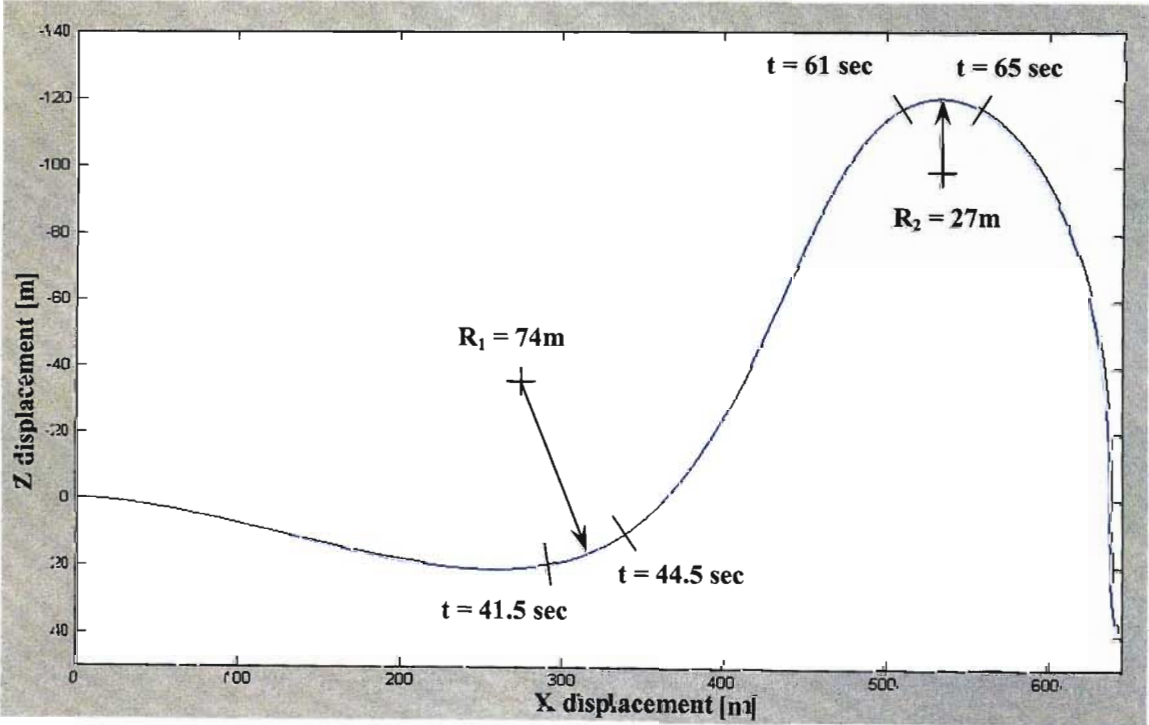


Fig. 5.9 Path taken by ADT during attempted lane change simulation

In many of the plots for the attempted lane change, the last 0.5 seconds of the simulation are not indicated due to the unrealistically high values achieved for many parameters at simulation failure. Where necessary these final parameter values are stated. The lateral acceleration plot, measured on the front and rear chassis at the positions used during the physical testing, is displayed in **Fig. 5.10**.

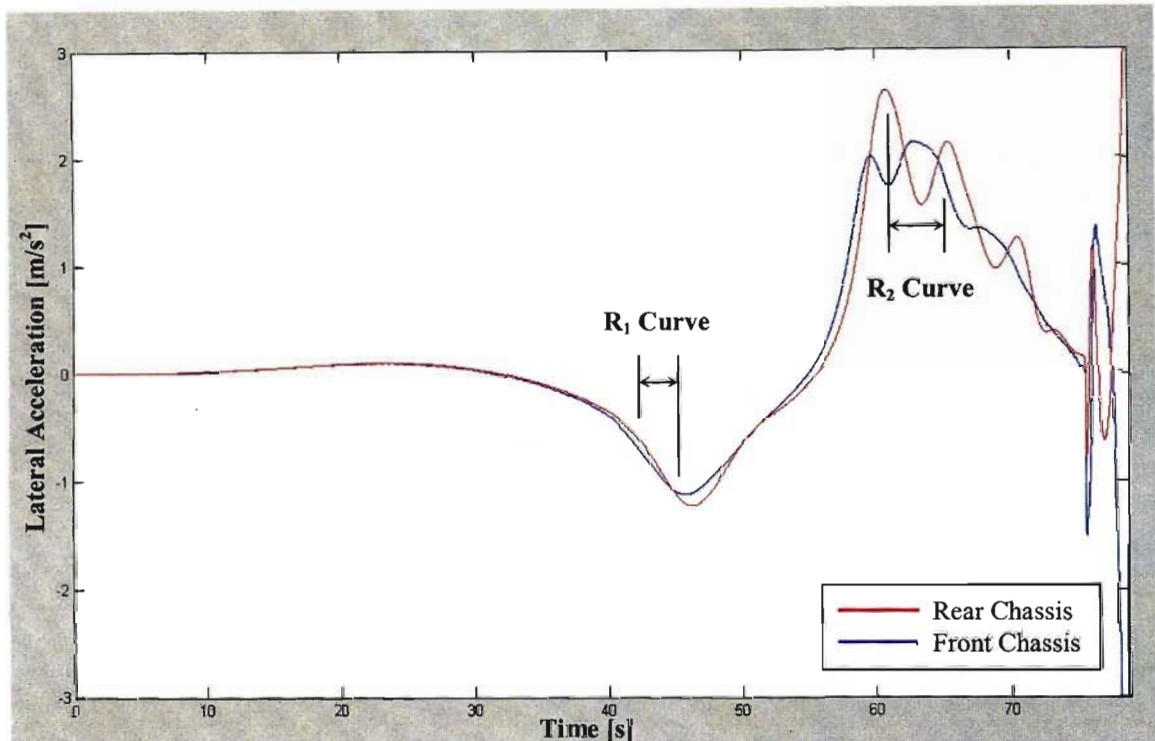


Fig. 5.10 Lateral acceleration of front and rear chassis during attempted lane change simulation

During the period of the first left hand turn at the radius of curvature R_1 (see **Fig. 5.9**) the lateral acceleration for both the rear and front chassis is not constant and the front chassis reaches a peak of 1.12 m/s^2 while the rear chassis reaches a peak of 1.21 m/s^2 approximately one second later. The rear chassis lateral acceleration should peak later but the fact that it withstands a slightly higher lateral acceleration indicates that it is able to follow a chosen path without sliding better than the front chassis i.e. they both have to traverse the same path but the higher value for the rear chassis indicates that it is able to round a curve faster than the front chassis before sliding. During the period of the second right hand turn of approximate radius R_2 (see **Fig. 5.9**) the accelerations are again not constant over a curve with a constant radius over at least 4 seconds. The lateral acceleration actually oscillates quite significantly. While one can see from the oscillations that the rear chassis still lags the front chassis the peak lateral acceleration for the rear chassis of 2.61 m/s^2 is achieved 2.1sec earlier than the peak lateral acceleration of 2.13 m/s^2 for the front chassis.

In addition to the accelerations not being constant over curves of approximately constant radii they are in fact too low. The lateral acceleration of an object traversing curved paths with radii of $R_1 = 74\text{m}$ & $R_2 = 27$ should be 2.6 m/s^2 & 7.2 m/s^2 respectively by the formula:-

$$a = \frac{v^2}{R}$$

where a = lateral acceleration [m/s^2]
 v = forward speed [m/s]
 R = path curve radius [m]

The fact that the measured values are not constant over a constant radius path of at least 3 seconds in addition to not being close to the theoretically calculated values above would strongly indicate that the ADT is sliding excessively around corners in the simulation i.e. that the forces that need to be generated at the tire contact patch to maintain the path required (and hence the require lateral acceleration) is not available from the tire.

Examining the roll angle of the front and rear chassis indicates anomalies in the simulated result in that there is period of large roll angle that would indicate that the ADT has rolled over and also that the rear and front chassis roll angles track each other exactly. However the ADT did not roll over at any time during the simulation and this is indicated by the fact that the vertical force at the contact patch of both tires at oppositely diagonal ends of the ADT (front left & right rear tires) at no point becomes zero during the simulation.

Fig. 5.11 indicates the roll angle of the front and rear chassis encompassing the entire range of roll angle to indicate the anomalous large roll values obtained for approximately 9 seconds from 68 to 77 seconds. An explanation for this could be in the way in which the roll angle measure was created in ADAMS. The roll angle was taken to be the rotation of the x-axis (see **Fig. 5.6**) of a “sensor marker” placed on each of the front and rear chassis’ at the points at which the real roll sensors (and acceleration sensors) were placed on the ADT during physical testing. Thus the roll angle was measured as the rotation of the sensor marker about its x-axis relative to the ADAMS global axis system. During the simulation period (68 to 77 seconds) the ADT begins to move in a direction that is parallel to the ADAMS global Z-axis. Thus the sensor marker’s x-axis is now orientated to the global Z-axis in ADAMS. This could explain the almost 180 degree deviation on the roll angle. Examining the measure for pitch angle, which was created in the same way, also indicates the same 180 degree deviation during the, 68 to 77 second simulation period. This would seem to corroborate the above argument.

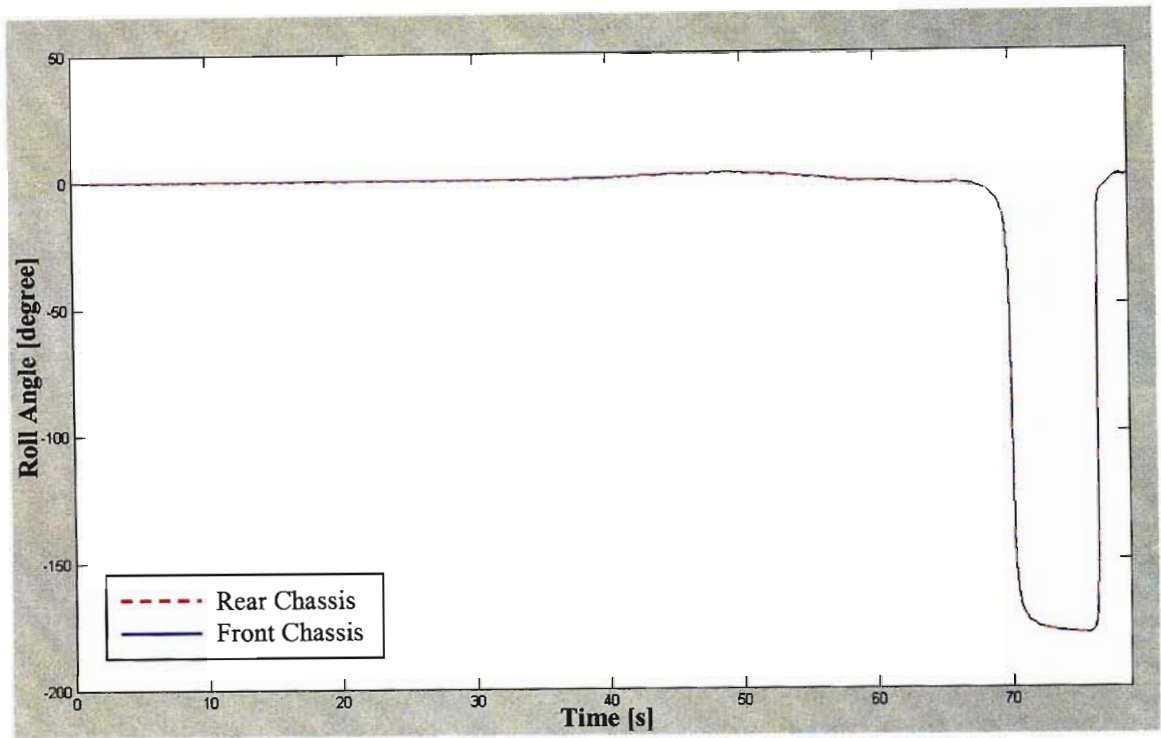


Fig. 5.11 Roll angle (encompassing entire range) of front and rear chassis during attempted lane change simulation

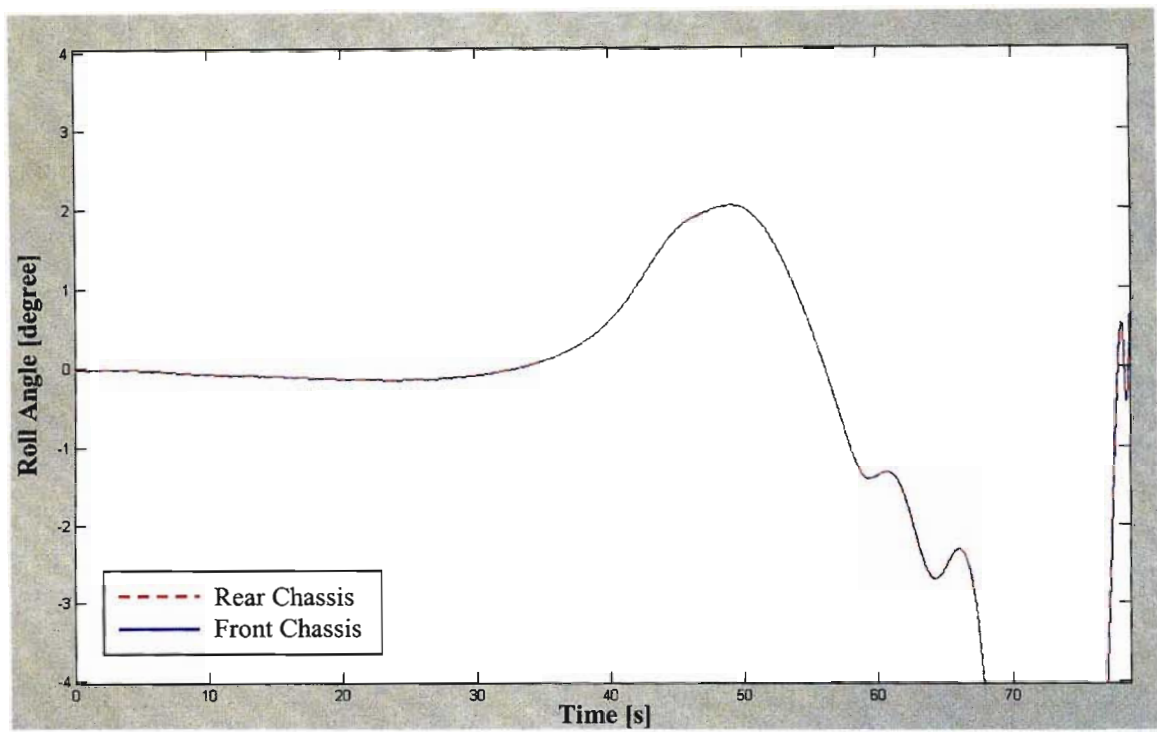


Fig. 5.12 Roll angle (range excludes anomaly of 180 degree variation) of front and rear chassis during attempted lane change simulation

Fig. 5.12 again represents the roll angle however this time excluding the 180 degree variation to better indicate the roll angles developed during the two constant radius curves traversed as

indicated in **Fig. 5.9**. The maximum roll angles are again too small and very between 2 and -2.7 degrees of roll for the two curves respectively. Here again it can be clearly seen that the front and rear chassis' roll angle track each other exactly. This however is obviously incorrect as the rear and front chassis have different roll centers and weights and have an independent roll degree of freedom due to the oscillation joint and should in essence roll by different amounts in the presence of a lateral acceleration as well as being offset from each other (front chassis roll should lead the rear chassis roll) due to the relative positional difference between them (i.e. front chassis is ahead of rear chassis).

It would seem from an examination of the above that not enough lateral force is being generated to create a significant roll angle as well as for the front chassis and rear chassis roll angle to diverge from each other. Examining the results of the simulation generated by the tires would seem to emphasis this analysis. **Fig. 5.13 to Fig. 5.15** represent the SAE tire forces developed at the tire patch for the front left and right rear tires. Firstly the vertical forces measured at the tire contact patch during the initial part of the simulation indicate the steady state load on the tires due to the weight of the vehicle. If summed across all tires this would indicate the total weight of the ADT. The vertical force measured on the front tire during the initial part of the simulation was 48 989N & that on the rear tire 30 370N. Considering that the weight distribution per wheel on each axle is 50:50 and that there is an approximately 50:50 rear chassis weight distribution across the walking beam, the total load of the ADAMS ADT model is calculated to be 219 458 N or 22 370 kg which is 6460kg less than the weight as measured of

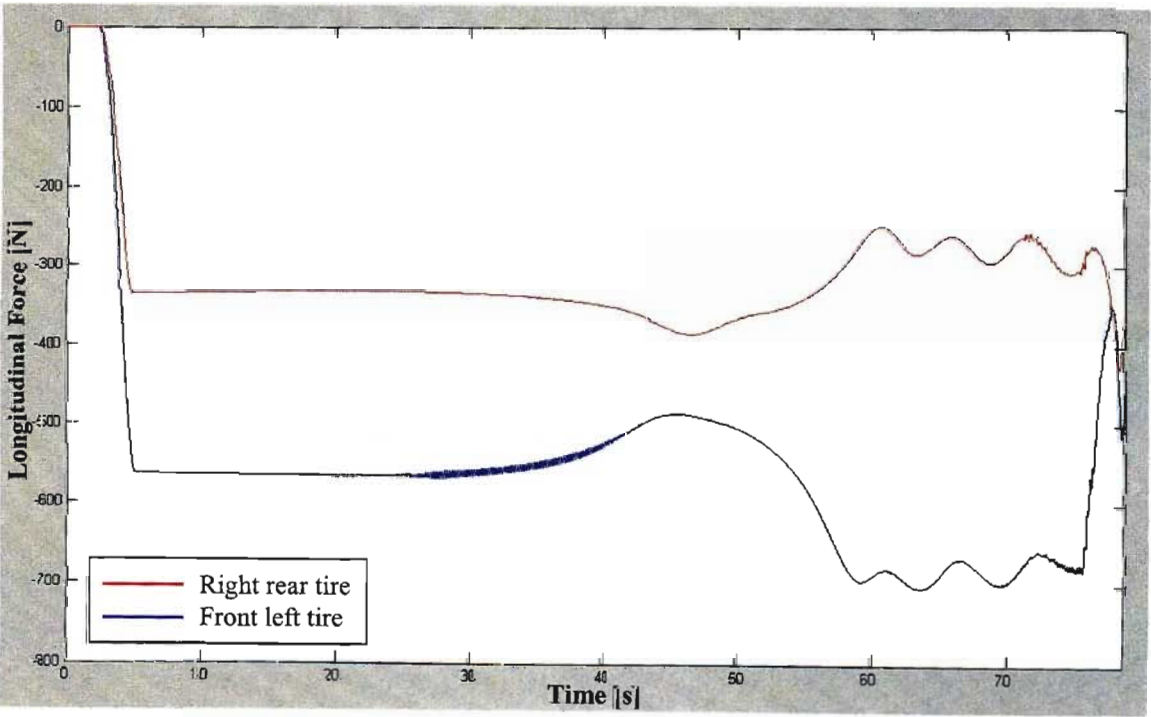


Fig. 5.13 Longitudinal force at tire contact patch for right rear and front left tire

the unladen ADT during the physical testing program. In addition the lateral as well as the longitudinal force values in the contact patch seems too low. Examining the tractive force “driving” the ADT (see Fig. 5.16) we see that the highest it becomes just prior to achieving the 50km/h set speed for the first time is 13 891 N at 20 sec. If one were to assume, at least in the

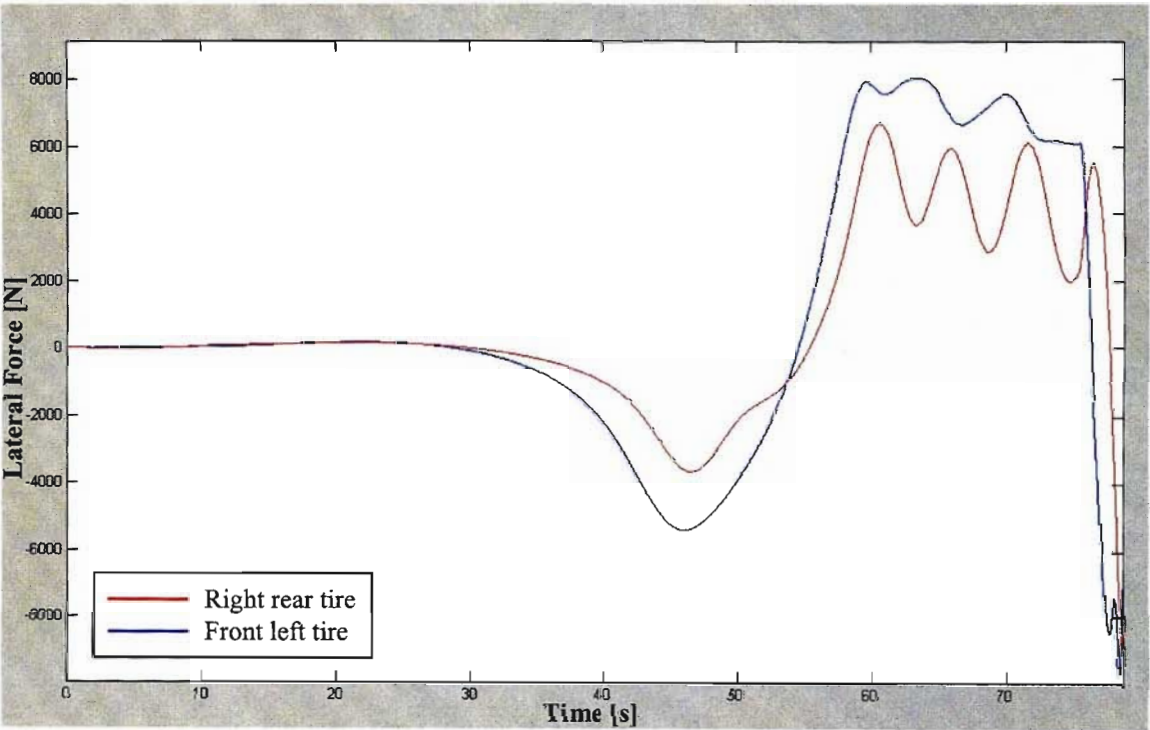


Fig. 5.14 Lateral force at tire contact patch for right rear and front left tire

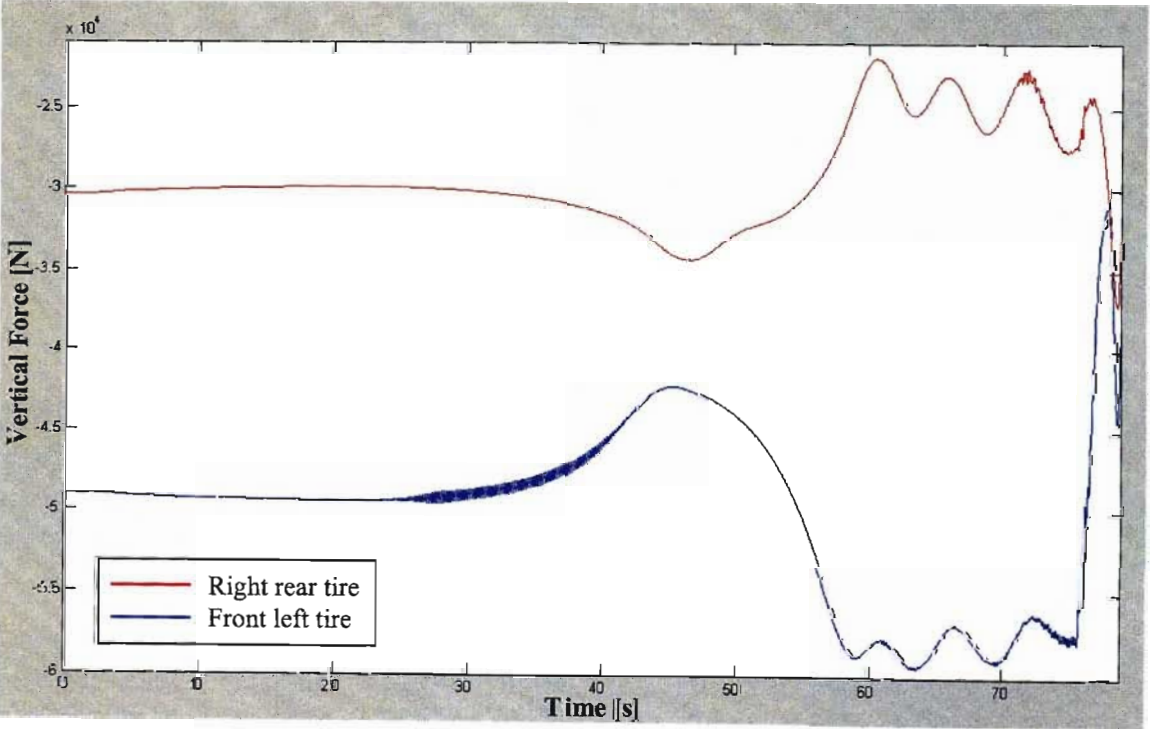


Fig. 5.15 Vertical force at tire contact patch for right rear and front left tire

initial stable part of the simulation when the ADT is accelerating in an approximately straight line, that the tractive effort required to accelerate the ADT would be equally split among the six tires, that would require each tire to contribute approximately 2300N of force. As can be seen in **Fig. 5.13** this is far from the case.

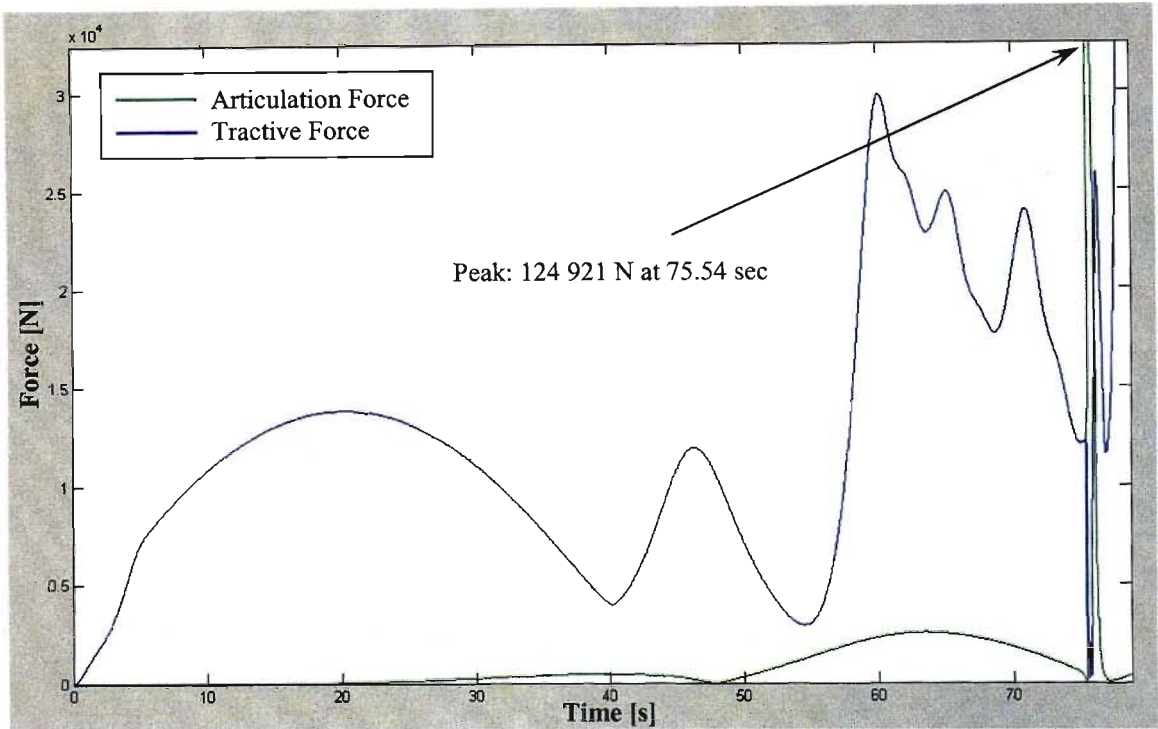


Fig. 5.16 Traction and articulation forces during attempted lane change simulation

In order to analyse further what is taking place at the contact patch, examining the slip angle, the longitudinal slip ratio as well as the dynamically changing frictional coefficient (between static and sliding) provides a better insight. **Fig. 5.17** displays the slip angle developed by the tires in question in addition to the articulation angle, **Fig. 5.18** displays the slip angle verses lateral force developed at the contact patch while **Fig. 5.19** plots the longitudinal slip ratio and **Fig. 5.20** the tire-road frictional coefficient. First to be seen is that the lateral force developed at the tire contact patch is lower than that expected. Also the slip angles are abnormally large. In **Fig. 5.18** which displays the slip angle vs. lateral force, what is highlighted in addition is that the maximum lateral force developed at a large slip angle of 48° is 9 700N for the front left tire. Considering that the lateral stiffness values used in the ADAMS tire property file for the front and rear tires were 10 430 N/deg & 6 977 N/deg respectively it is quite evident that the FIALA tire was not calculating representative values for the lateral forces for the tires. The dynamic frictional coefficient indicted for this simulation in **Fig. 5.20** also indicates that excessive sliding was occurring in the contact patch. The minimum frictional co-efficient for this simulation was 0.55 which is the frictional coefficient at which the tire is in a 100% sliding state and thus not

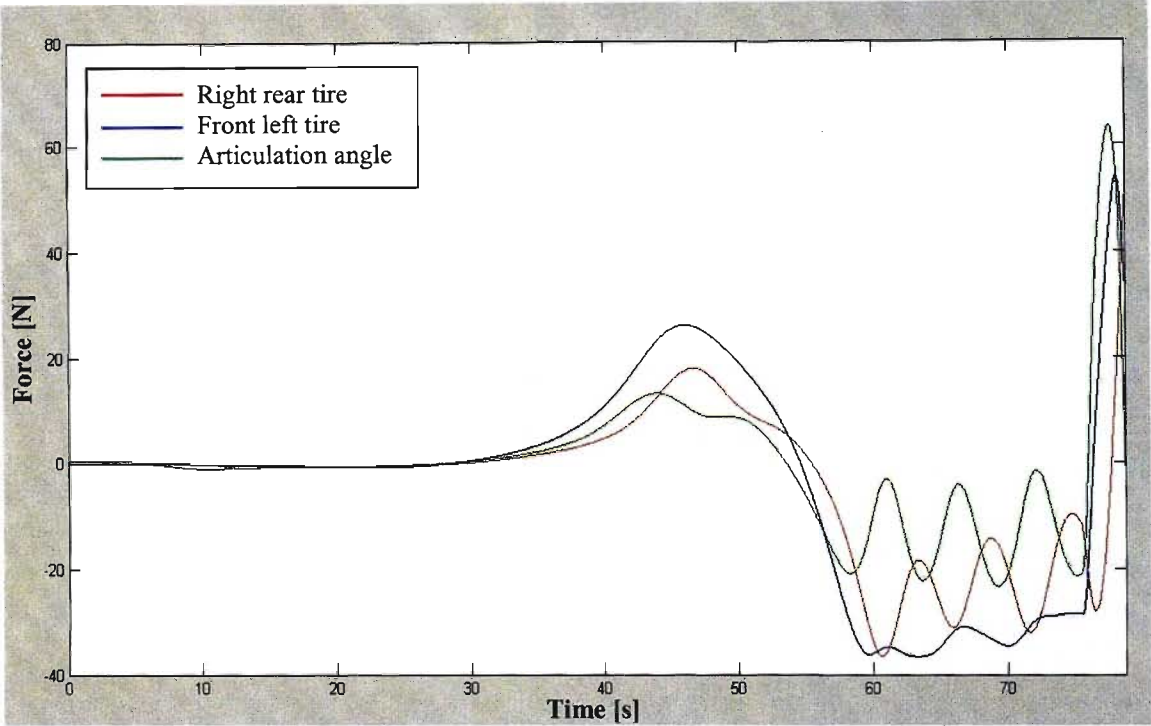


Fig. 5.17 Lateral slip angle of front and rear tires in comparison to articulation angle during attempted lane change simulation

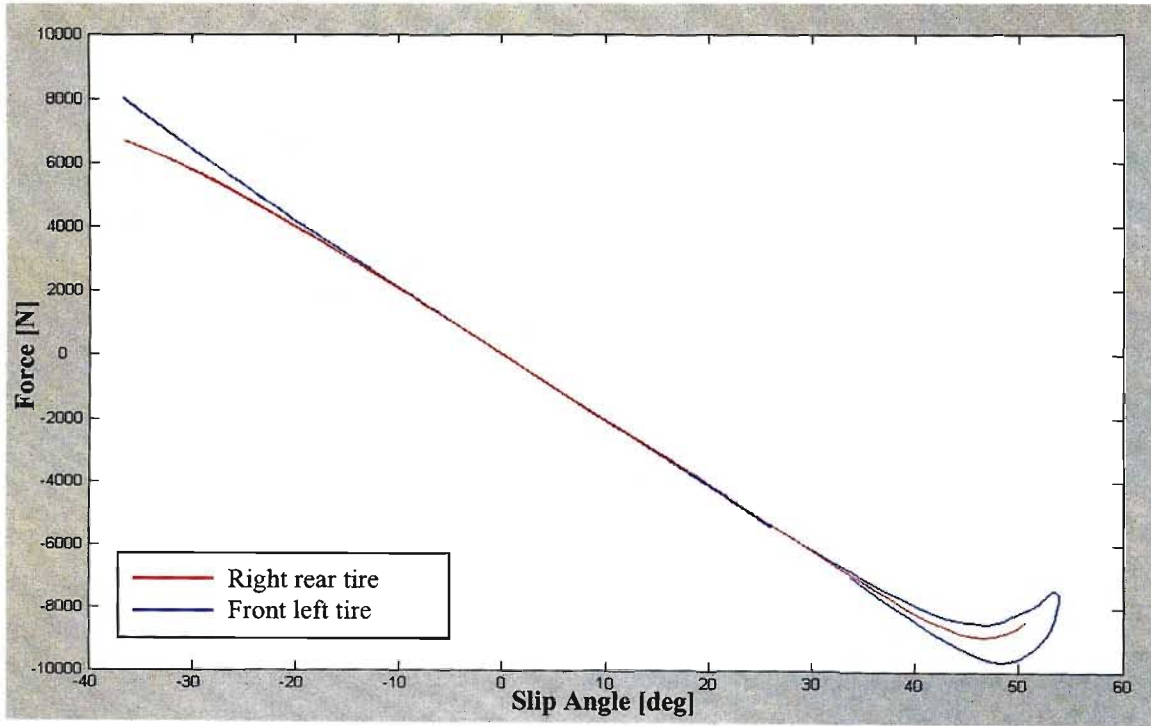


Fig. 5.18 Lateral slip angle of front and rear tires versus developed lateral force at tire patch during attempted lane change simulation

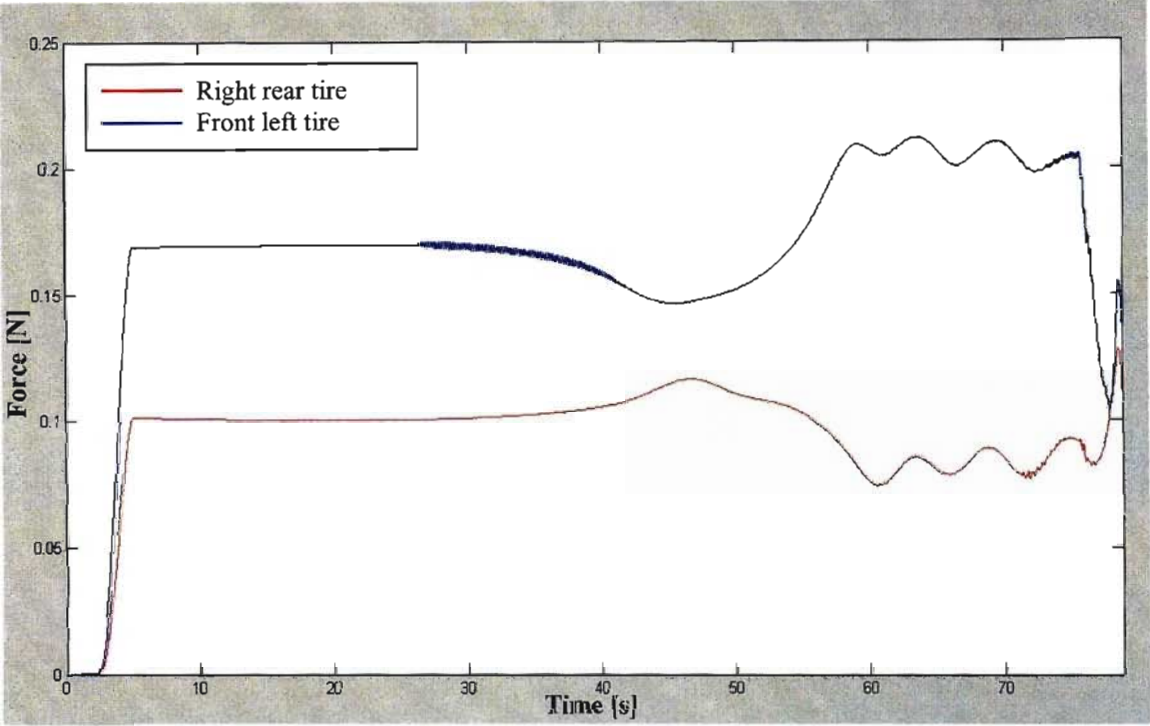


Fig. 5.19 Longitudinal slip ratio of front and rear tires during attempted lane change simulation

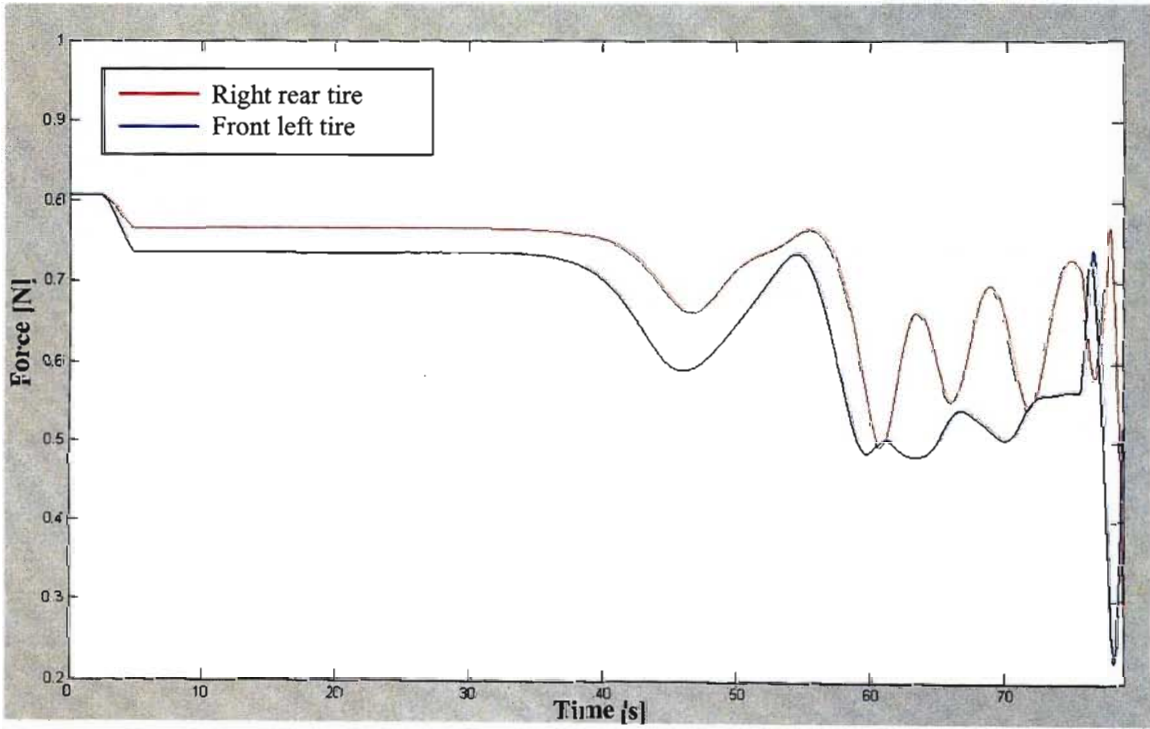


Fig. 5.20 Current coefficient of friction of front and rear tires during attempted lane change simulation

able to develop any further longitudinal or lateral force. From about 58 second of simulation onwards the frictional coefficients of both the front and rear tires were either well below this value or fluctuating about this point. While the ADAMS FIALA model does calculate a comprehensive slip ratio that takes into account both longitudinal and lateral slip properties, the simultaneous effects of lateral and longitudinal slip via the frictional ellipse concept, is not accurately modelled. Also as can be seen from **Fig. 5.18** the lateral force versus slip angle is in large respects (except for very high angles of slip) linear. For a real tire the lateral force vs. absolute slip angle (left and right hand turns) relationship becomes strongly non-linear from $< 3^\circ$ slip angle and the non linearity is exacerbated with changing vertical load conditions. It is thus obvious that the FIALA tire model is a poor tire model choice for the simulation of the BELL EQ. ADT.

A last comment on the results of the lane change simulation is to explain the significance of the low frequency fluctuations in all of the tire forces and kinematic parameters seen above. From approximately 60sec simulation time, a low frequency fluctuation can be observed in all the measured parameters presented above. This can be linked to the tractive force used to control the forward speed of the ADT via the speed controller presented in § 4.5.2. As the path controlling articulation force controller and the speed controller tend to counteract each other, any large outputs from either controller will affect the other. From about 60sec simulation time the speed controlling tractive force fluctuates sharply in its attempt to control the speed of the ADT to the 50km/h set point due to large articulation forces, this can be seen in **Fig. 5.8 & Fig. 5.16**. This fluctuation is hence transferred to all the tire parameters and forces as well as to the ADT front and rear chassis accelerations as well. This effect highlights as well the non-optimal approach of using a single tractive force applied to the vehicle's center of gravity to control the speed. It has the effect of "pulling along a vehicle mass" despite the conflicting physical capabilities of a vehicle's tires. Once a vehicle's tires have reached the saturating limit of lateral and longitudinal adhesion, no further inputs from steering angle and/or engine power and braking retardation *within* the vehicle will act to alter its path. This constraining principle is obviously violated by using the single tractive force control method which can be interpreted as being a completely *external* force.

Bump Test Simulation

The bump test simulation was by far the most unsuccessful simulation attempt. This can be attributed in whole to the incompatibility of the FIALA tire model to the simulation of quasi-discrete events such as the traversing of a bump to which a durability ADAMS tire model is more suited. Various attempts were made to try to overcome the inability to simulate this event which included loosening error tolerances on the ADAMS stiff solver settings and turning off

the speed controller just prior to the bump to exclude the effect of the speed controlling force, without positive results. The initial bump was modelled as a discrete trapezoidal cross-section as displayed in **Fig. 3.3**. This bump was exactly as used during the physical testing and the road data file is displayed in Appendix E-1. It was soon realised that further attempts at simulation using this type of obstacle would not be successful due to the sharp edges offered to the FIALA tire. Thus a road data file was created with a smoother change in elevation. The maximum height and length of the total obstacle were kept at the same dimensions as the trapezoidal cross sectioned obstacle. This road data file is also included in Appendix E-2. This also however brought about no change in the simulation as the simulation still failed without the front tires passing over the bump. The simulation was conducted at the same speed as in the real physical testing, i.e. 10km/h. At the last simulation attempt using the smooth bump road profile the maximum vertical acceleration recorded at simulation failure on the front axle was 118 m/s^2 or 12 g's of vertical acceleration. The maximum vertical acceleration recorded on the physical test for the front axle traversing the trapezoidal cross sectioned bump in the 0 – 100Hz frequency range was less than 1g peak acceleration. It is obvious from this that the FIALA tire model cannot capture the vertical dynamics of the model in response to a discrete road obstacle at even low speeds for the ADAMS ADT model.

Wheel Imbalance Simulation

The final simulation carried out with the model was a simulated wheel imbalance problem. This was in order to investigate the documented bounce and pitch resonance of the BELL EQ. B40 ADT under nominal haulage speeds of 55km/h exacerbated by imbalanced wheels [33]. In this simulation the truck articulation angle was constrained to allow the ADT to move in the straight ahead position (i.e. path controller was disabled and replaced by a zero motion constraint at the articulation joint) and the vehicle speed was gradually brought up from rest to 55km/h (15.26 m/s). To the right front wheel was added an imbalance mass at the periphery of the tire part, of 0.6kg. The simulation step size was $\Delta t = 0.01 \text{ sec}$.

Fig. 5.21 represents the speed profile of the ADT over the simulation period. As can be seen the set speed of 15.26 m/s is reached after 40 seconds. The wheel imbalance frequency at 15.26 m/s is calculated using :-

$$f = \frac{\left(\frac{V}{r}\right)}{2\pi}$$

where V = Vehicle speed [m/s]

r = Tire static loaded radius [m]

f = frequency [Hz]

and is found to be 2.86 Hz with a front tire static loaded radius of 0.849m derived from the Michlen tire charts [44] using the front tire loading condition of 7 tons & 3 bar pressure. The unloaded tire radius is given as 1.850m.

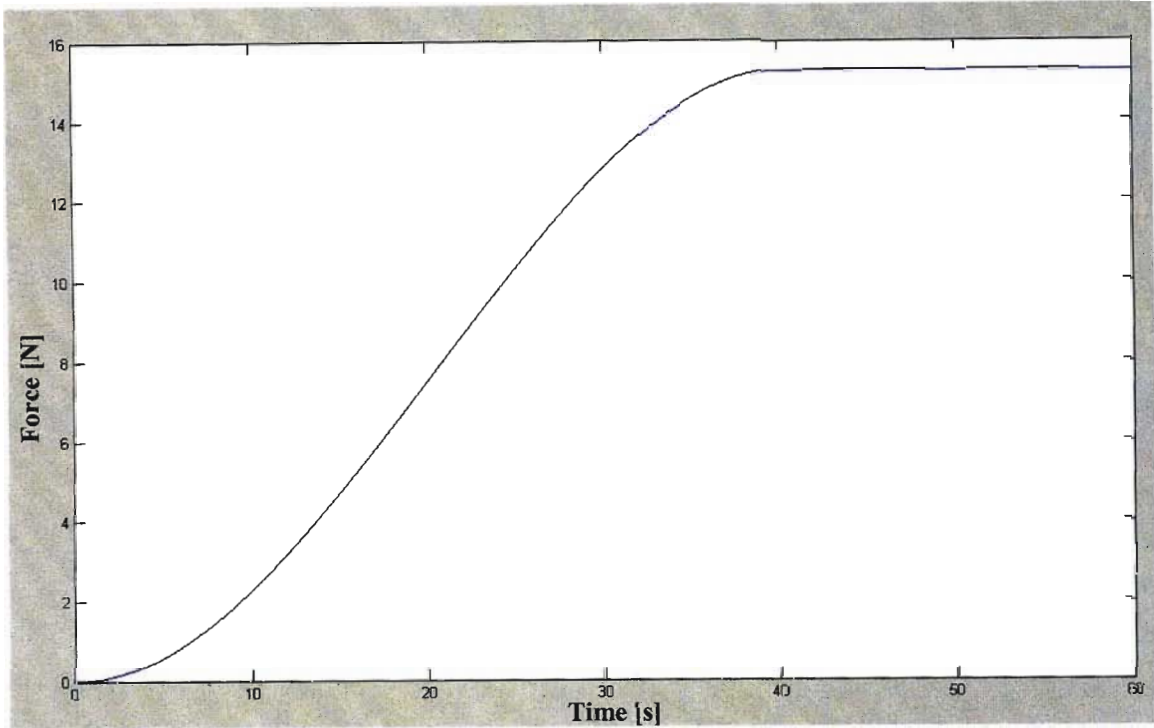


Fig. 5.21 ADT velocity profile during the imbalance simulation

Fig. 5.22 represents the vertical accelerations of the front axle at a point at the RHS wheel attachment point, the front chassis and the cab. Three distinct regions can be identified, a period between 28 & 30 seconds during which the cab has the highest resonance, a period between 33 and 38 seconds during which the front axle has the highest resonance and the period from 40 to 60 during which the “stationary” acceleration signal is developed at a constant vehicle speed of 55km/h. **Fig. 5.23 to Fig 5.25** represent these regions sliced out from the overall time signal.

Fig. 5.26 represents the frequency domain spectrum of the front axle (RHS wheel attachment point), front chassis and the cab for the period 28 – 30 seconds during which time the ADT speed increased from 11.8m/s to 12.9 m/s. The spectrum was calculated in MATLAB using the Welch modified periodogram method with a single FFT calculation ($N_{FFT} = 256$, Hanning window with $N_{WINDOW} = 256$). As can be seen the cab and front chassis have a vertical bounce resonance at 1.56Hz. The front axle vertical acceleration (RHS wheel attachment point) peaks at this frequency as well but the source of the vibration, from the imbalanced wheel is still lower than the cab and front chassis vertical vibration, hence indicating some resonance behaviour in the cab and front chassis. A second strong peak at 5.47 Hz for the front axle indicates another

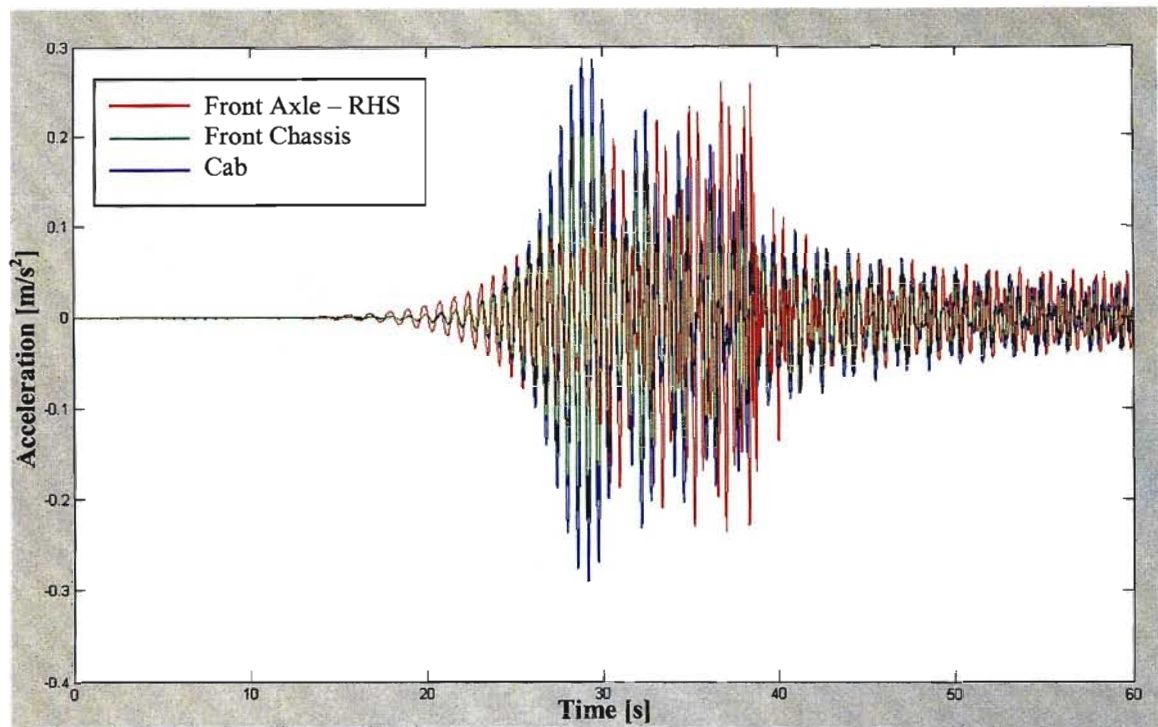


Fig. 5.22 Vertical accelerations of the front axle RHS wheel attachment point, the front chassis and the cab during the imbalance simulation

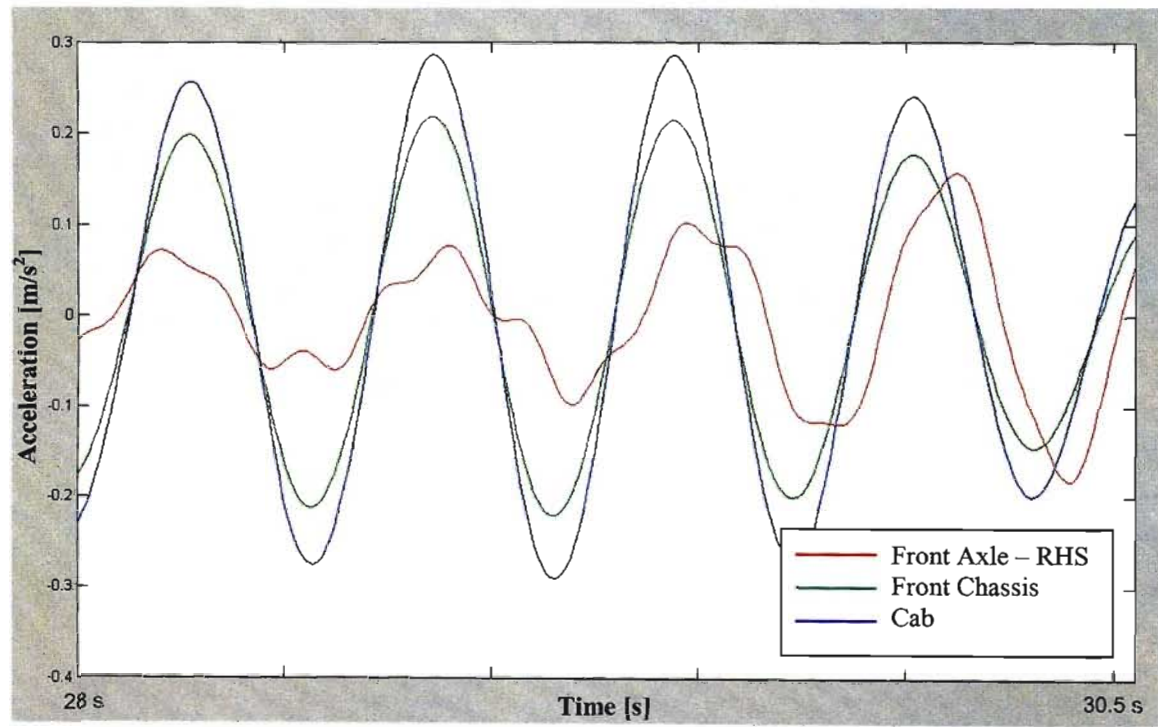


Fig. 5.23 Vertical accelerations of the front axle RHS wheel attachment point, the front chassis and the cab for the simulation period 28 – 30 seconds

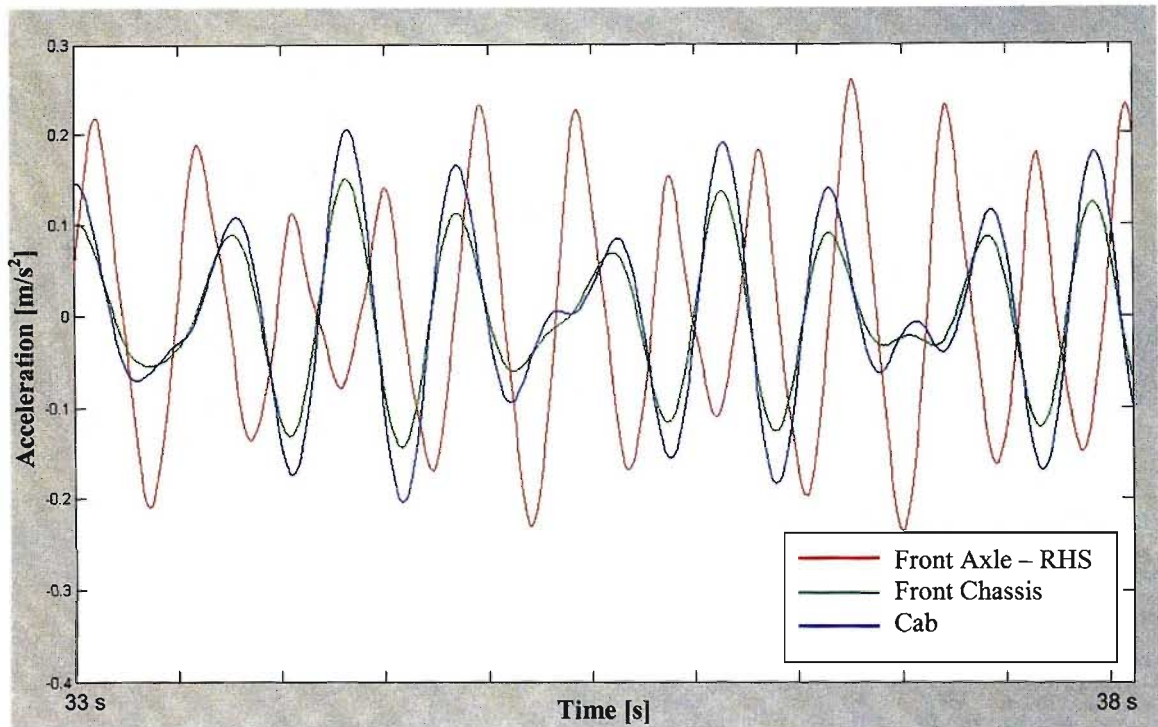


Fig. 5.24 Vertical accelerations of the front axle RHS wheel attachment point, the front chassis and the cab for the simulation period 33 – 38 seconds

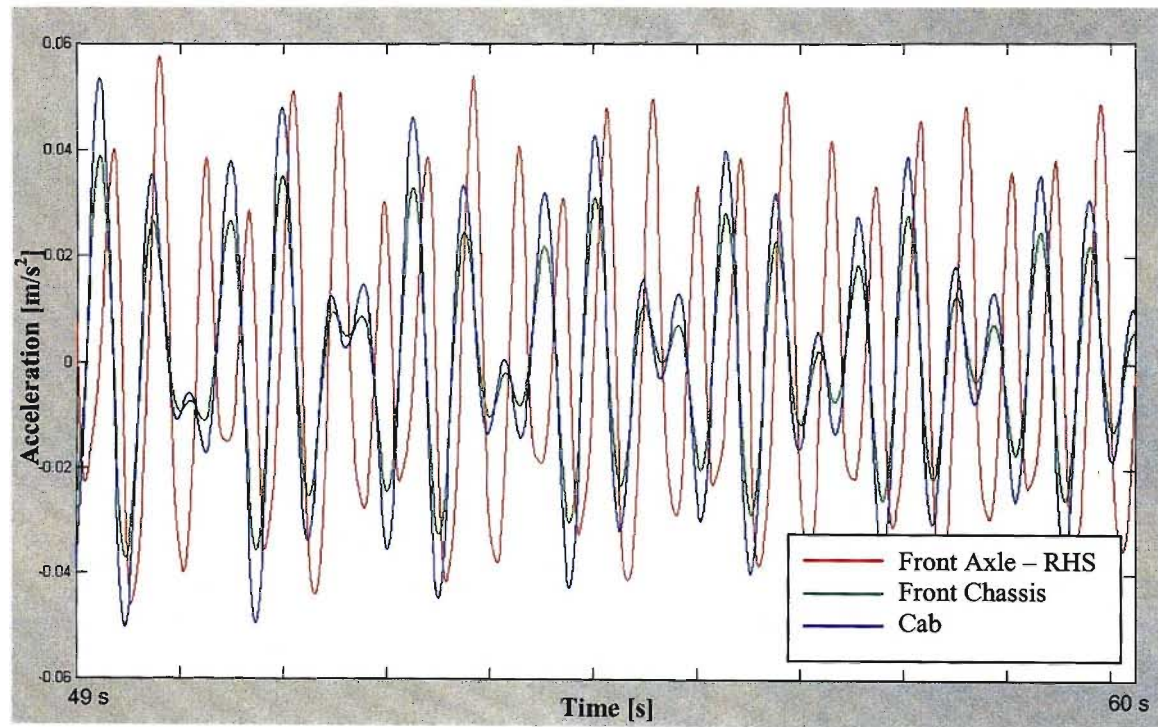


Fig. 5.25 Vertical accelerations of the front axle RHS wheel attachment point, the front chassis and the cab for the simulation period 49 – 60 seconds

resonance frequency of the front axle however this does not carry through strongly to the cab and the front chassis. Of concern here is that for the average speed of 12.35m/s during this simulation period the imbalance frequency would need to be 2.32Hz given a static rolling radius of 0.849m. The FFT resolution given a simulation step size of 0.01sec (hence a sampling frequency of 100Hz) and an FFT block size of 256 is 0.39Hz and more than sufficient to resolve a frequency at 2.32Hz given that the closest peaks are at 1.56Hz and 3.71Hz. This however does not show up. In fact in all further calculated FFT spectra of the vertical accelerations, the fundamental theoretical imbalance frequency does not show up. This can only be ascribed to a slipping and not rolling tire once again highlighting the non-optimal method of using a single tractive force attached to the COG of the vehicle as the prime tractive mover. In fact the lowest dominant frequency should be the imbalance frequency. Further indication that the wheels were slipping excessively is that should non-slip conditions be assumed, then the lowest significant frequency component (imbalance frequency) at the vehicle speeds during the particular analysis periods, would result in tire loaded radii of over 1m in all scenarios which is obviously not possible.

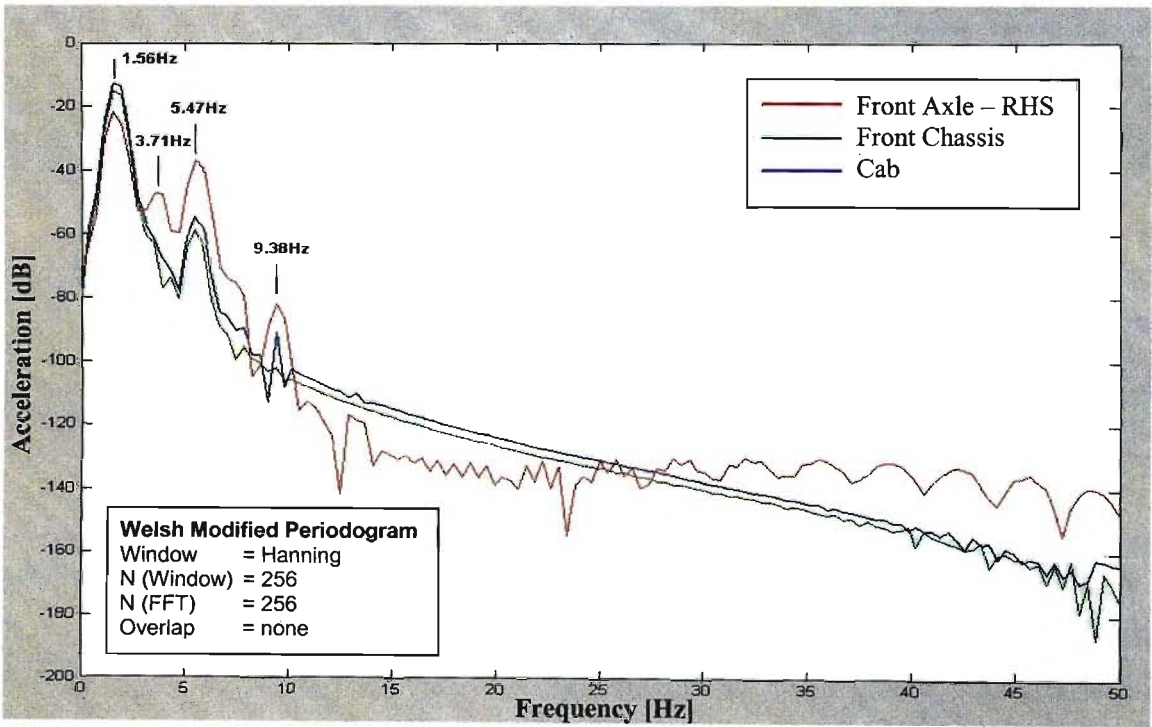


Fig. 5.26 PSD of the vertical accelerations of the front axle RHS wheel attachment point, the front chassis and the cab for the simulation period 28 – 30 seconds

Fig. 5.27 represents the second region of the simulation during which the front axle has the highest vertical vibration measurements. During this period from 33 – 38 seconds, the vehicle's speed increased from 14.0 m/s to 15.15m/s. As can be seen the 1.56Hz peak still exists for the cab and front chassis even though the imbalance fundamental has increased to 2.15Hz (as evidenced from the spectrum of the front axle RHS wheel attachment point acceleration) due to the increase speed of the vehicle. This confirms that the cab and front chassis have a bounce resonance at 1.56Hz. The front axle vertical acceleration spectrum shows some strong second and third wheel rotation order harmonics not evidenced before at lower speeds which could indicate that 2.15Hz is a resonance point of the front axle.

Fig. 5.28 shows the vertical acceleration spectra of the above mentioned ADT rigid body members (cab, front chassis & front axle) for a constant speed of 55km/h. The vibration levels among all three parts are now very similar even if not all in phase, or even having the same waveforms as can be seen in **Fig. 5.25**. An interesting development here is the close spacing of the two strong spectral peaks at 1.66Hz and 2.34Hz. The 2.34Hz is the fundamental imbalance frequency while the 1.66Hz frequency component is mostly likely an attenuated first bounce mode of the cab and front chassis, with the frequency slightly higher now than the 1.56Hz seen earlier. The two fundamental vibration modes seem to exert equal influence on each of the three parts in concern and results in two very strong and approximately equal amplitude peaks across all three rigid bodies (cab, front chassis and front axle). This results in the beat phenomenon and can be seen in the time waveform for this time period. Once again the front axle has many strong imbalance harmonics at this higher speed and seems to be the largest source of vertical resonance type vibration at higher speeds.

With regards the vibration modes on the axles it was noted that the middle and rear axles all had vertical accelerations across the length of the axles that were first of a much smaller order of magnitude than the front axle (of the order of 0.015m/s^2) and which were in phase i.e. the axles did not have any roll motion. The front axle however did have a non-constant phase across its length indicating that it had a roll motion and that in addition to the vertical bounce motion some roll mode resonance was also excited by the out of balance wheel.

In addition to the vertical bounce motion the ADT also displayed a pitching motion. The pitch of the ADT (the same for the front and rear chassis as they have no independent pitch degrees of freedom) is displayed in **Fig. 5.29**. The pitch frequency spectrum, shown in **Fig. 5.30** is very similar to the vertical bounce of the front chassis especially as regards the fundamental lower frequency signal components. The large DC component evident in the pitch frequency spectrum is due to the steady state pitch angle of the chassis. Upon examining the rear chassis bounce

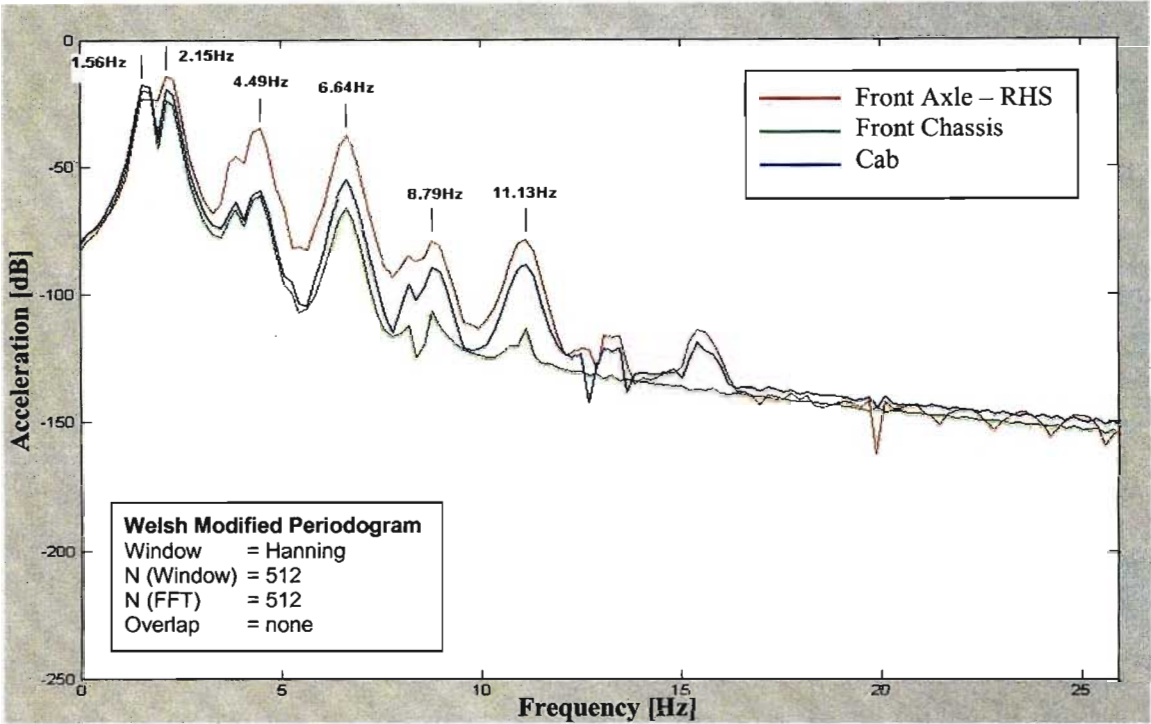


Fig. 5.27 PSD of the vertical accelerations of the front axle RHS wheel attachment point, the front chassis and the cab for the simulation period 33 – 38 seconds

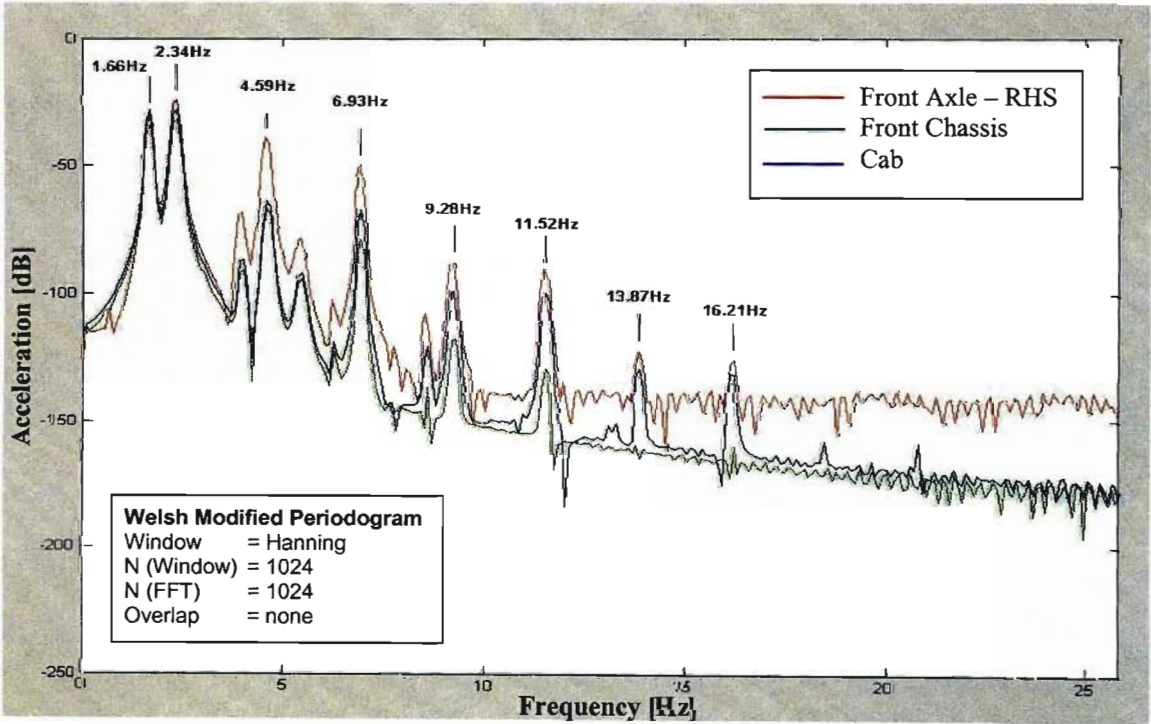


Fig. 5.28 PSD of the vertical accelerations of the front axle RHS wheel attachment point, the front chassis and the cab for the simulation period 49 – 60 seconds

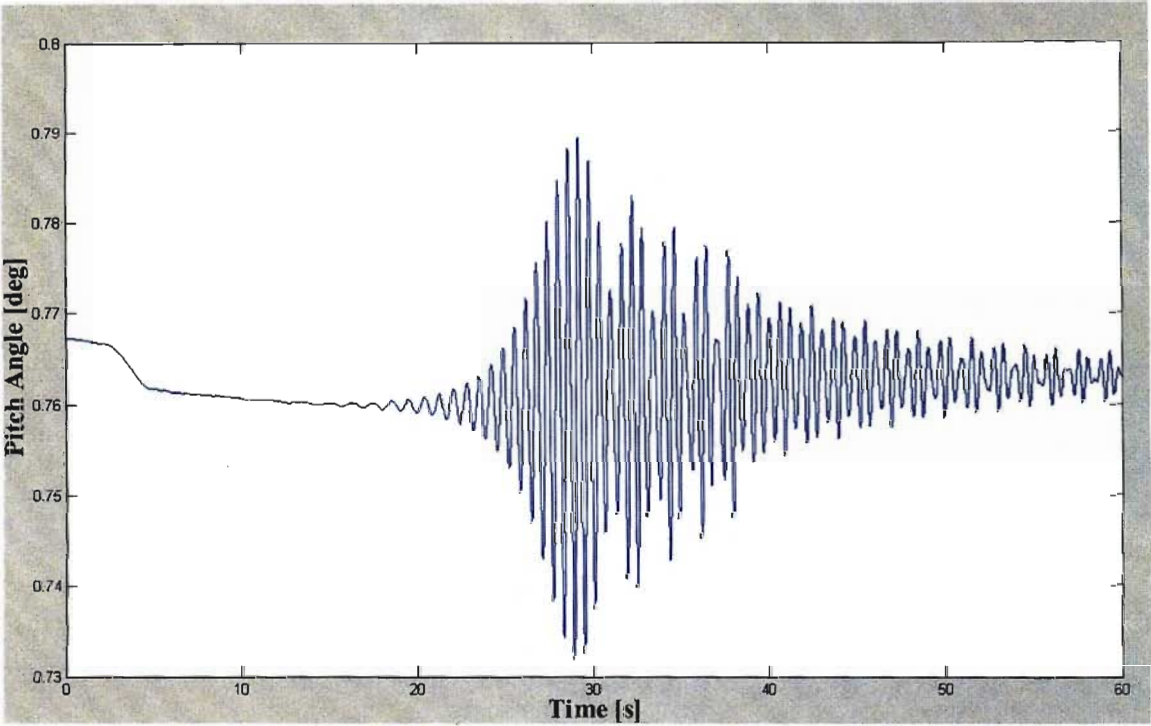


Fig. 5.29 ADT pitch angle waveform for the entire imbalance simulation

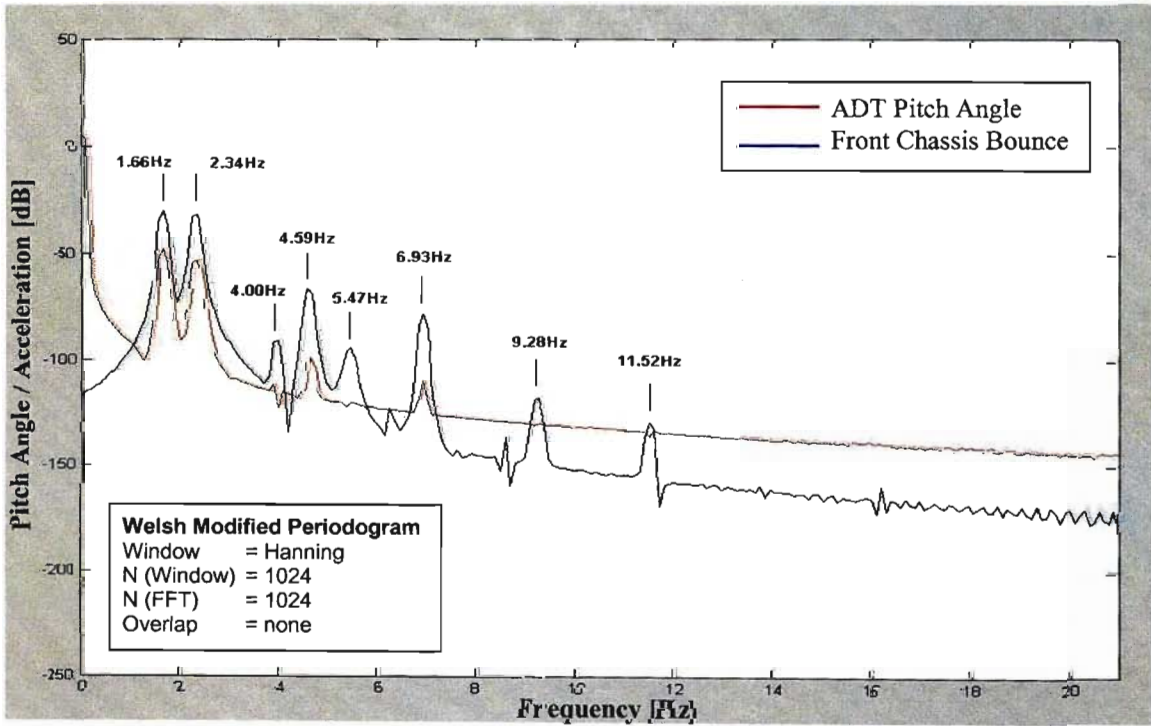


Fig. 5.30 PSD of the vertical acceleration of the front chassis and the ADT pitch angle for the simulation period 49 – 60 seconds

signal (see **Fig. 5.31**) the reason for this becomes clear. The rear chassis bounce is much smaller than the front and has an approximately sinusoidal waveform (of the frequency of the fundamental rotating imbalance on the front wheel) which indicates that the rear chassis bounce frequency or frequencies are not excited by the rotating imbalance of an ADT wheel. Thus the pitching motion, which is admittedly quite small (of the range of 0.05°) for this imbalance weight, stems from the vertical bounce of the front chassis and the relatively fixed position of the rear chassis.

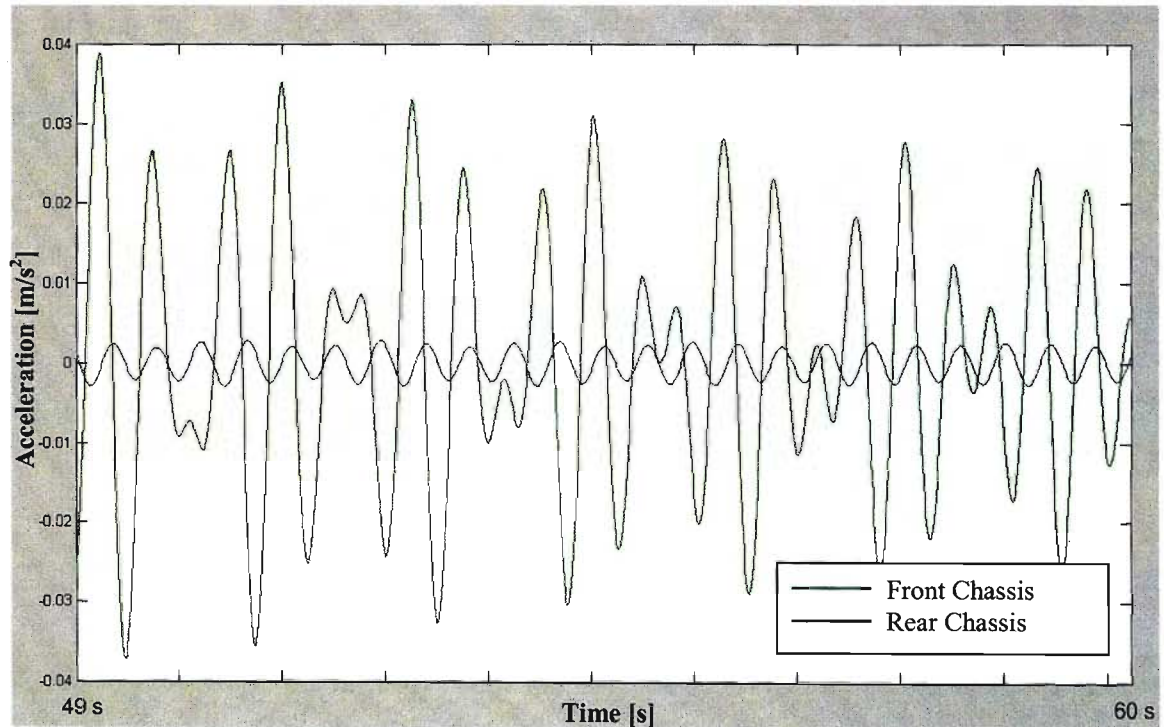


Fig. 5.31 Vertical accelerations of the ADT front and rear chassis' (bounce mode) for the simulation period 49 – 60 seconds

6. CONCLUSION

Virtual prototyping has taken on an increasingly critical role in the modern automotive industry. The earthmoving and construction machinery industry, as a specialized subset of automotive engineering is no different. Faster times to market, the ability to respond quickly to a global customer base and stringent modern legal requirements on safety and environmental issues has driven the virtual prototyping wave with its unique ability to save time and costs. This project represents a first attempt at introducing mechanical dynamic systems virtual prototyping, with specific regards to the vehicle dynamics of the 40 ton ADT, to BELL Equipment.

In the preceding pages, the first steps in the virtual prototyping of the BELL EQ. B40C ADT are presented. The ADAMS virtual prototyping software environment was presented and the construction of the ADT in ADAMS is detailed. The ability to construct the multibody system model graphically by replicating the geometry of the actual physical vehicle and to connect them via various connectors that represent the behaviour of the interacting bodies, greatly simplifies the process of synthesising the mathematical model of the vehicle dynamics of the ADT. While the construction of the model is time consuming with regards having to construct a three dimensional model, it represents the simplest part of the virtual prototyping process. By specifying the geometrical and inertial properties of the various bodies that make up the multibody (ADAMS automatically calculates this from the imported 3-D geometry), the synthesis of the equations of motion (EOM) is easily accomplished by the software. The various multibody formalisms that are used to synthesis the EOM have been well developed during the last century (see § 1.). The difficulty in replicating reality is to be found in the various joints and connectors of the various bodies in real vehicles. These are highly non-linear sub-systems and display hysteresis and sharp discontinuities, which are extremely problematic for the stability of the numerical solver routines available to solve the large number of EOM that full vehicle multibody models generate. In addition their behaviour varies with frequency as well. Traditional methods of frequency modelling and analysis are linear methods and preclude the modelling of the large scale non-linearity present in various automotive compliant components, while modelling non-linearity precludes the inclusion of frequency effects. Even though some recent applications of neural network theory has proved extremely successful in capturing the non-linearity's and frequency behaviour of automotive compliant components (see § 2.2), it is beyond the scope of this work and in general represents a significant investment in cost as the methods are proprietary and not available in the general literature.

It is still possible however to represent the compliant effects of the rigid body connectors in meaningful form by making some simplifying assumptions. For example the approach adopted with this work was to consider the compliant components as non-linear yet static components, i.e. no frequency modifying behaviour, as the vehicle dynamic problem especially with regards handling is largely quasi-static with large scale non linear displacements. Even then significant investment in time is required to characterise the components in terms of their stiffness and damping. As an indication an undergraduate project instituted in conjunction with this work to characterise the compliant components of the BELL EQ. ADT (see § 4.3), required a year to complete the testing of the components under various load and frequency conditions.

Another compliant component that is crucial to the accurate virtual modelling of a vehicle is the pneumatic tire. With an inaccurately modelled tire, force inputs to the rest of the system are incorrect and subsequent overall system behaviour in terms of vehicle handling is compromised. Section 2.1 details the behaviour of the pneumatic tire and gives an indication of the complications involved in modelling the tire. The development of a new tire model was beyond the scope of this project so effort was directed towards the understanding the Fiala tire model and developing its use for this project. The Fiala tire model is an analytical tire model that is part of the ADAMS Full Simulation package. It was initially considered to be adequate for a first approximation of the modelling of the ADT as discussed in the preceding pages. However it fails to fully represent the dynamics of the tire due to its simplified analytical nature. It assumes for example that the contact patch of the tire is rectangular and that pressure distribution is uniform across the contact patch. It also ignores the affects of camber in modifying the remaining tire forces and moments. Transient effects are not modelled so the model does not capture the lag in tire forces from the initial input. It is also not able to handle combined longitudinal and lateral slip and so limit handling behaviour is not well represented.

The derivation of the various input parameters for the Fiala tire model as used on the ADAMS MBS model of the ADT is detailed in § 4.4.1. While these parameters represent valid inputs for the Fiala tire model of the ADT's tires, the model itself proved to be completely inadequate in simulations carried out. Section 5.2 detailed results from the simulations and showed that in a handling type simulation such as the single lane change event the lateral tire forces generated were much below the expected values. This in addition to a non optimal path controller meant that the ADT was not able follow the lane change path. Perhaps the most accurate tire model to be considered in future work is the empirical model known as the 'Magic Formula' and discussed in § 2.1. While in essence a steady state model, numerous adaptations have been made to include the effects of combined slip and transient effects. Future work on the virtual

prototyping of the ADT should consider this type of tyre model as the first choice to fully represent the forces generated by the tire.

In addition for simulations that involve tire impacts with discrete events, the Fiala tire model was completely inadequate for use with the ADT model. Despite numerous attempts at simulations with changed simulation parameters and loosening the tolerances of the simulation no successful simulation of the ADT bump event, as conducted during the physical testing program, was possible. It is obvious that for simulations of this nature tire models more suitable, such as the Durability Tire model, must be considered.

For handling simulations, an accurate vehicle path controller is required. Section 4.5 detailed the development of two controllers that were used to control the speed and path heading of the ADT. The inability of the controllers to accurately control the ADT's path and speed to the chosen set points indicate the difficulty of developing these controllers within the ADAMS Basic Simulation environment. These controllers are however critical if real vehicle dynamics manoeuvres are to be carried out. Future work should concentrate on using the built in controllers for standard vehicle dynamics manoeuvres available within the ADAMS/Car environment. These purpose built controllers are easier to implement and have been tested before hand. While the methodology presented in § 4.5 of developing the controllers with the ADAMS/View Controls Toolkit is workable, much more effort would need to be expended in developing a controller with inter-dependent speed and path controlling terms as well as to design the controller such that the chosen parameters consider the ADT model during the initial controller design phase.

Future work should first proceed by simulating the rigid body model of the ADT as it exists and results should then be compared to the results of the physical testing. The model parameters such as suspension stiffness and damping should be modified and the tire model improved till confidence is obtained in the accuracy of the virtual model. The path and speed controllers are obviously a definite must. The model should then be gradually increased in complexity by including the effects of compliance to significant areas of the suspension and ADT frame and chassis. Future uses of a validated vehicle dynamics model could include investigating power-train effects such driveline chuggle, and hydraulic sub-systems such as the steering and braking system. This would allow for the development and specification of sub-systems in future model derivatives or to allow development of existing systems.

APPENDIX A

Methodology used by Undergraduate Student Project to calculate Damping Coefficient [61]

Pages 29 - 31

“The loss factor is defined as the ratio of the lost energy during a cycle, W , to be the peak potential energy, U , stored in the system during that cycle, multiplied by 2π ,

$$\eta = \frac{W}{2\pi U}$$

Where: $W = \pi F_o X_o \cos(\delta)$

$$U = \frac{1}{2} F_o X_o \cos(\delta)$$

δ = phase lag between F (force) and X (displacement)

Giving a loss factor : $\eta = \tan(\delta)$

This is the common way of characterizing rubber damping, and requires a single and constant phase lag between input and response. It also requires that the system be linear.

Viscous Damping

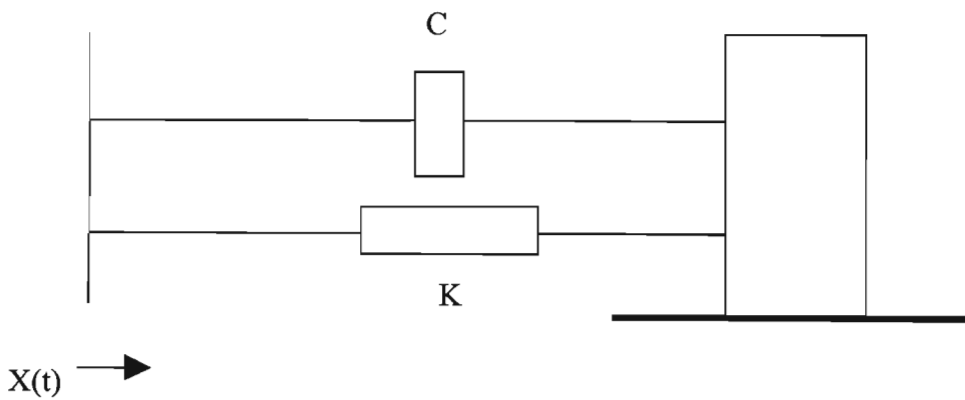


Figure 6.6 Viscous damping model

The net force acting on a single degree of freedom mass is given by:

$$F(t) + K \cdot X(t) + C \cdot \frac{dX(t)}{dt}$$

Letting : $F_d = C \frac{dX(t)}{dt}$ and $v = \frac{dX(t)}{dt}$, gives the energy dissipated due to damping in one cycle as:

$$W = \int_0^T F_d dx = \int_0^{\frac{2\pi}{\omega}} \left(\frac{C \cdot v dx}{dt} \right) dt = \int_0^{\frac{2\pi}{\omega}} C \cdot v^2 dt = \pi \cdot C \cdot \omega \cdot X_o^2$$

Yielding : $C = \frac{W}{\pi \omega X_o^2}$

where C is in Ns/m.

The potential energy in the system is given by : $U = \frac{1}{2} kX^2$

Giving a loss factor: $\eta = \frac{\pi C \omega X_o^2}{2\pi \cdot \frac{1}{2} k X_o^2} = \frac{C \omega}{K}$

where K = stiffness

Plotting the force against velocity gives the following graph:

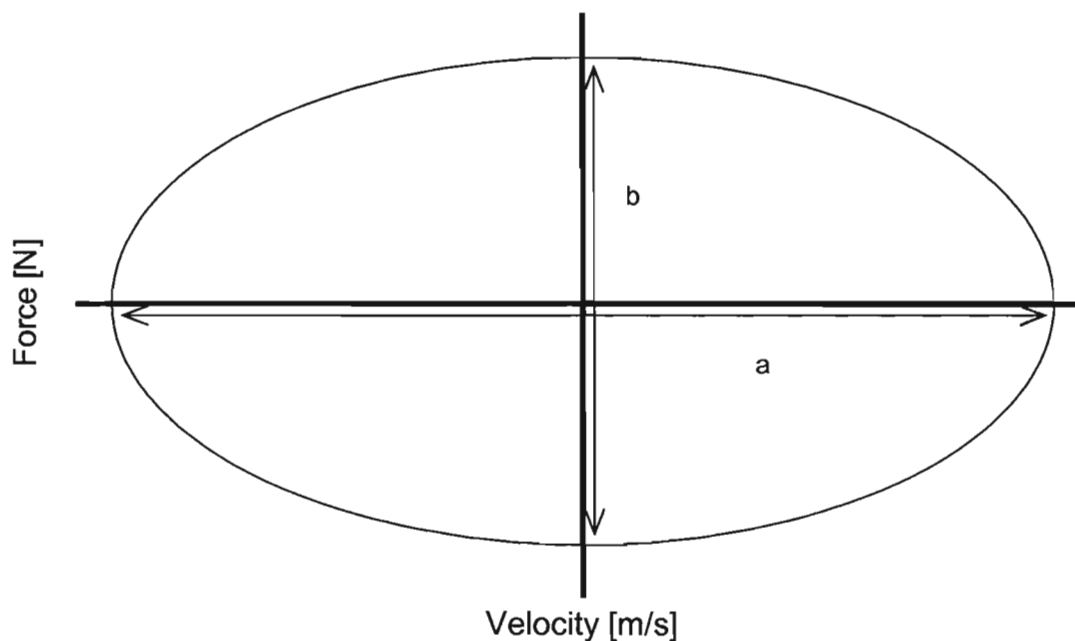


Figure 6.7 Force-Velocity hysteresis loop of rubber component: Sandwich block test data

From the area of this loop is equivalent to the power dissipated in one cycle. Thus the work dissipated in the cycle will be equivalent to the area multiplied by the time for one cycle. This is the method used in this project to evaluate the work dissipated in one cycle. An ellipse can approximate the area of this loop.

$$A_{loop} = \frac{\pi}{4} ab \quad "$$

APPENDIX B

MATLAB script file used to calculate stiffness and damping values for compliant suspension components from test data

```

Freq = 1           % Test frequency *** MUST FILL THIS IN BEFORE
                   % RUNNING SCRIPT FILE
Period = 1/Freq;   % Test period
tf = 2;            % Time duration of data loaded ==> load first
                   % three periods - use only one
fs = 1000;         % Data Acquisition Sampling frequency

load sbf1118       % Test file *** MUST FILL THIS IN BEFORE RUNNING
                   % SCRIPT FILE
j = 11;            % Pointer for array of values for each file - Vary
                   % this manually for each new file loaded

figure (1)

% Important:- Systems which have a true "zero,zero" point
% gives the graph a third zero crossing which leads to the
% wrong calculation in the if loops for the parameter "b"
% so must chop off the first part of the graphs if this is the case

F=-10.136*(A(1:tf*fs,2))*1e3; % Force vector in Newtons
X=-10.239*(A(1:tf*fs,3))*1e-3; % Displacement vector in metres
t = 0:1/fs:(tf - 1/fs);      % Original time vector for data loaded
plot (X,F,'b');
xlabel ('RAW DISPL [m]');
ylabel ('RAW FORCE [N]');
hold on;

% Spline does not "clean up" the raw data too well
fs_new = 10000;              % New sampling frequency
ts = 0:(1/fs_new):(tf - 1/fs_new);
F_new = spline(t,F,ts);
X_new = spline(t,X,ts);
plot(X_new,F_new,'r');
xlabel ('Spline DISPL [m]');
ylabel ('Spline FORCE [N]');

```



```

hold on;

% Poly fit gives a smoother loop curve of the raw data than the spline

F_Poly = polyfit(ts,F_new,12); % Can't use original 'F' and 'X'
                                % vectors as they must have same length
                                % as 'ts' so must used splined vectors

F_new_poly = polyval(F_Poly,ts);
X_Poly = polyfit(ts,X_new,12);
X_new_poly = polyval(X_Poly,ts);
plot(X_new_poly,F_new_poly,'g');
xlabel ('PolyFit DISPL [m]');
ylabel ('PolyFit FORCE [N]');

% Plots of displacement verses time
figure (2)
plot (t,X,'b*')
hold on;
plot (ts,X_new,'r')
hold on;
plot (ts,X_new_poly,'g>')
xlabel ('Time [s]');
ylabel ('Displ [m]');
hold off;

% Plots of Force verses time
figure (3)
plot (t,F,'b*')
hold on;
plot (ts,F_new,'r')
hold on;
plot (ts,F_new_poly,'g>')
xlabel ('Time [s]');
ylabel ('Force [F]');
hold off;

```

```

t_1 = length (t);
ts_1 = length (ts);

t(t_1);
ts(ts_1);

% *****
% Damping and stiffness calculation
% *****

X_t = X_new_poly';      % X Polynomial transposed
F_t = F_new_poly';      % F Polynomial transposed

q_p = Period*0.25;      % Quarter period
oq_p = Period*1.25;     % One and quarter period

index_1 = round(q_p*fs_new);
index_2 = round(oq_p*fs_new);

X_calc = X_t(index_1:index_2);    % one period in middle of poly-
                                   % fitted data loaded for
                                   % calculations
F_calc = F_t(index_1:index_2);    % one period in middle of poly-
                                   % fitted data loaded for
                                   % calculations

A2 = [X_calc F_calc];

figure (4)
plot (X_calc,F_calc);

Fmax = max(F_calc);
Fmin = min(F_calc);
Fave = (Fmax + Fmin)/2;
F_Peak_Peak = Fmax - Fmin;

Dmax = max(X_calc);
Dmin = min(X_calc);
Dave = (Dmax + Dmin)/2;
D_Peak_Peak = Dmax - Dmin;

```

```

len = length (A2);

dummy_1 = 100e6;
for n = 1:len
    if A2(n,1) < Dave                % First loop gets left or right
                                      % side of graph

        diff_1 = A2(n,2) - Fave;
        abs_diff_1 = abs(diff_1);
        if abs_diff_1 < dummy_1      % Second loop tries to
                                      % find Force average
                                      % crossing to get
                                      % displacement

            d_1 = n;
            dummy_1 = abs_diff_1;
        end;
    end;
end;

dummy_2 = 100e6;
for k = 1:len
    if A2(k,1) > Dave;
        diff_2 = A2(k,2) - Fave;
        abs_diff_2 = abs(diff_2);
        if abs_diff_2 < dummy_2
            d_2 = k;
            dummy_2 = abs_diff_2;
        end;
    end;
end;

Stiffness = (Fmax - Fmin) / (Dmax - Dmin);

Sin_phi = ((A2(d_2,1) - A2(d_1,1)) / 2) / (Dmax - Dave);

Omega = 2*pi*Freq;

Damping = (Stiffness * Sin_phi) / Omega;

```

```

% *****
% ARRAY OF VALUES FOR EACH DATA FILE READ IN
% *****

fmx(j,1) = Fmax;
fmn(j,1) = Fmin;
fpp(j,1) = F_Peak_Peak;

dmx(j,1) = Dmax;
dmn(j,1) = Dmin;
dpp(j,1) = D_Peak_Peak;

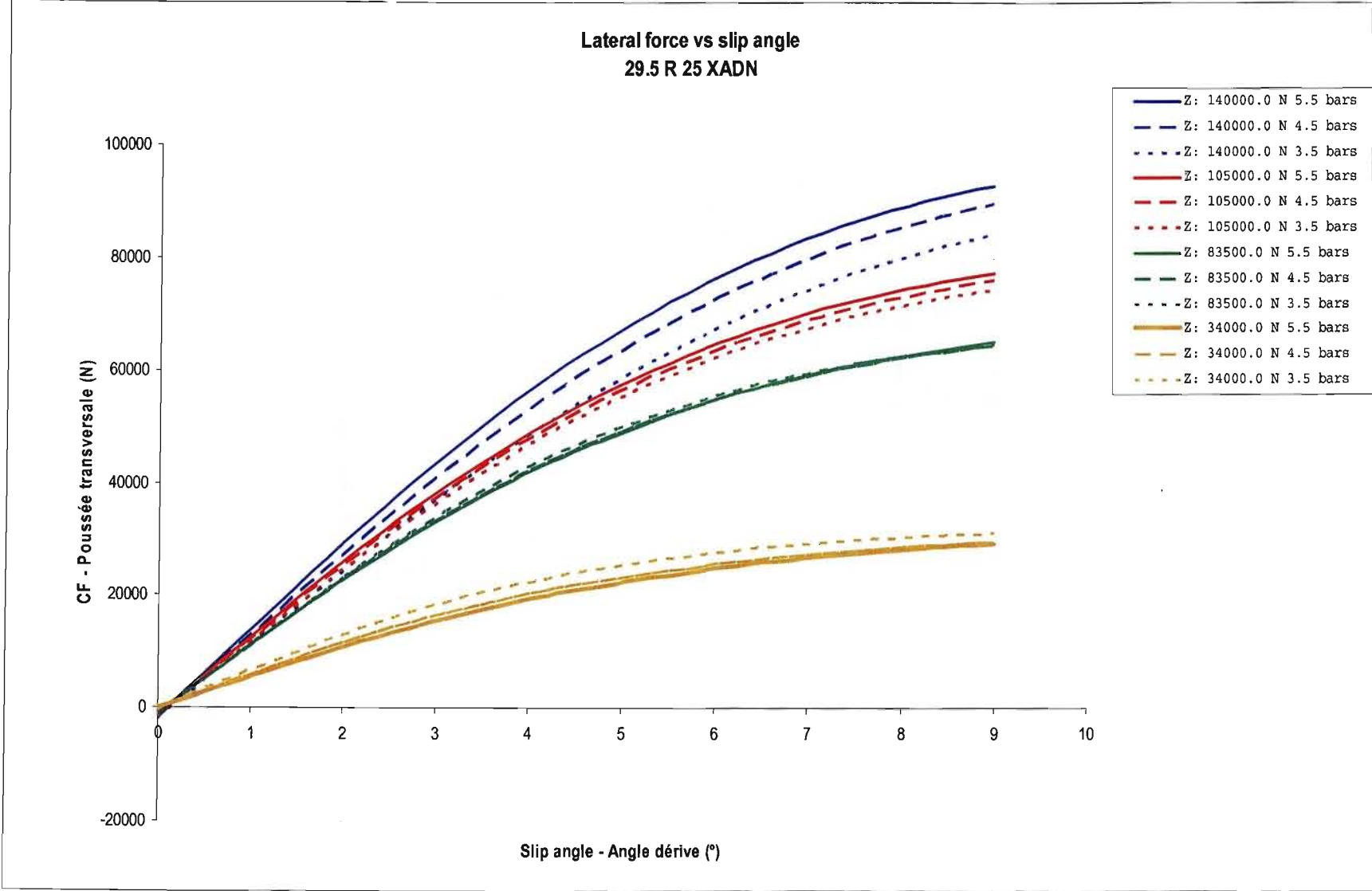
stiff(j,1) = Stiffness;
damp(j,1) = Damping;

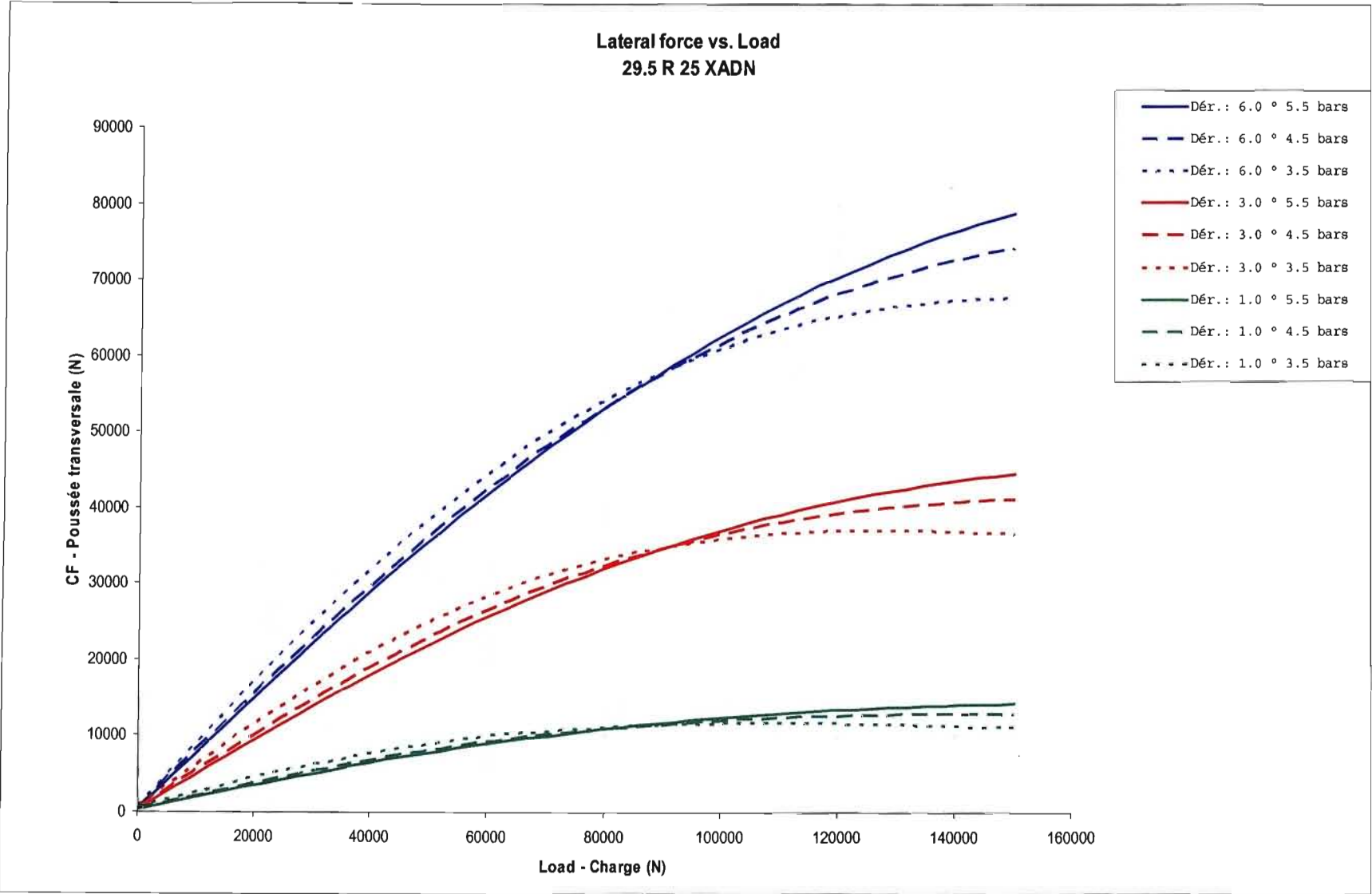
ARRAY = [fmx fmn fpp dmx dmn dpp stiff damp]

```

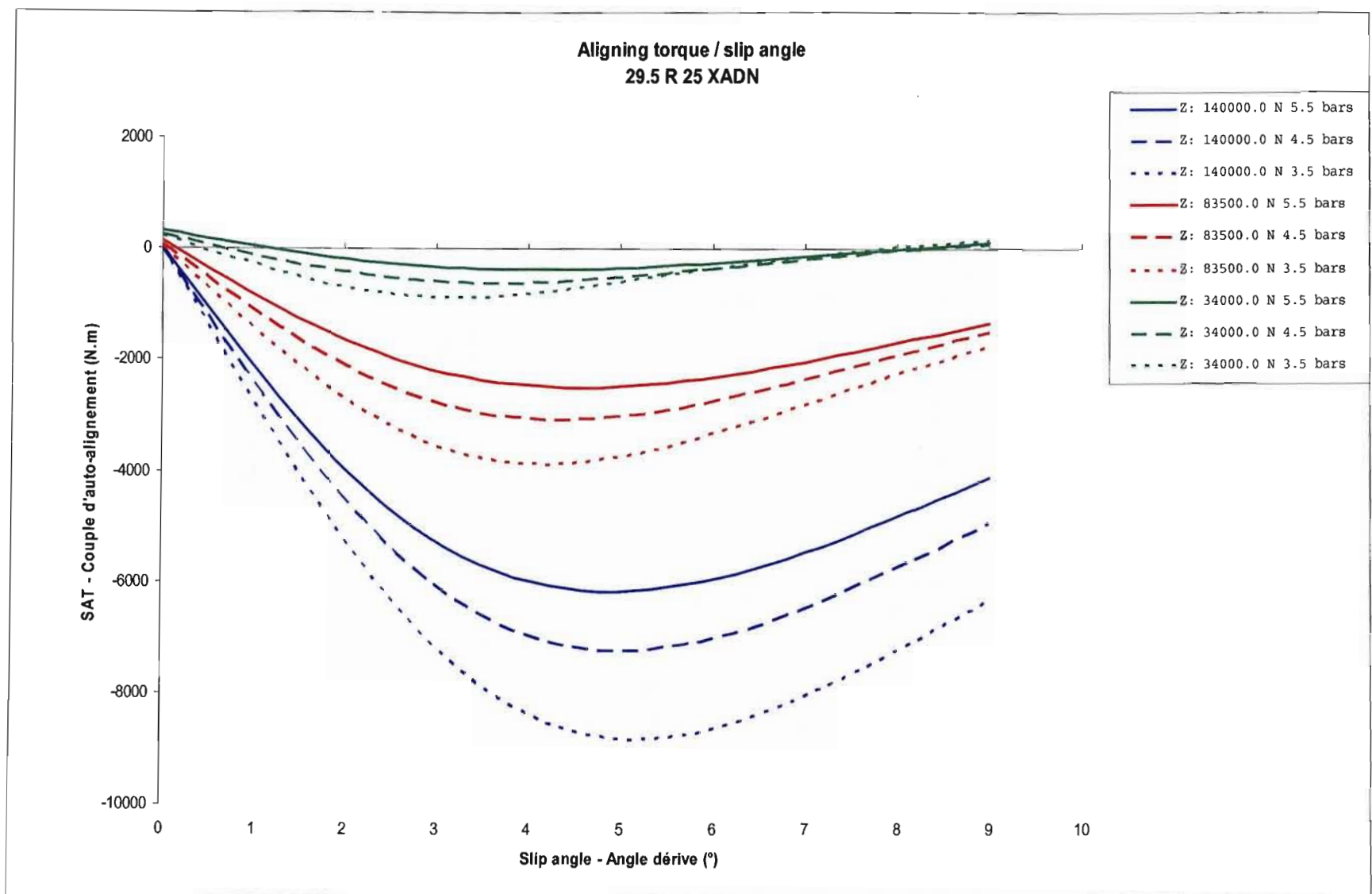
APPENDIX C

C-1. Lateral Force vs. Slip angle curves for the 29.5R25 XADN E3T TL 200B tyre [44]





C-2. Lateral Force vs. Vertical load curves for the 29.5R25 XADN E3T TL 200B tyre [44]



C-3. *Aligning Torque vs. Slip Angle curves for the 29.5R25 XADN E3T TL 200B tyre [44]*

APPENDIX D

Reproduction of section of reference [52] concerning Tire Radial Damping

7. OSCILLATORY TYRE IN-PLANE BEHAVIOUR

In this chapter the response of the axle forces F_x and F_z to in-plane axle motions (x, z) , road wavyness and tyre non-uniformities will be discussed. For a given tyre-wheel combination the response depends on rolling speed and frequency of excitation. This dependence, however, appears to be of much greater significance for the fore and aft force variation F_x than for the vertical load variation F_z .

An extensive experimental study on radial and lateral force variations due to vertical axle motions has been conducted by Fritz [7.1]. Experiments and theoretical analysis of the longitudinal force response to vertical axle motions have been reported in [7.2] and [7.3].

From the discussion of vertical force response we will gradually pass to the treatment of longitudinal force response. The vertical force response has a component due to hysteresis. The same mechanism is responsible for the generation of (at least an important portion of) the rolling resistance. A far more important coupling between vertical and longitudinal forces is due to the variation of the effective rolling radius of the tyre with fluctuating vertical deflections.

7.1 VERTICAL DAMPING AND ROLLING RESISTANCE VARIATIONS DUE TO TYRE HYSTERESIS

The rolling motion of the elastic tyre involves a continuous deformation process which through internal hysteresis induces rolling resistance. A model which provides a fair representation of the mechanism is shown in Fig. 7.1. A large number of radial dampers are thought to connect wheel rim and tread band. They will be considered as dry (Coulomb) friction elements. Deformations are assumed to take place only in the contact region. With this model it is intended to examine the effect of the rolling speed, \dot{R} , on the response of both the longitudinal resistance force, F_x , and the vertical force component due to hysteresis $F_{z,hys}$ to the time rate of change of the vertical tyre deflection, $\dot{\delta}$.

First consider the simple case of straight forward motion without vertical axle motion ($\dot{\delta} = 0$). Then the deformation rate shows an anti-symmetric distribution along the contact length. The resulting vertical force due to hysteresis is zero while the resulting longitudinal force acting from ground to tyre obtains a value different from zero and is directed rearwards. This rolling resistance force (which we shall call $F_{r,s}$) equals for the model:

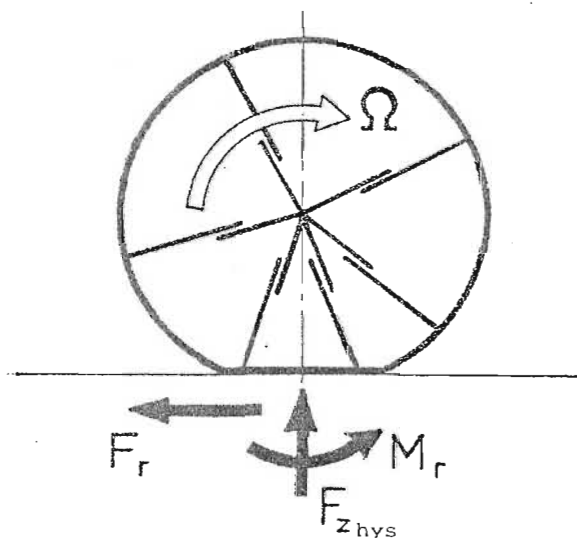


Fig. 7.1 In-plane hysteresis model of the tyre.

$$\begin{aligned}
 F_r = F_{r,s} &= K \int_{-\arctan a/r}^{\arctan a/r} |\sin \theta| d\theta \\
 &= 2K \left(1 - \frac{r}{\sqrt{r^2 + a^2}} \right) = 2K \left(1 - \frac{r}{r_f} \right) \\
 &\approx K \left(\frac{a}{r_f} \right)^2
 \end{aligned} \tag{7.1}$$

where K denotes the radially directed frictional force per unit angle of revolution and contact length $2a$ is assumed small with respect to the free tyre radius r_f .

If a quadratic relationship between a and ρ and a linear load-deflection relationship are assumed [7.4] we may write:

$$F_r = F_{r,s} = a_r \rho = A_r F_z \tag{7.2}$$

with a_r and A_r considered as constants. A_r is known as the rolling resistance coefficient.

For a standing tyre ($\Omega=0$) the distribution of the deflection rate along the contact length becomes symmetric, which causes the longitudinal force F_r to vanish. The vertical hysteresis force becomes:

$$F_{z,hys} = F_{z,hys,o} = 2K \frac{a}{r_f} \operatorname{sgn} \dot{\rho} \quad (7.3)$$

in which a is a function of ρ .

Now consider a combination of vertical deflection rate $\dot{\rho}$ and rolling speed Ω . In Fig. 7.2 the resulting distributions of vertical (or almost radial) deflection rates, V_d , and of vertical and longitudinal components of hysteresis forces acting upon the tyre, $q_{z,hys}$ and $q_{x,hys}$ respectively, have been shown. The resulting rolling resistance force is obtained from the integral

$$F_r = - \frac{K}{r_f^2} \left(\int_{-a}^e x dx - \int_e^a x dx \right) = \frac{K}{r_f^2} (a^2 - e^2) \quad (7.4)$$

where the distance, e , indicates the point where $V_d = e \Omega + \dot{\rho} = 0$.

We obtain for $|\dot{\rho}| \leq a \Omega$ in which range $|e| \leq a$:

$$F_r = K \left(\frac{a}{r_f} \right)^2 \left\{ 1 - \left(\frac{\dot{\rho}}{a\Omega} \right)^2 \right\} = a_r \rho \left\{ 1 - \left(\frac{\dot{\rho}}{a\Omega} \right)^2 \right\}. \quad (7.5)$$

At relatively large deflection rates or small rolling speeds $|\dot{\rho}| > a \Omega$, we have $|e| > a$ and a vanishing rolling resistance

$$F_r = 0 \quad (7.6)$$

which obviously is the result of the uniform direction of V_d .

In Fig. 7.3a the rolling resistance force F_r has been plotted as a function of the instantaneous value of $\dot{\rho}$ divided by $a \Omega$. The average value of the rolling resistance, $F_{r,ave}$, has been calculated for a sinusoidal variation of $\dot{\rho} = \dot{\rho} \cos \omega t$. At small deflection variations, with $|\dot{\rho}| \ll a\Omega$, F_r quickly approaches the steady-state value $F_{r,s}$ which is a function of ρ according to Eq. (7.2). Only at low Ω and relatively high frequencies ω larger values of $\dot{\rho}/a\Omega$ are attained and small values of F_r obtained. The reduction

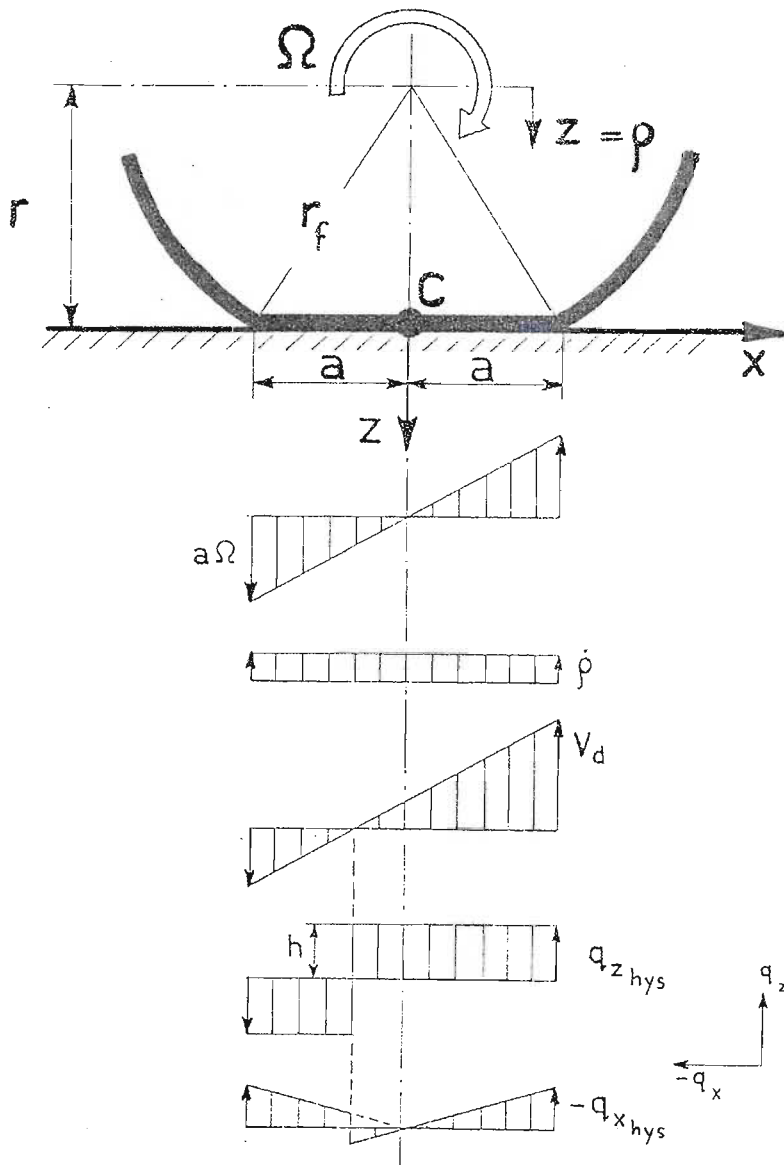


Fig. 7.2 Approximate distribution of radial damper velocity V_d , normal force $q_{z,hys}$ and longitudinal force $q_{x,hys}$.

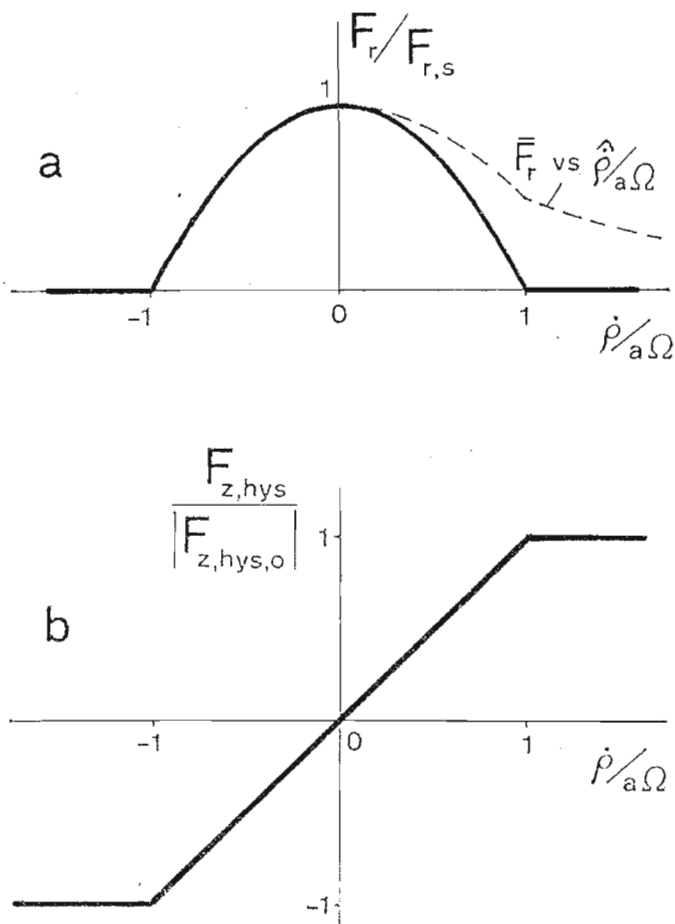


Fig. 7.3 Variations of the instantaneous rolling resistance force and the hysteresis component of the vertical load as a function of the radial deflection rate as a ratio to the speed of rolling. \bar{F}_r denotes the F_r value averaged over a period.

of F_r due to radial deflection rates $\dot{\rho}$ is small under normal conditions and will be neglected in the sequel.

The rolling resistance moment M_r maintains the equilibrium of the lower portion of the tread band (and of the wheel as a whole). Hence

$$M_r = rF_r \tag{.7.7}$$

with r denoting the axle height.

The vertical hysteresis force is obtained with the integral

$$F_{z,hys} = -\frac{K}{r} \left(\int_{-a}^e dx - \int_a^e dx \right) = -2 \frac{e}{r} K \quad (7.8)$$

which becomes for $|\dot{\rho}| \leq a\Omega$

$$F_{z,hys} = 2 \frac{K}{r} \frac{\dot{\rho}}{\Omega} \quad (7.9)$$

and for $|\dot{\rho}| > a\Omega$:

$$F_{z,hys} = 2K \frac{a}{r} \cdot \text{sgn } \dot{\rho}. \quad (7.10)$$

Fig. 7.3b shows the function of $F_{z,hys}$ divided by $|F_{z,hys,o}| = 2K a/r$. It is seen that the damping of the unsprung mass-tyre system will be very low indeed at normal operating conditions. For instance at deflection rate amplitudes $\hat{\rho} = \omega \hat{\rho} = \Omega \hat{\rho}$ with a deflection amplitude $\hat{\rho} = 0.2a$ we get for the abscissa a maximum value $\hat{\rho}/a\Omega = 0.2$ which corresponds to a maximum hysteresis force equal to only one fifth of the maximum available force with a standing tyre.

The total hysteresis force behaves like a force due to viscous damping up to the deflection velocity $\dot{\rho} = a\Omega$. From Eq. (7.9) the damping coefficient may be derived:

$$k = \frac{2K}{r\Omega} \quad (7.11)$$

which reduces with increasing Ω . This finding that at higher speeds the damping of the tyre becomes very low corresponds with experimental evidence (cf. Hahn [7.1]).

7.2 EFFECTIVE ROLLING RADIUS VARIATIONS AT FREE ROLLING AND LONGITUDINAL SLIP

Effective rolling radius

For a wheel with tyre which is uniform and which rolls freely at constant speed over an even horizontal road, the tractive force required is due to rolling resistance alone. Under these conditions, the effective rolling radius, r_e , relates speed of rolling, Ω , and forward speed, V :

APPENDIX E

E-1. ADAMS Road Data File (.rdf file) for a Trapezoidal Cross-section Bump

```

! -----
! | ROAD DATA FILE |
! -----
!
! Trapezoidal Cross-section Bump
!
METHOD
GENDATA
!
! Conversion factors
!
X_SCALE
1.0
Y_SCALE
1.0
Z_SCALE
1.0
!
!Road origin is located at the following global coordinates in the
!data set.
!
ORIGIN
0 0 0
!
!Road coordinate system is oriented with respect to the global origin
!by the following transformation matrix.
!
ORIENTATION
1 0 0
0 1 0
0 0 1
!
!Coordinates for the node points on road
!
NODES
12
1 -20.00 0.00 -25.00
2 -20.00 0.00 25.00
3 90.00 0.00 25.00
4 90.00 0.00 -25.00
5 90.12 0.12 -5.00
6 90.12 0.12 25.00
7 90.88 0.12 25.00
8 90.88 0.12 -25.00
9 91.00 0.00 -25.00
10 91.00 0.00 25.00
11 191.00 0.00 25.00
12 191.00 0.00 -25.00

```

!Connectivity of node points defining the triangular element
!

ELEMENTS

10				
1	2	4	1.00	1.00
2	3	4	1.00	1.00
3	4	6	1.00	1.00
4	5	6	1.00	1.00
5	6	8	1.00	1.00
6	7	8	1.00	1.00
7	8	10	1.00	1.00
8	9	10	1.00	1.00
9	10	12	1.00	1.00
10	11	12	1.00	1.00

E-2. ADAMS Road Data File (.rdf file) for a Smooth Bump

```

! -----
! | ROAD DATA FILE |
! -----
!
! SMOOTH BUMP - BELL B40C ADT MODEL
!
METHOD
GENDATA
!
! Conversion factors
!
X_SCALE
1.00
Y_SCALE
1.00
Z_SCALE
1.00
!
! Road origin is located at the following global coordinates in the
! data set.
!
ORIGIN
0 0 0
!
! Road coordinate system is oriented with respect to the global origin
! by the following transformation matrix.
!
ORIENTATION
1 0 0
0 0 1
0 1 0
!
! Coordinates for the node points on road
!
NODES
30
1 -20.00 -25.00 0.00
2 -20.00 25.00 0.00
3 195.00 -25.00 0.00
4 195.00 25.00 0.00
5 197.50 -25.00 0.00
6 197.50 25.00 0.00

```


7	200.00	-25.00	0.00
8	200.00	25.00	0.00
9	200.10	-25.00	0.02
10	200.10	25.00	0.02
11	200.20	-25.00	0.03
12	200.20	25.00	0.03
13	200.30	-25.00	0.06
14	200.30	25.00	0.06
15	200.40	-25.00	0.11
16	200.40	25.00	0.11
17	200.50	-25.00	0.12
18	200.50	25.00	0.12
19	200.60	-25.00	0.11
20	200.60	25.00	0.11
21	200.70	-25.00	0.06
22	200.70	25.00	0.06
23	200.80	-25.00	0.03
24	200.80	25.00	0.03
25	200.90	-25.00	0.02
26	200.90	25.00	0.02
27	201.00	-25.00	0.00
28	201.00	25.00	0.00
29	500.00	-25.00	0.00
30	500.00	25.00	0.00

!

! Element Connectivity

!

ELEMENTS

28

1	2	3	1.00	1.00
2	4	3	1.00	1.00
3	4	5	1.00	1.00
4	6	5	1.00	1.00
5	6	7	1.00	1.00
6	8	7	1.00	1.00
7	8	9	1.00	1.00
8	10	9	1.00	1.00
9	10	11	1.00	1.00
10	12	11	1.00	1.00
11	12	13	1.00	1.00
12	14	13	1.00	1.00
13	14	15	1.00	1.00
14	16	15	1.00	1.00
15	16	17	1.00	1.00
16	18	17	1.00	1.00
17	18	19	1.00	1.00
18	20	19	1.00	1.00
19	20	21	1.00	1.00
20	22	21	1.00	1.00
21	22	23	1.00	1.00
22	24	23	1.00	1.00
23	24	25	1.00	1.00
24	26	25	1.00	1.00
25	26	27	1.00	1.00
26	28	27	1.00	1.00
27	28	29	1.00	1.00
28	30	29	1.00	1.00

E-3. ADAMS Road Data File (.rdf file) for the BELL EQ. Test Track in Richards Bay

```

! -----
! | ROAD DATA FILE |
! -----
!
! BELL EQUIPMENT TEST TRACK
!
METHOD
GENDATA
!
! Conversion factors
!
X_SCALE
1.0
Y_SCALE
1.0
Z_SCALE
1.0
!
!Road origin is located at the following global coordinates in the
!data set.
!
ORIGIN
0 0 0
!
!Road coordinate system is oriented with respect to the global origin
!by the following transformation matrix.
!
ORIENTATION
1 0 0
0 0 1
0 1 0
!
!Coordinates for the node points on road
!
NODES
152

1 98.646248 10.515409 0.148309
2 103.251752 6.638591 0.407691
3 105.329041 18.454008 0.329250
4 109.890959 14.525992 0.420750
5 111.854041 26.032008 0.300318
6 116.415959 22.103992 0.411682
7 118.379041 33.610008 0.351716
8 122.940959 29.681992 0.402284
9 124.903893 41.187835 0.242324
10 129.466107 37.260165 0.415676
11 131.437119 48.776502 0.183890
12 135.980881 44.827498 0.460110
13 137.791130 56.058876 -0.000877
14 142.746870 52.641124 0.622877
15 143.188766 63.802478 -0.229922
16 148.669234 61.311522 0.639922
17 147.101817 72.253080 -0.548360
18 152.980183 70.954920 0.532360
19 149.179823 81.495139 -0.926916
20 155.188177 81.120861 0.300916
21 149.827770 90.811382 -0.981618
22 155.780230 91.710618 0.003618

```

23	148.512264	100.023829	-1.090442
24	154.115736	102.224171	-0.151558
25	145.205285	108.642292	-1.257548
26	150.196715	112.007708	-0.298452
27	139.849293	116.626298	-1.325515
28	144.392707	120.575702	-0.482485
29	133.542999	123.911656	-1.375424
30	137.601001	128.358344	-0.708576
31	126.237913	130.580390	-1.468044
32	130.148087	135.157610	-0.977956
33	118.640281	137.070815	-1.448975
34	122.539719	141.657185	-1.109025
35	111.023548	143.546739	-1.530397
36	114.920452	148.135261	-1.161603
37	103.400575	150.020716	-1.616618
38	107.297425	154.609284	-1.215382
39	95.778575	156.493716	-1.689607
40	99.675425	161.082284	-1.306393
41	88.156575	162.966716	-1.743679
42	92.053425	167.555284	-1.398321
43	80.534723	169.439590	-1.808449
44	84.431277	174.028410	-1.495551
45	72.911575	175.912716	-1.904051
46	76.808425	180.501284	-1.589949
47	65.289575	182.385716	-1.994326
48	69.186425	186.974284	-1.703674
49	57.667400	188.858865	-2.108294
50	61.564600	193.447135	-1.743706
51	50.045723	195.332590	-2.214943
52	53.942277	199.921410	-1.729057
53	42.590839	201.672836	-2.349959
54	46.151161	206.527164	-1.710041
55	34.724012	207.453593	-2.533539
56	37.901988	212.566407	-1.668461
57	26.942762	212.409668	-2.582843
58	28.697238	218.168332	-1.667157
59	18.181051	215.185795	-2.706334
60	18.388949	221.202205	-1.765666
61	8.684008	215.553467	-2.770367
62	7.917992	221.524533	-1.885633
63	-0.607331	214.423515	-2.728939
64	-2.558669	220.118485	-1.837061
65	-9.569275	211.403537	-2.565239
66	-12.502725	216.660463	-1.762761
67	-17.819134	206.848827	-2.400509
68	-21.592866	211.539173	-1.723491
69	-25.467298	200.702018	-2.269343
70	-29.510702	205.161982	-1.784657
71	-32.876148	193.985154	-2.094073
72	-36.919852	198.444846	-1.755927
73	-40.266378	187.284396	-1.969634
74	-44.345622	191.711604	-1.672366
75	-47.618965	180.509699	-1.838634
76	-51.701035	184.934301	-1.541366
77	-54.969127	173.728549	-1.713078
78	-59.050873	178.153451	-1.368922
79	-62.318965	166.948699	-1.600500
80	-66.401035	171.373301	-1.227500
81	-69.669127	160.167549	-1.501813
82	-73.750873	164.592451	-1.110187
83	-77.019277	153.387411	-1.440941

84 -81.100723 157.812589 -0.979059
 85 -84.356075 146.620595 -1.351843
 86 -88.465925 151.019405 -0.846157
 87 -91.509598 139.947747 -1.297167
 88 -95.926402 144.038253 -0.544833
 89 -98.025408 132.956380 -1.233114
 90 -102.974592 136.383620 -0.360886
 91 -103.326714 125.518477 -1.095348
 92 -109.045286 127.399523 -0.232652
 93 -106.317404 116.600487 -1.142029
 94 -112.288596 117.365513 -0.273971
 95 -107.565587 107.252112 -1.218165
 96 -113.576413 106.919888 -0.307835
 97 -107.121965 97.944749 -1.128283
 98 -112.920035 96.325251 -0.275717
 99 -104.623163 88.830818 -1.060554
 100 -110.054837 86.235182 -0.263446
 101 -100.669307 80.384148 -0.934659
 102 -105.392693 76.651852 -0.139341
 103 -94.837320 72.935622 -0.799645
 104 -98.872680 68.468378 -0.148355
 105 -87.663687 66.435377 -0.704043
 106 -91.234313 61.588623 -0.219957
 107 -79.690387 60.559672 -0.731743
 108 -83.111613 55.606328 -0.236257
 109 -71.420655 54.847323 -0.593816
 110 -74.925345 49.952677 -0.196184
 111 -63.289314 49.025078 -0.480984
 112 -66.794686 44.130922 -0.227016
 113 -55.159513 43.202221 -0.441894
 114 -58.664487 38.307779 -0.180106
 115 -47.029513 37.380221 -0.465975
 116 -50.534487 32.485779 -0.126025
 117 -38.899655 31.558323 -0.486299
 118 -42.404345 26.663677 -0.115701
 119 -30.768513 25.736221 -0.448985
 120 -34.273487 20.841779 -0.097015
 121 -22.638314 19.914078 -0.366264
 122 -26.143686 15.019922 -0.037736
 123 -14.508655 14.091323 -0.312368
 124 -18.013345 9.196677 0.020368
 125 -6.377513 8.269221 -0.246397
 126 -9.882487 3.374779 0.122397
 127 1.752487 2.447221 -0.197314
 128 -1.752487 -2.447221 0.197314
 129 9.882345 -3.374677 -0.155128
 130 6.377655 -8.269323 0.267128
 131 18.013686 -9.196922 -0.217803
 132 14.508314 -14.091078 0.377803
 133 25.533339 -14.682191 -0.258811
 134 23.248661 -20.251809 0.516811
 135 34.338857 -18.330364 -0.245687
 136 32.907143 -24.177636 0.605687
 137 43.492791 -20.626139 -0.169334
 138 43.177209 -26.637861 0.771334
 139 52.778820 -21.194503 -0.040187
 140 53.855180 -27.117497 0.780187
 141 62.040572 -19.569940 0.005697
 142 64.249428 -25.170060 0.784303
 143 70.683122 -16.249941 0.086982
 144 74.134878 -21.182059 0.661018

```

145 78.539759 -10.781232 0.076760
146 82.590241 -15.234768 0.599240
147 85.707836 -4.280194 0.126357
148 90.162164 -8.329806 0.599643
149 92.206180 2.864330 -0.032530
150 96.811820 -1.012330 0.394530
151 98.646180 10.515330 0.148309
152 103.251820 6.638670 0.407691

```

```

!
!Connectivity of node points defining the triangular element
!

```

```

ELEMENTS

```

```

150

```

```

1 2 3      1      1
4 3 2      1      1
3 4 5      1      1
6 5 4      1      1
5 6 7      1      1
8 7 6      1      1
7 8 9      1      1
10 9 8     1      1
9 10 11    1      1
12 11 10   1      1
11 12 13   1      1
14 13 12   1      1
13 14 15   1      1
16 15 14   1      1
15 16 17   1      1
18 17 16   1      1
17 18 19   1      1
20 19 18   1      1
19 20 21   1      1
22 21 20   1      1
21 22 23   1      1
24 23 22   1      1
23 24 25   1      1
26 25 24   1      1
25 26 27   1      1
28 27 26   1      1
27 28 29   1      1
30 29 28   1      1
29 30 31   1      1
32 31 30   1      1
31 32 33   1      1
34 33 32   1      1
33 34 35   1      1
36 35 34   1      1
35 36 37   1      1
38 37 36   1      1
37 38 39   1      1
40 39 38   1      1
39 40 41   1      1
42 41 40   1      1
41 42 43   1      1
44 43 42   1      1
43 44 45   1      1
46 45 44   1      1
45 46 47   1      1

```

48	47	46	1	1
47	48	49	1	1
50	49	48	1	1
49	50	51	1	1
52	51	50	1	1
51	52	53	1	1
54	53	52	1	1
53	54	55	1	1
56	55	54	1	1
55	56	57	1	1
58	57	56	1	1
57	58	59	1	1
60	59	58	1	1
59	60	61	1	1
62	61	60	1	1
61	62	63	1	1
64	63	62	1	1
63	64	65	1	1
66	65	64	1	1
65	66	67	1	1
68	67	66	1	1
67	68	69	1	1
70	69	68	1	1
69	70	71	1	1
72	71	70	1	1
71	72	73	1	1
74	73	72	1	1
73	74	75	1	1
76	75	74	1	1
75	76	77	1	1
78	77	76	1	1
77	78	79	1	1
80	79	78	1	1
79	80	81	1	1
82	81	80	1	1
81	82	83	1	1
84	83	82	1	1
83	84	85	1	1
86	85	84	1	1
85	86	87	1	1
88	87	86	1	1
87	88	89	1	1
90	89	88	1	1
89	90	91	1	1
92	91	90	1	1
91	92	93	1	1
94	93	92	1	1
93	94	95	1	1
96	95	94	1	1
95	96	97	1	1
98	97	96	1	1
97	98	99	1	1
100	99	98	1	1
99	100	101	1	1
102	101	100	1	1
101	102	103	1	1
104	103	102	1	1
103	104	105	1	1
106	105	104	1	1
105	106	107	1	1
108	107	106	1	1

107	108	109	1	1
110	109	108	1	1
109	110	111	1	1
112	111	110	1	1
111	112	113	1	1
114	113	112	1	1
113	114	115	1	1
116	115	114	1	1
115	116	117	1	1
118	117	116	1	1
117	118	119	1	1
120	119	118	1	1
119	120	121	1	1
122	121	120	1	1
121	122	123	1	1
124	123	122	1	1
123	124	125	1	1
126	125	124	1	1
125	126	127	1	1
128	127	126	1	1
127	128	129	1	1
130	129	128	1	1
129	130	131	1	1
132	131	130	1	1
131	132	133	1	1
134	133	132	1	1
133	134	135	1	1
136	135	134	1	1
135	136	137	1	1
138	137	136	1	1
137	138	139	1	1
140	139	138	1	1
139	140	141	1	1
142	141	140	1	1
141	142	143	1	1
144	143	142	1	1
143	144	145	1	1
146	145	144	1	1
145	146	147	1	1
148	147	146	1	1
147	148	149	1	1
150	149	148	1	1
149	150	151	1	1
152	151	150	1	1

REFERENCES

- [1] **Ageikin, Ia.S.** – *Off the Road Mobility of Automobiles*. New Delhi: Oxford and IBH Publishing Co. (1987)
- [2] **Allan, A.B., El Madanay, M.M. and Dokanish, M.A.** – “Articulated Vehicle Models” (SAE Paper 801420). Warrendale, Pa : Society of Automotive Engineers (1980)
- [3] **Allison, D.J. and Sharp, R.S.** – “On the Low Frequency In-Plane Forced Vibrations of Pneumatic Tyre / Wheel / Suspension Assemblies” in *Tyre Models for Vehicle Dynamic Analysis, Supplement to Vehicle System Dynamics, Volume 27*. (eds. *Bohm, F and Willumiet, H.P.*) Netherlands: Swets and Zeitlinger B.V. (1997)
- [4] **Barak, P.** – “Magic Numbers in Design of Suspensions for Passenger Cars.” (SAE Paper 911921). Warrendale, Pa: Society of Automotive Engineers. (1991)
- [5] **Barber, A.J.** – “Accurate Models for Bushings and Dampers using the Empirical Dynamics Method” in *Proceedings of International ADAMS User Conference*. Berlin: 17-19 November (1999)
- [6] **Bendat, J. S.** – *Nonlinear System Techniques and Applications*. New York: John Wiley & Sons, Inc. (1998).
- [7] **Berg, M.** – “A Non-Linear Rubber Spring Model for Rail Vehicle Dynamics Analysis”, in *Vehicle System Dynamics, Vol. 30*. Lisse: Swets and Zeitlinger. (1998)
- [8] **Da Cunha, R.H., Neto Á.C., Orado, M., Persegum, O.T. and Spinelli, D.M.** – “Handling Analysis of a Three-Axle Intercity Bus” in *Proceedings of 16th European ADAMS User Conference*. Berchtesgaden, Germany: 14-15 November (2001)
- [9] **Dennehy, D. J and R. P. Jones** – “Drive-by-tire”, in *Tire Technology International 2001: The Annual Review of Tire Materials and Tire Manufacturing Technology*. United Kingdom: UK & International Press (2001)
- [10] **Dieterich, J. S., Pelz, W. and Pottinger, M.G.** – “The BNPS Model – An Automated Implementation of the Magic Formula Concept” - SAE Paper 931909. Warrendale, Pa: Society of Automotive Engineers. (1993)
- [11] **Dixon, John C.** – *Tires, Suspension and Handling, Second Edition*. USA: Society of Automotive Engineers. (1996)
- [12] **Dutton, K., Thompson, S. and Barraclough, B.** – *The Art of Control Engineering*. United Kingdom: Addison Wesley Longman (1997)
- [13] **El-Gindy, M.** – “High Speed Predictions” in *Tire Technology International*. United Kingdom: UK & International Press, December (2000)

- [14] **Elliott A., Wheeler G. and Hodges H** – “Validation of ADAMS Models of Two USMC Heavy Logistic Vehicle Design Variants” in *Proceedings of 15th European ADAMS User Conference*. Rome: 15-16 November (2000)
- [15] **Ervin R.D., Winkler C.B., Bernard J.E. and Gupta R.K** – *Effects of Tire Properties on Truck and Bus Handling*. Washington: U.S. Government Printing Office (1976)
- [16] **Ewins, D.J.** – *Modal Testing: Theory and Practice*. England: Research Studies Press, Ltd. (1984)
- [17] **Fuller, D.L., Hall, G.L. and Conant F.S.** – “Effects of Testing Conditions on Rolling Resistance of Automobile Tires”, in *SAE Technical Paper Series*. USA: Society of Automotive Engineers (1984)
- [18] **Galganski, R.A.** – “Slippery when wet” in *Testing Technology International*. United Kingdom: UK & International Press, February (2000)
- [19] **Gan, H** – “An Integrated Multi-axial Force Model for Rubber Mount and Bushing” in *Proceedings of the 17th European ADAMS User Conference*. London, United Kingdom: December 2002
- [20] **Gerald, C.F. and Wheatley, P.O.** – *Applied Numerical Analysis, 5th Edition*. New York: Addison-Wesley Publishing Company (1970)
- [21] **Gillespie, T.D.** – *Fundamentals of Vehicle Dynamics*. USA: Society of Automotive Engineers, Inc. (1992)
- [22] **Govender, D.** – “Investigation of Data Acquisition Systems for the measurements system required for the Bell Equipment/University of Natal, B40C Articulated Dump Truck Virtual Prototyping Project.” Unpublished report (2000)
- [23] **Gunter, D.** – “Turn for the Better” in *Tire Technology International*. United Kingdom: UK & International Press, December (1999)
- [24] **Hanley, R. and Crolla, D.** – “Tire Modelling for Misuse Situations” in *Tire Technology International 2001: The Annual Review of Tire Materials and Tire Manufacturing Technology*. United Kingdom: UK & International Press (2001)
- [25] **Harris, J. and Stevenson, A.** – “On the roll of non-linearity in the dynamic behaviour of rubber components” in *Int. Journal of Vehicle Design, Vol. 8 No. 2*. United Kingdom: Inderscience Enterprises (1987)
- [26] **Heisler, H.** – *Advanced Vehicle Technology*. London: Edward Arnold (1989)
- [27] **Heltman, H.** – Discussion of calculations of stiffness and damping of rubber components from test data (2002)
- [28] **Heydinger, G. J.** – “Measured Success,” in *Testing Technology International*. United Kingdom: UK & International Press, February (2000)
- [29] **Higuchi, A. and Pacejka, H.B.** – “The Relaxation Length Concept at Large Wheel Slip and Camber” in *Tyre Models for Vehicle Dynamic Analysis, Vehicle System*

- Dynamics Vol. 27* (eds. Bohm, F and Willumiet, H.P.) (pp. 50-64). Netherlands: Swets & Zeitlinger (1997)
- [30] **Holdmann, P., Köhn, P. & Holtschulze, J.** – “Dynamic Tyre Properties Under Combined Slip Situations in Test and Simulation” taken from <http://www.ika.rwth-aachen.de/publikat/ph0799a/index.htm> (1999)
- [31] **Ifeachor, E.C. and Jervis, B.W.** – *Digital Signal Processing, A Practical Approach*. United Kingdom: Addison Wesley Longman Limited (1993)
- [32] **Inman, D.J.** – *Engineering Vibration*. New Jersey: Prentice-Hall, Inc. (1996)
- [33] **Kaczmarczyk, S.** – “The Analysis of the Resonance Bounce and Pitch Motion of the B40B Truck”. Unpublished paper, University of Natal, Durban, South Africa (1999)
- [34] **Kao, B.G., Loh, W.Y. and Greenberg, J.A.** – “A 3-D Dynamic Tire Model for Vehicle Handling Analysis,” in *Tire Technology International 2001: The Annual Review of Tire Materials and Tire Manufacturing Technology*. United Kingdom: UK & International Press, (2001)
- [35] **Kortum, W.** – “Review of Multibody Computer Codes for Vehicle System Dynamics” in *Multibody Computer Codes in Vehicle System Dynamics, Supplement to Vehicle System Dynamics, Volume 22*. (eds. Kortüm, W. and Sharp, R.S.) (pp. 3 –31). Amsterdam: Swets & Zeitlinger, (1993)
- [36] **Lai, E.** – “Practical Digital Signal Processing for Engineers and Technicians,” course notes. South Africa: IDC Technologies (2000)
- [37] **Lidner, L.** – “Experience with the Magic Formula Tyre Model” in *Tyre Models for Vehicle Dynamics Analysis, supplement to Vehicle System Dynamics, Vol. 21* (pp. 30-48) (Ed. H.B. Pacejka). Netherlands: Swets and Zeitlinger B.V. (1991)
- [38] **Mancuso, F** – “Overview of VERT Project: Prediction of Full Vehicle Behaviour in Dangerous Situations,” in *Proceedings of 16th European ADAMS User Conference*. Berchtesgaden, Germany: 14-15 November (2001)
- [39] **Maurice, J.P** – “Short Wavelength and Dynamic Tyre Behaviour under Lateral and Combined Slip Conditions” (PhD Thesis Abstract), taken from <http://www.wbmt.tudelft.nl/tt/vehicle/PAPERS/JPSummar.html> (2000)
- [40] **McBeath, S.** – “Virtually Physical,” in *Testing Technology International*. United Kingdom: UK & International Press, February (2000)
- [41] **Mechanical Dynamics Inc.** – *Using ADAMS/Solver*. USA: Mechanical Dynamics Inc. (2001)
- [42] **Mechanical Dynamics Inc.** – *Using ADAMS/View*. USA: Mechanical Dynamics Inc. (2001)

- [43] **Mechanical Dynamics Inc.** – *Basic Adams Full Simulation Package: Training Guide, Version 10.* USA: Mechanical Dynamics Inc. (1999)
- [44] **Michelin** – Technical Characteristics of the 29.5 R 25 XADN E3T TL 200B Earthmoving Machinery Tire – *Michelin Corporation internal test documents* (1997)
- [45] **Meriam, J.L. and Kraige, L.G.** – *Engineering Mechanics – Dynamics, Fourth Edition.* New York : John Wiley and Sons, Inc (1998)
- [46] **Milliken, W. F. and Milliken, D.A.** – *Race Car Vehicle Dynamics.* USA: Society of Automotive Engineers, Inc. (1995)
- [47] **MSC Software** – “Article 8978 – Computing the Derivative of a Run-time Function”. *ADAMS Knowledge Base Article*, taken from <http://support.adams.com/kb> (2000)
- [48] **Negrut, D. and Freeman J.S.** – “Dynamic Tire Modelling for Application with Vehicle Simulations Incorporating Terrain” (SAE Paper 940223). Warrendale, Pa: Society of Automotive Engineers. (1994)
- [49] **Newland, D.E.** – *An Introduction to Random Vibrations, Spectral and Wavelet Analysis, 3rd Edition.* United States: Longman Scientific and Technical (1993)
- [50] **Okano, T. and Koishi, M.** – “Treading Water” in *Tire Technology International.* United Kingdom: UK & International Press, December (2000)
- [51] **Orlande, N.V.** – “ADAMS Theory and Application” in *Third Seminar on Advanced Vehicle System Dynamics, Supplement to Vehicle System Dynamics Vol. 16* (eds. De Pater, A.D. and Pacejka, H.B.) (pp. 121-166). Lisse: Swets and Zeitlinger (1987)
- [52] **Pacejka, H.B.** – “Tyre Mechanics and Its Impact on Vehicle Dynamics: A Three Day Course in Collaboration with the Open University,” 21-23 March 1983. The International Association for Vehicle Design (1983)
- [53] **Pacejka, H.B.** – “The Role of Tyre Dynamic Properties” in *Smart Vehicles* (eds. Pauwelussen, J.P. & Pacejka, H.B.) Netherlands: Swets & Zeitlinger B.V (1997)
- [54] **Pacejka, H.B.** – “Lateral Dynamics of Road Vehicles” in *Third Seminar on Advanced Vehicle System Dynamics, Supplement to Vehicle System Dynamics Vol. 16* (eds. De Pater, A.D. and Pacejka, H.B.) (pp. 75-120). Lisse: Swets and Zeitlinger, (1987)
- [55] **Pacejka, H.B. and Bakker, E.** – “The Magic Formula Tyre Model” in *Tyre Models for Vehicle Dynamics Analysis, Supplement to Vehicle System Dynamics, Vol. 21* (ed. H.B. Pacejka) (pp. 1-18) Netherlands: Swets and Zeitlinger B.V. (1991)

- [56] **Pacejka, H.B. and Besselink, I.J.M.** – “Magic Formula Tyre Model with Transient Properties” in *Tyre Models for Vehicle Dynamic Analysis, Vehicle System Dynamics Vol. 27* (eds. Bohm, F and Willumiet, H.P.) (pp. 234-249) Netherlands: Swets & Zeitlinger (1997)
- [57] **Paulstra Automotive** – “Modelling of Automotive Antivibration Rubber Parts” in *Proceedings of the 13th European ADAMS User Conference*, Paris: 18-19 November. (1998)
- [58] **Pauwelussen. J.P.** – “Dutch Tests” in *Tire Technology International*. (pp 24-28) United Kingdom: UK & International Press December (1999)
- [59] **Prado, M., Cunha, R.H., Neto, Á.C., Costa, A. and D’Elboux, J.E.** – “Bus Handling Validation and Analysis Using ADAMS/ Car” in *Proceedings of 16th European ADAMS User Conference*. Berchtesgaden, Germany: 14-15 November (2001)
- [60] **Raghavan, M.** – “An Atlas of Linkages for Independent Suspensions,” taken from *SAE International: The Engineering Society for Advanced Mobility Land Sea Air and Space: Passenger Car Meeting and Exposition*. Tennessee: Society of Automotive Engineers (1991)
- [61] **Ramnarain, V., Dlamini, S. and Gunaselvam, J.** – “Dynamic Testing of Automotive Components”. Unpublished undergraduate report, University of Natal, Durban, South Africa (2001)
- [62] **SAE International** – “Steady-State Circular Test Procedure for Trucks and Buses,” (SAE International: Surface Vehicle Recommended Practice, Reference: J2181) (1996)
- [63] **SAE International** – “Free Rolling Cornering Test for Truck Tires,” (SAE International: Surface Vehicle Recommended Practice, Reference: J2429) (2001)
- [64] **SAE International** – “Vehicle Dynamics Terminology.” (SAE International: Surface Vehicle Recommended Practice, Reference: J670e) (1978)
- [65] **Schade, G. and Hamill, S.** – “Vehicle Ride Analysis of a Tractor-Trailer” in *Proceedings of 15th European ADAMS User Conference*. Rome: 15-16 November (2000)
- [66] **Schieschke, R. and Hiemenz, R.** – “The Decisive Role the Quality of Tyre Approximation Plays in Vehicle Dynamics Simulations” in *Tyre Models for Vehicle Dynamics Analysis, Vehicle System Dynamics Vol. 21* (ed. H.B. Pacejka) (pp. 156-166). Netherlands: Swets & Zeitlinger (1991)
- [67] **Shabana A.A.** – *Dynamics of Multibody Systems, Second edition*. New York: Cambridge University Press (1998)
- [68] **Shah, M.** – “RDF File” – E-mail correspondence with Shah, M. of MSC Software Company. <Manish.Shah@MSCsoftware.com> (06/08/2002)

- [69] **Shoop, S., Lacombe, J. and Haehnel, R.** – “Modelling Tire Performance for winter conditions.” in *Tire Technology International*. United Kingdom: UK & International Press, December (2001)
- [70] **Sjöberg, M.** – “Rubber Component Vibrations – Frequency and Amplitude Dependence”. Licentiate Thesis, Royal Institute of Technology (KTH). ISSN 1103-470X. Stockholm (2000)
- [71] **Sjöberg, M.** – “Dynamic Behaviour of Rubber Components in the Low Frequency Range – Measurements and Modelling”. *Proceedings, International Conference of Sound and Vibration [7]* (pp. 2955-2962) (2000)
- [72] **Sjöberg, M.** – “Rubber Isolators – Measurements and Modelling using Fractional Derivatives and Friction” (SAE Paper 2000-01-3518). USA: Society of Automotive Engineers (2000)
- [73] **Slättengren, J.** – “Frequency Dependent Elements in ADAMS” in *Proceedings of 12th European ADAMS User Conference*. Marburg, Germany: 14-18 November (1997)
- [74] **Slättengren, J.** – “Tire Damping for FIALA tire file”, *Thread title on ADAMS ASK discussion forum*. <http://ask.adams.com> (20/05/2002)
- [75] **Slättengren, J.** – “Differentiation of Run-time Variables for PID Control”, *Thread title on ADAMS ASK discussion forum*. <http://ask.adams.com> (26/01/2003)
- [76] **Stejskal, Vladimír and Michael Valášek** – *Kinematic and Dynamics of Machinery*. New York: Marcel Dekker, Inc. (1996).
- [77] **Stephens, D.R., Jones, W.C. and Dryden, D.M.** – “Virtual Future at Cooper” in *Tire Technology International*. United Kingdom: UK & International Press, December (1999)
- [78] **Sternberg, E. R.** – *Heavy-Duty Truck Suspensions*. USA: Society of Automotive Engineers, Inc. (1976)
- [79] **European Tyre School** – “Truck Tire Behaviour in Use and Testing Methods” taken from <http://www.tut.fi/plastics/tyreschool/teachingmodules.html> (2000)
- [80] **Van Oosten, J.J.M., Unrau, H.J., Riedel, G. and Bakker, E.** – “TYDEX Workshop: Standardisation of Data Exchange in Tyre Testing and Tyre Modelling” in *Tyre Models for Vehicle Dynamic Analysis, supplement to Vehicle System Dynamics Vol. 27 (eds. Bohm, F and Willumiet, H.P.)* Netherlands: Swets & Zeitlinger B.V. (1997)
- [81] **Van. Oosten, J.J.M. and Bakker, E.** – “Determination of Magic Tyre Model Parameters” in *Tyre Models for Vehicle Dynamics Analysis, supplement to Vehicle System Dynamics, Vol. 21 (Ed. H.B. Pacejka)* (pp. 19-29) Netherlands: Swets and Zeitlinger B.V. (1991)

- [82] **Wallentowitz, H.** – “Hardware and Software Demands on Adjustable Shock Absorbers for Trucks and Passenger Cars”, taken from <http://www.ika.rwth-aachen.de/publikat/> (2002)
- [83] **Walton, J.S., Hirbernik, M., Davis, J.C. and Vitz, F.** – “Video-Based Measurement of Dynamic Tire Envelopes,” in *SAE International: Concepts in Vehicle Dynamics and Simulation*. Detroit: Society of Automotive Engineers (1994)
- [84] **Weitz, P.** – “Layout of Test Circuit”, Surveyed drawings of BELL EQ. Test Track by *VGC Consulting Engineers Inc.* Empangeni [Tel: +27 (0)351-926192] (2001)
- [85] **Wenzhang, Z., Guobiao, L.Y.S. and Ligong, W.** – “Study on Non-Linear Characteristics of Vehicle Suspension Rubber Component” in *Proceedings of International ADAMS User Conference*. Florida: 19-21 June (2000)
- [86] **Whittaker, W.L.** – “Out of this World” in *Tire Technology International*. United Kingdom: UK & International Press, December (2000)
- [87] **Wong, J. Y.** – *Theory of Ground Vehicles, Second Edition*. New York: John Wiley and Sons, Inc. (1993)
- [88] **Wong, J.Y.** – *Terramechanics and Off-Road Vehicles*. Amsterdam: Elsevier Science Publishers B.V. (1989)
- [89] **Zegelaar, P.W.A.** – “The Dynamic Tyre Response to Brake Torque Variations and Road Unevennesses” (PhD Thesis Abstract), taken from <http://www.wbmt.tudelft.nl/tt/vehicle/PAPERS/Zegelaar.htm> (1998)
- [90] **Zegelaar, P.W.A. and Pacejka, H.B.** – “The Dynamic Tyre Response to Brake Torque Variations” in *Tyre Models for Vehicle Dynamic Analysis, Supplement to Vehicle System Dynamics, Volume 27* (eds. Bohm, F and Willumiet, H.P.) (pp. 66-79) Netherlands: Swets and Zeitlinger B.V. (1997)